On the role of acidity in amorphous silica-alumina based catalysts

On the Role of Acidity in Amorphous Silica-Alumina Based Catalysts

PROEFSCHRIFT

ter verkrijging van de graad van doctor aan de
Technische Universiteit Eindhoven, op gezag van de
rector magnificus, prof.dr.ir. C.J. van Duijn, voor een
commissie aangewezen door het College voor
Promoties in het openbaar te verdedigen
op dinsdag 5 april 2011 om 16.00 uur

door

Dilip Gopi Poduval

geboren te Chennai, India

Dit proefschrift is goedgekeurd door de promotoren:

prof.dr. J.A.R. van Veen
en
prof.dr.ir. E.J.M. Hensen

CIP-DATA LIBRARY TECHNISCHE UNIVERSITEIT EINDHOVEN

Poduval, Dilip G.

On the role of acidity in amorphous silica-alumina based catalysts /
by Dilip G. Poduval. - Eindhoven : Technische Universiteit Eindhoven, 2011.
Proefschrift.

A catalogue record is available from the Eindhoven University of Technology Library

ISBN: 978-90-386-2455-6

Trefwoorden: heterogene katalyse / amorf silica-alumina ; synthese / zuurheid ; zwaveltolerantie
Subject headings: heterogeneous catalysis / amorphous silica-alumina ; synthesis / acidity ; sulfur tolerance

The work described in this thesis has been carried out at the Schuit Institute of Catalysis, Laboratory of Inorganic Materials Chemistry, Eindhoven University of Technology, The Netherlands. Financial support has been provided by Shell Global Solutions.

Chapter 1

On the role of acidity in amorphous silica-alumina based catalysts

Summary

Catalysis plays a very important role in the oil refining and petrochemical industry for the upgrading of hydrocarbons streams to modern transportation fuels. Amorphous silica-alumina (ASA) is widely used as a solid acid catalyst in various chemical reactions including hydrocracking, isomerization, and alkylation, which are important in the oil refining and petrochemical industry. However, the nature of the acid sites in these materials has not yet been fully understood. The primary reason for this relates to the heterogeneous composition of the surface of ASAs. The present project was undertaken with the aim to monitor the synthesis of a set of well-defined ASA materials to understand the genesis of acid sites in ASAs and establish their role in industrially relevant catalytic reactions.

1.1 Catalysis

Catalysis is a phenomenon that was first recognized around 1816 by Davy with the discovery that the oxidation of coal gas is accelarated by platinum. Although nobody at that time was able to explain the catalytic action, it was Berzelius in 1835 who coined the name 'catalysis' as a "chemical event that changes the composition of a mixture". Besides a chemical driving force, he concluded that a reaction occurred by catalytic contact. Catalysts had been used already much earlier, for instance in fermentation processes or the production of sulfuric acid. The field of catalysis developed at the end of the nineteenth century when the influence of metals and oxides on the decomposition of several substances was studied more intensively. Van 't Hoff initiated this development with the formulation of the theory of chemical equilibria. It allowed more systematic, scientifically based research that lead to the first large-sclae industrial process in 1909, the synthesis of ammonia (Haber-Bosch process). From that moment on industrial catalysis has always been closely connected with changes in society and especially with the ever increasing need for energy. Several important discoveries may be mentioned such as catalytic coal liquefaction around 1913, the Fischer-Tropsch process to convert synthesis gas to motor fuels in 1923 and the catalytic cracking of oil in 1936 [1]. After the Second War, oil became the most important source of transportation fuels and chemicals in the developed world. Modern petroleum refineries are very complex chemical plants that convert crude oil into higher value products such as LPG, gasoline, kerosene, diesel, fuel oil, but also lubricants, bitumen and feedstocks for petrochemical industries.

The current oil-based chemical industry could not have grown to its present size solely on the basis of non-catalytic stoichiometric reactions. Catalysts enable us to carry out chemical reactions under relatively mild conditions. A prime example is the synthesis of ammonia, a chemical pivotal to the population growth in the last century as it is the feedstock to produce fertilizer. Without catalyst, production of ammonia would require very high pressure. With modern catalysts, this thermodynamically limited reaction can be carried out at relatively low temperatures and medium pressures. In this particular case, the catalyst's most important role is to activate the very strong nitrogen-nitrogen bond at mild conditions. Without catalysts, many reactions that are common in the chemical industry would not be possible and many other processes would not be economically feasible.

Three types of catalysis can be distinguished. Enzymes are Nature's catalysts. They are large proteins, the structure of which results in a very shape and reactant specific active site. Having a shape that is optimally suited to guide reactant molecules, commonly named substrates in biocatalysis, in the optimum configuration for reaction, an enzyme is a highly specific and efficient catalyst. In homogeneous catalysis, both the catalyst and the reactants are in the same phase. In contrast, heterogeneous catalysis involves the catalyst and reactants in different phases and, most frequently, the reactants and products are in the gas or liquid phase with a solid catalyst. Heterogeneous catalysts are preferred in industry because of the

ease of separation of the products from the catalyst [2]. In oil refining and the petrochemical industry, the use of heterogeneous catalysts is widespread.

1.2 Oil refining

A modern refinery is a highly integrated industrial enterprise, the main purpose of which is to efficiently produce a high yield of valuable products from a crude oil feed of variable composition. Employing different physical and chemical processes such as distillation, extraction, reforming, hydrogenation, cracking and blending the refinery converts crude oil to higher value products. The main products are liquid petroleum gas, gasoline, jet fuel, diesel fuel, wax, lubricants, bitumen and petrochemicals. Energy and hydrogen for internal and external use are also produced in a refinery [3]. Because of their high energy densities and convenient physical form, petroleum products are presently consumed in vast quantities and this consumption continues to grow at alarming rates. Transportation fuels, the major petroleum products, are receiving the highest scrutiny because of the pollution from the resulting exhaust gases. Environmental restrictions regarding the quality of transportation fuels and the emissions from the refinery itself are currently the most important and most costly issues. Pollutants of major concern include SO_x, NO_x, CO, particulates, olefins and aromatic hydrocarbons. The concern over carbon dioxide emissions, inherent to the burning of petroleum products, is also growing.

Fig 1.1 shows a basic layout of a modern oil refinery. Typically, the desalted crude oil is separated into different fractions by distillation. Atmospheric distillation usually ends around 360 °C. The remaining fraction (atmospheric residue) is often separated by further vacuum distillation into vacuum gas oil (VGO) and vacuum residue. The atmospheric residue fraction may be the dominant fraction for some heavy crudes and in such cases conversion into lighter products becomes especially important. The type and concentration of hetero-atoms such as sulfur and nitrogen vary significantly between the various fractions from the initial separation section. The various product streams are further refined and modified using a wide range of catalytic processes such as hydrogenation, isomerization, aromatization, alkylation, cracking and hydrotreating. Some of these processes serve to modify the molecular weight to arrive at high-quality transportation fuels (alkylation, hydrocracking), while others aim to reduce the content of hetero-atoms, most notably sulfur, which is important to comply with environmental legislation and to protect catalysts in downstream processes. Currently, sulfur levels of 10 ppm are permitted in transportation fuels in the developed world. Processes to remove organic sulfur from refinery streams are called hydrodesulfurization (HDS) and those aiming at the removal of nitrogen hydrodenitrogenation (HDN). There is typically no change in molecule size distribution of the hydrocarbon stream in these processes. Besides increasing sulfur levels, future crudes will be heavier implying a more important role of unit operations that reduce the molecular weight of the heavy fractions from the distillation operations. Hydrocracking is such a process, which involves a boiling-point shift of heavier fractions of crude oil towards lighter product streams through sequential steps of dehydrogenation of

paraffins, β-scission of intermediate olefins and hydrogenation of the smaller olefins to paraffins.

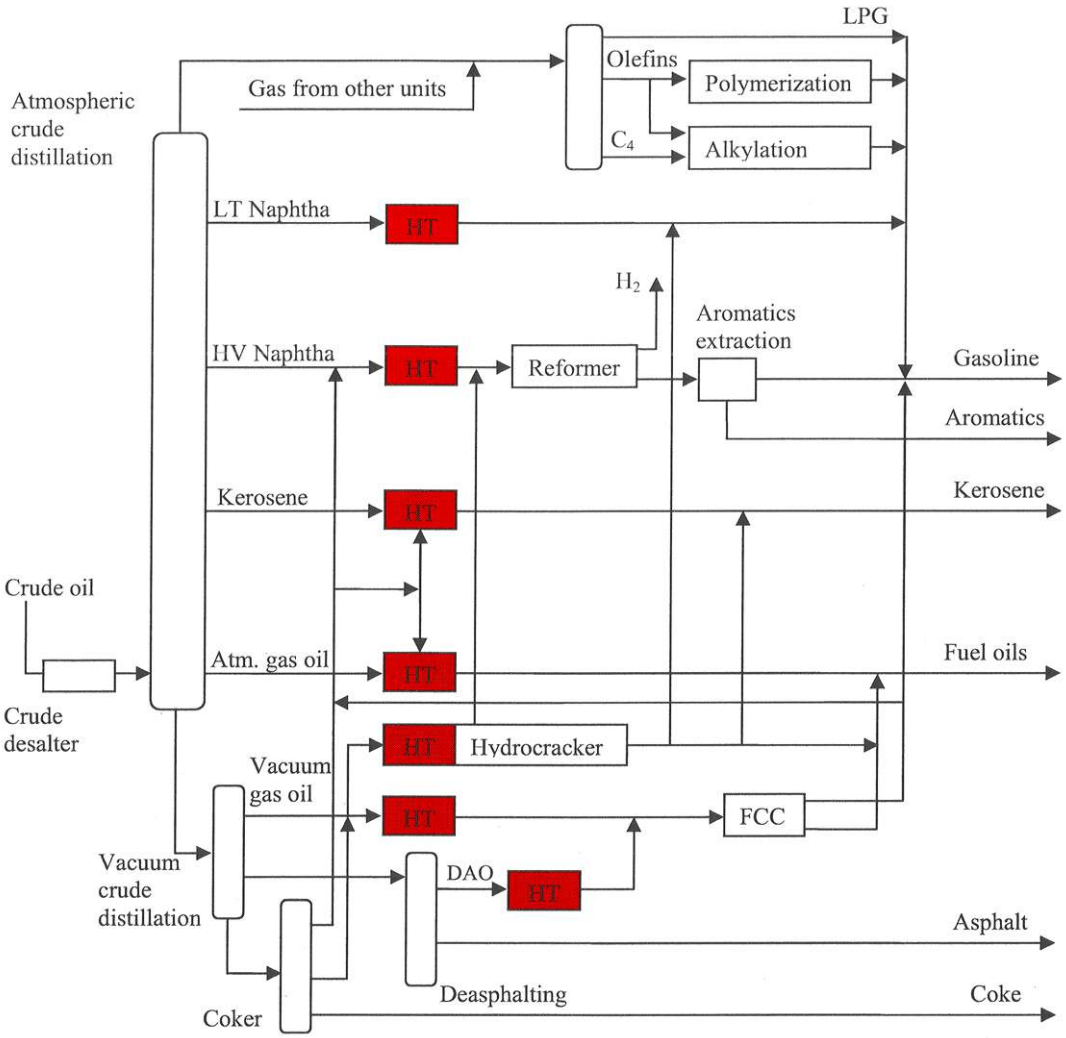

Figure 1.1: Schematic representation of a petroleum refinery. The hydrotreating operations are highlighted [3].

1.3 Hydroprocessing catalysts

The formulation of modern hydroprocessing catalysts originates from early research in catalytic coal liquefaction and coal liquids upgrading to automotive fuels in the 1920s and the 1930s in Germany. These catalysts were based on molybdenum and tungsten containing nickel or cobalt promoters [4–6]. Traditionally, the binary CoMo and NiMo sulfides have attracted most attention for hydrotreating applications, the former being more active in hydrodesulfurization, the latter being preferred when nitrogen removal becomes more important. NiW sulfides are less frequently employed in hydrotreating on the grounds of a lower performance in conventional HDS and HDN and because of cost reasons. They are however an important ingredient in hydrocracking catalysts because of their higher hydrogenation activity [7]. Deep hydrodesulfurization of gas oil may also be achieved by

employing noble metal catalysts. A number of reviews on the state-of-art in this field are available [8-12]. The activity of these hydrotreating catalysts has improved significantly as a result of continuous research and development in research institutions and petroleum companies worldwide, driven mainly by environmental legislation. Design approaches for developing more active catalysts are based on ideas to tailor the active sites for desired reactions.

To improve the performance of the HDS catalyst, all the steps in the preparation process of hydrotreating catalysts should be considered. The key parameters are the choice of the precursor of the metal oxide phase, the support, the exact method of preparation and sublteties such as the exact procedure of calcination. Another crucial parameter is the way of sulfidation. In laboratories, sulfidation is typically carried in a mixture of hydrogen sulfide with hydrogen, but industrial practice is to sulfide the oxidic precursor by organosulfur compounds added to the crude oil feed. Increasingly, pre sulfided catalysts are loaded into hydrotreating reactors with the aim to obtain optimum activity. The nature of the active phase can be modified by changing the amount of active component [13], introduction of additives and by changing the active component. Numerous additives have been studied, phosphorus [14-16] and fluorine [17-19] have received special attention. Various supports have been used to enhance the HDS performance such as carbon [20-23], silica [24-26], zeolites [27-29], titania and zirconia [30-32] and silica-alumina [33,34]. Combining new types of catalytic species with catalyst supports such as amorphous silica-alumina (ASA) can result in an extremely high desulfurization performance [35]. The application of amorphous silica-alumina-supported noble metal-based catalysts for the second-stage deep desulfurization of gas oil is another example [36,37].

Whereas these medium-pressure hydrotreating processes do not result in a decrease of the molecular weight of the product, hydrocracking of higher-boiling fractions, typically carried out above 100 bar hydrogen pressure, is employed to arrive at economically more profitable products such as gas oil and kerosene. The latter process is still gaining in importance, mainly because of the excellent product properties including very low sulfur contents and very good combustion properties. Hydrocracking typically requires bi-functional catalysts: they contain both acidic cracking and hydrogenation functions [38-40]. The acidity is provided by (stabilized) faujasite zeolites or amorphous silica–alumina for mild hydrocracking. Hydrogenation is provided by NiW mixed sulfides, NiMo mixed sulfides in the case nitrogen removal is important and Pt or Pd when sulfur concentrations are low as encountered in some two-stage configurations [40].

1.4 Support effects in hydroprocessing catalysts

The role of support interactions in HDS catalysts has been a central topic in many scientific investigations [9, 41]. Also from an industrial point of view, this is a very important topic since changing support properties are some of the key parameters used to control catalyst activity and selectivity. Most studies have dealt with the industrially important alumina-supported NiMo or CoMo catalysts. One of the main advantages of using alumina as a support is the ease of formation of small stable MoS_2 nanoclusters. The exact nature of active sites in Co–Mo or Ni–Mo catalysts is still a subject of debate, but the Co–Mo–S model is widely accepted nowadays [9]. The active Co–Mo–S phase consists of highly dispersed Co-sulfide particles dispersed over the edges of MoS_2 slabs that interact with the alumina support. Besides the stabilizing effect, the support interaction may also influence the intrinsic activity of the active sites in the Co–Mo–S structures. For example, some time ago it was observed [42] that increasing the sulfiding temperature may result in modified Co–Mo–S structures with substantially higher activity per Co edge atom than those formed at the lower temperature.

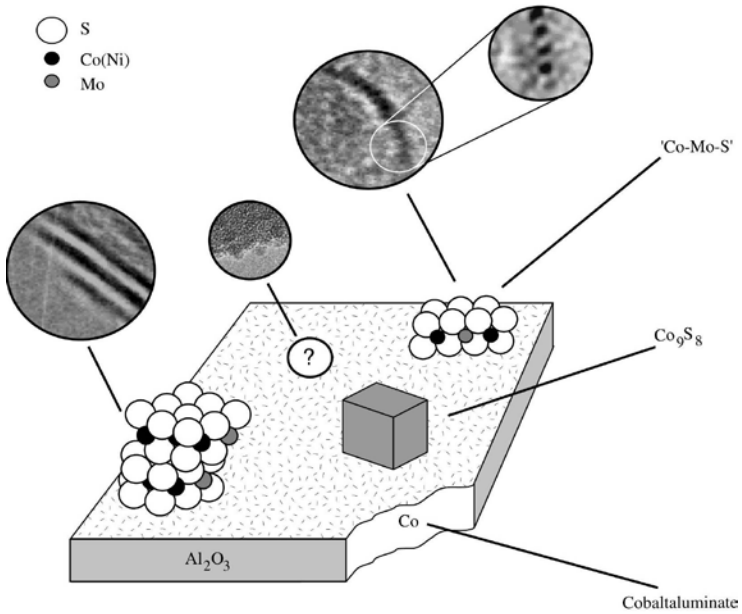

Figure 1.2: Schematic drawing showing Co–Mo–S and other Co sulfide structures on alumina and Co in the alumina [9].

Among the Co–Mo–S structures for alumina supported catalysts, the more active phase is referred to as type II and the less active phase as type I. The Type I Co–Mo–S structures are proposed to be incompletely sulfided and have some remaining Mo–O–Al linkages with the support [42]. The presence of such linkages has been related to the interaction which occurs in the calcined state between Mo and surface alumina OH groups leading to oxygen bridged monolayer-type structures that are difficult to sulfide completely. Several subsequent studies [43-45] have provided evidence for the existence of Mo–O–Al linkages in Type I structures.

In accordance with this picture, a weak support interaction favors the creation of Type II structures. The linkages to the support may be broken by high temperature sulfiding, but this is not be a desirable way of producing the highly active Type II structures, because the high temperatures may result in sintering and loss of important edge sites. Fig 1.2 shows the typical surface structures of a sulfided hydrotreating catalyst. In addition to the promoted MoS_2 phases, segregated Co(Ni) sulfided phases can also be present on the surface. The presence of segregated promoter phases is undesirable, as it leads to loss in hydrotreating activity. It is therefore desirable to find alternate production procedures, and it has been observed that the interaction with the support may be avoided by introduction of additives or chelating agents or by using weakly interacting supports such as carbon [46-49].

Hydroprocessing catalysts work in the presence of H_2S and of NH_3 which are often considered as simple inhibitors due to their competitive adsorption with unsaturated hydrocarbons as well as with S and N heterocompounds. However, studies in a wide range of partial pressures showed that H_2S has an effect that is more complex than simple inhibition of hydrogenation reactions [50]. This was also the case with hydrodenitrogenation where H_2S was found to have both a promoting effect (at low H_2S partial pressure) and an inhibiting effect (at high H_2S partial pressures) [51,52]. A certain lack of knowledge regarding all the elementary steps involved in the reaction and their mechanism can explain the difficulties in representing a general picture of the kinetics of hydrotreating reactions and more specifically in quantifying the effect of H_2S and NH_3. The inhibiting effect of H_2S on the HDS of DBT and the more refractory alkylated DBTs (e.g. 4,6-DMDBT) has been investigated in many studies using different types of catalysts. The inhibition effect of H_2S on the two main desulfurization routes of DBT type compounds is not the same. H_2S is a strong inhibitor for sulfur removal via direct desulfurization (DDS) route, but only has a minor effect on hydrogenation route (HYD) [53-57]. Sensitivities to H_2S poisoning are different for different types of catalysts. $NiMo/Al_2O_3$ catalyst is more susceptible to H_2S inhibition than $CoMo/Al_2O_3$ catalyst [58-61]. The inhibiting effect of H_2S is less pronounced in the HDS of sterically hindered alkylated DBTs such as 4,6-DMDBT than the HDS of DBT. This has been confirmed by many other studies [62-64]. The differences in the degree of inhibition observed between different catalysts (e.g. $NiMo/Al_2O_3$ and $CoMo/Al_2O_3$), different types of sulfur compounds (e.g. DBT and 4,6-DMDBT), and between DDS and HYD pathways have been explained on the basis of different catalytic sites involved in DDS and HYD reactions, as well as based on the mode of adsorption of the reactants. In addition to the removal of sulfur and nitrogen species down to ppm levels, there is an increasing need for aromatics saturation due to stricter environmental legislations. Noble metal catalysts such as alumina-supported platinum and palladium catalysts are known to be highly active in the hydrogenation of aromatics [36,37]. However, one of the major problems associated with the use of platinum and palladium is their high sensitivity to sulfur compounds that are usually present in hydrogenation feedstocks. Two deactivation routes of noble metals by sulfur have been proposed: (i) direct poisoning of the metal surface due to the high affinity of sulfur to

noble metals and (ii) migration of the small metal particles resulting in the formation of large metal clusters. The high stability of the metal sulfide species results in a rapid deactivation of the metallic function, even at a very low sulfur concentration in the feedstock [65-67]. Acidic supports have been shown to have a significant influence on the sulfur sensitivity of noble metals. Noble-metal catalysts on acidic supports, such as HY zeolite [68], MCM-41 [69], mordenite [70] and silica-alumina [71] have been reported as highly sulfur-tolerant aromatic hydrogenation catalysts. The enhancement of activity has been explained by the presence of additional hydrogenation sites in the metal-acid interfacial region, which contributed to the overall rate of hydrogenation. Another explanation for the higher resistance towards sulfur poisoning may be the electron deficiency of metals when supported on acidic materials. The latter concept was first proposed by Dalla Betta and Boudart [72]. A lower electron density on the metal weakens the metal–sulfur bond strength. As a result a significant change in turnover frequency of the hydrogenation reaction can be observed [73, 74].

ASA supports have one important advantage over zeolites related to their mesoporous structure that prevents diffusion limitations even when bulky hydrocarbons need to be converted. Further, ASAs usually exhibit more moderate acid sites than those usually present in zeolites. Strongly acidic supports cause excessive coke formation and hydrocracking of the feedstock, which lead to a decrease in the middle distillate yields. Therefore, the potential of ASA-supported noble metal (and base metals) is a promising alternative. However, accurate control of the acidic properties of these materials is hampered by a lack of understanding the origin of acid sites in these materials. One of the main reasons is the heteregenous surface arising from typical preparation routes of amorphous silica-aluminas.

1.5 Scope of thesis

Amorphous silica-alumina (ASA) is widely used as a solid acid catalyst in various chemical reactions including hydrocracking, isomerization, and alkylation, which are important in the oil refining and petrochemical industry. However, the nature of the acid sites in these materials has not yet been fully understood. The primary reason for this is due to the heterogeneous composition of the surface of ASAs. The present project was undertaken with the aim to monitor the synthesis of a set of well-defined ASA materials to understand the genesis of acid sites in ASAs and establish their role in industrially relevant catalytic reactions.

Chapter 2 describes the results of a detailed study of the generation of strong Brønsted acid sites in amorphous silica-alumina. To this end, amorphous silica-aluminas were prepared in an as controlled manner as possible, that is by the homogeneous deposition of aluminium on a reactive silicagel. Using ^{27}Al NMR spectroscopy, the grafting of aluminium on the silica surface was followed at each stage of the preparation. In order to establish the exact nature of the Brønsted acid sites in amorphous silica-aluminas, Chapter 3 reports about a novel method to quantify strong Brønsted acid sites in aluminosilicates. In chapter 4, this method is benchmarked against a large number of common methods to characterize the surface

properties with an emphasis on the acidity. Based on the large number of results, a description of the surface of amorphous silica-alumina is provided.

The second part of this thesis deals with the influence of the surface acidity and composition of ASAs on the catalytic activity of supported transition metal sulfides and noble metal phases. A critical issue in industrial practice is the sulfur and nitrogen tolerance because hydrogen sulfide and ammonia formed during hydrodesulfurization and hydrodenitrogenation reactions in hydrotreating and hydrocracking units inhibit the catalytic activity. In Chapter 5, the effect of ammonia on the HDS activity of thiophene on supported CoMo catalysts is described. Chapter 6 examines in detail the sulfur tolerance of ASA supported noble metal and transition metal sulfides. ASA supports of equal acidity but varying composition and a set of supports with similar composition but varying acidity were used to prepare the supported hydrogenation catalysts. These catalysts were then tested for their activity in hydrodesulfurization of model sulfur compounds, namely thiophene and dibenzothiophene, to ensure that the active phase in these catalysts is similar. The sulfur tolerance of these catalysts is evaluated by measuring their activity in the hydrogenation of toluene as a function of the hydrogen sulfide partial pressure and the origin of the sulfur tolerance of ASA-supported catalysts is discussed.

References

1. R.A. van Santen, P.W.N.M. van Leeuwen, J.A. Moulijn, B.A. Averill, Catalysis: An Integrated Approach 2nd Ed, 1999.
2. I. Chorkendorff, J.W. Niemantsverdriet, Concepts of modern catalysis and kinetics, Wiley –VCH, 2003.
3. W.W. Irion, O.S. Neuwirth, Oil Refining, Wiley – VCH, 2005.
4. F. Fischer, F. Abh. Kohle. 1 (1915) 231.
5. F.Bergius, J. Bilwiller, German Patent. 30 (1919) 1231.
6. A. Mittasch, Berichte 59 (1926) 13.
7. J.A.R. van Veen, in: M. Guisnet, J.-P. Gilson (Eds.), Zeolites for Cleaner Technologies, Imperial College Press, 2002, .
8. R. Prins, V.H.J. de Beer, G.A. Somorjai, Catal. Rev.-Sci. 31(1989) 1.
9. H. Topsøe, B.S. Clausen, F.E. Massoth, Hydrotreating Catalysis, Springer, Berlin, 1996.
10. P.T. Vasudevan, J.L.G. Fierro, Catal. Rev.-Sci. Eng. 38 (1996) 161.
11. S. Eijsbouts, Appl. Catal. A. 158 (1997) 53.
12. M. Breysse, E. Furimsky, S. Kasztelan, M. Lacroix, G. Perot, Catal. Rev. 44 (2002) 651.
13. H. Qabazard, F. Abuseedo, A. Stanislaus, M. Andari, M. Absihalabi, Fuel Sci. Technol. Int. 13 (1995) 1135.
14. R.E. Tischer, N.K. Narain, G.J. Stiegel, D.L. Cillo, Ind. Eng. Chem. Res. 26 (1987) 422.
15. S. Eijsbouts, J.N.M. van Gestel, J.A.R. vanVeen, V.H.J. de Beer, R. Prins, J. Catal. 131(1991) 412.
16. J.A.R. van Veen, H.A. Colijn, P. Hendriks, A.J. van Welsenes, Fuel Process. Technol. 35 (1993) 137.
17. H. Kim, J.J. Lee, S.H. Moon, Appl. Catal. B 44 (2003) 287.
18. W.P. Zhang, M.Y. Sun, R. Prins, J. Phys. Chem. B 107 (2003) 10977.
19. V. Schwartz, M.Y. Sun, R. Prins, J. Phys. Chem. B 106 (2002) 2597.
20. M. Breysse, B.A. Bennett, D. Chadwick, J. Catal. 71 (1981) 430.

21. A.J. Bridgewater, R. Burch, P.C.H. Mitchell, Appl. Catal. 4 (1982) 267.
22. J.C. Duchet, E.M. van Oers, V.H.J. de Beer, R. Prins, J. Catal. 80 (1983) 386.
23. H. Topsøe, R. Candia, N.Y. Topsøe, B.S. Clausen, Bull. Soc. Chim. Belg. 93 (1984) 783.
24. G. Muralidhar, F.E. Massoth, J. Shabtai, J. Catal. 85 (1984) 44.
25. Y.I. Yermakov, A.N. Startsev, V.A. Burmistrov, Appl. Catal. 11 (1984) 1.
26. R. Cattaneo, T. Shido, R. Prins, Hydrotreatment and Hydrocracking of Oil Fractions, Amsterdam, 1999.
27. M. Breysse, E. Furimsky, S. Kasztelan, M. Lacroix, G. Perot, Catal. Rev.-Sci. Eng. 44 (2002) 651.
28. F. Bataille, J.L. Lemberton, G. Perot, P. Leyrit, T. Cseri, N. Marchal, S. Kasztelan, Appl. Catal. A 220 (2001) 191.
29. V. Fornes, M.I. Vazquez, A. Corma, Zeolites 6 (1986) 125.
30. J.G. Weissman, E.I. Ko, S. Kaytal, Appl. Catal. A 94 (1993) 45.
31. M.J. Vissenberg, Y. van der Meer, E.J.M. Hensen, V.H.J. de Beer, A.M. van der Kraan, R.A. van Santen, J.A.R. van Veen, J. Catal. 198 (2001) 151.
32. K. Tanabe, H. Sasaki, H. Hattori, K. Ouchi, K. Makino, H. Itoh, G. Takeya, Fuel Process. Technol. 2 (1979) 253.
33. L. Qu, W. Zhang, P.J. Kooyman, R. Prins, J. Catal. 215 (2003) 7.
34. I.V. Babich, J.A. Moulijn, Fuel 82 (2003) 607.
35. H.R. Reinhoudt, M. van Gorsel, A.D. van Langeveld, J.A.R. van Veen, S.T. Sie, J.A. Moulijn, Hydrotreatment and Hydrocracking of Oil Fractions 127 (1999) 211.
36. H.R. Reinhoudt, R. Troost, A.D. van Langeveld, S.T. Sie, J.A.R. van Veen, J.A.Moulijn, Fuel Process. Technol. 61 (1999) 133
37. J. Scherzer, A.J. Gruia, Hydrocracking Science and Technology, Marcel Dekker, New York, 1996.
38. I.E. Maxwell, J.K. Minderhoud, W.H.J. Stork, J.A.R. van Veen, in: G. Ertl, H. Knözinger, J. Weitkamp (Eds.), Handbook of Heterogeneous Catalysis, Wiley/VCH, New York/Weinheim, 1997, p. 2017.
39. M. Breysse, P. Afanasiev, C. Geantet, M. Vrinat, Catal. Today 86 (2003) 5.
40. R. Candia, B.S. Clausen, H. Topsøe, in: Proceedings of the 9th Iberoamerican Symposium on Catalysis, Lisbon Portugal, 1984, p.211.
41. E. Diemann, Th. Weber, A. Muller, J. Catal. 148 (1994) 288.
42. R.G. Leliveld, A.J. van Dillen, J.W. Geus, D.C. Konigsberger, J. Catal. 165 (1997) 184.
43. J.A.R. van Veen, E. Gerkema, A.M. van der Kraan, A. Knoester, J. Chem. Soc. Chem. Commun. 22 (1987) 1684.
44. J.P.R. Vissers, B. Scheffer, V.H.J. de Beer, J.A. Moulijn, R. Prins, J. Catal. 105 (1987) 277.
45. L. Medici, R. Prins, J. Catal. 163 (1996) 38.
46. L. Coulier, G. Kishan, J.A.R. van Veen, J.W. Niemantsverdriet, J. Phys. Chem. B 106 (2002) 5897.
47. S.Kasztelan, D. Guillaume, Ind. Eng. Chem. Res. 33 (1994) 203.
48. M.J. Girgis, B.C. Gates, Ind. Eng. Chem. Res. 30 (1991) 2021.
49. G. Perot, Catal. Today. 10 (1991) 447.
50. M. Egorova, R. Prins, J.Catal. 225 (2004) 417.
51. D.D. Whitehurst, T. Isoda, I. Mochida, Adv. Catal. 42 (1998) 345.
52. V.Meille, E.Schulz, M.Lemaire, M.Vrinat, J.Catal. 170 (1997) 29.
53. F. Bataille, J.L. Lenibcrton, P. Michanct, G. Perot, M. Vrinat, M. Lemaire, E. Schulz, M. Breysse, S. Kastzelan, J. Catal. 191 (2000) 409.
54. H. Farag, I. Mochida, K. Sakanishi, Appl. Catal. A: Gen. 194–195 (2000) 147.
55. S. Texier, G. Berhault, G. Perot, V. Harle, F. Diehl, J. Catal. 223 (2004) 404.

56. S. Kasahara, T. Shimizu, M. Yamada, Catal. Today. 35 (1997) 59.
57. E. Lecrenay, K. Sakanishi, I. Mochida, Catal. Today. 39 (1997) 13.
58. J. Van Gestel, L. Finot, J. Leglise, J.E. Duchet, Bull. Soc. Chim. Belg.104 (1995) 189.
59. T. Kabe, K. Akamatsu, A. Ishihara, S. Otsuki, M. Godo, Q. Zhang, W. Qian, Ind. Eng. Chem. Res. 36 (1997) 5146.
60. H. Farag, K. Sakanishi, I. Mochida, D.D. Whitehurst, Fuel 13 (1999) 449.
61. K. Sakanishi, T. Nagamatsu, I. Mochida, D.D. Whitehurst, J. Mol. Catal. A: Chem. 155 (2000) 101.
62. J. Barbier, E. Lamy-Pitara, P. Marecot, J..P. Boitiaux, J. Cosyns, F. Verna, Adv. Catal. 37 (1990) 279.
63. J. Oudart, Catal. Rev-Sci. Eng. 22(2) (1980) 171.
64. J. Oudart, Stud. Surf. Sci. Catal. 11 (1982) 258.
65. H. Yasuda, Y. Yoshimura, Catal. Lett. 46 (1997) 43.
66. A. Corma, A. Martinez, V. Martinez-Soria, J. Catal. 169 (1997) 480.
67. S.D. Lin, C. Song, Catal. Today 31 (1996) 93.
68. R.M. Navarro, B. Pawelec, J.M. Trejo, R. Mariscal, J.L.G. Fierro, J. Catal. 189 (2000) 184.
69. R.A. Dalla Betta, M. Boudart, Proc. 5th Int. Congr. Catal. 1972, p. 1329.
70. T. T. Phuong, J. Massardier, P. Gallezot, J. Catal. 102 (1986) 456.
71. R. Szymanski, H. Charcosset, P. Gallezot, J. Massardier, J. L.Tournayan, J. Catal. 97 (1986) 366.

Chapter 2

Formation of acid sites in amorphous silica-alumina

Summary

A suite of amorphous silica-aluminas (ASAs) was prepared by homogeneous deposition-precipitation (HDP) of aluminium on a silica surface followed by calcination. The HDP process was investigated in detail by ^{27}Al NMR spectroscopy of solid and liquid aliquots of the synthesis mixture. Deposition occurs predominantly via hydrolytic adsorption of aluminium onto the hydroxyl groups of the silica surface. Precipitation becomes more significant at higher aluminum concentration. Depending on the aluminium loading, the surface contains four- and six-coordinated aluminium as well as patches of aluminium hydroxides. Calcination results in two competing process, that is the diffusion of aluminium into the silica network and sintering of aluminium into separate patches of a phase which mainly consists of octahedral Al. These ASAs exhibit Brønsted acidity similar to industrial amorphous silica-aluminas prepared by grafting of aluminium on very reactive silica-gels. Their acidity does not vary systematically with the aluminium concentration, except below 5 wt% Al_2O_3. The acidity increases with the calcination temperature. The active sites form due to diffusion of aluminium into the silica network at high temperatures, leading to Al substitutions of Si atoms. This is expected as the acidity does not correlate with anything else, *viz.*, the amount of four-coordinated aluminium nor the presence of segregated Al or five-coordinated aluminium at the interface of these domains and the mixed silica-alumina phase. The surface of an amorphous silica-alumina consists of isolated aluminium grafted to the silica surface (pure silica-alumina phase) with a very small amount of aluminium in the silica network, which brings about the Brønsted acidity, and small patches of aluminium oxides.

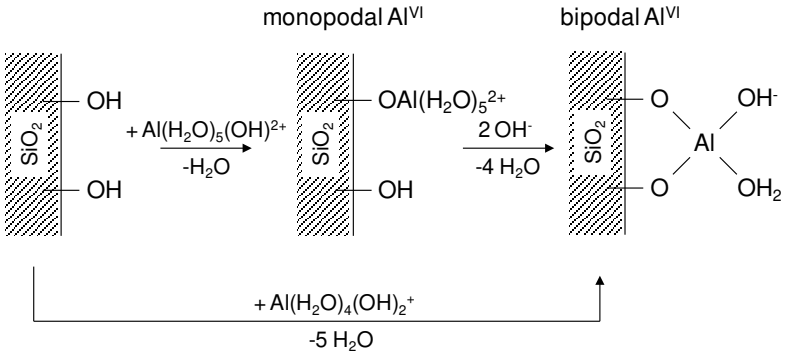

Published in *Journal of Catalysis 269 (2010) 201-218.*

2.1 Introduction

Amorphous silica-alumina (ASA) is widely used as a solid acid catalyst in various chemical reactions including hydrocracking, isomerization, and alkylation, which are important in the oil refining and petrochemical industry [1,2]. Hydrocracking involves a boiling-point shift of heavier fractions of crude oil towards lighter product streams through sequential steps of dehydrogenation of paraffins, β-scission of intermediate olefins and hydrogenation of the smaller olefins to paraffins. The catalysts are bifunctional and contain most often mixed metal sulfides for (de)hydrogenation and a cracking component of variable Brønsted acidity. As, at least in Europe, the demand for middle distillates is strongly increasing, balanced acidity in these catalysts to achieve high conversion, yet with high selectivity to diesel and kerosene fractions, is pivotal. Here, ASAs with only moderate acidity are preferred. Besides, present-day composite hydrocracking catalysts nearly always contain an ASA component next to steam stabilized faujasite zeolite.

Accurate control of the acidic properties of ASAs is hampered by two factors: a lack of the understanding of the origin of Brønsted acidity in these mixed oxides and the inhomogeneous composition resulting from typical preparation methods. Regarding the former, the nature of the Brønsted acid sites (BAS) has not been unequivocally established. The more widely shared opinion is that the Brønsted acidity derives from tetrahedral Al^{3+} in the silica network, as initially proposed by Thomas [3] and Tamele [4] in the late 1940s. However, evidence in this debate remains inconclusive, because the corresponding strongly acidic bridging hydroxyl groups, which should be similar in nature to those well-established in crystalline zeolites, have eluded direct spectroscopic observation until now. Thus, alternative explanations for ASA's acidity have been invoked. These include Lewis acidic Al ions substituting for protons of surface silanol groups [5,6] and the higher acidity of silanol groups in the presence of neighbouring aluminium surface atoms [7]. The latter model forms the basis for the more recent proposals of paired (SiOH, Al) sites [8-10], which involve aluminium as part of the silica network or of an interface region between silica and alumina [11,12]. The interface in the latter interpretation is made up by five-coordinated Al. Similarly, controversy exists about the intrinsic acidity of the protons in ASAs, which is thought to differ from that in zeolites. The higher flexibility of the bonds around the bridging hydroxyl groups in a non-crystalline material may explain the lower acidity [13]. A crucial question is whether the overall Brønsted acidity in ASAs is caused by a few strongly acidic sites or by a large number of weaker ones.

The other reason that surface acidity of ASAs is understood to a much lesser extent than that of zeolites relates to the complex surface composition of these mixed oxides. ASAs are made by co-precipitation, cogelation or grafting processes [14-16], and the content of alumina is between 5–60 wt%. In nearly all cases, the resulting materials contain a non-random distribution of aluminium in silica, because formation of Al-O-Al bonds is faster than of Al-O-Si bonds [17-19]. Beside isolated aluminium ions on the silica surface, small clustered aluminium oxides are present ranging from nanoclusters up to sizes where rather

the presence of a separate alumina-type phase should be considered [20]. Obviously, depending on the preparation route and further calcination aluminium can end up in the silica network as a substituent for tetrahedral Si [20-22]. The negative charge of the silica following substitutions of Si for Al can be compensated by protons at the surface which could in principle display strong Brønsted acidity, or by internal silanol groups [23] and surface mono- or polymeric hydroxyaluminium cations [20].

The present project was undertaken with the aim of (i) synthesizing a set of ASA materials by as controlled a method as possible for future use in catalytic studies and (ii) learning more about the genesis of Brønsted acid sites in ASAs and their strength. The synthesis method chosen was a well-defined variant of grafting, *viz.*, homogeneous deposition-precipitation [24]. An acidic starting solution of Al^{3+} is homogeneously basified through thermal decomposition of urea in the presence of a silica aerogel. Urea slowly decomposes in aqueous solutions when the temperature is raised above 343 K, which ensures a slow homogeneous release of hydroxyl anions and avoids pH inhomogeneities as would be present when a base is added dropwise. As urea decomposition proceeds rather slowly, the hydrolysis of Al can be followed by ^{27}Al NMR spectroscopy [25]. Thus, one can in principle follow the deposition of aluminium on silica as a function of pH and the initial aluminium concentration. The precursors are subsequently calcined to give the desired ASAs. These materials are compared to ASAs prepared by cogelation [15], alumination of silica by $(NH_4)_3AlF_6$ [26] and the co-condensation of an organometallic double alkoxide containing silicon and aluminium with tetramethoxysilane [27]. ^{27}Al NMR spectroscopy will be the main technique to follow the aluminium coordination during its deposition on silica and upon further calcination. The acidity of the calcined support materials is evaluated from their acid catalytic activity in the hydroconversion of *n*-heptane, after loading with palladium, under conditions where the isomerization step is rate limiting, and compared to that of a commercial ASA.

As an introduction, the various structures to which the presence of six-, five-, and four-coordinated Al atoms in amorphous silica-aluminas have been assigned is described here in some detail. This discussion is guided by Table 2.1, which summarizes the most important structural models of aluminium-containing phases in ASAs. The early work of De Boer [5] discussed the binding of Al to two or three vicinal silanol groups on the surface and the resulting surface tetrahedral Al ion was coined to be the acidic site. Tamele [4] suggested the reaction of $Al(OH)_3$ with three silanol groups. The substitution of Si by Al with respective formal charges of 4+ and 3+ in the silica network [3,4] induces a negative charge on the oxygen atoms around the Al atoms, which is compensated by cations. This view was further developed by Fripiat and co-workers [20-22] and Boehm and Schneider [28]. Boehm and Schneider mention that high temperature calcination facilitates the diffusion of aluminium into the silica network. The model of Fripiat describes ASAs in terms of a negatively charged aluminosilicate core and positively charged surface species. When the negative charge is formed by a surface substitution of Si by Al and compensated by a proton, a truly BAS should be obtained. Tetrahedral Al can also become part of a transitional alumina phase

which may form following segregation during the preparation and upon calcination. Likewise, the presence of octahedral coordination of Al in these amorphous mixed oxides points to the presence of transitional aluminas or at least some polymeric form of Al. Octahedral Al is the dominant coordination in many transitional aluminas [29,30]. Various authors [31,32] have also proposed that hydroxyaluminium cations present on the surface act as charge compensating cations.

Table 2.1: Assignments of four- (tetrahedral), five- (penta-coordinated) and six- (octahedral) coordinated aluminium atoms (chemical shifts indicated by δ) in ASA.

Coordination	Assignments	References
four ($\delta \approx 54$ ppm)	Grafted aluminium	De Boer [5]
	Aluminium isomorphously substituting Si^{4+} in silica	Thomas [3], Tamele [4], Hansford [7], Boehm and Schneider [28]
	Four-fold coordinated aluminium in (transition) aluminas	Mackenzie et al. [29,30]
five ($\delta \approx 30$-35 ppm)	Interface between alumina and silica or aluminosilicate	De Witte et al. [33]
	Five-fold coordinated aluminium in transition aluminas	Mackenzie et al. [29,30]
	Distorted tetrahedral species	Peeters and Kentgens [34]
	Associated with ASA phase	Williams et al. [31], Omegna et al. [37]
six ($\delta \approx 0$ ppm)	γ-Al_2O_3 after calcination	e.g., Mackenzie et al. [29,30]
	Amorphous polymeric aluminium oxide (boehmite) phase	Cloos et al. [20]
	Charge-compensating cation	Williams et al. [31], Stone et al. [32]

The assignment of five-coordinated Al species in ASAs is under debate [33,34]. This coordination state has been identified in ^{27}Al NMR spectra as a resonance between 30 and 35 ppm for zeolites, phyllosilicates and ASAs [33,35,36]. For zeolites, such a species has been interpreted in terms of a distorted tetrahedral species [26], or as part of an extraframework silica-alumina phase as typically found in steam calcined zeolites [37]. In phyllosilicates, five-coordinated aluminium species exist as an interface species between alumina and a mixed silica-alumina phase [36]. Similarly, five-coordinated aluminium in ASAs was assigned to the interface between an alumina-type phase and a truly mixed silica-alumina phase [31]. Five-coordinated Al has been identified as an intermediate coordination state during the strong atomic rearrangements during dehydration processes of alumina precursors [38-42].

More detailed information on the Al speciation is obtained by recording ^{27}Al NMR spectra before and after exposure to ammonia. The changes in the Al coordination upon exposure to ammonia for aluminosilicates have been described by several groups [43,44]. For BETA [43]

and faujasite zeolites [44], dehydration and adsorption of ammonia resulted in strong changes in the aluminium coordination: part of six-coordinated Al converted to a tetrahedrally coordinated species. The initial explanation has been that some framework octahedral Al^{3+} exhibit six-fold coordination with four framework oxygen species, an hydroxyl group and one water molecule [44]. A more reasonable explanation was put forward by Omegna et al. [37], who state that the flexible coordination in steam calcined faujasite is limited to the aluminium atoms which are part of an extraframework phase with an amorphous silica-alumina character. Similarly, in ASAs only those aluminium atoms associated with a mixed phase change their coordination upon ammonia adsorption. The aluminium atoms that are constituent of a separate alumina-type phase do not change their coordination [31].

2.2. Experimental section

2.2.1 Synthesis of materials

Homogeneous aluminium deposition-precipitation. ASAs were prepared by deposition of aluminium on silica by homogeneous basification of an aqueous starting solution containing aluminium nitrate. The starting materials were a commercial silica (Sipernat 50, Degussa, surface area 400 m^2/g, hydroxyl density 4.1 OH/nm^2), $Al(NO_3)_3.9H_2O$ (Merck, purity 99 %) and urea (Merck, purity 99 %). The hydroxyl density of silica was determined from the weight loss between 473 and 1073 K in a TGA experiment. In a typical synthesis, silica was suspended in demineralized water together with the desired amount of aluminium nitrate and urea in a stirred double-walled reaction vessel. The initial aluminium concentration ($[Al]_0$) was varied between 0.03-0.11 M, while the urea concentration was kept constant at 0.76 M. To prepare an ASA with a higher alumina content, a synthesis was carried out at $[Al]_0 = 0.16$ M and a urea concentration of 1.1 M. The temperature of the well-stirred suspension was increased to 363 K by circulating thermostat-controlled water between the inner and outer walls of the vessel. During the entire synthesis the pH of the suspension was monitored. The aluminosilicates were recovered by filtration, washed with demineralized water and dried at 393 K and finally calcined in static air at 773 K or 1073 K. The samples are denoted by ASA(*X*/*Y*, *T*), where *X* and *Y* refer to the alumina and silica contents by weight and *T* refers to the calcination temperature. Unless stated otherwise, the loadings of Al are expressed as a weight percentage of Al_2O_3. In a set of related syntheses, the suspension was removed from the reaction vessel at a certain pH and cooled in an ice-bath to prevent further decomposition of urea. The resulting materials are denoted by ASA(*X*/*Y*, *S*, *T*) where *S* stands for the pH at which the synthesis mixture was unloaded. To compare the influence of the silica source, fumed silica (VWR, surface area 390 m^2/g, hydroxyl density 1.2 OH/nm^2 from TGA) was used to prepare ASA(5/95,fumed).

Cogelation. Sodium silicate (Merck, 30 wt% SiO_2) was added under vigorous stirring to a solution of aluminium chloride (Merck, 99 %), following a modification of a patent recipe [15]. The pH was brought to 7 with acetic acid and the mixture was further stirred for 1 h. The sample was then recovered by filtration and washed repeatedly with distilled water. Ion-

exchange with 0.3 M NH_4NO_3 solution was carried out seven times under refluxing to remove the sodium ions. The final sodium content was below 0.1 wt%. The material was finally dried overnight at 393 K and calcined in static air at 923 K for 4 h. This sample is referred to as ASA(5/95,cogel).

Alumination of SiO_2. Alumination of a silica was carried out with ammonium aluminiumhexafluoride [26]. First, ammonium hydroxide was added to an aqueous suspension of silica (Sipernat 50) to adjust the pH to 9. An aqueous solution of $(NH_4)AlF_6$ (Alfa-Aesar, 99 %) was then added slowly in 1 h to obtain the desired amount of aluminium (SiO_2/Al_2O_3 = 19). The resulting solution was stirred overnight at room temperature. The sample was recovered by filtration, washed with distilled water and dried overnight at 393 K. The sample was then calcined at 773 K for 4 h and is referred to as ASA(5/95,F).

Organometallic precursor. An organometallic route consisted of mixing tetramethylorthosilicate (TMOS, Merck, 99 %) with an amount of di-*sec*-butoxyaluminotriethoxysilane (Alfa Aesar) to obtain a homogeneous mixture. The ratio of TMOS and the double-alkoxide was chosen such that a final SiO_2/Al_2O_3 ratio of 4 was obtained. To this mixture, 40 ml of water was added and stirred overnight at room temperature. The solution was then transferred into an autoclave and kept at 373 K for 72 h. The sample was recovered by filtration, washed with water, dried overnight at 393 K and finally calcined at 823 K for 4 h. This sample is designated ASA(20/80,alkoxide).

Commercial samples. A commercial ASA reference sample (55 wt% Al_2O_3) prepared by grafting aluminium to *in situ* prepared silica-gel at pH 3 was used as received. The ASA was calcined at 773 K and 1073 K. These samples are denoted by ASA(comm). An ultrastabilized Y zeolite with a silica-to-alumina ratio of 9.3, denoted by USY(9.3), was used as received from Zeolyst International.

2.2.2 Characterization

The elemental composition of the calcined ASAs was determined by ICP analysis. Prior to analysis on a Spectro CIROS^{CCD} ICP optical emission spectrometer, the samples were dissolved in a mixture of stoichiometric ratio by volume of hydrofluoric acid, nitric acid and water.

Thermogravimetric analysis was carried out for the parent silicas on a Shimadzu TGA-50 equipped with a platinum sample holder. The samples were heated in air at a rate of 10 K/min to 1073 K. The hydroxyl density of the silica supports was calculated from the water loss between 473 K to 1073 K.

The surface area of the ASAs was determined from N_2 adsorption measurements at liquid nitrogen temperature with a Micromeritics Tristar 3000. Prior to the measurements, the samples were dried at 573 K for 3 h. The surface areas were determined using the Brauner-Emmet- Teller method.

Magic-angle spinning (MAS) ^{27}Al NMR spectra were recorded on a Bruker DMX500 spectrometer operating at an Al NMR frequency of 130 MHz and equipped with a 4-mm

MAS probe head. The ^{27}Al chemical shifts are referenced to a saturated $Al(NO_3)_3$ solution. An accurately weighed amount of sample was packed in a 2.5 mm zirconia rotor. Typically, the aluminosilicates were exposed to a saturated water vapor at room temperature overnight. The sample rotation speed was 25 kHz. For quantitative MAS ^{27}Al NMR spectra single-pulse excitation was used with a single 36° pulse of 2 μs and an interscan delay of 1 s. It was checked for a few typical samples that shortening the excitation pulse to 1 μs or increasing the interscan delay to 2 or 5 s did not affect the relative signal intensities in the spectra.

^{27}Al MQMAS NMR spectra with a zero-quantum filter were recorded by use of the three-pulse sequence p_1-t_1-p_2-τ-p_3- t_2 with strong pulses p_1= 3.0 μs, p_2 = 1.2 μs at a radio-frequency field strength of 150 kHz and a weak pulse p_3 = 11 μs at a field strength of 7 kHz. The evolution time t_1 was sampled with 64 time increments of 20 μs, the signal was recorded during t_2 with a sample time of 10 μs up to 10.3 ms and the filter time τ was 20 μs. Another set of NMR experiments was carried out for amorphous silica-aluminas after dehydration and adsorption of ammonia. To this end, an amount of sample was heated in a flow of He from room temperature to 393 K at a rate of 6 K/min followed by exposure to a flow of 1 vol% NH_3 for 1 h. The sample was then cooled to room temperature in the same gas mixture and transferred into a nitrogen-flushed glovebox to be packed into a 2.5 mm NMR rotor.

Rotational-resonance ^{27}Al NMR experiments were carried out by using the pulse sequence θ_{+x} - τ - $\theta_{\pm x}$ - t_{mix} – θ_{ϕ} - t_2 with θ ~30° pulses of 1.8 μs. The sample-rotation rate ν_r was matched to the frequency separation $\Delta\nu$ between the tetrahedral and octahedral Al signals at, respectively, ~56 and ~6 ppm , $\nu_r = \Delta\nu$ ~ 6.5 kHz. The interval τ was adjusted to ½.$\Delta\nu$ of about 71 μs (corrected for the θ pulse duration). The carrier frequency was set $\Delta\nu$ upfield of the octahedral signal. Under these conditions, the θ_{+x} - τ - $\theta_{\pm x}$ sequence produces tetrahedral and octahedral Al polarization with opposite signs. The polarization of either the octahedral or tetrahedral ^{27}Al spins was inverted in an alternating way by changing the phase of the second pulse. After the selective inversion, the octahedral and tetrahedral Al spins were given the opportunity to exchange spin polarization during the following mixing time t_{mix}. The third θ pulse at the end of t_{mix} rotates the respective polarization vectors of the octahedral and tetrahedral sites into the xy plane, and the corresponding NMR signals are measured during the acquisition time t_2 with a scan accumulation scheme following the alternating sign of the second pulse and the phase ϕ of the third pulse. For comparing the polarization exchange to the recovery of the polarization caused by spin-lattice relaxation, also a background experiment with equal polarization perturbation of the octahedral and tetrahedral Al sites was carried out by taking τ = 2.5 μs. A phenomenological bi-exponential decay

$$R(t) = A.\exp(-t/T_{1A}) + B.\exp(-t/T_{1B}) \qquad (2.1)$$

is fitted to the background decay. With $R(t)$ determined from the background decay, the rotational-resonance exchange data are then fitted with a model of the form

$$I(t) = I(0)\ \{A_T.\exp(-t/\tau_{se}) + 1 - A_T\}.R(t) \qquad (2.2).$$

To analyze the rotational-resonance (R^2) spin-exchange curves, we employ a simple two-site exchange model for the alumina phase extendeded with two isolated sites representing tetrahedral and octahedral Al sites in the aluminosilicate phase. The fractions of aluminium in the alumina and aluminasilicate phase are respectively denoted f_a and f_s, and the respective tetrahedral and octahedral fractions in the two phases by $f_{a,T}$, $f_{a,O}$, $f_{s,T}$ and $f_{s,O}$ with $f_{a,T} + f_{a,O} = f_{s,T} + f_{s,O} = 1$). The combined intensity $I_T(t)$ of the NMR signals of tetrahedral Al in the alumina and aluminosilicate phase at time t after the initial polarization perturbation is given by $f_a f_{a,T}\, p_{a,T}(t) + f_s f_{s,T}\, p_{s,T}(t)$ with $p_{a,T}(t)$ and $p_{s,T}(t)$ the relative polarization with respect to the thermal-equilibrium polarization p^{eq}. Analogous expressions can be constructed for the octahedral Al in the two phases. At $t = 0$ the polarization of tetrahedral Al in both phases is equally perturbed, $p_{a,T}(0) = p_{s,T}(0) \equiv p_T(0)$. In the absence of relaxation, the polarization of tetrahedral Al in the aluminosilicate phase would stay the same. However, the tetrahedral Al in the alumina phase quickly exchanges polarization with the neighboring octahedral Al sites, until their polarization has become the same $p_a^{\infty} = f_{a,T}.p_{a,T}(0) + f_{a,O}.p_{a,O}(0)$. For such case one can derive the expression for the tetrahedral signal intensity $I_T(t)$ under the influence of first-order exchange

$$I_T(t) = \left(f_s f_{s,T}\ p_T(0) + f_a f_{a,T}\ \left\{ p_T(0) - p_a^{\infty} \right\} \exp(-t/\tau_{se}) + f_a f_{a,T}\ p_a^{\infty} \right) \qquad (2.3)$$

with τ_{se} the characteristic time of ^{27}Al spin exchange in the alumina phase under R^2 conditions. In combination with a monotonously decaying factor $R(t)$ representing the effect of spin-lattice relaxation, which is supposed to be phase- and Al-type independent, this equation can be rewritten in a form, which is more practical form for fitting the spin-exchange curves

$$I_T(t) = I_T(0) \left\{ A_T\ \exp\left(-t/\tau_{se}\right) + 1 - A_T \right\} R(t) \qquad (2.4)$$

with the relative amplitude A_T of the fast decay component given by

$$A_T = \frac{f_a f_{a,T} f_{a,O}\ \left\{1 - p_O(0)/p_T(0)\right\}}{f_s\ f_{s,T} + f_a f_{a,T}} \qquad = \kappa \frac{N_{a,T}}{N_{s,T} + N_{a,T}} \qquad (2.5)$$

with $\kappa = f_{a,O}\ \{1\text{-}p_O(0)/p_T(0)\}$, and $N_{a,T}$ and $N_{s,T}$ the number of tetrahedral Al sites in the alumina and aluminosilica phase, respectively. As a consistency check, we note that no spin-exchange component is present, if the alumina phase would not contain octahedral sites, because $\kappa = 0$ in case $f_{a,O} = 0$. Likewise, no net spin exchange occurs after equal polarization perturbation of the tetrahedral and octahedral ^{27}Al spins at $t = 0$, $p_T(0) = p_O(0)$. In the case of perfect anti-phase perturbation, $p_T(0)$ and $p_O(0)$ would have exactly opposite values, so that $1\text{-}p_O(0)/p_T(0)$ would be equal to 2.

MAS ^{29}Si NMR spectra were recorded on a Bruker DMX500 operating at Si NMR frequency of 99 MHz. Direct ^{29}Si excitation with a single 90º pulse of 5 μs was combined with high-power proton decoupling and a recycle delay of 180 s between subsequent scans. Tetramethylsilane (TMS) was used as an external reference for the chemical shift.

Electron microscopy analysis was done using a JEOL 2100F transmission electron microscope (TEM) interfaced with a ThemoNoran NSS energy dispersive X-ray

spectrometer. The TEM was operated at 200 kV. Sections of the sample were prepared by embedding the powder in polymethylmethacrylate and using an ultramicrotome (model Leica EM UC6) to prepare sections with a nominal thickness of 50 nm. The local variation in the composition of the samples was measured using energy dispersive X-ray spectrometry (EDS). Two linescans were collected from each sample in the scanning mode with a nominal spot size of 1 nm. A typical measurement consisted of 100 equally spaced points along a line approximately 5 μm long. The dwell time per point was 100 and 30 seconds for ASAs with alumina contents of 5 and 20 wt%, respectively. The relative elemental concentration was calculated using the Cliff-Lorimer method without any absorption corrections. Peak fitting was made using a digital top hat filter to remove the background from the spectra before fitting the spectrum with a reference spectrum.

The concentration of strong Brønsted acid sites in the aluminosilicates was evaluated from catalytic activity measurements in the hydroconversion of *n*-heptane of Pd-loaded aluminosilicates. To this end, a sieve fraction (177-420 μm) of the dried support was loaded with 0.4 wt% Pd via incipient wetness impregnation with a solution of appropriate concentration of $Pd(NH_3)_4(NO_3)_2$. The resulting materials were calcined at 573 K. Prior to testing, the catalysts were reduced at 713 K at 30 bar in flowing hydrogen. Hydroconversion of *n*-heptane was carried out at 30 bar at a H_2/hydrocarbon ratio of 24 mol/mol. The reaction temperature was lowered from 713 K till 473 K at a rate of 0.2 K/min. The kinetics of bifunctional, aluminosilicate-catalyzed hydroconversion of *n*-alkanes is well understood [45,46]. *n*-Heptane hydroconversion involves the dehydrogenation of *n*-heptane by the noble metal phase, isomerization or β-scission by strong Brønsted acid sites and hydrogenation of the *i*-olefins to *i*-paraffins. Meeting the requirement of sufficient hydrogenation activity is easily met if the metal loading is not too low (see Supporting Information). In such case, the Brønsted-acid catalysed conversion step of the intermediate olefins via carbenium-ion chemistry is rate limiting and the catalytic activity scales with the density of acid sites if their acidity is assumed to be constant. To verify this assumption, we have recently conducted an extensive spectroscopic study, involving H/D exchange with C_6D_6, which shows that it is only the relatively homogeneous group of strong acid sites of zeolitic strength that is responsible for the isomerization activity [47]. The activity of the catalyst is expressed as the temperature at which a hydrocarbon conversion of 40 % was achieved. Assuming first-order kinetics in the reactant hydrocarbon and a constant pre-exponential factor, we can relate the number of acid sites (N'_{iso}) to the temperature required to obtain a conversion of *n*-heptane of 40 % (T_{40}) according to

$$\ln N'_{iso} = C + \frac{E_{act}}{RT_{40}} \qquad (2.6)$$

in which E_{act} (kJ mol^{-1}) is the activation energy, R (kJ mol^{-1} K^{-1}) the gas constant and C is a constant. Hence, the term E_{act}/RT_{40} scales with the number of active sites.

Table 2.2: Textural properties of the various starting silicas and calcined ASAs. The final pH values and alumina contents of the ASA syntheses are given.

Sample	Final pH of synthesis	Al_2O_3 (wt%)	Surface area (m^2/g)	Pore volume (ml/g)[1]
Sipernat-50	-	-	400	n.d
Fumed silica	-	-	390	n.d
ASA(5/95)	6.2	5.1	410	2
ASA(10/90)	5.5	10.1	398	1.8
ASA(15/85)	4.3	15.1	380	1.6
ASA(20/80)	3.3	16	n.d. [3]	n.d
ASA(20/80) [2]	5.5	20	354	1.4
ASA(5/95,3)	3	4.3	419	2
ASA(5/95,4)	4	5.1	412	2
ASA(10/90,3)	3	9	397	1.8
ASA(15/85,3)	3	12.1	373	1.6
ASA(20/80,3)	3	10	364	1.4
ASA(5/95,fumed)	6.5	4.2	400	2
ASA(5/95,cogel)	7	5	463	1.6
ASA(5/95,F)	9	5.1	402	2.1
ASA(20/80,DA)	-	20	372	1.4

[1] Water pore volume; [2] Preparation at a urea concentration of 1.1 M; [3] Not determined.

2.3. Results and discussion

2.3.1 Homogeneous deposition-precipitation of aluminium on silica

The grafting of aluminium on silica as a function of $[Al]_0$ and the pH was investigated with the aim to prepare acidic ASA supports. In the acidic aqueous starting solution of $Al(NO_3)_3$ and urea, decomposition of urea via $(NH_2)_2CO + 3H_2O \rightarrow 2\ NH_4^+ + CO_{2g} + 2\ OH^-$ starts above 343 K [24], and results in a gradual and homogeneous release of hydroxyl anions in the well-stirred solution. Fig. 2.1 shows the evolution of pH as a function of time and $[Al]_0$. Four main regions can be distinguished. Region I starts when the aluminium nitrate solution is added resulting in a decrease of the pH. At the same time the temperature of the solution is increased. The end point of Region I is defined as the minimum in the pH curve. This point corresponds to the state when the temperature of the solution exceeds 343 K, resulting in the start of urea hydrolysis. Initially, the pH increased quite strongly followed by a gradual increase of the pH. Region III is characterized by a steep increase of the pH and finally a relatively stable pH plateau defines region IV. The final pH of the synthesis mixture decreased with increasing $[Al]_0$ for ASAs with an alumina content up to 15 wt% as more OH^- was used to hydrolyze aluminium. The final pH of ASA(20/80) was higher than that of ASA(15/85) because of the higher urea concentration (1.1 M) employed to prepare ASA(20/80). An ASA(20/80) prepared at a urea concentration of 0.76 M had a final pH of 3.3 and the alumina content was only 16 wt%. Table 2.2 lists the composition and textural

properties of the calcined ASAs. The surface areas and pore volumes decrease with increasing aluminium content.

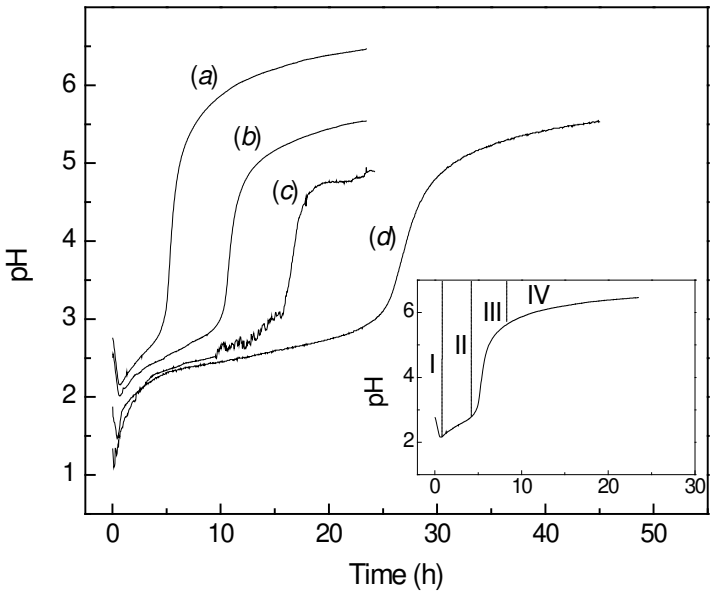

Figure 2.1: Evolution of pH with time during homogeneous deposition-precipitation of aluminium on silica following addition of aluminium nitrate to an aqueous suspension of silica aerogel containing urea. The temperature is then increased to 363 K. The initial aluminium concentration was varied to obtain ASAs with nominal alumina contents of 5 wt% (a), 10 wt% (b), 15 wt% (c) and 20 wt% (d). The inset indicates the various regions on the pH curve for ASA(5/95).

The deposition process of aluminium was studied in more detail by MAS ^{27}Al NMR spectroscopy. Firstly, the coordination of the Al species in the synthesis mixture and deposited on silica in ASA(5/95) was determined. Secondly, NMR spectra of ASA(5/95) at various stages of the synthesis were compared. In order to understand the deposition process, the Al^{3+} species in an aqueous solution as a function of pH was also studied. Similar to the work of Vogels et al. [25], the forced hydrolysis of Al was carried out in the presence of urea. For this experiment, the concentrations of aluminium nitrate and urea were 0.03 M and 0.7 M, respectively. Liquid samples were withdrawn from the solution and immediately cooled in an icebath to prevent further urea decomposition. Fig. 2.2 shows ^{27}Al NMR spectra of the liquid samples at pH 3, 4.7, and 5.5. At pH 3, the spectrum is dominated by a resonance at -0.11 ppm due to $Al(H_2O)_6^{3+}$. The resonance at -2.67 ppm is due to the replacement of one water ligand by urea in $[Al(H_2O)_5(urea)]^{3+}$ [48]. The broad peak around 4.4 ppm indicates the presence of dimeric $[Al_2(OH)_2(H_2O)_8]^{4+}$, or trimeric $[Al_3O_2(OH)_4(H_2O)_8]^{+}$ Al complexes [49,50]. At pH 4.7, the spectrum contains two resonances at 0.3 ppm and 63.0 ppm. Further hydrolysis of aquated Al^{3+} ions resulted in a downfield shift of the Al resonance and an increase of the line width [51]. In line with literature [25], the disappearance of the poly-aluminium complexes characterized by a resonance at 4.4 ppm goes with the appearance of a

sharp signal around 63.0 ppm. This feature is caused by the symmetric tetrahedral coordination of Al in the Al_{13} complex $[AlO_4Al_{12}(OH)_{24}(H_2O)_{12}]^{7+}$ with the Keggin structure [52,53].

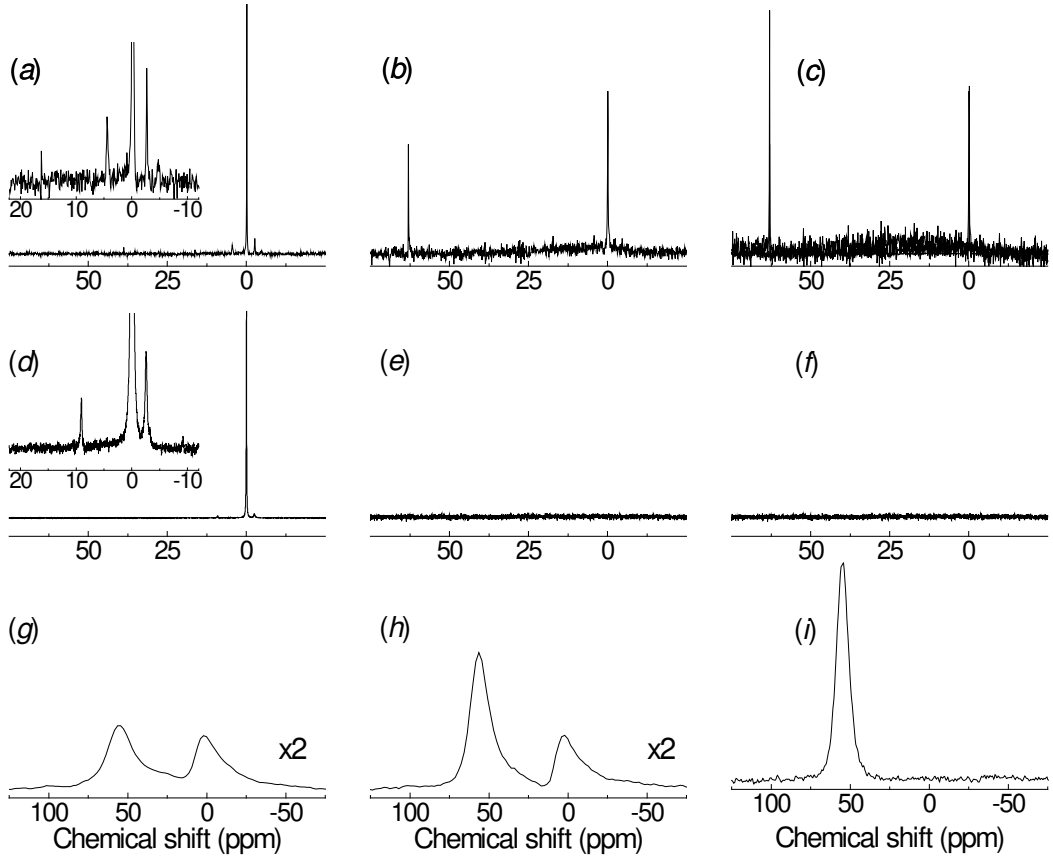

Figure 2.2: ^{27}Al NMR spectra of an aqueous 0.03 M aluminium nitrate solution during urea (0.76 M) decomposition at a temperature of 363 K at pH 3 (a), pH 4.7 (b) and pH 5.5 (c). Spectra of the solution (d-f) and dried solids (g-i) removed during the preparation of ASA(5/95) at pH 3 (d,g), pH 4 (e,h) and pH 6.5 (f,i).

The octahedral Al in this complex, which has been reported to give a characteristic resonance around 12 ppm [25], is absent in our spectrum, probably as a result of the strong quadrupolar line broadening caused by the asymmetry around the Al nuclei. Therefore, the resonance around 0 ppm should be mainly due to hydrolyzed aluminium complexes. The spectrum at pH 5.5 contains a single resonance at 63.0 ppm, which indicates that the solution contains predominantly Al_{13} complexes. Under these conditions, neither a signal of $Al(OH)_4^-$ at 80 ppm [54] nor of a suspected dimer Al_{13} complex at 70 ppm [55] are observed. As the pH rises above 5, the solution, which was clear at the beginning, becomes turbid which points to the onset of precipitation. Later, a distinct white precipitate is observed, which is pseudo-boehmite.

Subsequently, the synthesis of ASA(5/95) was examined by taking aliquots of the suspension at three stages: (i) at the end of region II (pH 3), (ii) during the strong pH increase

in region III (pH 4) and (iii) at the end of region IV (pH 6.5). After cooling, the solid was immediately separated from the liquid by a filter (Millipore, 0.4 μm) and ^{27}Al NMR spectra of the liquid and the dried solid were recorded. The resulting spectra and the loadings of the solids are given in Fig. 2.2 and Table 2.2, respectively. In region II, the coordination number of Al in the solution is 6 as follows from the dominance of the signals at -0.11 and -2.67 ppm. The signal at 4.4 ppm is absent and instead a weak resonance around 9 ppm is observed. The assignment of this signal is not clear, but various six-fold coordinated species have been observed between 12.6 and 4 ppm [25]. The Al content of the solid extracted at pH 3 is 4.3 wt% Al_2O_3. Thus, a large part of the Al has been grafted already to the surface at relatively low pH. A substantial part (60 %) is present in tetrahedral coordination (Al^{IV}, ~55 ppm) on the silica surface, the remaining Al species are in octahedral coordination (Al^{VI}, ~1.8 ppm). In the middle of region III at pH 4, all Al has been grafted to the silica surface, as the solid contains the 5.1 wt% Al_2O_3. In line with this, no Al is detected in the solution extracted at pH 4. Compared to the sample at pH 3, the solid contains a higher contribution of Al^{IV} (70 %). After completion of the synthesis, the solid contains exclusively Al^{IV} species. As the final ASA(5/95) and the sample extracted at pH 4 contain the same amount of Al, it follows that the atomic organization around the grafted Al^{3+} has changed markedly in region III.

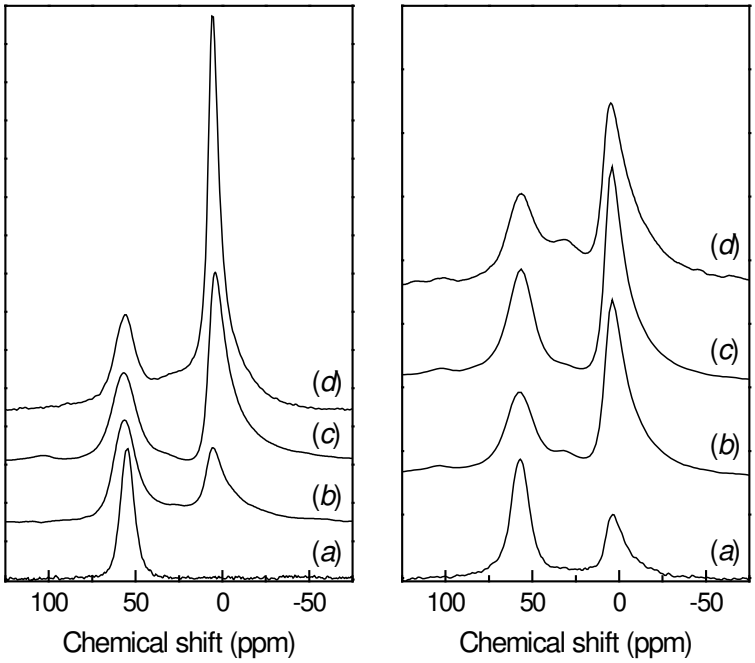

Figure 2.3: ^{27}Al NMR spectra of dried ASAs as a function of the aluminium concentration following completion of urea decomposition (left) and taken out at a pH of 3 (right) with targetted alumina contents of 5 wt% (a), 10 wt% (b), 15 wt% (c) and 20 wt% (d). Note that the actual alumina concentrations in the samples taken out at pH 3 deviate from the targetted concentrations.

Subsequently, the synthesis of ASA(5/95) was examined by taking aliquots of the suspension at three stages: (i) at the end of region II (pH 3), (ii) during the strong pH increase in region III (pH 4) and (iii) at the end of region IV (pH 6.5). After cooling, the solid was immediately separated from the liquid by a filter (Millipore, 0.4 μm) and ^{27}Al NMR spectra of the liquid and the dried solid were recorded. The resulting spectra and the loadings of the solids are given in Fig. 2.2 and Table 2.2, respectively. In region II, the coordination number of Al in the solution is 6 as follows from the dominance of the signals at -0.11 and -2.67 ppm. The signal at 4.4 ppm is absent and instead a weak resonance around 9 ppm is observed. The assignment of this signal is not clear, but various six-fold coordinated species have been observed between 12.6 and 4 ppm [25]. The Al content of the solid extracted at pH 3 is 4.3 wt% Al_2O_3. Thus, a large part of the Al has been grafted already to the surface at relatively low pH. A substantial part (60 %) is present in tetrahedral coordination (Al^{IV}, ~55 ppm) on the silica surface, the remaining Al species are in octahedral coordination (Al^{VI}, ~1.8 ppm). In the middle of region III at pH 4, all Al has been grafted to the silica surface, as the solid contains the 5.1 wt% Al_2O_3. In line with this, no Al is detected in the solution extracted at pH 4. Compared to the sample at pH 3, the solid contains a higher contribution of Al^{IV} (70 %). After completion of the synthesis, the solid contains exclusively Al^{IV} species. As the final ASA(5/95) and the sample extracted at pH 4 contain the same amount of Al, it follows that the atomic organization around the grafted Al^{3+} has changed markedly in region III.

Table 2.3: Coordination of aluminium in dried and calcined ASAs. The values represent the deconvoluted fractions of Al ions in Al^{IV} ($\delta \approx 54$ ppm), Al^{V} ($\delta \approx 30$-35 ppm) and Al^{VI} ($\delta \approx 0$ ppm) coordination.

Sample	393 K			773 K			1073 K		
	Al^{IV}	Al^{V}	Al^{VI}	Al^{IV}	Al^{V}	Al^{VI}	Al^{IV}	Al^{V}	Al^{VI}
ASA(5/95)	100	0	0	60	0	40	48	7	45
ASA(10/90)	50	6	44	44	14	42	50	8	42
ASA(15/85)	35	0	65	45	11	43	38	17	45
ASA(20/80)	24	6	70	30	16	54	26	14	60
ASA(5/95,3)	57	2	38	57	0	43	56	0	44
ASA(10/90,3)	35	4	61	45	2	53	48	4	48
ASA(15/85,3)	40	0	59	40	6	54	45	4	51
ASA(20/80,3)	24	16	60	42	10	48	41	22	37
ASA(5/95,cogel)	100	0	0	57 [1]	4 [1]	39 [1]			
ASA(5/95,fumed)	52	8	40	30	18	52			
ASA(5/95,F)	100	0	0	92	0	8			
ASA(20/80,DA)	80	0	20	47 [2]	10 [2]	43 [2]			

[1] Calcined at 923 K; [2] Calcined at 823 K.

In a similar manner, ^{27}Al NMR spectra of the ASAs with a higher alumina content extracted at pH 3 and after completion of the synthesis were recorded (Fig. 2.3). The spectra were deconvoluted into contributions of Al^{IV} and Al^{VI} (Table 2.3). The higher the starting concentration $[Al]_0$, the higher the content of octahedral Al. Note that the aluminium contents of the samples taken out at pH 3 are lower than for the samples prepared at a higher final pH. For some samples, a small contribution of a resonance between 30 and 35 ppm is noted, which is due to distorted four-coordinated or five-coordinated Al species [33,35,36]. The absolute amount of tetrahedral Al depends only weakly on the aluminium content. In contrast, the amount of Al^{VI} increases strongly with the aluminium content of the ASA.

The deposition of aluminium on silica will now be discussed as a function of the pH and the aluminium content. The synthesis of ASAs starts with the addition of aluminium nitrate to the urea-containing suspension of the silica aerogel. A hexa-aqua aluminium complex $[Al(H_2O)_6]^{3+}$ is formed, which hydrolyzes according to

$$[Al(H_2O)_6]^{3+} \leftrightarrows [Al(H_2O)_5(OH^-)]^{2+} + H^+ \qquad (2.7),$$

explaining the strong pH decrease. The initial pH decrease becomes more pronounced with higher $[Al]_0$ (Fig. 2.1). At low pH, further hydrolysis of the aluminium complexes is limited. The temperature of the suspension is raised in region I and urea decomposition commences above 343 K. As a result, the pH increases in region II. For ASA(5/95), the pH increased strongly in region II. With increasing $[Al]_0$, however, an initial strong pH increase was followed by a more gradual increase of pH with synthesis time. The initial increase is due to the establishment of a new equilibrium between the various charged Al species after the start

of urea decomposition. The relatively slow increase at higher $[Al]_0$ comes from the buffering effect from the continuous hydrolysis of the solvated Al^{3+} through

$$[Al(H_2O)_6]^{3+} + OH^- \rightarrow [Al(H_2O)_5(OH^-)]^{2+} + H_2O \qquad (2.8).$$

As this buffering effect becomes smaller at lower $[Al]_0$, a more pronounced pH increase with synthesis time is noted.

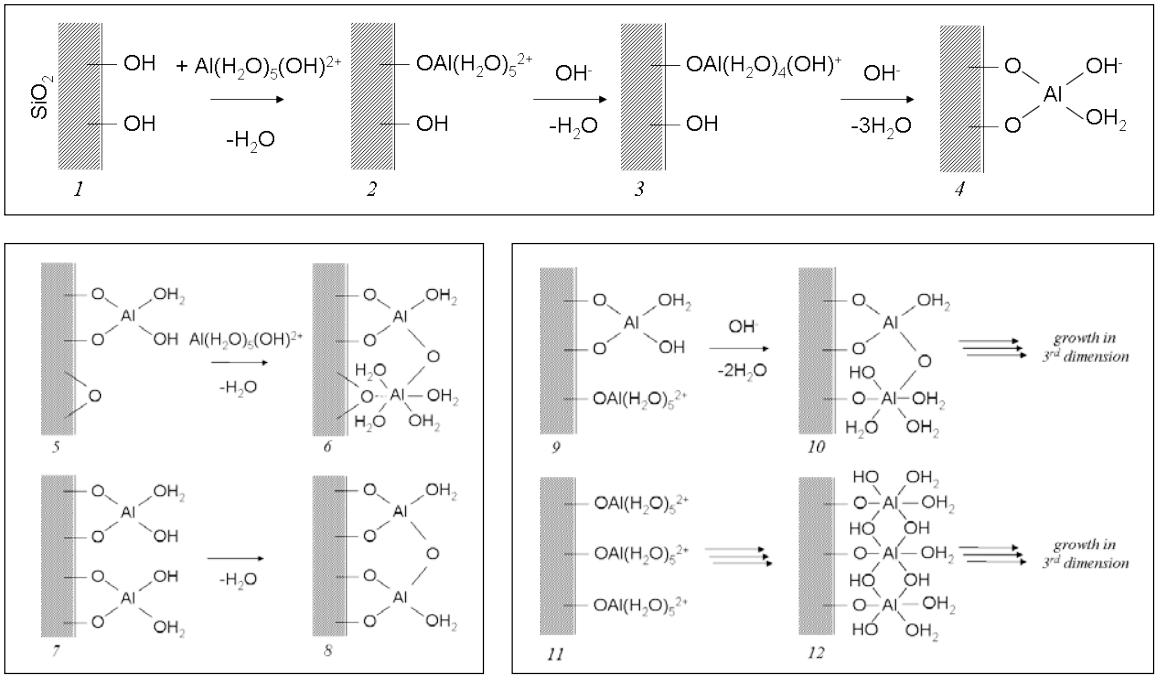

Figure 2.4: Schematic representation of grafting of partially hydrolyzed aluminium ions on silanol groups (*1*) resulting in monopodal (*2*) and bipodal (*4*) aluminium ions; the grafting of partially hydrolyzed aluminium ions to already grafted aluminium (*5* → *6*) and the condensation of hydroxyl groups of promixate bipodal surface aluminium (*7* → *8*) and condensation reactions between grafted bipodal and monopodal aluminium and proximate monopodal aluminium to polymeric forms of aluminium.

As follows from the investigation of the synthesis of ASA(5/95), a substantial amount of Al is grafted in region II (pH 3). All Al is grafted below pH 4. In order to account for the deposition of aluminium species on silica below pH 3, electrostatic interactions and hydrolytic adsorption should be considered. Electrostatic interactions between the positively charged metal-aquo complexes and its hydrolyzed form(s) with a negatively charged silica surface should, however, not be important under these conditions. Although the point of zero charge of silica is 2, the development of negative charge on its surface is very small below pH 6 [23]. Thus, the contribution of electrostatic interactions should be minor. For pH < 2, as is initially the case for the synthesis with high $[Al]_0$, the silica surface is positively charged, completely precluding such interactions. Alternatively, deposition can proceed via hydrolytic adsorption. This involves the condensation between partially hydrolysed aquated metal ions with the hydroxyl groups of metal oxides [41]. The dominant Al solution species at pH 3 are

six-fold coordinated $Al(H_2O)_6^{3+}$ and $Al(H_2O)_{6-x}(OH)_x^{3-x}$ (x = 1-2). Fig. 2.4 summarizes the reactions of $Al(H_2O)_5(OH)^{2+}$ with silanol groups at relatively low $[Al]_0$. Initially, hydrolytic adsorption results in a grafted octahedral Al^{3+} species (structure *2*). This species can further hydrolyze to structure *3* and a second condensation reaction with a proximate silanol group becomes possible. The resulting grafted Al species (structure *4*) is tetrahedrally coordinated. This structure was earlier proposed by De Boer [5] and Danforth [56] for the reaction between silica and aluminium ions under acidic conditions. De Boer also postulated the reaction of an $Al_2(OH)_6$ species with one silanol group to form a $\equiv SiO\text{-}Al_2(OH)_5$ species. Tamele [4] further proposed the reaction of hydrolyzed Al^{3+} species carrying three hydroxyl groups with three silanol groups on the surface, but such condensed species should not exist under these relatively acidic conditions.

Fig. 2.4 explains the changes in the aluminium coordination following the increase of the pH. At pH 3, already a substantial amount of Al (4.3 wt% Al_2O_3) is grafted to the silica surface. The contribution of Al^{IV} (Al^{VI}) is 60 % (40 %). These species are represented by structures *2* and *4*, respectively. The reaction from structure *2* to *4* implies that OH^- is not only used to hydrolyze the aluminium-aquo complexes in the solution but also grafted Al^{VI}. At the point where the majority of aluminium species have been hydrolyzed, the pH increases strongly due to further release of OH^- from urea. This defines the start of region III. The remaining Al species are deposited on the surface below pH 4. The dominant species in the solution between pH 3 and 4 should still be six-fold coordinated Al, although some Al_{13} complexes may be present as well. The Al coordination in ASA(5/95,4) already indicates that part of the initially grafted monopodal Al^{VI} species (structure *2*) have transformed into bipodal Al^{IV} species (structure *4*). The sample obtained after complete synthesis contains only Al^{IV} species, which is attributed to the further hydrolysis and condensation of all grafted Al^{VI} complexes with silanol groups during the further increase of the pH to its final value of 6.5 (region IV). Thus, condensation reactions between $Al(H_2O)_5(OH)^{2+}$ and silanol groups result in the formation of monopodal Al^{VI} species, which are then further converted upon base-catalyzed hydrolysis and condensation to bipodal Al^{IV} species. It is also possible that some of the grafting occurs via condensation of $Al(H_2O)_4(OH)_2^+$ with two silanol groups. If, during the deposition of aluminium on silica, each Al^{3+} reacts with two silanol groups, one would expect a maximum of 6.5 wt% Al_2O_3 as bipodal Al^{IV} species for this silica aerogel. Indeed, samples prepared at a higher aluminium content contain octahedral Al. The amount of Al^{IV} species in the final dried samples which varies slightly, that is 5.1 wt% Al_2O_3 for ASA(5/95,393), 6.1 wt% for ASA(10/90,393), 5.1 wt% for ASA(15/85,393), and 4.2 wt% for ASA(20/80,393), remains below the predicted maximum of 6.5 wt%. The distribution in Al coordination can be compared with those of the solids extracted at pH 3 (Table 2.2). Similar to ASA(5/95), a substantial fraction of Al has already been deposited on the silica surface in ASA(10/90,3). Part of these Al atoms present as Al^{VI} species at pH 3 change their coordination to tetrahedral during completion of the synthesis. The final pH of the synthesis of ASA(10/90) is a bit lower than that of ASA(5/95) as more hydroxyl anions were used to

hydrolyze Al. For ASA(15/85) and ASA(20/80), the amount of Al^{IV} decreases. A considerably smaller fraction of the total amount of Al in the synthesis mixture is grafted at pH 3 at this higher Al content. It is then interesting to determine under what conditions the remaining Al species are grafted. When the regular amount of urea was used in the preparation of ASA(20/80), the alumina content was limited to 16 wt% at a final pH of 3.3. When the final pH was increased to 5.5 by using a higher initial urea concentration of 1.1 M, the desired final loading was obtained. Thus, for pH < 3 about 10 wt% Al_2O_3 is grafted, for 3 < pH < 3.3 a further 6 wt% and, for pH > 3.3, the remaining amount of aluminium. These results suggest that most of the deposition of Al takes place below pH 4, even for the most aluminium-rich composition.

On the basis of the Al^{IV} content in ASA(10/90,3) of 3.6 wt%, we calculate that the remaining silanol groups can in principle accommodate an additional 6 wt% Al^{VI} species. The amount of Al^{VI} species in the solid at this stage of the synthesis is 5.4 wt%. However, it is then difficult to see how the amount of Al^{IV} species can increase to 6.1 wt.% after a further increase of pH to 5.5. A reasonable explanation is the condensation between an already grafted Al^{IV} species with aluminium species in the solution. The resulting Al^{VI} species should be more loosely bonded and may for instance interact with a surface siloxane bridge. This deposition reaction is shown in Fig. 2.4 (structure *5* → *6*). A consequence is that part of the silanol groups remain available for the formation of bipodal Al^{IV} species upon further hydrolysis at a later stage of the synthesis process. This explanation is not unreasonable, because it is well known that the rate of homocondensation between hydrolyzed Al species is higher than the rate of condensation between silanol and aluminol groups [17]. Moreover, grafting of $Al(H_2O)_5(OH)^{2+}$ on vicinal silanol groups should be unfavourable because of the charge repulsion between the grafted species. Another indication is that the amount of Al^{IV} in ASA(10/90) is close to the maximum predicted value of 6.5 wt%. In some cases, a small amount of distorted distorted Al^{IV} or Al^{V} species are observed and, tentatively, these are attributed to condensation between proximate bipodal Al^{IV} species, giving structure *8* (Fig. 2.4) which can be considered as distorted tetrahedral Al. Upon a further increase of $[Al]_0$, the amount of Al^{IV} species in the interrupted and final samples decreases. This can be understood in terms of an increased formation of grafted Al^{VI} species despite the resulting charge repulsion. Further reactions that can take place are those between monopodal Al^{VI} species and bipodal Al^{IV} species (Fig. 2.4, structure *9* → *10*). Obviously, condensation reactions between the grafted surface Al species and Al in the solution should also be considered at higher $[Al]_0$. Such reactions may lead to the growth of a polymeric aluminium hydroxide phase over the silica surface which may extend in the third dimension as would occur if further Al is grafted on top of structures *10* and *12*.

In summary, grafting of aluminium species on silica takes place via hydrolytic adsorption involving condensation reactions between silanol groups and hydrolyzed Al complexes from the solution at relatively low pH. At low $[Al]_0$, monopodal Al^{VI} species are formed which then further condense with proximate silanol groups to bipodal Al^{IV} species when the pH is

increased. An increase of $[Al]_0$ reduces the amount of grafted Al^{IV} species to some extent and leads to the presence of Al^{VI} species on the silica surface, which most likely have reacted with surface Al. At higher aluminium concentration, a polymeric aluminium hydroxide network is formed which may extend into the third dimension. The majority of Al species deposit at relatively low pH where grafting via heterolytic and homolytic adsorption is dominant over precipitation.

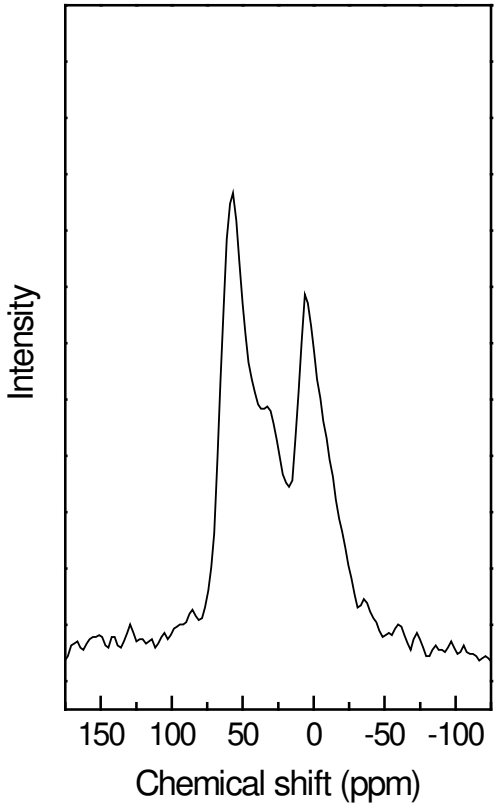

Figure 2.5: ^{27}Al NMR spectrum of ASA(5/95, fumed). The hydroxyl density of the fumed silica starting material is substantially lower (1.2 OH/nm^2) than that of the silica aerogel (4.1 OH/nm^2).

To validate the role of the surface hydroxyl group density in the deposition process, a further ASA synthesis was carried out with a fumed silica. The fumed silica has a lower hydroxyl density (1.2 OH/nm^2) than the Sipernat-50 silica (4.1 OH/nm^2). The aluminium loading of ASA(5/95,fumed) is somewhat lower at 4.2 wt% Al_2O_3 compared to ASA(5/95). The final pH values of the two syntheses (Table 2.2) are very similar. Fig. 2.5 shows the ^{27}Al NMR spectrum of dried ASA(5/95,fumed). This ASA contains five- and six-coordinated Al next to four-coordinated Al. Thus, at a lower surface hydroxyl concentration fewer sites are available for the grafting of aluminium to bipodal Al^{IV} and a larger part of the deposition takes place via condensation reactions with aluminium species already grafted to the surface. Indeed, the Al^{IV} content of 2.1 wt% in ASA(5/95,fumed) corresponds well to the expected maximum value of 2 wt% based on the hydroxyl density of the fumed silica.

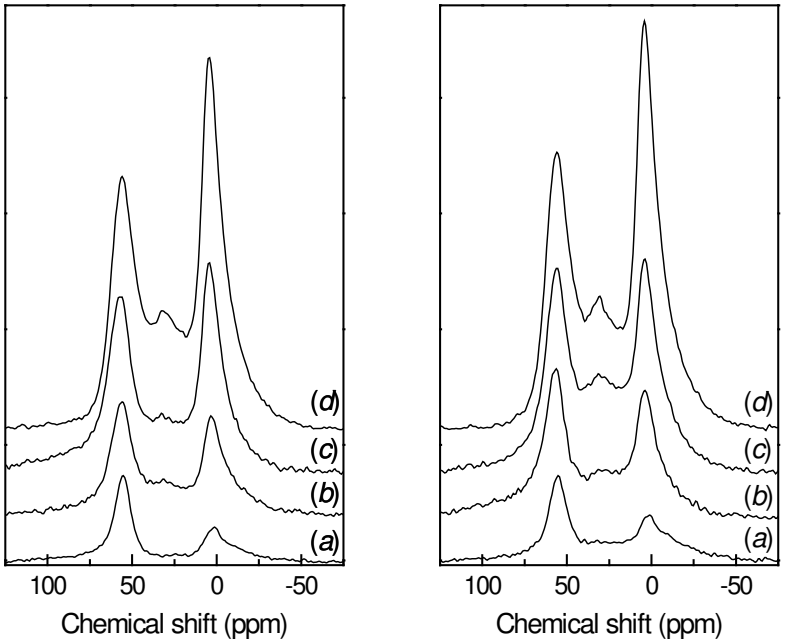

Figure 2.6: ^{27}Al NMR spectra of ASA(5/95) (a), ASA(10/90) (b), ASA(15/85) (c) and ASA(20/80) (d) calcined at 773 K (left) and 1073 K (right).

2.3.2 Calcination

Prior to their use as catalysts, ASA precursors are typically calcined at temperatures around 773 K to bring about the desired acidity. As will be shown below, these ASAs display the typical catalytic activity of industrial ASAs in alkane hydroconversion. Since calcination at 1073 K afforded more active catalysts, a detailed comparison of calcination at 773 and 1073 K was made. Firstly, the coordination of aluminium in the calcined ASAs will be compared by ^{27}Al NMR spectroscopy. The stepwise calcination up to 773 K will be investigated in more detail for a few samples. ^{29}Si NMR spectra at varying loading will be compared. Secondly, transmission and secondary electron microscopy were employed to study the spatial distribution of aluminium on the silica surface. Finally, the presence and composition of the segregated alumina phase was investigated by two methods of NMR, namely rotational resonance ^{27}Al NMR to probe the proximity of octahedral to tetrahedral Al nuclei as is typical found in transition aluminas and ^{27}Al NMR after ammonia adsorption to distinguish octahedrally coordinated Al atoms in a mixed silica-alumina phase from those in separate alumina domains.

Coordination environment of aluminium in calcined ASAs

Fig. 2.6 shows the ^{27}Al NMR spectra of the calcined ASAs. By comparison to those of the dried precursors, considerable changes in the chemical environment of aluminium are apparent. Firstly and foremost, the major part of the redistribution of the coordination environment of aluminium occurs upon calcination at 773 K (Fig. 2.6a). The changes after calcination at 1073 K (Fig. 2.6b) are relatively minor. Calcination at 773 K converts part of the four-coordinated Al in ASA(5/95) and ASA(10/90) to six-coordinated Al, whereas the reverse holds for ASA(15/85) and ASA(20/80). A preliminary explanation is one in terms of the formation of a separate transition alumina phase on the surface. The fraction of tetrahedral aluminium in spinel-structure transition aluminas is between 25 and 37 % [57]. At low alumina content, the appearance of octahedral Al points to agglomeration of isolated Al via formation of Al-O-Al bonds. The changes at higher aluminium concentrations can be attributed to dehydration of the polymeric aluminium oxo-hydroxide network in which octahedral Al is dominant into a transition alumina phase. The corresponding spectra of the calcined ASAs prepared at final pH 3 (Fig. 2.7) show similar trends, albeit that the changes are now less pronounced. Brønsted acidity induced by calcination is most likely due to the diffusion of aluminium atoms into the silica surface, where it substitutes Si^{4+} and induces a negative charge at the surface which requires compensation. Although tetrahedral Al at the surface cannot be distinguished from tetrahedral Al in the surface, the current thinking is that only very few such substitutions exist in the silica network [31].

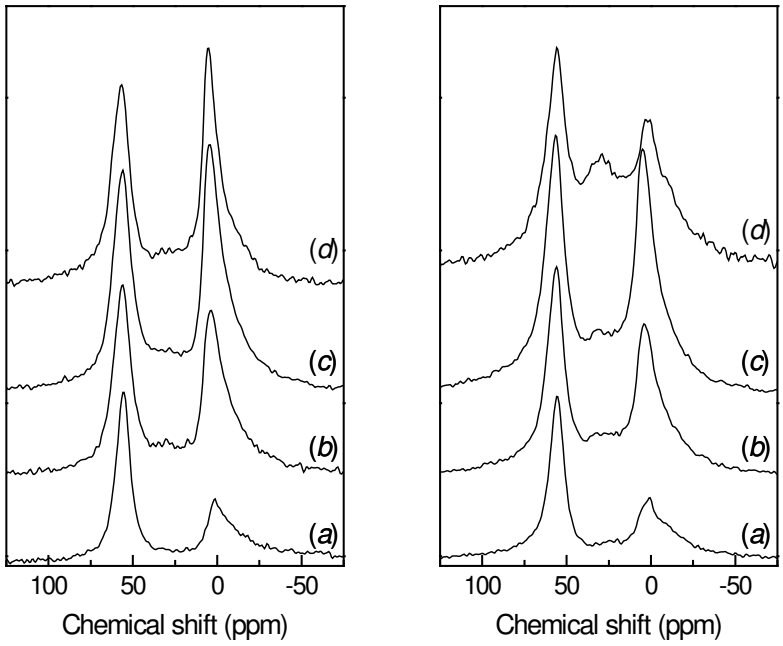

Figure 2.7: ^{27}Al NMR spectra of ASA(5/95,3) (a), ASA(10/90,3) (b), ASA(15/85,3) (c) and ASA(20/80,3) (d) calcined at 773 K (left) and 1073 K (right).

Secondly, the presence of a weak signal between 30 and 35 ppm in some of the ^{27}Al NMR spectra is noted. The amount of such species increased with the aluminium concentration.

This peak stems either from tetrahedral Al shifted by a strong quadrupolar distortion or from a five-fold coordinated Al species (Al^{V}). Multiple Quantum MAS NMR measurements can distinguish between these two coordination states by separating the quadrupolar and chemical effects on the chemical shift. To verify the assignment to five-coordinated Al for these ASAs, MQMAS NMR measurements for ASA(5/95,1073) and ASA(15/85,1073) were recorded (not shown). These data unequivocally show the presence of five-coordinated Al at a isotropic chemical shift around 30 ppm. The contribution of these aluminium species increased with the aluminium concentration. The single pulse ^{27}Al NMR spectra were deconvoluted into lineshape components attributed to Al^{IV}, Al^{V}, and Al^{VI}. Typically, deconvolution required two Gaussian components to fit the lineshape of Al^{VI}; the Al^{V} and Al^{IV} signals were fitted with single Gaussian lineshapes. The results for a large set of ASAs are listed in Table 2.3.

To understand the redistribution upon calcination, the evolution in the aluminium coordination of ASA(5/95) as a function of temperature was followed. ASA(5/95) was chosen because the surface of the dried precursor is expected to contain quite uniformly distributed grafted Al^{IV} atoms. As the surface density of Al most likely plays a role in the redistribution process, the calcination of an ASA with a substantially lower Al content, ASA(1/99), prepared in a similar manner as ASA(5/95) was investigated as well. Fig. 2.8 shows NMR spectra of the stepwise calcination. Calcination at 473 K results in the appearance of an octahedral signal in ASA(5/95) with a contribution of about 28 % (Fig. 2.8a).

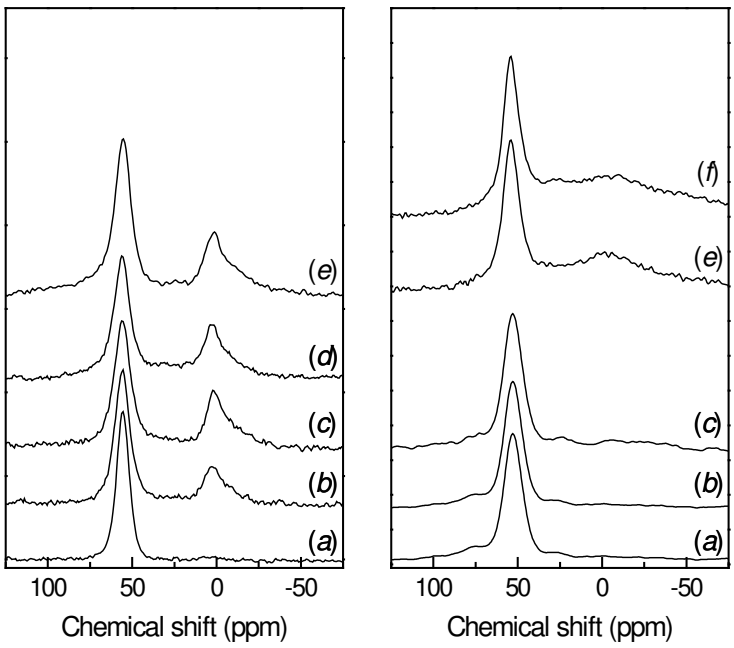

Its contribution grows further after calcination at 573 K and then remains constant up to a

Figure 2.8: ^{27}Al NMR spectra of ASA(5/95) (left) and ASA(1/99) (right) after calcination at 393 K (a), 473 K (b), 573 K (c), 673 K (d), 773 K (e) and 1073 K (f).

calcination temperature of 773 K. In comparison, the grafted Al^{IV} species in ASA(1/99) are stable at least until calcination at 573 K and further calcination at 773 K and 1073 K brings about only a weak and broad signal around 0 ppm (Fig. 2.8b).The difference between ASA(1/99) and ASA(5/95) indicates that the agglomeration of grafted Al^{IV} species on the silica surface strongly depends on their surface density. When the surface coverage with bipodal Al^{IV} is high, condensation reactions take place between the Al^{IV} already at quite low temperature. These reactions should involve the rupture of the bonds with the silica surface and it can be envisioned that associated water plays a role in the rehydrolysis of the Si-O-Al bonds. On the other hand, when grafted Al^{IV} become more diluted, they are thermally stable

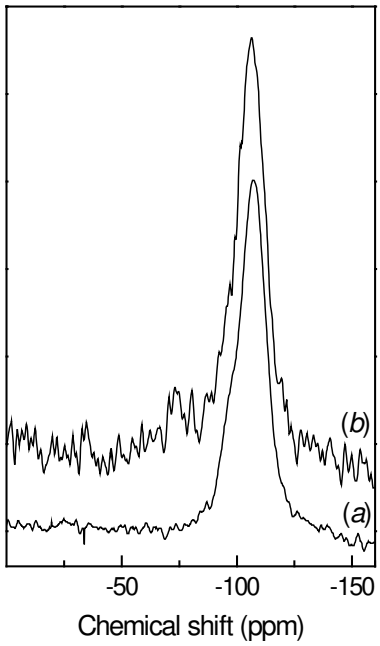

Figure 2.9: ^{29}Si NMR spectra of two amorphous silica-aluminas prepared in a similar manner as ASA(5/95,773) (a) and ASA(15/85,773) (b).

and do not agglomerate, even when the material is calcined at 1073 K.

High-power decoupled ^{29}Si NMR spectroscopy

Fig. 2.9 shows the proton-decoupled MAS ^{29}Si NMR spectra of two ASAs with nominal alumina contents of 5 and 15 wt% and calcined at 773 K prepared in a similar manner. The ^{29}Si NMR chemical shift is mainly affected by the chemical composition of the first and second coordination. The spectra are made up of two overlapping contributions from silicon atoms with tetrahedral oxygen coordination. The dominant resonance at –107 ppm is due to ^{29}Si with Q^4 coordination, *i.e.* four silicon atoms in the second coordination sphere. The asymmetric lineshape indicates the contribution of a resonance at -97 ppm, which belongs to Q^3-type silicon sites with three silicon atoms and either a hydrogen or aluminium atom in the second coordination sphere. The ^{29}Si NMR lineshape for the sample with the low and high alumina concentration is practically the same. Lineshape deconvolution indicates similar Q^3 fractions of 16 ± 1 %. The fact that the Q^3 fraction does not increase at increasing Al content

above 5 wt% Al_2O_3 suggests that, above a certain Al content, additional aluminium is not built into the aluminosilica phase anymore, but into a separate alumina phase. Extensive diffusion of aluminium into the silica is not expecteed during calcination at 773 K.

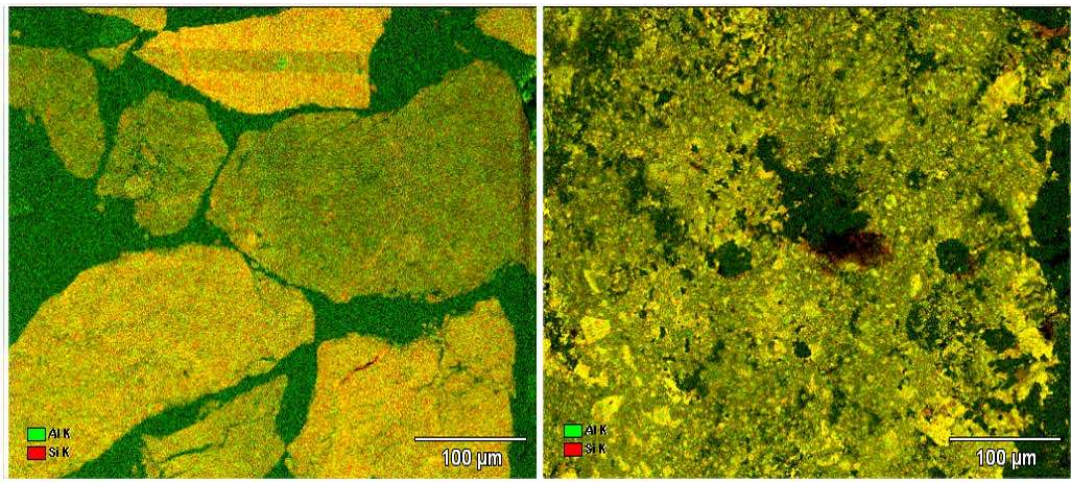

Figure 2.10: SEM/EDS micrographs of block faces of ASA(5/95,773) and ASA(20/80,773) (red: regions rich in silicon; green: regions rich in aluminium).

Homogeneity of the grafting process

To obtain an impression about the homogeneity of the surface distribution of aluminium, scanning electron micrographs of the block faces were recorded for ASA(5/95,773) and ASA(20/80,773). Fig. 10 shows that the aluminium density differs slightly between various silica particles. Heterogeneity on the scale of the silica grains should be due to differences in the hydroxyl density, which is a reasonable explanation as the parent silica was prepared by spray draying. In passing, we note that the substantial difference between ASA(5/95,773) and ASA(20/80,773) with open and compact morphologies, respectively, must have arisen during post-processing steps (filtration, calcination) of the materials.

For some ASAs the distribution of aluminium was analyzed in more detail by scanning transmission electron microscopy using line scans over areas of 5 × 5 µm. The samples in this case were Pd-loaded catalysts to be used for the alkane hydroconversion activity measurements. Fig. 2.11 shows representative results for ASA(5/95,1073), ASA(20/80,773), and ASA(20/80,3,1073). For ASA(5/95,1073), regions are observed where aluminium is rather uniformly distributed, *e.g.* position 2 in Fig. 2.11a, as follows from the linear relation between the signals of the Si and Al K edges. On the other hand, regions with a less homogeneous Al distribution were also observed. The variance in aluminium content per particle is exemplified for two particles in ASA(5/95,1073) with average values of 5.3 wt% (covariance 11.6 %) and 5.9 wt% (covariance 6.1%). Compared to ASA(20/80,773), however, the distribution is rather homogeneous. The aluminium distribution in ASA(20/80,773) varies quite strongly with the position. The differences between particles are also pronounced, *e.g.* two different particles contained 20.8 and 24.1 wt% Al_2O_3. The less

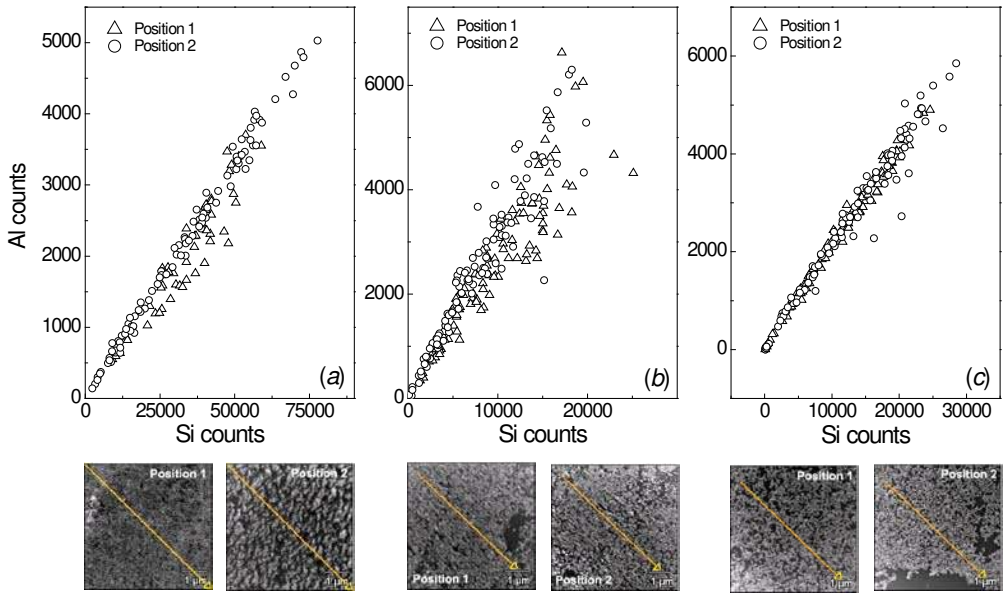

Figure 2.11: Si and Al counts across a diagonal line scan of a section of 5 × 5 μm measured by scanning TEM/EDS in ASA(5/95, 1073) (a), ASA(20/80, 773) (b) and ASA(20/80, 3, 1073) (c), each at two different positions. The corresponding electron micrographs are given below.

uniform aluminium distribution with increasing aluminium concentration agrees with the deposition model discussed above.

A considerable part of aluminium in ASA(20/80) reacts with initially grafted Al species. This may give rise to local concentration gradients of surface Al. The final pH of the synthesis of ASA(20/80) is 5.5, which means that some precipitation of pseudo-boehmite might have taken place. This is further supported when the data for ASA(20/80,3,1073) are taken into account. In the case that the deposition-precipitation process was stopped at pH 3, aluminium was found to be distributed quite homogeneously over the surface. Moreover, the alumina contents of two particles (16.8 and 16.9 wt% Al_2O_3) are quite similar. Grafting of aluminium to the silica surface and to already grafted Al species is the dominant process under these conditions and results in a homogeneous Al distribution. In summary, the electron microscopy analyses show that deposition of Al occurs rather homogeneously on the local scale for pH < 3. At higher pH, there is much more variation in the aluminium content, which is due to competition of precipitation with the grafting reactions. On the scale of the silica particles inhomogeneities are noted, presumably because of variations in the hydroxyl densities of the silica grains.

Distribution of Al in a mixed silica-alumina phase and alumina domains

The different changes in Al distribution following calcination for ASAs prepared at low and high aluminium content suggest that a fraction of aluminium is converted into domains of alumina. For a commercial ASA with a higher aluminium content, the presence of γ-Al_2O_3 is

evident in transmission electron micrographs by observation of nanometer-sized crystalline particles with the typical *d*-spacings of γ-alumina. No evidence for the presence of γ-Al_2O_3 was found in the set of HDP ASAs, suggesting that such particles, if at all present, should be very small. The flexibility of of the coordination of octahedral Al in ASAs can be used to distinguish between Al in alumina domains and Al in a mixed silica-alumina phase [31,37]. For example, the coordination of octahedral Al in γ-alumina does not change upon exposure to ammonia. Part of octahedral Al in ASAs change their coordination and are therefore considered to be part of the mixed phase. Williams et al. [31] assumed that non-flexible Al^{VI} in ASAs is present as γ-Al_2O_3 domains (tetrahedral Al:octahedral Al = 3:7). With this

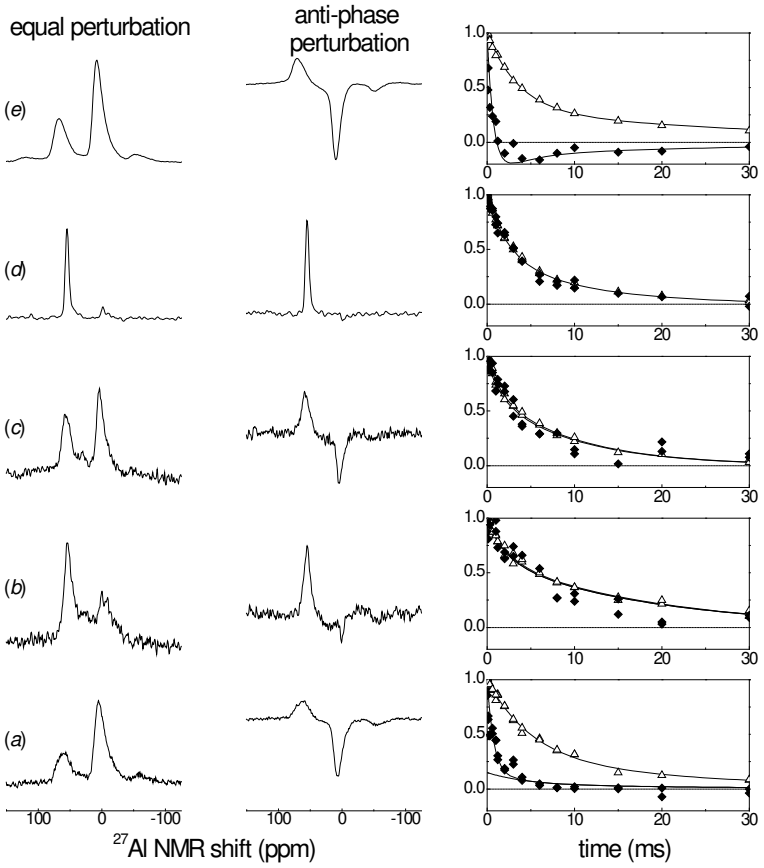

Figure 2.12: ^{27}Al spin exchange between octahedral and tetrahedral Al in ASAs: (a) ASA(55/45), (b) ASA(20/80, 1073) and (c) ASA(5/95, 1073). For comparison the upper part of the figure shows the results for (d) zeolite HZSM-5 (Si/Al = 20) and (e) γ-Al_2O_3. The left column shows the ^{27}Al NMR spectra with equally excited tetrahedral and octahedral Al nuclei. The center column reflects the anti-phase perturbation prior to mixing time. The right column shows the decay of the tetrahedral Al signal at 56 ppm (♦) during the mixing time as the combined result of spin exchange in the alumina phase and spin lattice relaxation. For comparison spin-lattice relaxation has also been measured separately (△).

assumption, the distribution of aluminium over γ-Al_2O_3 and a mixed silica-alumina phase can be calculated. The assumption that alumina occurs as γ-Al_2O_3 does not introduce a large error as the fraction of Al^{IV} in typical transition aluminas varies between 27-35 % [57].

Before discussing NMR data before and after ammonia adsorption, we first verified whether the HDP ASA contain the suspected transition alumina phase. To distinguish between tetrahedrally coordinated aluminium atoms in the mixed silica-alumina and alumina phases in ASA, we make use of the fact that Al atoms in a pure silica-alumina phase have only Si neighbours, whereas the alumina phase contains neighbouring tetrahedral and octahedral Al atoms at typical separation of 3 Å. At such distance, Al nuclei have a homonuclear dipolar coupling with a constant of about 140 Hz. In principle, this ^{27}Al-^{27}Al coupling between octahedral and tetrahedral Al atoms could be used as a distinguishing feature between Al in the mixed silica-alumina and alumina phase. However, the same magic-angle spinning that is required for ^{27}Al NMR line narrowing also suppresses the ^{27}Al-^{27}Al coupling, in general. Fortunately, an exceptional situation arises, if the sample-rotation rate matches the peak separation. Then, constructive interference occurs between the periodic modulations in the dipolar Hamiltonian by the sample rotation and chemical-shift difference, and spin polarization may be exchanged between the coupled nuclei. Such special dipole-coupling effect when the sample rotation matches the peak separation, is called rotational resonance (R^2) and it has been employed to measure coupling constants of isolated spin 1/2 pairs, such as ^{13}C-^{13}C for distance measurements in solid organic compounds [58]. For quadrupolar nuclei, like ^{27}Al with spin 5/2, the case becomes complicated by cross-interference with the quadrupolar coupling, as well as possible pulse-selectivity artefacts. In addition, the ^{27}Al nuclei in the alumina phase do not occur as isolated pairs, and thus multispin effects arise. Therefore, the polarization transfer is expected to proceed in a spin-diffusive, rather than an oscillatory way.

Aiming at a semi-quantitative NMR tool, we have empirically tested the R^2 technique for ^{27}Al NMR of pure γ-alumina with neighbouring tetrahedral and octahedral Al, on the one hand, and zeolite HZSM-5 with isolated tetrahedral Al only, on the other. Fig. 2.12 shows the polarization recovery of the tetrahedral ^{27}Al nuclei after a selective pulse scheme which alternatingly inverts the polarization of Al spins resonating at either 56 or 6 ppm. Such pulse scheme yields anti-phase polarization, *i.e.* the tetrahedral and octahedral Al spins are prepared with opposite polarization. In the subsequent 'mixing time' the neighbouring tetrahedral and octahedral Al alumina are given the opportunity to exchange polarization. The polarization of the isolated Al sites in the zeolite only changes under the influence of spin-lattice relaxation. This relaxation, which affects the ^{27}Al spins in alumina as well, can be independently measured in control experiments with a non-selective polarization perturbation of both the tetrahedral and octahedral ^{27}Al nuclei. In all cases, the sample-rotation rate was matched to the chemical-shift difference (~ 7.5 kHz).

As can be seen in Fig. 2.12d and 2.12e, alumina and zeolite HZSM-5 behave markedly different. For the zeolite the rate at which the tetrahedral signal at 56 ppm recovers after the

selective pulse is the same as after the nonselective pulse. For γ-Al_2O_3, in contrast, the recovery of the tetrahedral Al polarization after the anti-phase polarization perturbation of the tetrahedral and octahedral Al spins strongly differs from the background relaxation. This is a consequence of the R^2 effect, which induces polarization exchange between the octahedral and tetrahedral Al nuclei, and yields a fast redistribution of the perturbed polarization over the two Al types in alumina before the whole system of octahedral and tetrahedral Al relaxes back to thermal equilibrium, as a homogeneously polarized ensemble.

Given the different R^2 behaviour of tetrahedral Al in alumina and zeolite HZSM-5, the technique was employed as a semi-quantitative tool for discriminating between tetrahedral Al in the alumina and the mixed silica-alumina phases in ASA. Fig. 2.12a-c shows the results for ASA(5/95,1073), ASA(20/80,1073), and a commercial ASA with an nominal Al_2O_3 content of 55 wt%, here denoted by ASA(55/45). The commercial ASA contains γ-alumina as evidenced by TEM. It is immediately clear from this figure that the tetrahedral Al in ASA(5/95) and ASA(20/80) behave as isolated sites without octahedral Al neighbours. This indicates that up to such Al concentrations no predominant alumina phase is present in ASA. ASA(55/45), however, shows faster R^2 exchange than spin-lattice relaxation. The behaviour is in between that of HZSM-5 and γ-Al_2O_3.

To analyze the R^2 curves in more detail and estimate the alumina fraction in ASA from the bi-component behaviour in the R^2 exchange, we have taken a two-site exchange model for polarization exchange between neighbouring tetrahedral and octahedral ^{27}Al spins in the alumina phase, and extended this with two isolated sites representing ^{27}Al spins in the mixed silica-alumina phase (see Supporting Information). On the basis of this model we have analyzed the recovery curves in terms of a fast R^2 spin-exchange component and a slow background-decay, according to

$$I_T(t) = I_T(0)\left\{A_T \exp\left(-t_{mix}/\tau_{se}\right) + 1 - A_T\right\} R(t_{mix}) \qquad (2.9),$$

with A_T and τ_{se} being the amplitude and characteristic time of the fast decay component caused by spin exchange, respectively. $R(t_{mix})$ is the background decay determined independently from the spin-lattice relaxation after nonselective perturbation. In all cases, the background decays turned out to well described by a bi-exponential curve of the form

$$R_0(t_{mix}) = I_0^{'}\left\{A \exp\left(-t_{mix}/T_{1A}\right) + B \exp\left(-t_{mix}/T_{1B}\right)\right\} \qquad (2.10),$$

with A, B , T_{1A}, and T_{1B} being, respectively, phenomenological fractions and spin-lattice relaxation times. For every alumina and ASA sample measured, the background decays for the tetrahedral and octahedral aluminium nuclei were the same within error, as consistent with the polarization averaging resulting from spin diffusion. The deviation from mono-exponential behaviour need not reflect heterogeneity, since spin-lattice relaxation of quadrupolar nuclei in solid-state NMR can be described intrinsically bi-exponential [59]. According to this model, the relative amplitude A_T of the fast decay components related to the relative number of tetrahedral Al in the alumina phase, as

$$A_T = \kappa \frac{N_{Al2O3,T}}{N_{Al2O3,T} + N_{AS,T}} \qquad (2.11),$$

with $N_{Al2O3,T}$ and $N_{AS,T}$ being the number of tetrahedral Al sites in the alumina and a mixed silica-alumina phase, respectively. The proportionality constant κ equals $f_{Al2O3,O}(1-p_O(0)/p_T(0))$ where $f_{Al2O3,O}$ denotes the fraction of octahedral sites in the alumina phase, and $p_O(0)$ and $p_T(0)$ the polarization of the octahedral and tetrahedral Al spins and $p_O(0)$ and $p_T(0)$ immediately after the selective perturbation preceding the mixing time. Note that κ and the spin-exchange component vanish, if the octahedral and tetrahedral Al sites are equally perturbed prior to the mixing time t_{mix}. Indeed, this exactly corresponds to the experimental condition to measure the relaxation background decay $R(t_{mix})$ without R^2 exchange. The largest amplitude of the spin-exchange component occurs for perfect anti-phase perturbation, *i.e.* if the initial polarization values of the tetrahedral and octahedral sites have opposite values, $p_O(0) = - p_T(0)$. As for the other parameter $f_{Al2O3,O}$, γ-Al_2O_3 and several other transition alumina types, have a typical octahedral Al fraction of about 0.7. Under these conditions κ reduces to 1.4.

Table 2.4: Parameters used to fit the model described by Eqs. 2.9 and 2.10 to the R^2-exchange and spin-lattice relaxation data.

R^2-exchange			spin-lattice relaxation			
Sample	A_T	τ_{sd} (ms)	A	T_{1A} (ms)	T_{1B} (ms)	$T_{1,av}$[1] (ms)
γ-Al_2O_3	1.4	0.86	0.67	3.3	29	4.6
HZSM-5	0.0	0.86[2]	0.55	2.2	10	3.6
ASA(5/95,1073)	0.0	0.86[2]	0.35	2.2	18	5.0
ASA(20/80,1073)	0.0	0.86[2]	0.33	1.6	9.9	3.6
ASA(55/45)[3]	0.85	0.83	0.77	4.2	33	5.9
	0.87	0.88	0.77	4.2	33	5.9

[1] Average relaxation time $T_{1,av} = [A/T_{1A}+B/T_{1B}]^{-1}$ are given for comparison.
[2] For HZSM-5, ASA(5/95) and ASA(20/80), τ_{se} was fixed to the value found for γ-Al_2O_3 and ASA(55/45).
[3] The R^2 curve for ASA(55/45) was measured twice and analyzed with the same T_1 relaxation parameters.

Table 2.4 summarizes the fit parameters extracted from the R^2 exchange curves in Fig. 2.12 by use of Eqs. 7 and 8. Parameters A, B, T_{1A}, and T_{1B} in Eq. 8 were determined independently in separate spin-lattice relaxation experiments. Only $I_T(0)$, A_T, and τ_{se} were allowed to vary during fitting of Eq. 2.9 to the observed R^2-exchange curves for γ-Al_2O_3 and ASA(55/45). The R^2 curve of the latter was measured twice to check the reproducibility of the experiment and analysis. For HZSM-5, ASA(5/95), and ASA(20/80), τ_{se} was fixed to the value 0.86, *i.e.* the characteristic spin-exchange time found for γ-Al_2O_3 and the alumina phase in ASA(55/45). The low amount of Al in ASA(5/95) caused severe scattering of the R^2 exchange data measured with ^{27}Al NMR. The bi-exponential fit to the non-exponential spin-

lattice relaxation decays comes with large correlation errors in the fit parameters. For better comparison the more significant weight-average relaxation times $T_{1,av} = [A/T_{1A}+B/T_{1B}]^{-1}$, with A+ B = 1, are also given in Table 2.4. The value $A_T = 1.4$ extracted from the R^2 decay of γ-Al_2O_3 perfectly corresponds to theoretical value for a pure Al_2O_3 (fraction tetrahedral 30 %), in combination with perfect anti-phase perturbation of the Al spins prior to the mixing time. This indicates that, despite the simplifications in the model such as neglecting the influence of the quadrupolar interaction, the estimated fraction tetrahedral Al atoms in the alumina phase from resonance NMR may be correctly estimated. With the proportionality constant $\kappa = 1.4$, the average value A_T of 0.86 obtained for ASA(55/45) suggests that about 60 % of the tetrahedral Al atoms are located in the alumina phase. The two ASAs prepared by homogeneous deposition-precipitation do not contain octahedral Al near tetrahedral Al. The content of a separate phase with the characteristic presence of octahedral and tetrahedral Al in close proximity can therefore be considered to be negligible. Instead, this phase only contains octahedral Al.

Fig. 2.13 shows then the NMR spectra before and after NH_3 adsorption for the HDP ASAs. The single pulse ^{27}Al NMR spectra were deconvoluted into Al^{IV}, Al^{V}, and Al^{VI} contributions and the results are listed in Tables 2.5 and 2.6. The initial spectrum of ASA (5/95,773) contains an Al^{IV} signal at 55 ppm and two contributions of Al^{VI} signals around 0 ppm. After dehydration and adsorption of ammonia, the signal of Al^{IV} has slightly grown at the expense of the octahedral Al signal. Thus, a small fraction of the Al^{VI} in ASA(5/95,773) displays flexible coordination. After calcination at 1073 K, the changes are more pronounced. In this case, a small downfield shift of the Al^{IV} signal is observed from 55 to 59 ppm. The changes for the two ASA(5/95,3) samples are much more pronounced. All octahedral Al in ASA(5/95,3,773) reverted to tetrahedral coordination after adsorption of ammonia. Thus, ASA(5/95,3,773) is a rather pure amorphous silica-alumina sample free of alumina domains. The shift in the Al^{IV} peak position relates to the ligand exchange. With increasing aluminium content, the changes in aluminium coordination become less pronounced. The changes are larger for the complete synthesis ASAs than for the ASAs prepared at final pH 3.

The presence of Al^{VI} atom that cannot be reinserted into the mixed phase points to the presence of very small clusters of aluminium oxide. It should be noted beforehand that some of the six-coordinated Al changes its coordination to a five-fold one upon ammonia adsorption. Further MQMAS NMR measurements are needed to determine whether these Al atoms exhibit distorted tetrahedral coordination or are truly five-coordinated. However, for the present discussion their flexibility will be taken as an argument that they are part of the mixed silica-alumina phase.

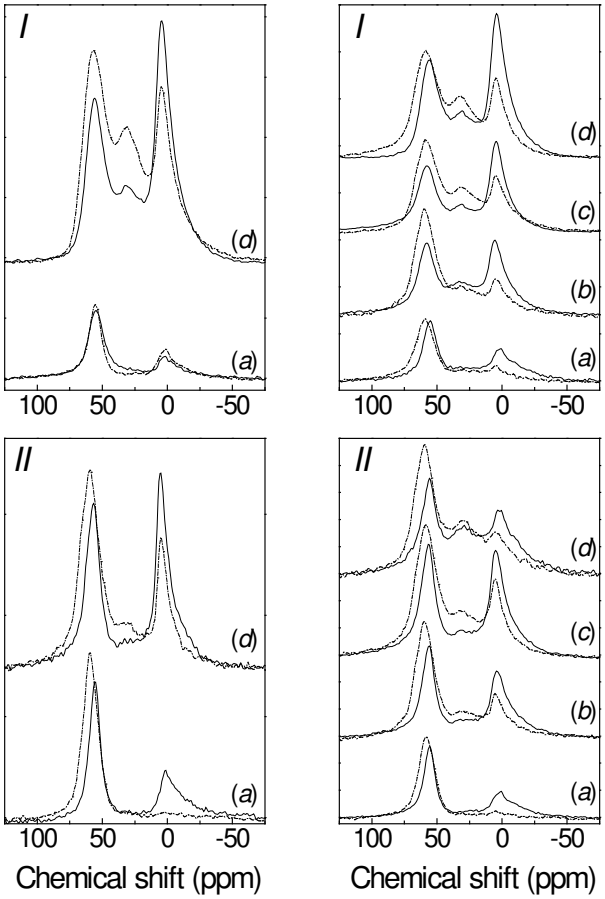

Figure 2.13: ^{27}Al NMR spectra of ASAs following full synthesis (I) and until pH 3 (II) calcined at 773 K (left) and 1073 K (right) before (full line) and after (dashed line) ammonia adsorption: ASA(5/95) (a), ASA(10/90) (b), ASA(15/85) (c) and ASA(20/80) (d).

Table 2.5: Distribution of Al in mixed silica-alumina and alumina phases in ASAs calcined at 773 K. NMR spectra recorded before and after exposure to ammonia (indicated by suffix NH_3). Values represent the percentages of the total amount of Al. The nominal Al content (w_{Al2O3}) of both phases are given as well.

Sample	Al coordination			Mixed phase[1]			Alumina domains[2]	
	Al^{IV}	Al^{V}	Al^{VI}	$Al^{IV}+Al^{VI}$	Interface	w_{Al2O3} (wt%)	Al^{VI}	w_{Al2O3} (wt%)
ASA(5/95)	60	0	40	66	3	3.5	31	1.6
ASA(5/95)-NH_3	66	3	31					
ASA(5/95,3)	57	0	43	100	0	4.3	0	0
ASA(5/95,3)-NH_3	100	0	0					
ASA(20/80)	30	16	54	33	26	12	39	8.0
ASA(20/80)-NH_3	33	26	39					
ASA(20/80,3)	42	19	48	65	6	7.1	29	2.9
ASA(20/80,3)-NH_3	65	6	29					

[1] Mixed phase contains Al^{IV} and Al^{VI} reverted to Al^{IV} after ammonia adsorption ($Al^{IV}+Al^{VI}$) and Al^{V} after ammonia adsorption (interface); [2] Alumina domains contain Al^{VI} whose coordination does not change following ammonia adsorption.

The distribution of Al in a mixed silica-alumina phase and alumina domains for a subset of ASAs is presented in Tables 2.5 and 2.6. We make use here of the finding by R^2 NMR that

octahedral Al nearby enough to tetrahedral Al to consider the presence of a transition alumina phase is absent in the sample with the highest Al content. Thus, the amount of inflexible Al^{VI} corresponds to the amount of a separate aluminium oxide phase. As will be shown below, the amount of Al^{V} after ammonia adsorption represents the interface between the alumina domains and the mixed phase in line with the conclusion of Williams et al. [31]. Furthermore, Al^{V} is considered part of the mixed silica-alumina phase. Some general trends will be discussed here. Only at the lowest alumina content, the surface of the ASA prepared at final pH 3 can be considered a pure mixed silica-alumina phase. The absence of octahedral Al after ammonia adsorption shows that ASA(5/95,3,773) contains no alumina domains. Only a very small amount of alumina domains is found after calcination at 1073 K. In line with the larger tendency of tetrahedral Al in ASA(5/95) to agglomerate, the amount of alumina domains is higher for ASA(5/95,773) and ASA(5/95,1073). In general, the higher the aluminium content of the ASA, the higher the amount of alumina domains. The contribution of alumina domains is higher for the full synthesis ASAs than for the ASAs prepared at final pH 3 in an absolute and relative sense. This difference agrees with the finding that surface grafting is dominant until pH 3, whereas precipitation becomes a competing mechanism at higher pH. Furthermore, the amount of alumina domains does not depend strongly on the calcination temperature.

Table 2.6: Distribution of Al in mixed silica-alumina and alumina phases in ASAs calcined at 1073 K. NMR spectra recorded before and after exposure to ammonia (indicated by suffix NH_3). Values represent the percentages of the total amount of Al. The nominal Al content (w_{Al2O3}) of both phases are given as well.

Sample	Al coordination			Mixed phase			Alumina domains[1]	
	Al^{IV}	Al^{V}	Al^{VI}	Al^{IV}+Al^{VI}	interface	w_{Al2O3} (wt%)	Al^{VI}	w_{Al2O3} (wt%)
ASA(5/95)	48	7	45	74	6	4.0	20	1.0
ASA(5/95)-NH_3	74	6	20					
ASA(10/90)	50	8	42	64	12	7.7	24	2.4
ASA(10/90)-NH_3	64	12	24					
ASA(15/85)	38	17	45	44	28	10.9	28	4.2
ASA(15/85)-NH_3	44	28	28					
ASA(20/80)	26	14	60	48	30	15.6	22	4.4
ASA(20/80)-NH_3	48	30	22					
ASA(5/95,3)	56	0	44	87	0	3.7	13	0.6
ASA(5/95,3)-NH_3	87	0	13					
ASA(10/90,3)	48	4	48	66	12	7.0	22	2.0
ASA(10/90,3)-NH_3	66	12	22					
ASA(15/85,3)	45	4	51	59	16	9.1	25	3.0
ASA(15/85,3)-NH_3	59	16	25					
ASA(20/80,3)	41	22	37	59	11	7.0	30	3.0
ASA(20/80,3)-NH_3	59	11	30					
ASA(5/95,cogel)	57	4	39	84	4	4.4	12	0.6
ASA(5/95,cogel)-NH_3	84	4	12					

[1] Mixed phase contains Al^{IV} and Al^{VI} reverted to Al^{IV} after ammonia adsorption (Al^{IV}+Al^{VI}) and Al^{V} after ammonia adsorption (interface); [2] Alumina domains contain Al^{VI} whose coordination does not change following ammonia adsorption.

2.3.3 ASAs prepared by alternative methods

A few other preparation methods to arrive at ASAs were explored. The first one consisted of cogelation of a mixture of sodium silicate in an aqueous aluminium chloride solution. Gelation was brought about by lowering pH to 7. ASA(5/95,cogel) has a surface area of 463 m^2/g and a pore volume of 1.6 ml/g. After exchange of all sodium by ammonium ions, the ^{27}Al NMR spectrum of the dried material (Fig. 2.14a) shows that aluminium is exclusively present in tetrahedral coordination. In principle, one expects that the aluminium atoms become highly dispersed in the silica particles. When this material is calcined at 923 K, the presence of both five- and six-coordinated Al becomes apparent. Analysis of the ^{27}Al NMR after adsorption of ammonia shows that the majority of aluminium in this catalyst is part of a mixed silica-alumina phase and only 0.4 wt% Al_2O_3 has segregated to alumina domains. Thus, the aluminium distribution of ASA(5/95,cogel) is quite similar to ASA(5/95,3,1073).

The dried precursor to ASA(5/95,fumed) contains already five- and six-coordinated aluminium due to the lower hydroxyl density. This difference with ASA(5/95), which contains exclusively four-coordinated Al, implies that the fraction of Al which has been grafted to the already deposited Al or has precipitated should be larger than in ASA(5/95). Indeed, after calcination at 773 K further agglomeration of aluminium takes place, as follows from the increased contribution of octahedral Al. After calcination at 1073 K, the amount of octahedral Al is lower again. This behaviour is quite similar to the HDP ASAs prepared at higher $[Al]_0$. These results suggest that this ASA contains a more substantial amount of alumina domains.

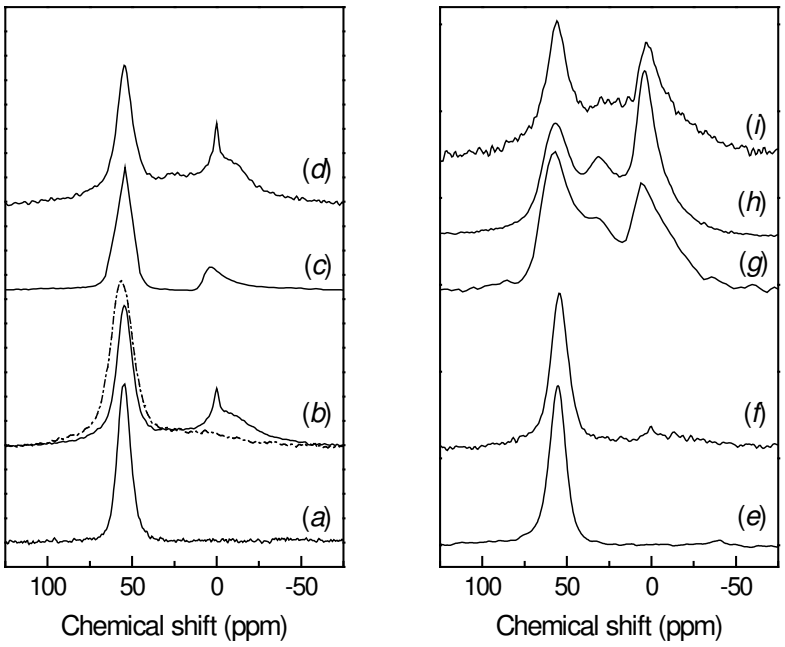

Figure 2.14: ^{27}Al NMR spectra of various ASAs: ASA(5/95, cogel, 393) (a), ASA(5/95, cogel, 923) (b), ASA(20/80, DA, 393) (c), ASA(20/80, DA, 823) (d), ASA(5/95, F, 393) (e), ASA(5/95, F, 773), (f), ASA(5/95, fumed, 393) (g), ASA(5/95, fumed, 773) (h) and ASA(5/95, fumed, 1073) (i). For ASA(5/95, cogel), the spectrum after ammonia adsorption is also shown (dashed line).

Alumination of a reactive silica surface with ammonium hexafluoroaluminate results in the exclusive formation of tetrahedral Al species. In this synthesis, the pH of an aqueous suspension of silica was adjusted to 9 and grafting was started by introduction of ammonium hexafluoroaluminate. In the strongly basic solution, octahedral AlF_6^- hydrolyze to tetrahedral $[Al(OH)_4]^-$ species [27] via

$$AlF_6^{3-} + 4OH^- \rightarrow Al(OH)_4^- + 6F^- \quad (2.12).$$

As the silica surface is negatively charged under these conditions, the dominant deposition mechanism should be direct condensation of $Al(OH)_4^-$ through

$$2 \equiv SiO^- + [Al(OH)_4]^- + H_2O \rightarrow (\equiv SiO)_2\text{-}Al(H_2O)(OH^-) + 3\ OH^- \quad (2.13).$$

Upon calcination at 773 K, the coordination of Al does not change as pronouncedly as observed for the other amorphous silica-aluminas. About 90 % of aluminium remains tetrahedral and thus a considerable fraction of aluminium resists agglomeration to polymeric forms. The reason for this is not clear. Possibly, strong rearrangements of the silica surface, such as opening of siloxane bonds, can take place under the rather basic conditions and in the presence of fluoride anions. This can give rise to the formation of favorable binding sites for aluminium.

Fig. 2.14c shows the ^{27}Al NMR spectrum of dried ASA(20/80,DA). The use of the molecular di-*sec*-butoxyaluminotriethoxysilane precursor with preformed Si-O-Al linkages yields an ASA with a higher amount of tetrahedral Al compared to HDP ASAs of similar Al content. The higher fraction of tetrahedral Al (70 %) in the dried precursor compared to ASA(20/80) (20 %) suggests that a large part of the hydrolysed aluminium-alkoxy groups react with hydrolyzed silicon-alkoxy groups. Nevertheless, due to the faster hydrolysis of aluminium-alkoxy groups compared to silicon-alkoxy groups [17] and the tendency of Al to condense with other Al species, the Al coordination is not purely tetrahedral. Upon calcination at 773 K (Fig. 2.14d), the fraction of tetrahedral Al strongly decreases to 47 %. The distribution in aluminium coordination is then quite comparable to ASA(20/80,3,773).

2.3.4 Catalytic activity of amorphous silica-aluminas

The acidity of the calcined ASAs was evaluated by determining their catalytic activity in the hydroconversion of *n*-heptane. In the presence of Pd metal, the reaction proceeds by a bifunctional reaction mechanism involving dehydrogenation of the paraffin to an olefin and the reverse hydrogenation as well as the isomerization and cracking of olefins by Brønsted acid sites. There is a general agreement that the isomerization and cracking of alkenes at moderate temperature requires strong Brønsted acid sites [45,46,60,61]. The temperature to obtain an *n*-heptane conversion of 40 % (T_{40}) is taken as the activity parameter, because it correlates to the number of Brønsted acid sites when their intrinsic strength is constant [47].

A steam calcined faujasite zeolite (USY(9.3), T_{40} = 506 K) and a commercial ASA calcined at 773 K (T_{40} = 623 K) and 1073 K (T_{40} = 613 K) were used as reference catalysts.

The kinetic parameters of *n*-heptane hydroconversion for the set of ASAs are presented in Table 2.7. The HDP ASAs exhibit comparable acid activity to industrial ASAs. The acid activity of ASAs is considerably lower than that of a USY zeolite. Assuming constant acidity of the acid sites, this result implies that the acid site density of ASAs is at least two orders of magnitude lower. The Brønsted acidity of the various ASAs is very similar. ASAs calcined at 1073 K are more acidic than those calcined at 773 K. The differences as a function of the aluminium concentration are relatively small. The one notable exception in this series is the low activity of ASA(1/99, 1073) which was about four times less active than ASA(5/95,1073). In general, the acidities of ASAs prepared at final pH 3 are slightly more acidic than their companions synthesized following completion of urea decomposition, albeit that the most acidic catalyst is ASA(15/85,1073). The activity of ASA(5/95,fumed) is very similar to that of ASA(5/95,773). ASA(5/95,F) has a very low acidity. The two most acidic ASAs are ASA(5/95,cogel) and ASA(20/80,DA).

Table 2.7: Catalytic activities of *n*-heptane hydroconversion of Pd-loaded support materials (N'_{iso} is proportional to the number of Brønsted acid sites and defined as unity for ASA(5/95,773)).

Catalyst	773K			1073K		
	T_{40} (K)	E_{act} (kJ/mol)	N'_{iso}	T_{40} (K)	E_{act} (kJ/mol)	N'_{iso}
ASA(5/95)	630	132	1.0	618	130	1.6
ASA(10/90)	630	125	1.4	618	127	1.9
ASA(15/85)	625	129	1.4	604	128	3.5
ASA(20/80)	626	136	1.0	611	128	2.5
ASA(5/95,3)	620	129	1.3	612	133	2.0
ASA(10/90,3)	622	130	1.5	612	131	2.2
ASA(15/85,3)	627	131	1.2	612	126	2.6
ASA(20/80,3)	625	134	1.1	608	125	3.2
ASA(5/95,fumed)	628	132	1.1	626	127	1.4
ASA(5/95,cogel)[1]	599	120	5.5			
ASA(5/95,F)	652	132	0.4			
ASA(20/80,DA)[2]	598	131	4.0			
ASA(1/99)				659	130	0.37
ASA(comm)	623	129	1.5	613	128	2.3
USY(9.3)	506	128	473			

[1] Calcined at 923 K; [2] Calcined at 823 K.

3.5 Surface structure and Brønsted acidity of amorphous silica-aluminas

A common preparation method for ASAs consists of the grafting of Al to a silica surface. Here, the controlled grafting of aluminium to a reactive silica aerogel with a hydroxyl density of about 4 OH/nm^2 was investigated following the homogeneous release of hydroxyl anions through urea decomposition starting from pH ~2. Two sets of ASA precursors with increasing aluminium content were prepared in this manner. In the preparation of the first set,

the deposition of aluminium was carried out until all urea was decomposed. The deposition of aluminium was stopped when the pH reached a value of 3 in the preparation of the second set. The surface of the dried precursors is occupied by a variety of Al species depending on the final pH and $[Al]_0$. At pH 3 and relatively low Al content, the surface contains mainly monopodal Al^{VI} and bipodal Al^{IV} (structures *2* and *4* in Fig. 2.4). An increase of pH to about 6 results in the exclusive presence of four-coordinated Al. The change in coordination is due to further condensation of grafted Al with the surface silanol groups, although some grafting of an Al_{13} complex is suspected. When, at pH 3, $[Al]_0$ is increased, the surface will also contain Al^{VI} that has been grafted to bipodal Al^{IV} (structure *6*) and monopodal Al^{VI} (*e.g.*, due to reaction of $Al(H_2O)_5(OH^-)^{2+}$ with structure *2*). The aluminium loading is limited to approximately 12 wt% Al_2O_3 in this case. This loading corresponds to a molar silanol/Al ratio of approximately 1. When the pH is further increased, the rest of Al is deposited below pH 5. Therefore, it is reasonable to expect that the majority of Al species are grafted to the already present surface Al species. At higher loading, some precipitation of aluminium hydroxides occurs as follows from the less homogeneous Al distribution by electron microscopy analysis. The Al species tend to form an increasingly polymeric aluminium hydroxide network with increasing $[Al]_0$.

Calcination results in a redistribution of the surface aluminium species. Firstly, diffusion of aluminium into the silica network generates the necessary $Si^{4+} \rightarrow Al^{3+}$ substitutions to induce Brønsted acidity [3,4,7,28] as follows from the acid activity measurements. Alternative models to explain acidity do not seem to be consistent with our results. Neither a correlation of the acidity with the amount of grafted Al [5-10] nor with five-coordinated aluminium [11,12] is evident. Crépeau et al. [10] suggest that such Brønsted acid sites in ASAs have an intrinsic acidity close to that of zeolites. Combined with the present catalytic activity results, this implies that the much lower activity of ASAs is due to their very low acid site density. Thus, only a very small fraction of tetrahedral Al as detected by ^{27}Al NMR spectroscopy gives rise to Brønsted acid sites [31]. It implies that the extent of diffusion of Al into silica is very limited. Due to the very low concentration of such BAS, spectroscopic identification of these sites has not been achieved yet [10]. The small variation in the acidity in the present suite of ASAs makes it difficult to draw pertinent conclusions about the genesis of Brønsted acid sites. Nevertheless, the increase in the surface acidity with calcination temperature is reasonably explained by the diffusion of more Al into the silica network. This effect of the calcination temperature was earlier discussed by Boehm and Schneider [28]. The acidity does not vary much with aluminium concentration for the ASAs as long as the surface of the precursor is fully covered with aluminium species. In accordance with this, only an appreciably lower Al content results in a much lower acidity. The ASAs prepared at final pH 3 are more acidic than their complete synthesis counterparts. This difference is particularly evident for ASA(5/95) and ASA(10/90) after calcination at 773 K. It suggests that monopodal octahedral Al is a better precursor to the formation of Brønsted acid sites than bipodal tetrahedral Al. A reason is perhaps that bipodal Al^{IV} represents a stable surface arrangement

less conducive to the rearrangements of the silica surface required to facilitate diffusion of Al into the silica than the more loosely grafted Al^{VI}. Indeed, the acidity of ASA(5/95,F), which contains quite stable tetrahedral Al sites as follows from the minor changes in the ^{27}Al NMR spectrum upon calcination, is very low. Finally, the higher acidity of ASA(5/95,cogel) may be due to the higher amount of Al ending up in the silica network because the silica network is formed during the deposition of Al. This also explains the higher acidity of ASA(20/80,DA).

Secondly, the surface Al species tend to agglomerate and partially form small patches of aggregated aluminium oxide. The dried precursors prepared after completion of urea decomposition contain about 5 wt% tetrahedral Al. Calcination results in the agglomeration of Al. Part of the octahedral Al atoms do not change their coordination upon ammonia adsorption, because they are part of a separate alumina phase. Typically, the contribution of such a phase is calculated on the basis of an assumed fixed Al^{IV}:Al^{VI} ratio of 3:7 in transition aluminas. From the R^2 NMR measurements, it follows that such alumina domains only contain octahedral Al. This octahedral Al phase can be probed quantitatively by their inaccessibility to ammonia. Only for an ASA with a substantially higher Al content, *i.e.* ASA(55/45), a free transition alumina phase is readily apparent from R^2 NMR measurements.All tetrahedral Al is part of the mixed silica-alumina phase for the HDP ASAs.

The amount of such segregated domains of aluminium oxide increases with the aluminium concentration. The formation of alumina domains is only completely avoided in ASA(5/95,3,773) for which the deposition of Al is fully dominated by grafting of Al to silanol groups. Even so, a small fraction of Al segregates into an aluminium oxide phase upon calcination at 773 K. The surface of ASA(5/95,3,773) can be considered a pure amorphous silica-alumina phase. It contains monopodal octahedral Al and bipodal tetrahedral Al. Octahedral Al atoms become tetrahedrally coordinated upon ammonia adsorption. ASA(5/95) contains a slightly higher amount of aluminium. All Al is tetrahedrally coordinated in this sample. Calcination of this precursor at 773 K induces segregation of about 30 % of Al into aluminium oxide domains. This segregation could be due to the higher Al density on the surface, but also to the suspected presence of a small amount of Al_{13} complexes with the Keggin structure, which may have been deposited above pH 3. In any case, calcination of ASA(5/95) at 473 K already results in octahedral Al, indicating surface mobility and agglomeration. With increasing Al concentration, the amount of segregated Al increases. This trend is more pronounced for the complete synthesis ASAs, which contain more aluminium, than for their counterparts prepared until pH 3. The formation of a considerable amount of segregated aluminium oxide domains in ASA(15/85) and ASA(20/80) agrees with the structural model of a polymeric aluminium hydroxide phase being grafted above pH 3 upon the first layer of grafted aluminium. The R^2 NMR measurements suggest that this phase does not convert to a transition alumina phase, but consists of a polymeric network of octahedral Al.

After calcination, the ASAs contain varying amounts of five-coordinated aluminium. Fig. 2.15 evidences a strong correlation between the amount of Al^V probed by ^{27}Al NMR and the content of alumina domains. This correlation confirms the assumption that five-coordinated Al forms the interface between the domains of segregated octahedral Al atoms and the mixed silica-alumina phase as proposed earlier [31]. It is finally worthwhile to mention that the amount of Al^V is comparable to the amount of Al in the alumina domains, which implies that the size of the domains should be small.

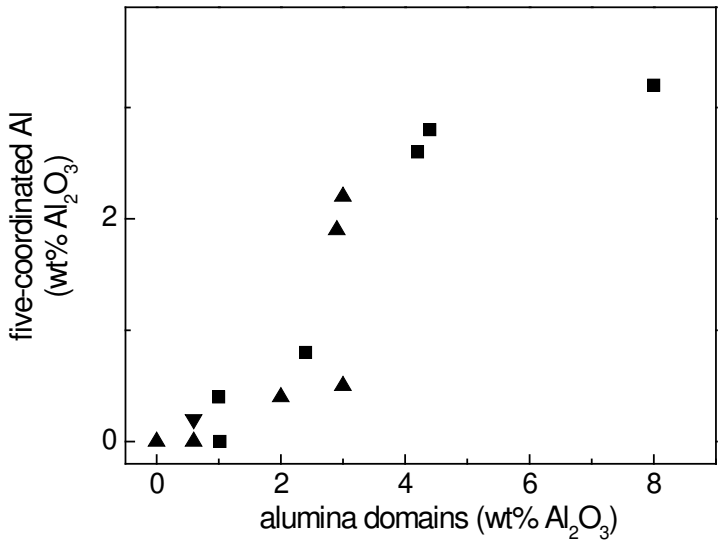

Figure 2.15: Relation between the amount of five-coordinated aluminium as observed by ^{27}Al NMR spectroscopy after ammonia adsorption and the amount of segregated aluminium oxide domains: ASAs prepared following completion urea decomposition (■), ASAs prepared at a final pH of 3 (▲) and ASA(5/95, cogel) (▼).

The surface model for a typical amorphous silica-alumina which arises from this study contains two major ingredients, *i.e.* (i) a mixed silica-alumina phase and (ii) domains of segregated octahedral Al. The aluminium speciation in the mixed amorphous silica-alumina phase is as follows:

- Four-coordinated Al species. These share two oxygen atoms with the silica network (structure *4* in Fig. 2.4). In accord with this, the amount of Al^{IV} never exceeds the amount corresponding to a molar silanol/Al ratio of 2 in the calcined materials prepared by homogeneous deposition-precipitation.
- Six-coordinated Al species. Some are isolated and coordinate to one oxygen anion of the subjacent silica support (structure *2* in Fig. 4), others have agglomerated to some extent forming one or perhaps more Al-O-Al linkages (*e.g.*, the octahedral Al in structure *10* in Fig. 2.4). Upon ammonia adsorption, this form of octahedrally coordinated Al becomes tetrahedrally coordinated. A small fraction of octahedrally coordinated Al is present at the interface between the mixed phase and the alumina domains. These octahedral Al species become five-coordinated upon ammonia adsorption.
- Five-coordinated Al species. These are at the interface between the mixed silica-alumina phase and the domains of aluminium oxide.

The aluminium oxide phase is present as very small domains containing only only octahedral Al. This form of Al is not accessible by NH_3 which allows their quantification by ^{27}Al NMR. The aluminium oxide phase is connected to the mixed silica-alumina phase by five-coordinated aluminium. This surface model seems to be applicable for the wider range of ASAs synthesized in this study.

2.4. Conclusion

It is possible to prepare amorphous silica-aluminas via homogeneous deposition-precipitation of aluminium on a silica surface followed by calcination. These ASAs exhibit similar Brønsted acidity as industrial amorphous silica-aluminas prepared by grafting of aluminium on very reactive silica-gels. Their acidity does not vary systematically with the aluminium concentration, except at aluminium contents below 5 wt% Al_2O_3. The acidity increases with increasing calcination temperature. The active sites form due to diffusion of aluminium into the silica network at high temperatures, leading to Al substitutions for Si atoms. This is expected, as the acidity does not correlate with anything else, *viz.*, the amount of four-coordinated aluminium nor the presence of segregated Al or five-coordinated aluminium at the interface of these domains and the silica-alumina phase. Deposition occurs predominantly via hydrolytic adsorption of aluminium to the hydroxyl groups on the silica surface and already grafted aluminium. Precipitation becomes more significant at higher aluminum concentration. After grafting, the surface contains four- and six-coordinated aluminium as well as domains of a more polymeric form of aluminium hydroxides. Calcination results in two competing processes, namely the diffusion of aluminium into the silica network and sintering of aluminium into separate domains of a phase in which octahedral Al is dominant. The surface of an amorphous silica-alumina consists of isolated aluminium grafted to the silica surface (pure silica-alumina phase), domains of aluminium oxides and a very small amount of aluminium in the silica network, which brings about the Brønsted acidity.

Acknowledgements

The authors are very thankful to Dr. Ralph Haswell of Shell Global Solutions for TEM and SEM measurements.

References

1. J. Ward, Fuel Process. Technol. 35 (1993) 55.
2. J. Scherzer, A.J. Gruia, Hydrocracking Science and Technology, Dekker, New York, 1996, p. 215.
3. C.L. Thomas, Ind. Eng. Chem. 41 (1949) 2564.
4. M.W. Tamele, Disc. Faraday Soc. 8 (1950) 270.
5. J.H. De Boer, Disc. Faraday Soc. 52 (1971) 109.
6. K.G. Miesserov, J.Catal. 13 (1969) 169.
7. R.S. Hansford, Ind. Eng. Chem. 39 (1947) 849.
8. M. Trombetta, G. Busca, S. Rossini, V. Piccoli, U. Cornaro, A. Guercio, R. Catani, R.J. Willey, J. Catal. 179 (1998) 581.

9. W. Daniell, U. Schubert, R. Glockler, A. Meyer, K. Noweck, H. Knözinger, Appl. Catal. A 196 (2000) 247.
10. G. Crépeau, V. Montouillout, A. Vimont, L. Mariey, T. Cseri, F. Maugé, J. Phys. Chem. B 110 (2006) 15172.
11. C.-P. Hwang, C.-T. Yeh, J. Catal. 182 (1999) 48.
12. S. Blonski, S.H. Garolfini, J. Phys. Chem. 100 (1996) 2201.
13. J.A. Rabo, G.J. Gajda, Catal. Rev-Sci. Eng. 31 (1989) 385.
14. R. Brace, E. Matijevic, Colloid Polym. Sci. 255 (1977) 153.
15. United States Patent 3536605, 1968.
16. R. Mokaya, W. Jones, J. Mater. Chem. 9 (1999) 555.
17. C.J. Brinker, G.W. Scherer, Sol–Gel Science: The Physics and Chemistry of Sol–Gel Processing, Academic Press, San Diego, 1990.
18. J.W. Kriesel, M.S. Sander, T.D. Tilley, Chem. Mater. 13 (2001) 3554.
19. J.W. Kriesel, M.S. Sander, T.D. Tilley, Adv. Mater. 13 (2001) 331.
20. P. Cloos, A.J. Leonard, J.P. Moreau, A. Herbillon, J.J. Fripiat, Clays Clay Miner. 17 (1969) 279.
21. A. Leonard, S. Suzuki, J.J. Fripiat, C. de Kimpe, J. Phys. Chem. 68 (1964) 2608.
22. J.J. Fripiat, A. Leonard, J.B. Uytterhoeven, J. Phys. Chem. 69 (1965) 3274.
23. R.K. Iler, The Chemistry of Silica, Wiley-VCH, Weinheim, 1979.
24. J.W. Geus, A.J. van Dillen, in: G. Ertl, H. Knözinger, J. Weitkamp, (Eds.), Preparation of Solid Catalysts, Wiley-VCH, Weinheim, 1999; chapter 4.6.
25. R.J.M.J. Vogels, J.T. Kloprogge, J.W. Geus, J. Colloid Interfac. Sci. 285 (2005) 86.
26. A. Samoson, E. Lippmaa, G. Engelhardt, U. Lohse, H.-G. Jerschkewitz, Chem. Phys. Lett. 134 (1987) 589.
27. H.-M. Kao, C.-C. Ting, S.-W. Chao, J. Mol. Catal. A 235 (2005) 200.
28. H.P. Boehm, M. Schneider, Z. Anorg. Chem. 316 (1962) 128.
29. K.J.D. MacKenzie, J. Temuujin, K. Okada, Thermochim. Acta 327 (1999) 103.
30. K.J.D. MacKenzie, J. Temuujin, M.E. Smith, P. Angerer, Y. Kameshima, Thermochim. Acta 359 (2000) 87.
31. M.F. Williams, B. Fonfé, C. Sievers, A. Abraham, J.A. van Bokhoven, A. Jentys, J.A.R. van Veen, J.A. Lercher, J. Catal. 251 (2007) 485.
32. W.E.E. Stone, G.M.S. El Shafei, J. Sanz, S.A. Selim, J. Phys. Chem. 97 (1993) 10127.
33. B.M. de Witte, P.J. Grobet, J.B. Uytterhoeven, J. Phys. Chem. 99 (1995) 6961.
34. M.P.J. Peeters, A.P.M. Kentgens, Solid State Nucl. Magn. Reson. 9 (1997) 203.
35. J.-P. Gilson, G.C. Edwards, A.W. Peters, K. Rajagopalan, R.F. Wormsbecherp, T.G. Roberie, M.P. Shatlock, J. Chem. Soc., Chem. Commun. (1987) 91.
36. J. Sanz, A. Madani, J.M. Serratosa, J.S. Moya, S. Aza, J. Am. Ceram. Soc. 71 (1988) 418.
37. A. Omegna, J.A. van Bokhoven, R. Prins, J. Phys. Chem. B 107 (2003) 8854.
38. D. Coster, J.J. Fripiat, J. Chem. Mater. 5 (1993) 1204.
39. T.E. Wood, A.R. Siedle, J.R. Hill, R.P. Skajune, C.J. Goodbrake, J. Mater. Res. Soc. Symp. Proc. 180 (1990) 97.
40. S.M. Bradley, R.A. Kydd, R.F. Howe, J. Colloid Interface Sci. 159 (1993) 405.
41. S. Acosta, R.J.P. Corriu, D. Leclercq, P. Lefevre, P.H. Mutin, A. Vioux, J. Non-Cryst. Solids 170 (1994) 234.
42. Y. Mizushima, M. Hori, J. Non-Cryst. Solids 167 (1994) 1.
43. E. Bourgeat-Lami, P. Massiani, F.D. Renzo, P. Espiau, F. Fajula, Appl. Catal. A 72 (1991) 139.
44. J.A. van Bokhoven, A.M.J. van der Eerden, D.C. Koningsberger, Stud. Surf. Sci. Catal. 142 (2002) 1885.
45. G.E. Gianetto, G.R. Perot, M.R. Guisnet, Ind. Eng. Chem. Prod. Res. Dev. 25 (1986) 481.
46. J.W. Thybaut, C. S. Laxmi Narasimhan, J.F. Denayer, G.V. Baron, P.A. Jacobs, J.A. Martens, G.B. Marin, Ind. Eng. Chem. Res. 44 (2005) 5159.
47. E.J.M. Hensen, D.G. Poduval, D.A J.M. Ligthart, J.A.R. van Veen, M.S. Rigutto, submitted.
48. R.J.M.J. Vogels, G. Caminiti, V. Crisponi, A. Nurchi, Z. Lai, Z. Naturforsch. A 39 (1984) 1235.
49. J.W. Akitt, A. Farthing, J. Chem. Soc. Dalton Trans. (1981) 1624.
50. J.W. Akitt, J.M. Elders, X.L.R. Fontaine, A.K. Kundu, J. Chem. Soc. Dalton Trans. (1989) 1889.
51. J.T. Kloprogge, D. Seykens, J.B.H. Jansen, J.W. Geus, J. Non-Cryst. Solids 152 (1993) 207.

52. C.F. Baes, R.E. Mesmer, The Hydrolysis of Cations, John Wiley, New York, 1976, p. 112.
53. A.V. Plyasunov, I. Grenthe, Geochim. Cosmochim. Acta 58 (1994) 3561.
54. J.W. Akitt, Prog. Nucl. Magn. Reson. Spectrosc. 21 (1989) 1.
55. G. Fu, L.F. Nazar, A.D. Bain, Chem. Mater. 3 (1991) 602.
56. J.D. Danforth, J. Phys. Chem. 59 (1955) 564.
57. R.H. Meinfold, R.C.T. Slade, R.H. Newman, Appl. Magn. Reson. 4 (1993) 121.
58. D.P. Raleigh, M.H. Levitt, R.G. Griffin, Chem. Phys. Lett. 146 (1988) 71.
59. A. Abragam, The Principles of Nuclear Magnetism, Oxford University Press, Oxford, 1961.
60. A. van de Runstraat, J.A. Kamp, P.J. Stobbelaar, J. van Grondelle, S. Krijnen, R.A. van Santen, J. Catal. 171 (1997) 77.
61. V.M. Akhmedov, S.H. Al-Khowaiter, Catal. Rev. Sci. Eng. 1 (2007) 33.

Chapter 3

Quantification of strong acid sites in aluminosilicates

Summary

By following the selective H/D exchange of acidic hydroxyl groups in aluminosilicates by IR spectroscopy clear evidence is provided for the existence in amorphous silica-aluminas (ASAs) of Brønsted acid sites comparable in strength to the bridging hydroxyl groups in zeolites. The method distinguishes various types and strengths of strong Brønsted acid sites in aluminosilicates (zeolites, clays, ASAs) and can be used to quantify them. The concentration of strong Brønsted acid sites in ASAs is 2-3 orders of magnitude lower than in zeolites. The acid catalytic activity in *n*-alkane hydroconversion correlates well with the number of strong Brønsted acid sites, as probed by our method, for steam stabilized zeolites, clays and ASAs. The strong Brønsted acid sites in these aluminosilicates arises from hydroxyl groups located between aluminium and silicon occupied oxygen tetrahedra. Differences in Brønsted acidity are caused by differences in the concentrations of strong Brønsted acid sites.

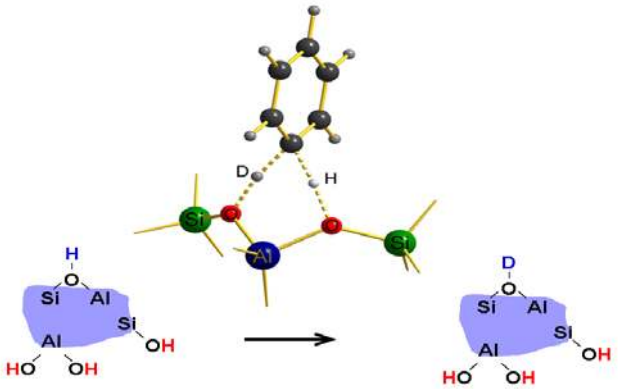

Parts of this chapter published in Journal of Physical Chemistry C 114 (2010) 8363-8374 & Chemical Communications 46 (2010) 3466-3469.

3.1 Introduction

Aluminosilicates such as zeolites and amorphous silica-aluminas are technologically important materials which are extensively used in the oil refining and petrochemical industry as acid catalysts to crack carbon-carbon bonds, isomerize and oligomerize alkenes and alkylate aromatics, to name the most important reactions [1-3]. Many aspects of zeolite acidity are well understood [4-6], but establishing quantitative relations between zeolite properties and catalytic activity is still proving difficult[7,8]. One key problem is that conventional tools to characterize acidity [9] tend to prove inadequate when applied to the complex materials that commercial zeolite powders, amorphous silica-aluminas or catalysts containing them invariably are. As a rule, application of such tools does not generate satisfactory correlations with catalytic performance, even in simple test reactions. Hydrocracking catalysts are a case in point here. They often contain a zeolite and it is almost always some variety of zeolite Y. Their acid catalytic activity resides in sites involving tetrahedral aluminium cations in substitution positions for silicon in the framework [4,5]. Zeolite Y has the faujasite structure which features a single crystallographic tetrahedral site. Ideally, at high Si/Al ratios, dilute Brønsted acid sites (BAS) in a pure zeolite Y material will therefore be equivalent [4,10]. At high Al content (Si/Al<3), the next-nearest neighbour model explains the lower acidity [11]. In practice, a catalyst will contain stabilized faujasites with Si/Al molar ratios in the 4.5-50 range. Even in simple test reactions, like cracking or hydroconversion of alkanes, materials of similar composition can display hugely different activities. The usual interpretation of such differences involves the assumption that zeolitic acid sites can differ in strength. Non-framework aluminium species due to partial framework dealumination can boost a zeolite's activity in cracking reactions or affect its selectivity [12,13]. These strongly Lewis acidic aluminium species do not seem to be catalytically active, but they are believed to enhance the strength of Brønsted acid sites in their vicinity [14,15].

What is true for zeolites is even more true for the wider class of aluminosilicates. Since the 1960s, Uytterhoeven and co-workers [16], Haag, Lago and Weisz [17] and others [8,18] have aimed for a coherent picture of aluminosilicate acidity that would include not only zeolites but also amorphous silica-aluminas and, in some cases, clays, essentially hypothesizing that acid sites in all of these materials are similar. In this work, we will provide the evidence that they sought. Amorphous silica-aluminas (ASAs) are much less acidic than zeolites and are, therefore, preferred in hydrocracking catalysts when middle distillates are desired instead of naphtha-range products. Compared to zeolites, their acidity is not understood in much detail. It is usually assumed that these materials contain sites that are similar to the Brønsted acid sites in zeolites but, somehow, of lower strength. Haag, Lago and Weisz [17] suggested that the low acidity of ASAs might be the consequence of a very low concentration of sites of similar acidity as the bridging hydroxyl groups in zeolites. This implies that ASAs contain aluminium substitutions in the amorphous silica network. Besides their low abundance, the

rather complex surface structure of ASAs presents a challenge in the characterization of their acidity.

The role of charge-compensating protons to explain acidity of ASAs was earliest mentioned by Thomas [19] and Tamele [20], well before acidity of zeolites was understood in detail. A typical stretching vibration of bridging hydroxyl groups has not been systematically reported in IR spectra of typical ASAs. Datka and co-workers have reported a band around 3610 cm^{-1} in silica-aluminas synthesized in the presence of structure directing agents [21,22]. Other techniques which have been successfully employed to characterize surface acidity of zeolites fail to produce evidence for the presence of such bridging hydroxyl groups. As a consequence, a variety of alternative explanations have been invoked [18,23-35]. Trombetta et al. [29] proposed that the acid sites consist of silanol groups in the vicinity of coordinatively unsaturated Al^{3+} surface sites. Others have followed up on this idea [18,31,34]. Crépeau et al. [18] have used strongly red-shifted hydroxyl band complexes upon CO chemisorption to suggest the presence of strongly acidic hydroxyl groups in ASAs, yet quantification has not been possible. Recently, Chizallet and Raybaud [34] have performed a computational study and concluded that ASA acidity resides in pseudo-bridging hydroxyl groups following water adsorption to Si-O-Al fragments. Others [28,30] have pointed out the importance of an interface region, consisting of five-coordinated Al, between the silica-alumina phase and the segregated alumina domains. An important challenge remains to evidence that the Brønsted acidity in ASAs is the result of a very few hydroxyl groups having zeolite-like acidity or, in case such sites would turn out not be present, to determine the nature and density of weak surface hydroxyl groups to account for the acidity.

Herein we will show that ASAs contain strongly acidic hydroxyl groups in very small quantities. These sites can be made to react selectively with deuterated benzene to produce the corresponding deuteroxyl groups that can be observed by IR spectroscopy. The suitability of H/D exchange of strongly acidic protons in zeolites with perdeuterobenzene has been earlier shown by Haw and co-workers [35] and has recently been confirmed [36]. Zeolites are used to benchmark our method [37,38]. The unprecedented sensitivity of FTIR spectroscopy in combination with selective H/D exchange allows a first direct spectroscopic glance at and subsequent quantification of acid sites in ASAs, allowing the catalytic activities of a range of aluminosilicates to be correlated with BAS concentrations over several orders of magnitude.

3.2 Experimental Methods

3.2.1 Materials

To validate our spectroscopic method, two faujasite zeolite with silica to alumina ratios (SAR) of 9.6 and 5 were used. The former was obtained through treatment of a faujasite zeolite with $(NH_4)_2SiF_6$, which replaces part of the framework aluminium by silicon.[39] The latter is a faujasite zeolite with a framework SAR of 5. The method was further applied to steam stabilized zeolites, clays and amorphous silica-aluminas: seven steam stabilized faujasite zeolites (Zeolyst International), two saponite clays (a commercial Mg-saponite clay

material from Kunimine Industries and a Mg-saponite prepared according to the method by Vogels et al. [40]), and ASAs prepared by homogeneous deposition of aluminium on silica [41] and by cogelation of a mixture of sodium silicate and aluminium chloride [42]. Control experiments were carried out with silica (SiO_2, Sipernat 50) and γ-alumina (Ketjen CK-300). Details of these samples are listed in Table 3.1.

Table 3.1: List of aluminosilicates, their silica-to-alumina ratio (SAR) and origin.

Sample	SAR	Origin
HY(5)	5	Faujasite zeolite (Akzo-Nobel, PA 73022)
USY(9.6, F)	9.6	Partial removal of framework Al from faujasite via $(NH_4)_2SiF_6$ treatment[1]
USY(8.1, I)	8.1	Steam calcined faujasite
USY(8.1, II)	8.1	Steam calcined faujasite (different batch)
USY(9.3)	9.3	Steam calcined and acid leached faujasite
VUSY(26.3)	26.3	Steam calcined and acid leached faujasite
VUSY(33.1)	33.1	Steam calcined and acid leached faujasite
XVUSY(70)	70	Steam calcined and acid leached faujasite
XVUSY(85)	85	Steam calcined and acid leached faujasite
Mg-SAP(33)	33	Saponite clay (Kunimine Industries)
Mg-SAP(13)	13	Saponite clay[2]
ASA(5/95,*x*)[3]	32	Homogeneous deposition route
ASA(10/90,*x*)[3]	15	Homogeneous deposition route
ASA(15/85,*x*)[3]	9.6	Homogeneous deposition route
ASA(20/80,*x*)[3]	6.8	Homogeneous deposition route
ASA(5/95,3)[4]	38	Homogeneous deposition route, stopped at pH=3
ASA(10/90,3)[4]	17	Homogeneous deposition route, stopped at pH=3
ASA(15/85,3)[4]	12	Homogeneous deposition route, stopped at pH=3
ASA(5/95,cogel)[5]	32	ASA synthesized by cogelation[6]

[1] Synthesized according to Ref. [39]; [2] Synthesized according to Ref. 40; [3] Synthesized according to Ref. [41]; *x* stands for calcination temperature (773 K or 1073 K); [4] Calcined at 1073 K; [5] Calcined at 923 K; [6] Synthesized according to Ref. [42].

3.2.2 Infrared spectroscopy of H/D exchange with perdeuterated benzene

H/D exchange of hydroxyl groups with perdeuterated benzene was followed *in situ* by infrared spectroscopy. Infrared spectra were recorded in transmission mode in a Bruker IFS-113v FTIR spectrometer equipped with a deuterated triglycine sulfate detector. Typically, a powdered sample was pressed into a self-supporting wafer with a density $\rho = 9$ mg/cm^2. The wafer was placed in a home-made controlled-environment transmission cell equipped with CaF_2 windows. The stainless-steel cell is double walled. Through the outer part thermostated ethylene glycol was pumped. By heating the cell body to 393 K physisorbed water was removed from its inner walls. The cell is connected to a gas supply section for sample pre-treatment and a section for dosing of small quantities of probe gases or evacuation. This latter section can also be heated to remove physisorbed water. These provisions were implemented after an initial set of experiments (*vide infra*) had shown that residual water affected the results negatively.

A typical experiment was carried out as follows: a sample wafer was first calcined in flowing oxygen (4 ml/min) under heating from ambient temperature to 823 K at a rate of 5 K/min followed by an isothermal period of 2 h. During pre-treatment, the cell body and vacuum section of the cell were heated to 353 K to remove physisorbed water and prevent readsorption of water from sample dehydration. Subsequently, the cell was evacuated for 30 min and the sample was then cooled to 303 K. The final pressure was lower than 2×10^{-6} mbar. A background spectrum was recorded. Perdeuterobenzene (C_6D_6, Merck, purity 99.96 %) was introduced into the cell from a glass ampoule. The ampoule was connected to the cell via a computer-controlled pneumatic valve (V1). The closable glass ampoule was filled with C_6D_6 in a N_2-flushed glove box. Accurate dosing of C_6D_6 is possible via a computer controlled sequence, which involves closing of the pneumatic vacuum valve (V2) between the cell and the vacuum pump and opening valve V1 to the ampoule. The pressure in the cell was monitored by an online pressure gauge and valve V1 was closed after reaching a pressure of 10 mbar. The total volume of C_6D_6 administered to the cell was 0.33 mmol ± 1 %. The sample was exposed to C_6D_6 for 10 s followed by evacuation for 30 min by opening valve V2. The final pressure was lower than 10^{-5} mbar. Then, a next spectrum of the partially exchanged sample was recorded. This sequence was automatically repeated with exposure times of 30 s, 5 min, 10 min, 20 min, 30 min at 303 K, 30 min at 323 K, 30 min at 353 K, 30 min at 373 K, 30 min at 423 K and 30 min at 523 K. For each spectrum, 125 scans were accumulated at a resolution of 2 cm^{-1}. Difference spectra were obtained by subtracting the initial spectrum of the dehydrated sample from the spectra after exposure to C_6D_6.

3.2.3 Catalytic activity measurements

The concentration of strong Brønsted acid sites in the aluminosilicates was evaluated from catalytic activity measurements in the hydroconversion of *n*-heptane of Pd-loaded aluminosilicates. The dried support was shaped in a sieve fraction (177-420 μm) and loaded with 0.4 wt% Pd via incipient wetness impregnation with a solution of appropriate concentration of $Pd(NH_3)_4(NO_3)_2$. The resulting materials were calcined at 573 K. Prior to testing, the catalysts were reduced at 713 K at 30 bar in flowing hydrogen. Hydroconversion of n-heptane was carried out at 30 bar at a H_2/hydrocarbon ratio of 24 mol/mol. The reaction temperature was lowered from 713 K till 473 K at a rate of 0.2 K/min. The kinetics of bifunctional, aluminosilica-catalyzed hydroisomerization of *n*-alkanes is well understood [43,44]. *n*-Heptane hydroisomerization involves the dehydrogenation of n-heptane by the noble metal phase, isomerization by strong Brønsted acid sites and hydrogenation of the *i*-olefins to *i*-heptanes. The extent of hydrocracking is limited at the conversions at which the catalysts were compared. Meeting the requirement of sufficient hydrogenation activity is easily met if the metal loading is a few tenths of weight percent. In such case, the Brønsted-acid catalyzed isomerization step of the intermediate olefins via carbenium-ion chemistry is rate limiting and the catalytic activity scales with the density of acid sites if their acidity is assumed to be constant. The activity of the catalyst is expressed as the temperature at which a

hydrocarbon conversion of 40% was achieved. Hydroisomerization/hydrocracking of *n*-heptane is a first order reaction. From the temperature required to obtain 40% conversion, relative values for the rate constant k for two catalysts at a reference temperature T_{ref} can be determined using the expression

$$\ln(k_1/k_2) = E_{act,1}/R(1/T_{40,1} - 1/T_{ref}) - E_{act,2}/R(1/T_{40,2} - 1/T_{ref}) \quad (3.1a)$$

or, if we choose the second catalyst as the reference $T_{ref} = T_{40,2}$:

$$\ln(k/k_{ref}) = E_{act}/R(1/T_{40} - 1/T_{40,ref}) \quad (3.1b).$$

in which E_{act} is the activation energy (kJ mol^{-1}) and R (kJ mol^{-1} K^{-1}). If we assume the intrinsic acidity to be a constant, $E_{act}/R(1/T_{40} - 1/T_{40,ref})$ scales with the ratio of the acid site densities between the two catalysts.

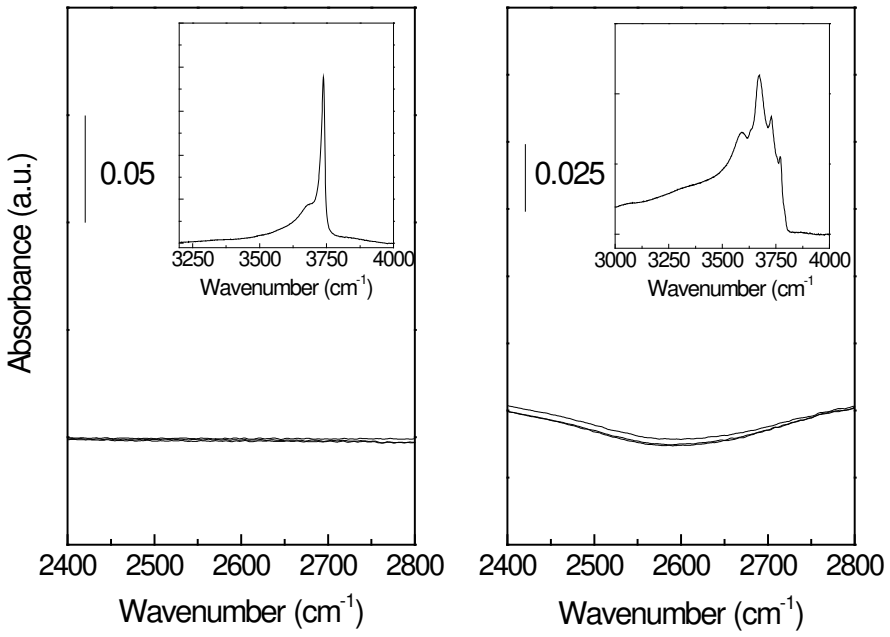

Figure 3.1: FTIR spectra of a dehydrated steam stabilized zeolite, USY (8.1, I), after perdeuterobenzene exchange at 303 K with increasing exposure times without removal of physisorbed water from the cell body (a) and after extensive removal of physisorbed water (b).

3.3. Results and discussion

3.3.1 Method development

A key finding of this chapter is that strong Brønsted acid sites in aluminosilicates can be made to react selectively with C_6D_6. We first checked that the simple oxides of silicon and aluminium do not exchange their surface protons with the deuterons of C_6D_6. To this end, silica and γ-alumina were exposed to C_6D_6. Silica was chosen, because zeolites contain silanol groups at their external surface and at defect sites inside their pore system. A transition alumina was included, as such aluminas are often present as small domains on the

surface of ASAs [45]. Silica and γ-alumina did not exchange their surface protons after exposure to C_6D_6 at a temperature of 353 K for 30 min (Fig. 3.1). In the course of our investigations, we found that selective hydrogen-deuterium (H/D) exchange not only requires the dehydration of the aluminosilica sample, but also extensive removal of physisorbed water from the inner parts of the infrared cell assembly. This ensures that no water physically adsorbed to the inner parts of the cell readsorb on the dehydrated sample at room temperature. To exemplify the usefulness of this approach, Fig. 3.2 shows the infrared spectra after progressive H/D exchange at 303 K for a steam-stabilized faujasite zeolite, USY (8.1, II), with and without removal of physisorbed water from the inner parts of the cell.

In the latter case, H/D exchange is not limited to the strong Brønsted acid sites. Concomitant with the appearance of bands at 2620 cm^{-1}, 2660 cm^{-1}, 2672 cm^{-1} caused by H/D exchange of strongly acidic hydroxyl groups (original hydroxyl bands at 3550 cm^{-1}, 3606 cm^{-1} and 3630 cm^{-1}, respectively), the appearance of bands around 2750 cm^{-1} and 2707 cm^{-1} shows that silanol and hydroxyl groups connected to extraframework aluminium also undergo H/D exchange. As silica and γ-alumina did not exchange their surface protons under these conditions, the extensive exchange of non-acidic hydroxyl groups in the zeolite must be the consequence of secondary reactions. After removal of physisorbed water, the H/D exchange proceeds at a lower rate and, more importantly, the degree of exchange of silanol groups is much smaller than that of the bridging hydroxyl groups. This improved selectivity after removal of physisorbed water from the cell evidences that residual water in the cell causes the undesired exchange of less acidic hydroxyl groups.

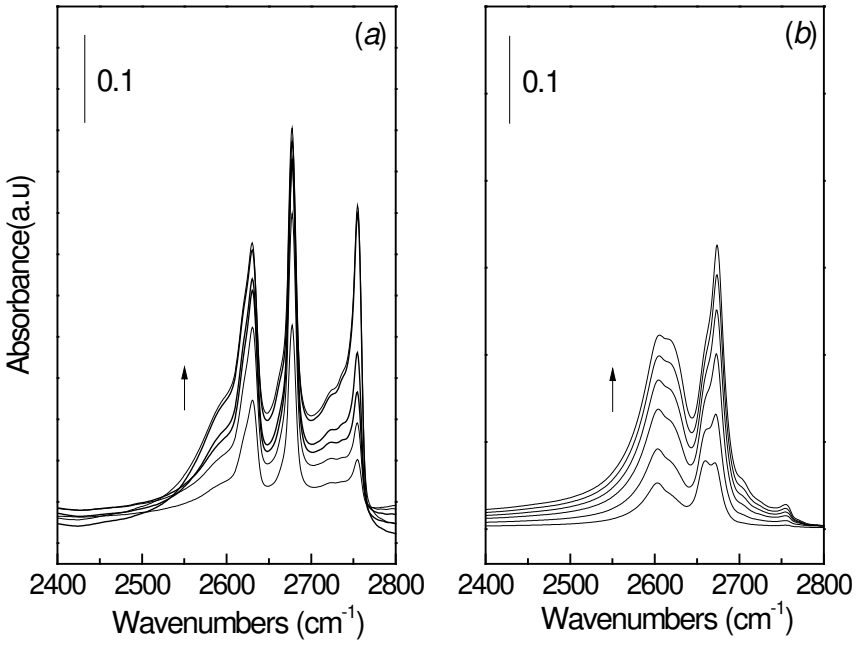

Figure 3.2: FTIR spectra of a dehydrated steam stabilized zeolite, USY (8.1, I), after perdeuterobenzene exchange at 303 K with increasing exposure times without removal of physisorbed water from the cell body (a) and after extensive removal of physisorbed water (b).

The method was validated using two zeolites that contain predominantly aluminium at framework positions. Fig. 3.3 shows the hydroxyl region of the infrared spectra of USY(9.6, F) before and after extensive H/D exchange with perdeuterated benzene. The ^{27}Al NMR spectrum of USY(9.6, F) (not shown) is dominated by a signal around 60 ppm indicative of framework tetrahedral Al with a small contribution (3 %) of octahedral Al. Besides silanol groups on the external zeolite surface, the infrared spectrum contains high-frequency (HF) and low-frequency (LF) hydroxyl bands [10]. The (HF)OH band in USY(9.6, F) is located at 3628 cm^{-1}. The very weak band at 3672 cm^{-1} is caused by extraframework aluminium hydroxide species is observed. After extensive H/D exchange at varying temperatures and exposure times (final temperature 423 K), the largest part of the acidic hydroxyl groups has exchanged, yet the signal of the non-acidic silanol groups has remained nearly constant. The spectra in the deuteroxyl region after H/D exchange of USY(9.6, F) show that the H/D exchange proceeds with high selectivity. Only above 323 K bands of silanol (SiO-D) and aluminol (AlO-D) groups are observed. The exchange of the Brønsted acid hydroxyl groups is complete at 323 K. In comparison, the H/D exchange of the (HF) and (LF)OH groups in HY(5) continues up to 423 K, which is caused by the lower intrinsic acidity of the protons in HY(5).

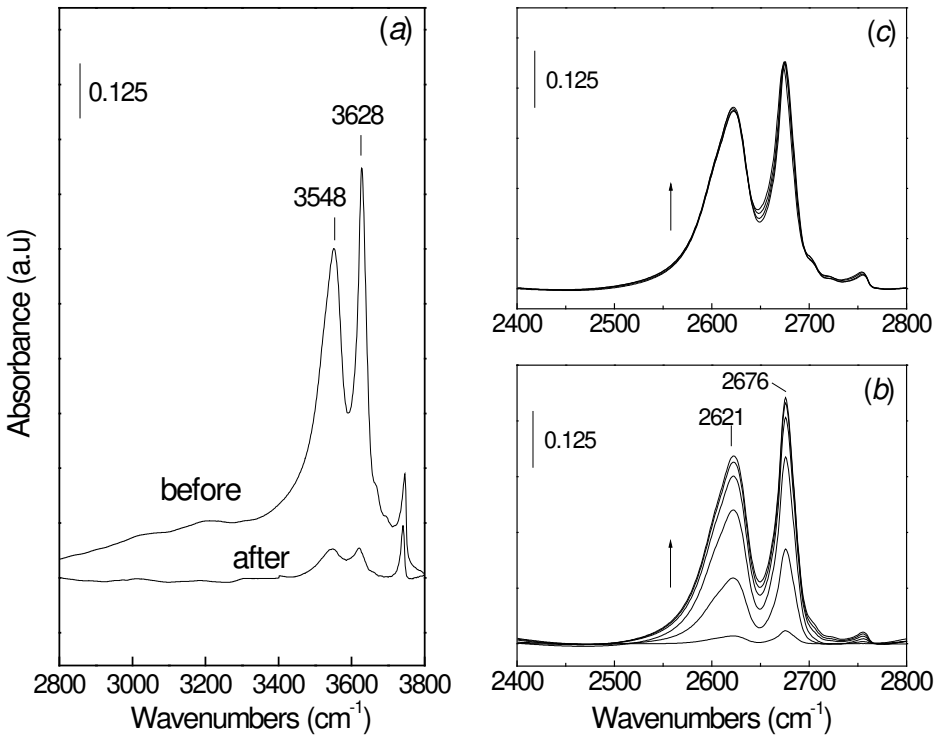

Figure 3.3: FTIR spectra of hydroxyl region of dehydrated USY(9.6, F) (a) before and after progressive H/D exchange at 423 K and of the deuteroxyl region of after exposure to C_6D_6 at 303 K for increasing exposure times (10 s, 30 s, 300 s, 600 s, 1200 s, 1800 s) at 303 K (b) and for an exposure time of 1800 s at increasing temperatures (323 K, 353 K, 373 K and 423 K) (c). In this and subsequent FTIR spectra of H/D exchange the arrow indicates the progression of H/D exchange.

USY(9.6, F) was used as the reference sample because this zeolite contains a very small amount of extraframework aluminium. We developed a procedure that gives the correct Brønsted acid concentration based on the deconvolution and quantification of the deuteroxyl groups after H/D exchange. First, we determined the concentration of Brønsted acid sites from the hydroxyl region of the parent spectrum and then from the deuteroxyl region of infrared spectra after progressive H/D exchange. Quantificiation from the hydroxyl group's intensities is only possible for a zeolite that is devoid of extraframework aluminium-containing phases, because otherwise other hydroxyl groups of weaker acidity in the region 3540-3670 cm^{-1} overlap with the bands belonging to the strong acid sites [15]. The (HF)OH band of the spectrum of dehydrated USY(9.6, F) can be fitted by a mixed Gaussian/Lorentzian peak. Fitting of the (LF)OH band was much more complex. Initial attempts to use functions representing a simple tailing peak shape were not successful. As the broad tailing (LF)OH band derives from a distribution of hydroxyl groups with an increasing degree of hydrogen bonding to the zeolite oxygen anions [46], we used a function to simulate such a distribution of Gaussian peak shapes, *i.e.*

$$G(\nu,\nu_i) = \frac{1}{\sqrt{\pi}} e^{\left[\frac{-(\nu-\nu_i)^2}{2a_0{}^2}.\frac{1}{(1+a_1(\nu_0-\nu_i))}\right]} \qquad (3.2),$$

in which a_0 is the width of the Gaussian present at a base frequency ν_0. For Gaussians generated at a frequency ν_i different from ν_0, the peak width changes with a factor $(1+a_1(\nu_0-\nu_i))$. These Gaussians become wider for $\nu_i < \nu_0$, which simulates the increasing line broadening upon perturbation of the hydroxyl groups by oxygen anions. The intensity as a function of the wavenumber follows from the integration of the function $G(\nu, \nu_i)$ for all Gaussians via

$$I(\nu) = \int_{\nu_0}^{0} -G(\nu,\nu_i).a_2.e^{\left[-\frac{\nu_0-\nu_i}{a_3}\right]}.\mathrm{d}\nu_i \qquad (3.3).$$

The function $G(\nu, \nu_i)$ is weighted with an exponentially decaying function to introduce the decreasing contribution of hydroxyl groups at lower frequencies with a decay constant $1/a_3$ (equivalent to a Boltzmann distribution). a_2 is a normalization factor. This function was implemented in a Levenberg-Marquardt non-linear minimization algorithm for peak fitting. Every iteration step involved the computation of the integral in equation 3. The analytic peak area is obtained by integration of $I(\nu)$ over all frequencies. The approach allowed for the simultaneous use of other peak functions. The concentrations of the various hydroxyl components were then calculated from the areas of the peak contributions by Beer-Lambert's law employing

$$N = \frac{A}{\varepsilon.\rho} \qquad (3.4),$$

in which N is the concentration of the vibrating species (μmol g^{-1}), A is the intensity of the band (cm^{-1}), ε is the extinction coefficient (cm μmol^{-1}) and ρ is the wafer thickness (g cm^{-2}).

In order to calculate the wafer thickness, the sample weight was corrected for the amount of physisorbed water. As outlined by Makarova et al. [46], the (LF)OH band can be interpreted as a perturbed (HF)OH band caused by the interaction of the hydroxyl group with the oxygen anions in the sodalite cage. These authors determined how the extinction coefficient of a perturbed band depends on the frequency shift compared to the unperturbed band for the high-silica zeolite HZSM-5. Here, we employ this relation

$$\varepsilon_{(\mathrm{LF})\mathrm{OH}} = (1 + 0.018.\Delta\nu_{\mathrm{OH}}).\varepsilon_{(\mathrm{HF})\mathrm{OH}} \qquad (3.5)$$

to calculate the molar extinction coefficient of the (LF)OH groups. Δν is the frequency shift between the two bands. The extinction coefficient of the (HF)OH groups was determined in such way that the total amount of Brønsted acid protons, $N_{(\mathrm{HF})\mathrm{OH}}$+$N_{(\mathrm{LF})\mathrm{OH}}$, equals 2.78 mmol g^{-1}. This latter value is the concentration of Brønsted acid sites based on the amount of tetrahedral Al. The molar extinction coefficient for (HF)OH is $\varepsilon_{(\mathrm{HF})\mathrm{OH}}$ = 2.9 cm μmol^{-1}. This value is conveniently close to values of 3.1 and 3.2 cm μmol^{-1} for $\varepsilon_{(\mathrm{HF})\mathrm{OH}}$ reported by Emeis et al. [47] and Makarova et al. [46], respectively. From the IR spectra, we found a contribution of (HF)OH groups of 57 % and HF/LF proton ratio of 1.30. This ratio compares quite well to the ratio of HF/LF protons of 1.28 from ^{1}H NMR spectroscopy of well dehydrated USY(9.6, F).

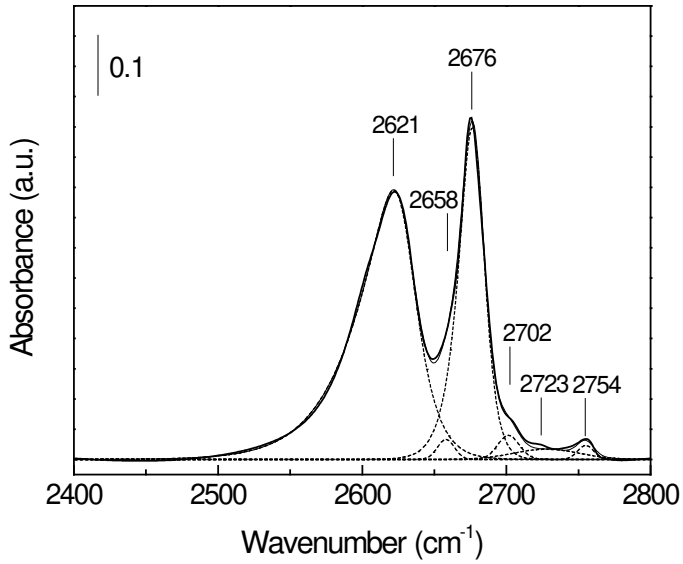

Figure 3.4: FTIR spectrum of USY(9.6, F) after H/D exchange at 323 K for 30 min and its deconvolution into various peaks.

Our method consists of deconvoluting the spectra in the deuteroxyl region after progressive H/D exchange. The results for USY(9.6, F) are used to validate the method. As an example, Fig 3.4 shows the deconvolution of the deuteroxyl region of the difference spectrum of USY(9.6, F) at an exchange temperature and time of 323 K and 30 min. The asymmetric Gaussian distribution was used to fit the (LF)OD and (HF)OD bands. A small feature at 2658 cm^{-1} was fitted by a Gaussian/Lorentzian peak shape. This band, which is denoted by (HF')OD, is a deuteroxyl group in the supercage with enhanced acidity as a result

of the presence of the very small amount of extraframework Al species. These enhanced sites will be discussed below in more detail for steam calcined Y zeolites which contain a more substantial amount of extraframework aluminium. Other weak bands at 2702 cm^{-1}, 2732 cm^{-1} and 2754 cm^{-1} represent weakly or non-acidic aluminol and silanol groups.

Based on the extinction coefficient for (HF)OH protons, the concentrations of deuteroxyl groups were calculated employing Beer-Lambert's law. The extinction coefficient $\varepsilon_{(HF)OD}$ was determined by employing $\varepsilon_{(HF)OD} = C.\varepsilon_{(HF)OH}$. This correlation factor (C) follows from the changes in the integrated intensities in the deuteroxyl and the hydroxyl for the whole set of exchange experiments of a particular material. For the family of faujasite zeolites the correlation factor (C) varied between 0.63-0.78. The variations are due to differences in the crystallite size of the zeolite that results in variations in the Mie scattering. To calculate the extinction coefficient of the (LF)OD band, we employ

$$\varepsilon_{(LF)OD} = (1 + \frac{0.018.\Delta\nu_{OH}}{0.737}).\varepsilon_{(HF)OD} \qquad (3.6).$$

Table 3.2 summarizes the results of the quantification of the various bridging deuteroxyl groups during progressive H/D exchange of USY(9.6, F). A very small contribution of enhanced sites is included. After exchange at 323 K for 30 min the total concentration of deuteroxyl groups is close to the expected hydroxyl concentration. About 97 % of the hydroxyl groups have exchanged under these conditions. Exchange at 353 K did not lead to significant changes. Apparently, not all the bridging hydroxyl groups can be exchanged. Perhaps, perdeuterobenzene cannot reach a small portion of the protons in the zeolite crystal.

The bands of the (HF)OD and (LF)OD components appear concomitantly during exchange. Although this result may be interpreted as if the LF protons were to undergo direct H/D exchange with C_6D_6, this is not the case as it is well known that the sites in the sodalite cages are not accessible to typical probe molecules. For example, carbon monoxide does not directly interact with the hydroxyl groups in the small cages [37]. On the other hand, the case for carbon monoxide applies to much lower temperatures and involves lower heats of adsorption than the benzene case. For benzene, it is possible that adsorption will promote proton migration at some measurable rate. Thus, we invoke (LF)OH↔ (HF)OH exchange to explain the participation of (LF)OH groups. However, if ones assumes only one type of crystallographic Al, it is difficult to see why there should be specific Al sites bearing (HF)OHs and Al sites bearing (LF)OHs. An equilibrium (HF)OH/(LF)OH distribution and hopping of a proton from one oxygen site to another in the same aluminium-occupied oxygen tetrahedron can also explain these observations.

Table 3.2: Concentration of Brønsted acid deuteroxyl groups as probed by progressive H/D exchange of USY(9.6, F). $N_{(HF)OD}$ and $N_{(LF)OD}$ refer to bridging deuteroxyl groups in supercages and sodalite cages, respectively. $N_{(HF')OD}$ refers to enhanced Brønsted acid sites located in supercages and N_{total} is the sum of the various deuteroxyl site densities.

$T_{exchange}$ (K)	$t_{exchange}$ (s)	N_{total} (mmol g^{-1})	$N_{(HF)OD}$ (mmol g^{-1})	$N_{(HF')OD}$ (mmol g^{-1})	$N_{(LF)OD}$ (mmol g^{-1})
303	10	0.11	0.08	0.0	0.037
303	30	0.91	0.55	0.0	0.36
303	300	1.82	1.09	0.0	0.73
303	600	2.29	1.35	0.0	0.95
303	1200	2.49	1.45	0.0	1.04
303	1800	2.56	1.46	0.0	1.10
323	1800	2.71	1.52	0.014	1.17
353	1800	2.73	1.54	0.014	1.17

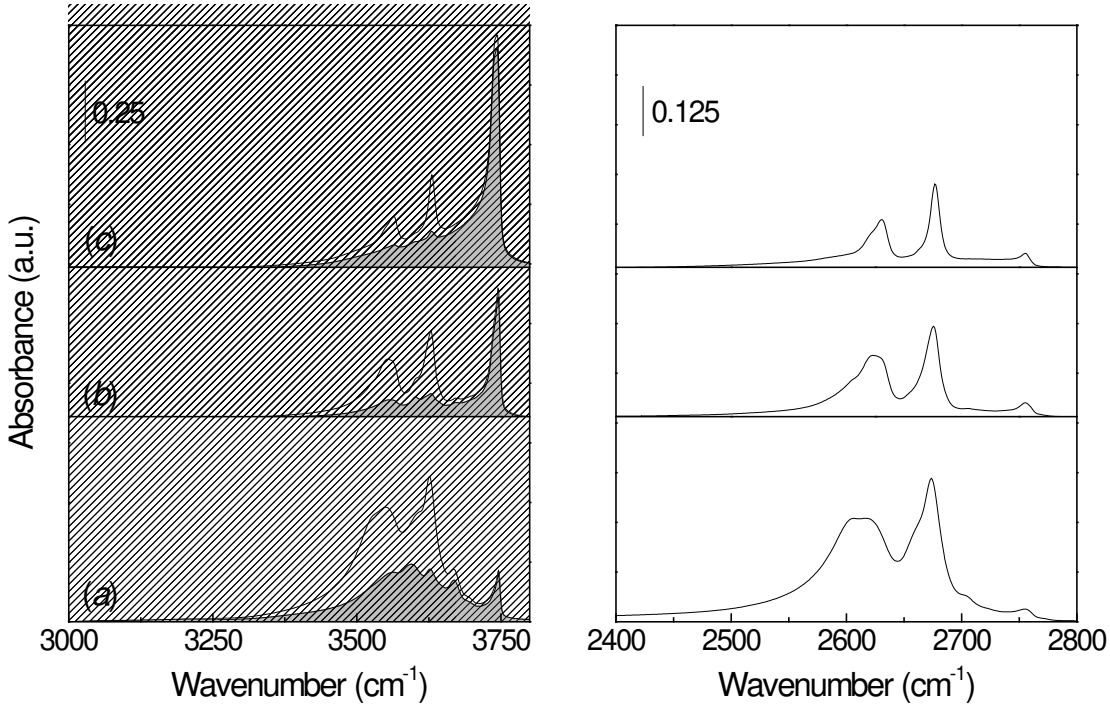

Figure 3.5: FTIR spectra of USY(8.1, II) (a), VUSY(26.3) (b) and XVUSY(70) (c) of the hydroxyl region before and after (filled) H/D exchange (left) and the deuteroxyl region after H/D exchange (right). Exchange conditions were 323 K and 30 min after progressive exchange.

3.3.2 H/D exchange of steam stabilized faujasites.

We next consider a number of ultra-stable Y zeolites made by steam stabilization with a wide variation in composition. The IR spectra of USY(8.1, II), VUSY(26.3) and XVUSY(70) will be shown here. The hydroxyl region of the infrared spectra of the dehydrated zeolites before and after H/D exchange at 323 K and 30 min and of the deuteroxyl region after H/D exchange are collected in Fig. 3.5. A few trends are immediately apparent from the spectra in the deuteroxyl region and more clearly so than from the parent spectra. Spectra of steam stabilized zeolites rich in non-framework aluminium, *e.g.* USY(8.1, II), USY(8.1, I) and

USY(9.3) (the latter two not shown here), contain multiple HF and LF deuteroxyl (hydroxyl) bands. The peaks become narrower with increasing Si/Al ratios, as acid sites become more diluted. Inspection of the remaining hydroxyl groups after extensive H/D exchange shows a broad band that can be assigned to a weakly acidic extraframework aluminium oxide phase. Such a phase has properties similar to an amorphous silica-alumina [48]. The infrared spectra after H/D exchange indicate that this phase becomes less significant with decreasing aluminium concentration. This is due to the removal of extraframework aluminium by acid leaching steps in the preparation of these materials. Evidently, quantification of Brønsted acid sites can be carried out much more straightforwardly by deconvoluting the deuteroxyl region after H/D exchange compared to deconvolution of the hydroxyl region of the parent spectra, because of the presence of bands of weakly acidic hydroxyl groups in the latter spectra.

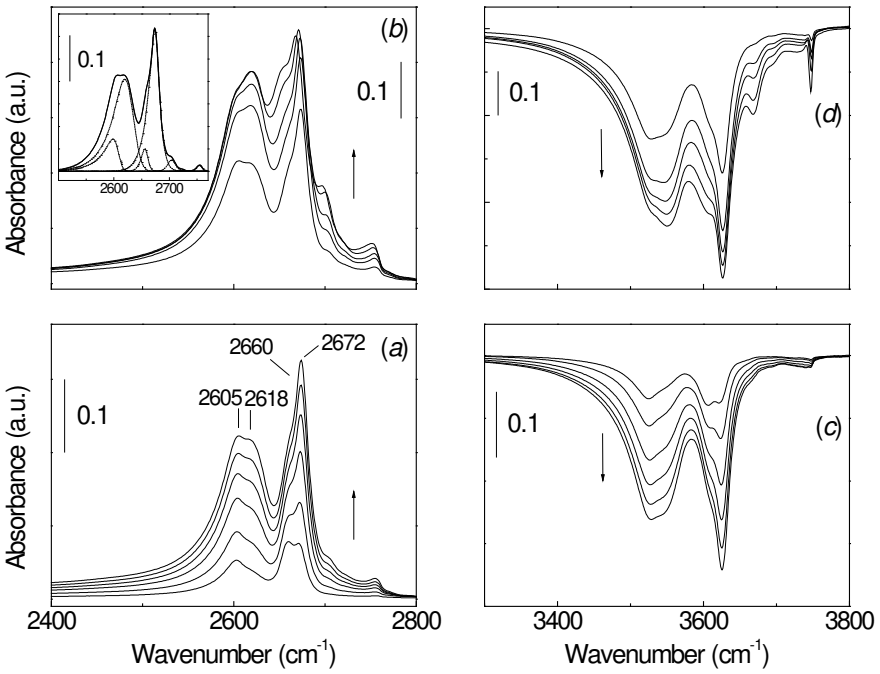

Figure 3.6: FTIR spectra of USY(8.1, II) in the deuteroxyl region (a and b) and the hydroxyl region (c and d) after H/D exchange for increasing exposure times (10, 30, 300, 600, 1200, and 1800 s) at 303 K (a and c) and for an exposure time of 1800 s at increasing temperatures (323, 353, 373 and 423 K) (b and d). The inset shows the fitted spectrum after H/D exchange at 323 K for 1800 s.

Next, we discuss the infrared spectra and their deconvolution upon progressive H/D exchange of USY(8.1, II), VUSY(26.3) and XVUSY(70) in more detail. These zeolites originate from the same parent faujasite zeolite. The relevant spectra for USY(8.1, II) are shown in Fig. 3.6. After exposure for 10 s, four infrared bands are observed in the deuteroxyl region. The bands at 2660 cm^{-1} and 2672 cm^{-1} are now easily identified as (HF')OD and (HF)OD groups, respectively. The bands at 2605 cm^{-1} are of enhanced (LF')OD sites. This band seems to contain a shoulder at the high-frequency side, which stems from (LF)OD groups (ν_{OD} = 2618 cm^{-1}). With increasing exposure to deuterated benzene the intensities of

the (HF')OD and (LF')OD bands increase more pronouncedly than those of the (HF)OD and (LF)OD bands. The difference is more evident for the HF'/HF couple than for the LF'/LF one. The faster exchange and higher acidity of the (HF')OH and (LF')OH agrees with earlier assignments of the corresponding OH peak pair, around 3608 and 3526 cm^{-1} respectively, to hydroxyl groups of enhanced acidity [15]. The H/D exchange of the silanol and aluminol groups is very limited.

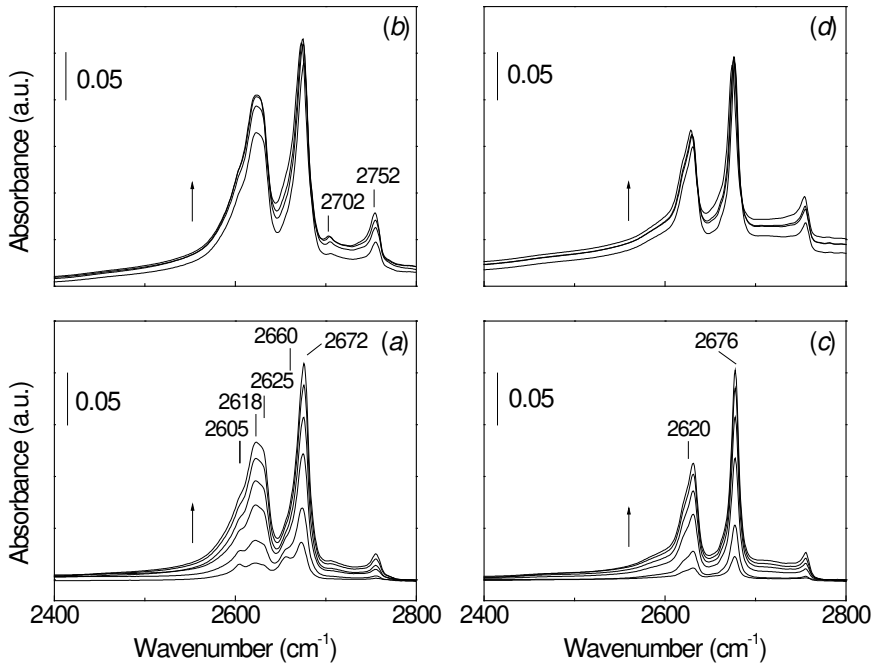

Figure 3.7: FTIR spectra in the deuteroxyl region of (bottom) VUSY(26.3) and (top) XVUSY(70) after H/D exchange for increasing exposure times (10 s, 30 s, 300 s, 600 s, 1200 s, 1800 s) at 303 K (a and c) and for an exposure time of 1800 s at increasing temperatures (323 K, 353 K, 373 K and 423 K) (b and d).

An increase of the exchange temperature to 323 K leads to further exchange of acid sites, while the exchange of non-acidic hydroxyl groups is apparent only above 323 K. Besides the bands of silanols and aluminols, the development of a band around 2653 cm^{-1} indicates that the hydroxyl groups of the non-framework silica-alumina phase start to exchange under these conditions. The concentrations of the various Brønsted acid sites for USY(8.1, II) were calculated by deconvoluting the difference spectra in the deuteroxyl region. As the case of USY(9.6,F) has shown the exchange of nearly all strong Brønsted acid sites at 323 K, our procedure consisted of deconvoluting the relevant spectra up to and including this temperature. First, the spectrum after H/D exchange at 303 K and 10 s was fitted. Inclusion of the earlier mentioned distribution function of asymmetric Gaussians was necessary for the four acidic deuteroxyl bands (Fig. 3.6b).

The high-frequency bands are modelled by relatively narrow peak shapes at 2673 cm^{-1} and 2658 cm^{-1}, corresponding to the (HF)OD and (HF')OD bands. The corresponding frequencies of the hydroxyl groups are 3627 cm^{-1} and 3607 cm^{-1}, respectively. At first sight, the enhanced

component (LF')OD seems to dominate the LF pair. However, deconvolution showed that instead this part of the spectrum is better fitted by a tailing (LF)OD feature with a relatively weak contribution of the enhanced (LF')OD sites. Alternative initial estimates led to the same result. The further evolution of the bands confirms that this combination is the best fit. The further spectra were then deconvoluted by using the fit of the previous spectrum as an initial estimate. In general, this procedure led to increases of the intensities of the peaks with only minor variations in their shapes. The concentrations of the various acidic deuteroxyl groups for USY(8.1, II) are listed in Table 3.3. The concentration of Brønsted acid sites for USY(8.1, II) is 1.25 mmol g^{-1} with contributions from HF and LF sites of 0.69 and 0.42 mmol g^{-1}, respectively. There is a small contribution of enhanced sites with concentrations of 0.05 and 0.08 mmol g^{-1} located in supercages and smaller cages, respectively.

We will now discuss the progress of the H/D exchange of the various sites. Table 3.3 shows that the protons of the enhanced sites exchange faster than those of the unperturbed sites and this is more evident for the sites in the supercages. These observations can be attributed to the difference in Brønsted acidity of the various sites and their location. The enhanced sites in the supercages appear as being most acidic, as they undergo direct H/D exchange. This should also relate to the accessibility of these sites. As the protons in the smaller cages cannot directly interact with deuterated benzene, they undergo H/D exchange via a secondary process, that is, the exchange with proximate deuterated sites or via proton migration as outlined above. Likewise, the quantitative data show that the (HF)OH sites exchange faster than the (LF)OH sites. Finally, we note that there is only a marginal difference in the degree of H/D exchange of the strong Brønsted acid sites when the temperature is increased to 323 K.

Table 3.3: Concentration of Brønsted acid deuteroxyl groups as probed by progressive H/D exchange of USY(8.1, II).

$T_{exchange}$ (K)	$t_{exchange}$ (s)	N_{total} (mmol g^{-1})	$N_{(HF)OD}$ (mmol g^{-1})	$N_{(HF')OD}$ (mmol g^{-1})	$N_{(LF)OD}$ (mmol g^{-1})	$N_{(LF')OD}$ (mmol g^{-1})
303	10	0.28	0.15	0.04	0.07	0.02
303	30	0.46	0.26	0.04	0.12	0.03
303	300	0.72	0.41	0.05	0.22	0.05
303	600	0.92	0.52	0.05	0.29	0.06
303	1200	1.07	0.61	0.05	0.34	0.06
303	1800	1.20	0.69	0.05	0.38	0.09
323	1800	1.25	0.69	0.05	0.42	0.08

The spectra for VUSY(26.5) and XVUSY(70) evolve in a similar manner as for USY(8.1, II). The spectra in the deuteroxyl are given in Fig. 3.7 and the deconvolution of the spectra at reference conditions in Fig. 3.8. Besides differences in the contribution of the various deuteroxyl components, deconvolution of the spectra of VUSY(26.5) required the addition of a (LF)OD band at 2625 cm^{-1}. The origin of this band ((LF")OD) is not clear. In contrast to the more complex infrared spectra of the aluminium-rich zeolites, those of XVUSY (70) only

show the development of two distinct acidic OD bands around 2620 cm^{-1} and 2676 cm^{-1} in the deuteroxyl region. The latter (HF)OD band grows faster than the (LF)OD band. A somewhat more pronounced exchange of the weakly acidic silanol group is observed, which is the result of the higher silanol density in this sample. Exchange above 323 K results in some additional exchange of silanol groups. The total number of Brønsted acid sites for VUSY(26.5) is 0.52 mmol g^{-1}. The contribution of enhanced sites is much lower than for USY(8.1, II). The lower contribution of these enhanced sites stems from the removal of extraframework aluminium species. For XVUSY(70), the acid site concentration is lower at 0.29 mmol g^{-1}. Only a very low concentration of enhanced sites is present in this silica-rich zeolite.

The next objective is to relate the Brønsted acidity of the faujasite zeolites to the catalytic activity in a representative acid-catalyzed reaction. Catalytic activity measurements of the hydroisomerization of *n*-heptane were carried out for the same set of zeolites after Pd was introduced. The acid catalytic activities and the acid site densities determined by FTIR spectroscopy of H/D exchanged aluminosilicates are collected in Table 3.4.

Table 3.4: Concentration of Brønsted acid sites of the faujasite zeolites and clays and contributions of various sites for the zeolites by FTIR spectroscopy after progressive H/D exchange (final exchange temperature and time are 323 K and 30 min, respectively) and catalytic activities of palladium-loaded zeolites in *n*-heptane isomerization.

Sample	$N_{\text{acid sites}}$ (mmol g^{-1})	$N_{(HF)OH}$ (mmol g^{-1})	$N_{(HF')OH}$ (mmol g^{-1})	$N_{(LF)OH}$ (mmol g^{-1})	$N_{(LF')OH}$ (mmol g^{-1})	T_{40} (K)	E_{act} (kJ mol^{-1})	ln N_{isom}
USY(9.6, F)	2.69	1.47	0.09	1.13	0.00			
USY (8.1,I)	0.80	0.37	0.05	0.37	0.01[1]	493	131	1.247
USY (8.1,II)	1.25	0.69	0.05	0.42	0.08	486	130	1.694
USY (9.3)	0.27	0.11	0.05	0.09	0.01[1]	506	128	0.415
VUSY (26.5)	0.52	0.31	0.02	0.11	0.08[1]	499	143	0.941
VUSY (33.1)	0.23	0.14	0.02	0.05	0.02	508	137	0.316
XVUSY (70)	0.29	0.19	0.01	0.05	0.03[1]	536	146	-1.470
XVUSY (85)	0.13	0.10	0.00	0.02	0.01	563	146	-3.042
Mg-SAP(33)	0.048					516	135	-0.184
Mg-SAP(13)	0.012					555	132	-2.343

[1] two contributions for the enhanced (LF)OH.

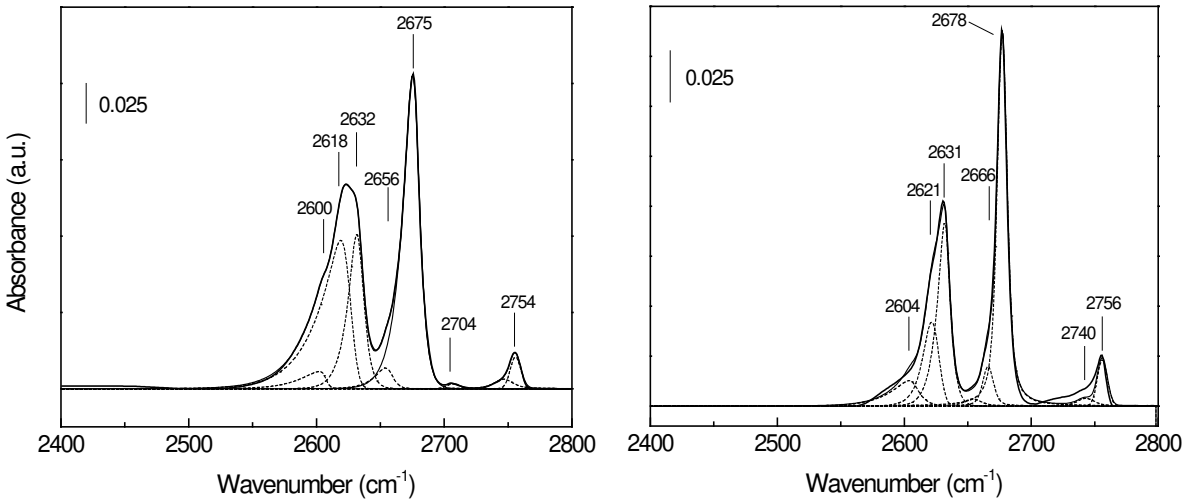

Figure 3.8: FTIR spectrum of VUSY(26.3) and XVUSY(70) after H/D exchange at 323 K for 30 min and its deconvolution into various peaks.

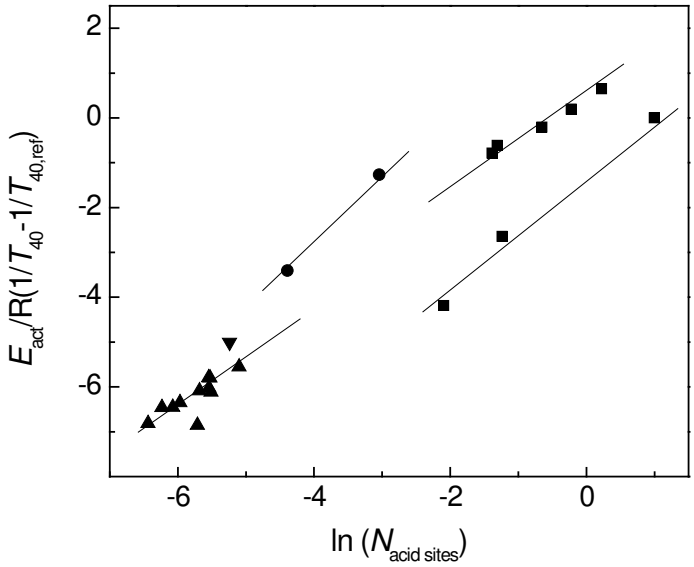

Figure 3.9: Comparison of catalytic activity in hydroconversion of *n*-heptane and the concentration of acid sites (mmol g^{-1}) determined by FTIR spectroscopy of H/D exchanged (■) zeolites, (●) clays, (▲) ASAs prepared by homogeneous deposition -precipitation and (▼) the ASA prepared by cogelation. The reference catalyst is USY(8.1, II). The lines are guide to the eyes.

Fig. 3.9 significantly evidences the strong correlation between catalytic activity and the concentration of strong Brønsted acid sites for the zeolites. We find that the zeolites fall into two categories: (i) zeolites that contain a substantial amount of extraframework aluminium and (ii) zeolites which do not contain or at most a small amount of extraframework aluminium. The first category of zeolites produce more active catalysts. We expect a

correlation between the acidity required for hydroconversion and the exchange a deuteron with a proton in benzene, since the Wheland-ion-like transition state for aromatic H/D exchange [49] and the transition states for key elementary reactions involving zeolite alkoxides, like isomerization and β-scission, are all fairly ionic and hence expected to display a similar dependence on the strength of the acid [50]. We surmise that the quite substantial difference in activity between the two sets of zeolites is caused by the difference in concentration of enhanced Brønsted acid sites. We will briefly return to this point below.

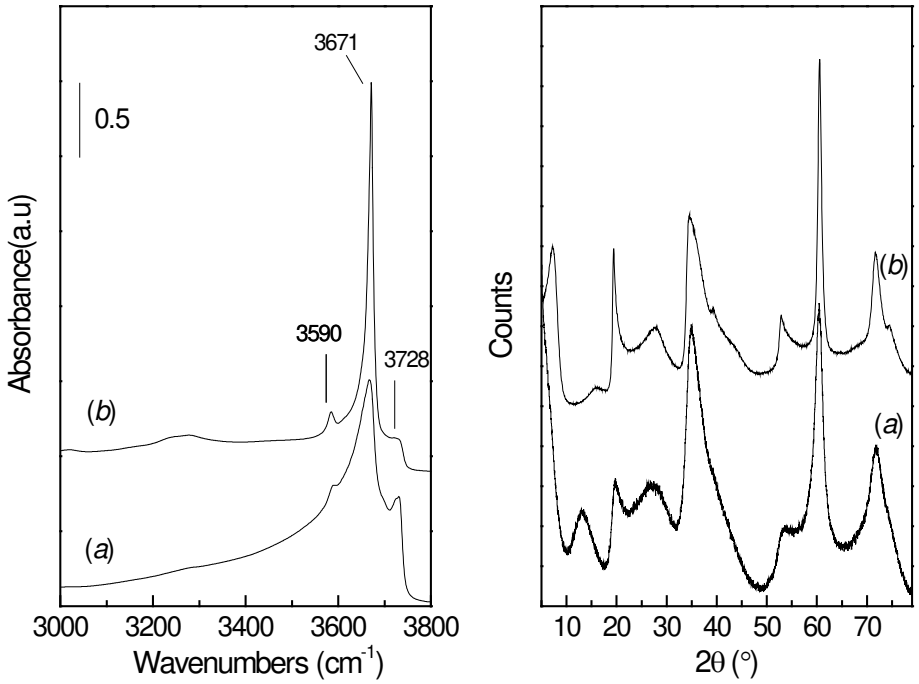

Figure 3.10: (left) FTIR spectra and (right) powder X-ray diffractograms of hydroxyl region of calcined saponite clays: MgSAP(13) (a) and MgSAP(33) (b).

3.3.3 H/D exchange of saponite clays

Clays are minerals consisting of negatively charged aluminosilicate layers that are kept together by cations [51]. In saponites, each of these layers is made up of two tetrahedral silica sheets that enclose a layer containing octahedrally coordinated cations. Brønsted acidity mainly arises from the isomorphous substitution of Si^{4+} by Al^{3+} in the tetrahedral sheets. As the atomic ordering of the aluminosilicate layers does not extend beyond the constituent layers, clays may be regarded as two-dimensional analogues of zeolites. The infrared spectra of the saponite clays (Fig. 3.10) show bands at 3671 cm^{-1} (Mg-OH [52]), 3728 cm^{-1} (silanol groups at the surface of the clay particles or at structural defects [53]) and around 3590 cm^{-1}. This latter band is due to the bridging Si(OH)Al groups in the tetrahedral sheets of the saponite clay [54,55]. The frequency suggests a higher acidity than the protons in zeolites, but this has not been confirmed yet. The infrared spectra show that MgSAP(33) contains more Brønsted acid sites than MgSAP(13). This IR band in MgSAP(13) is partially hidden by

a broad tailing band. The broader infrared bands of MgSAP(13) are caused by the lower crystallinity compared to that of the hydrothermally synthesized saponite (Fig. 3.10).

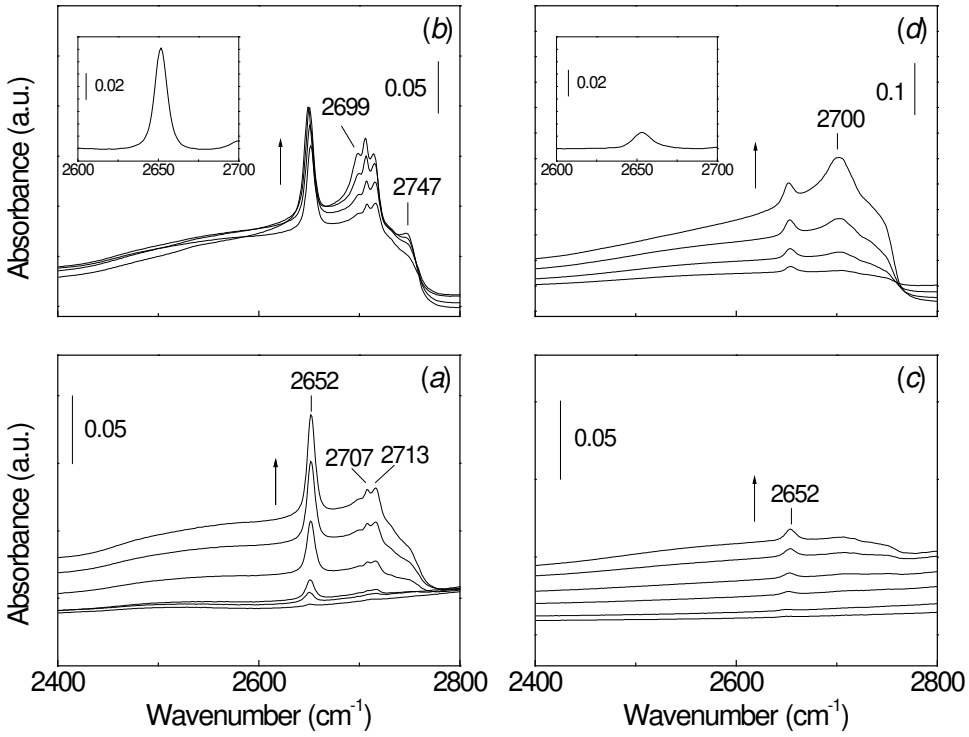

Figure 3.11: FTIR spectra in the deuteroxyl region of MgSAP(13) and MgSAP(33) after H/D exchange for increasing exposure times (10 s, 30 s, 300 s, 600 s, 1200 s, 1800 s) at 303 K (a and c) and for an exposure time of 1800 s at increasing temperatures (323 K, 353 K, 373 K and 423 K) (b and d). Insets show the deuteroxyl region of the spectra after H/D exchange at 323 K after background subtraction.

Fig. 3.11 depicts the deuteroxyl region of IR spectra after progressive H/D exchange. By comparison with the spectra of the dehydrated clays, it is immediately clear that the hydroxyl groups at 3590 cm^{-1} selectively undergo H/D exchange to give a band around 2652 cm^{-1}. With increasing exposure time and temperature, the less acidic hydroxyl groups attached to magnesium and silicon start to exchange. For MgSAP(13), the appearance of a broad band at 2707 cm^{-1}, perhaps with a shoulder at 2713 cm^{-1}, and a weak band around 2750 cm^{-1} are observed. Next to the appearance of a strong band from the bridging deuteroxyl groups and a weak one of Si-OD groups, three resolved bands at 2699 cm^{-1}, 2707 cm^{-1} and 2713 cm^{-1} are observed for the more crystalline MgSAP(33) [56]. The exact assignment of the three Mg-OD bands around 2700 cm^{-1} is not clear, although at least one band could alternatively be caused by deuterated aluminol bands. Only a single band around 2700 cm^{-1} can be discerned for MgSAP(13).

Moreover, the appearance of a broad band under the spectra below 2750 cm^{-1} is observed. Such a band was not present in the spectra of the zeolites. This band most likely originates from the hydrogen bonding of the many Mg-OH and Si-OH groups [57]. Their presence is

also evident in the hydroxyl region of the infrared spectra of the dehydrated clays and is more pronounced for MgSAP(13). The unsymmetrical part extending at the low-frequency side of these bands has been typically attributed to relatively strongly hydrogen-bonded hydroxyl oscillators and is typical for oxide glasses such as silica and silica-aluminas [58,59]. Exchange of this broad band starts already at 303 K after prolonged exposure to C_6D_6. As we did not observe any H/D exchange in silica, we conclude that the exchange of these hydrogen-bonded hydroxyl groups in the two clays is a secondary process. The exchange of these hydroxyl groups is most likely facilitated by their close proximity to the strong Brønsted acid sites. A clear difference from the IR spectra between the zeolites and the clays is the much higher surface density of non-acidic hydroxyl groups. It is evident that the bands of the Brønsted acid sites are much better resolved in the deuteroxyl region after H/D exchange than in the parent spectra. The reason is the selective nature of the H/D exchange. We deconvoluted the difference spectra of the two clays after H/D exchange at 323 K for 30 min. A simple linear baseline was used to remove the broad band under the distinct deuteroxyl vibrational bands and these spectra were fitted with a Gaussian function. The computed acid site densities and the corresponding catalytic activities are collected in Table 3.4. The higher catalytic hydroisomerization activity of MgSAP(33) agrees with its higher Brønsted acid site density.

3.3.4 H/D exchange of amorphous silica-aluminas

We now turn to the question whether selective H/D exchange of the suspected strongly acidic bridging hydroxyl groups in ASAs allows their identification and perhaps their quantification. The ASA materials have been prepared by controlled deposition of Al^{3+} on silica followed by calcination. The synthesis of such ASAs has been studied in detail elsewhere [41]. In contrast to zeolites and clays, the IR spectrum of well-dehydrated amorphous silica-alumina (Fig. 3.12) resembles that of dehydrated silica and does not provide any evidence for the presence of bridging hydroxyl groups. A single intense silanol band with a strong tail at the low-frequency side is observed in the infrared spectra of ASAs. The intensity of this band decreases with increasing aluminium content of the ASA, because of the replacement of silanol groups by surface aluminium.

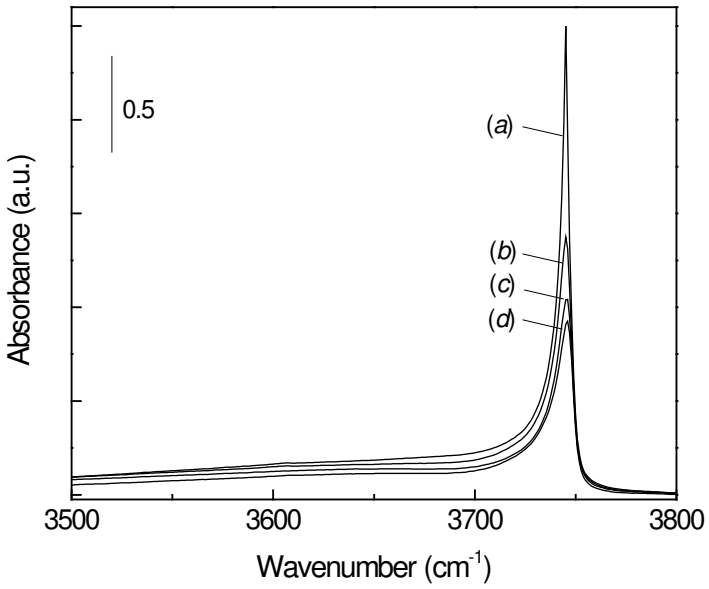

Figure 3.12: Infrared spectra of dehydrated ASA(5/95, 1073) (a), ASA(10/90, 1073) (b), ASA(15/95, 1073) (c), ASA(20/80, 1073) (d).

Fig. 3.13 shows the difference spectra after H/D exchange of ASA(5/95, 1073). Up to an exposure time of 300 s at 303 K only very weak H/D exchange of silanol groups occurs, as follows from the weak feature developing in the region 2752-2758 cm^{-1} (ν_{OH} = 3734-3742 cm^{-1}). At an exposure time of 300 s, an additional feature is observed around 2683 cm^{-1}. It develops into a clear band at 2683 cm^{-1} (ν_{OH} = 3638 cm^{-1}) after further exchange. The final spectrum after exchange at 303 K for 30 min also contains a very weak feature at 2633 cm^{-1} (ν_{OH} = 3570 cm^{-1}). The broad feature below 2756 cm^{-1} develops in a similar manner as in the saponite clays. We observe the following changes with increasing temperature of H/D exchange: (i) the broad band below 2756 cm^{-1} further grows into the spectra concomitant with an increase of a deuteroxyl band from silanol groups, (ii) the band at 2683 cm^{-1} increases up to 353 K and then becomes less pronounced and (iii) the band at 2633 cm^{-1} appears to go through a maximum at 423 K. Notably, the bands at 2633 cm^{-1} and 2683 cm^{-1} become obscured by the broad deuteroxyl band after H/D exchange at 523 K. Inspection of the hydroxyl region of the difference spectra does not evidence negative features around 3570 cm^{-1} and 3638 cm^{-1}, as these bands are still hidden under the broad hydroxyl band. The negative silanol feature in this case contains two components, one at 3750 cm^{-1} and one around 3733 cm^{-1}. Clearly, the extent of the first negative feature is much higher than the corresponding feature in the deuteroxyl region. We attribute this to minute traces of water adsorbing to the surface, as directly after dehydration the silanol band is very sharp and intense, but decreases and broadens with time caused by hydrogen bonding of readsorption of residual water. The appearance of the second band appears to agree with the appearance of deuteroxyl bands around 2752-2758 cm^{-1}. The spectrum in the hydroxyl region after exchange at 523 K shows the exchange of the broad tailing band.

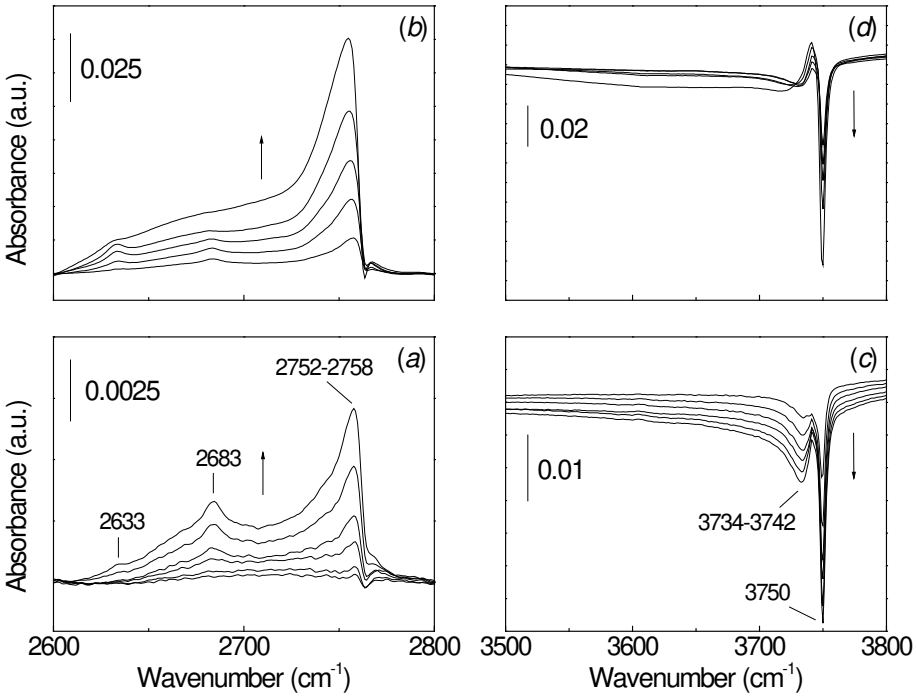

Figure 3.13: FTIR spectra of ASA(5/95, 1073) in the deuteroxyl region (a and b) and the hydroxyl region (c and d) after H/D exchange for increasing exposure times (10 s, 30 s, 300 s, 600 s, 1200 s, 1800 s) at 303 K (a and c) and for an exposure time of 1800 s at increasing temperatures (323 K, 353 K, 373 K and 423 K) (b and d).

The most striking feature of the difference spectra of ASA(5/95, 1073) is the presence of weak, yet distinct bands at 2683 cm^{-1} and 2633 cm^{-1}. These deuteroxyl bands derive from H/D exchange of hydroxyl stretching bands located at 3638 cm^{-1} and 3570 cm^{-1}, respectively. These latter bands are obscured in the spectra of the dehydrated ASA by the broad hydroxyl band. Thus, H/D exchange occurs with such selectivity for this ASA that very weak features around 3635 cm^{-1} and 3564 cm^{-1} can be observed as their corresponding deuteroxyl groups. The bands at 2683 cm^{-1} and 2630 cm^{-1} become obscured again, following the development of a broad deuteroxyl band after more extensive H/D exchange.

As their position and their appearance at room temperature agree well with the findings for the zeolites and clays, we suspect that these sites exhibit similar Brønsted acidity. To verify this assignment, we determined the concentrations of these sites in several ASAs and evaluated whether the acid site densities correlate with the catalytic activities in *n*-heptane hydroisomerization. Before doing so, we will discuss the H/D exchange results of two ASAs similar to ASA(5/95, 1073), but with higher aluminium concentration. The evolution of the difference spectra in the deuteroxyl region during H/D exchange is shown in Fig. 3.14. The trends of H/D exchange of these ASAs are similar to that of ASA(5/95, 1073). After the initial exposures to the probe at 303 K, only the band around 2758 cm^{-1} can be discerned. The band at 2683 cm^{-1} starts to develop after H/D exchange at 303 K for 10 min. The occurrence

of a band around 2633 cm^{-1} is in line with the result for ASA(5/95, 1073). The two bands continue to grow further with increasing temperature.

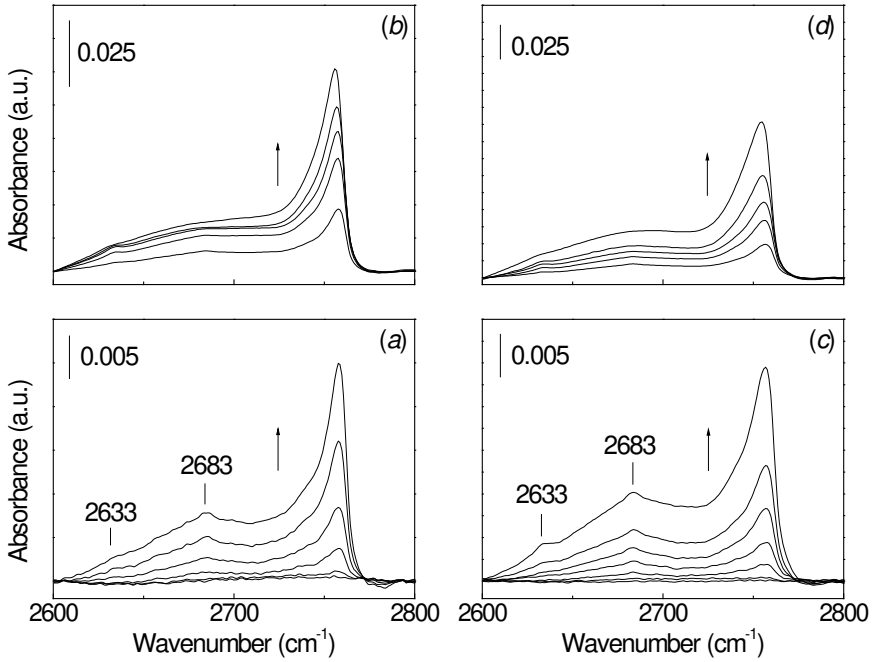

Figure 3.14: FTIR spectra of ASA(10/90, 1073) (a and b) and ASA(15/85, 1073) (c and d) in the deuteroxyl region after H/D exchange for increasing exposure times (10 s, 30 s, 300 s, 600 s, 1200 s, 1800 s) at 303 K (a and c) and for an exposure time of 1800 s at increasing temperatures (323 K, 353 K, 373 K and 423 K) (b and d).

For quantification, we follow the same approach as for the zeolites and clays. The concentrations of acid site was determined from the difference spectra after H/D exchange at 323 K for 30 min. The deconvolution of these spectra was found to be more complex than for the zeolites and clays, because of the broad background. Prior to deconvolution, a subtraction was carried out by using a cubic function in order to remove the broad background under the bands around 2633 and 2683 cm^{-1}. The baseline-corrected spectra for the four ASAs calcined at 1073 K are given in Fig. 3.15. The deuteroxyl band at 2633 cm^{-1} was fitted by a Gaussian/Lorenztian peak shape, while the band at 2683 cm^{-1} was fitted with the asymmetric Gaussian distribution function. In some cases, a better fit was obtained by introducing a second feature around 2683 cm^{-1} in addition to the broad feature. A typical example is the fit for ASA(15/85, 1073), which is given in Fig. 3.15. From the intensities of these bands and their frequencies, the concentrations were calculated. As we cannot determine the correlation coefficient C in the relation $\varepsilon_{(HF)OD} = C.\varepsilon_{(HF)OH}$ for these ASA, we used a value for C of 0.69, *i.e.* the average of the coefficients for the faujasite zeolites.

Evidence for the strongly acidic nature of these hydroxyl groups in ASAs follows from a comparison of their concentration with the catalytic activity. The concentrations of strong acid site and kinetic parameters for hydroisomerization are listed in Table 3.5. Clearly, the concentrations of acid sites in ASAs are 2-3 orders of magnitude lower than in zeolites. Fig. 3.9 shows the acid catalytic activities as a function of the Brønsted acid site densities for the

complete set of aluminosilicates. The good correlation between these two parameters for these ASAs strongly suggests that the bands around 2633 and 2683 cm^{-1} are the active sites for the isomerization. Moreover, the correlation holds for the broader set of aluminosilica materials, ranging from the amorphous mixed oxides to the crystalline zeolites including the clays. This graph provides strong evidence that the low overall Brønsted acidity of ASAs is caused by the presence of a very small number of bridging hydroxyl groups with an acidity close to that of zeolites.

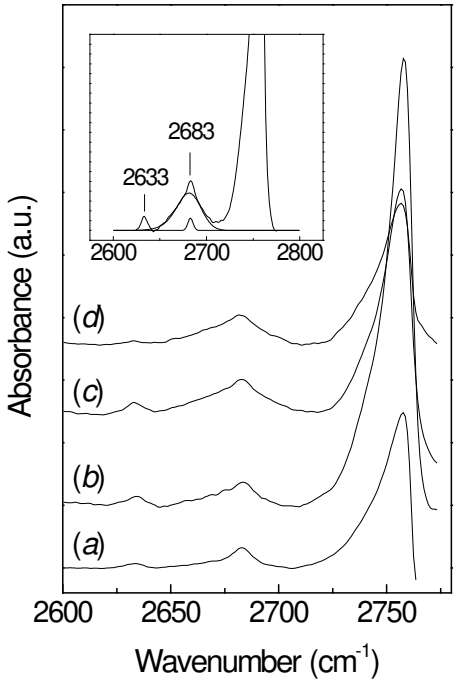

Figure 3.15: FTIR spectra of H/D exchanged ASAs after background subtraction: ASA(5/95, 1073) (a), ASA(10/90, 1073) (b), ASA(15/85, 1073) (c) and ASA(20/80, 1073) (d). The inset shows the fit for ASA(15/85, 1073).

Table 3.5: Concentration of Brønsted acid sites of a set of amorphous silica-aluminas determined by by FTIR spectroscopy after progressive H/D exchange (final exchange temperature and time are 323 K and 30 min, respectively) and catalytic activities of palladium-loaded supports in *n*-heptane hydroconversion.

Sample	$N_{\text{acid sites}}$ (μmol g^{-1})	T_{40} (K)	E_{act} (kJ mol^{-1})	ln N_{isom}
ASA(5/95, 773)	1.6	630	132	-5.750
ASA(10/90, 773)	2.3	630	125	-5.445
ASA(15/85, 773)	2.0	625	129	-5.423
ASA(20/80, 773)	3.3	626	136	-5.759
ASA(5/95, 1073)	2.6	616	130	-5.303
ASA(10/90, 1073)	3.4	618	127	-5.101
ASA(15/85, 1073)	6.1	604	128	-4.488
ASA(20/80, 1073)	4.0	611	127	-4.816
ASA(5/95, 3, 1073)	4.0	612	133	-5.047
ASA(10/90, 3, 1073)	3.9	612	131	-4.971
ASA(15/85, 3, 1073)	3.9	612	126	-4.781
ASA(5/95, cogel)	5.3	599	120	-4.041

3.3.5 Intrinsic acidity of hydroxyl groups

By following the H/D exchange at 303 K, we attempted to determine possible differences in the intrinsic Brønsted acidity of the various aluminosilicates. To this end, we calculated the first-order rate constant from the degree of exchange as a function of time (Fig. 3.16). This rate constant reflects an intrinsic reaction rate, because pores and Brønsted sites are saturated with the C_6D_6 reactant under the conditions of the measurement. For the faujasite zeolites, the concentration of (HF)OH groups was followed, as these sites are involved directly in H/D exchange. The enhanced sites in the supercages exchange much faster and most of these sites have already been deuterated at the first exchange step. For the ASAs, the exchange rate was determined for the protons identified by the band at 2683 cm^{-1}, because the other band appears to be of lower acidity and its contribution to the overall acidity is very low in any case. Table 3.6 lists the first order rate constants ($k_{H/D}$) for a number of aluminosilicates (kinetic plots in the Supporting Information). The exchange rates ($k_{H/D}$) of the steam stabilized zeolites are quite similar (2.1±0.5 h^{-1}) and considerably higher than the value of 0.3 h^{-1} of HY(5). $k_{H/D}$ is slightly higher for USY(9.6, F) than for the other dealuminated zeolites. It is not clear what causes this difference, but tentatively the higher intrinsic activity may be caused by the more crystalline framework of USY(9.6, F) than its steam calcined counterparts. Although similar plots could not be made for the enhanced sites in the faujasite zeolites, we estimate that their exchange rate should be between 2-10 times higher than of the unperturbed hydroxyl groups. This high acidity implies that despite the relatively low density of such sites their contribution to the overall Brønsted acidity should be substantial. Cracking activity enhancement in steamed zeolites cannot therefore be simply due to enhanced adsorption at low partial pressures, as Van Bokhoven et al. [60] state. This statement is fortified by the little variation of the apparent activation energies in *n*-heptane hydroisomerization among the aluminosilicates. This is line with our conclusion that the intrinsic isomerization activity per site of a wide range of aluminosilicates falls within a reasonably narrow range. The exchange rates of the amorphous silica-aluminas lie between those of the steam stabilized zeolites and HY(5). For ASA(5/95, 1073), the value of $k_{H/D}$ = 1.0 h^{-1} indicates an acidity intermediate between the very strong Brønsted acidity in steam stabilized faujasite and the weaker Brønsted acidity in HY(5). With increasing aluminium concentration, $k_{H/D}$ decreases for the ASAs calcined at 1073 K.

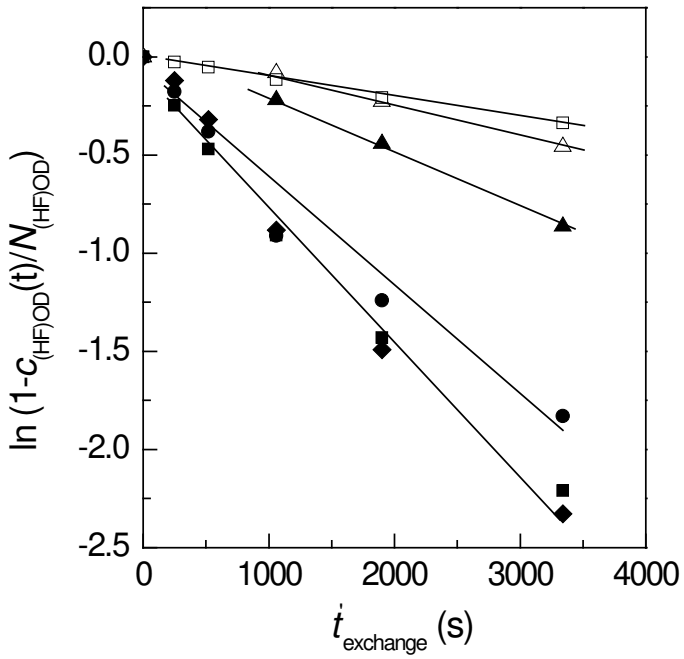

Figure 3.16: First-order plot of the rate of appearance of strongly acidic deuteroxyl groups (c_{OD}(t): concentration of deuteroxyl groups H/D exchange as a function of exchange time at 303 K; N_{OD}: acid site density) for a set of aluminosilicates:□ - HY(5), □ - USY (8.1, II), □ - VUSY (26.5), □- XVUSY (70), ▲ - ASA (5/95, 1073), □- ASA (20/80, 1073). A value of 240 s was added to the exchange time because evacuation of the sample after exposure to C_6D_6 is not infinitely fast (typical time to reach a pressure below 10^{-5} mbar ~ 300 s).

Table 3.6: H/D exchange rate ($k_{H/D}$) at 303 K for various aluminosilicates.

Catalyst	$k_{H/D}$ (h^{-1})
USY(9.6, F)	3.6
HY(5)	0.32
USY(8.1,I)	1.6
USY(8.1,II)	2.3
USY(9.3)	2.3
VUSY(26.5)	1.8
VUSY(33.1)	1.9
XVUSY(70)	2.6
XVUSY(85)	2.5
ASA(5/95, 1073)	1.0
ASA(10/90,1073)	0.72
ASA(15/85,1073)	0.68
ASA(20/80, 1073)	0.60

Finally, compelling evidence for the strong acidity of the hydroxyl groups around 2683 cm^{-1} in the H/D exchanged ASAs follows from infrared spectra of adsorbed carbon monoxide. The frequency shift of a hydroxyl group upon perturbation by CO is a well-known method to probe zeolite acidity [37,61-63]. Thus, we determined values for $\Delta\nu_{OH}$ of 330 cm^{-1} and 278 cm^{-1} for (HF)OH in USY(9.6, F) and HY(5), respectively, upon CO adsorption at

liquid nitrogen temperature. In literature, values of 250-280 cm^{-1} and of 300-350 cm^{-1} for the unperturbed (HF)OH in non-dealuminated and dealuminated Y zeolites, respectively, have been reported. For comparison, the shifts reported for zeolitic silanol and aluminol groups are much lower (90 cm^{-1} and 190 cm^{-1}, respectively). After partial H/D exchange of these two zeolites, we found that $\Delta\nu_{OD}$, *i.e.* the shifts of the acidic (HF)OD band upon CO chemisorption, correspond to 212 cm^{-1} and 182 cm^{-1} for USY(9.6, F) and HY(5), respectively. Fig. 3.17 shows the subtracted infrared spectra of H/D exchanged ASA(5/95, 1073) with increasing CO coverage. As discussed earlier [37] and similar to the corresponding spectra of the zeolites, these spectra show a negative-positive absorbance, which is likely the result of a small shift of the silanol groups upon introduction of CO. More importantly, the infrared band around 2683 cm^{-1} becomes perturbed asymmetrically by CO. First, the low-frequency tail of this band gives rise to a band around 2483 cm^{-1} with $\Delta\nu_{OD}$ = 175 cm^{-1} (corresponding $\Delta\nu_{OH}$ = 272 cm^{-1}). The perturbed band shifts with increasing CO coverage as does the negative feature at higher frequency. These shifts point to the presence of sites of varying acidity. Finally, the band around 2683 cm^{-1} becomes perturbed and shifts to 2530 cm^{-1}. The shift corresponds to $\Delta\nu_{OH}$ = 238 cm^{-1}. These results evidence that the asymmetric band around 2683 cm^{-1} derives from strongly acidic hydroxyl groups on the ASA's surface. The decreasing $\Delta\nu_{OD}$ ($\Delta\nu_{OH}$) with increasing CO coverage points to the presence of multiple types of sites of slightly different acidity. This result is not surprising in view of the much less defined structure of ASAs compared to the crystalline framework of zeolite Y. We note that the sites probed by H/D exchange at 303 K from which $k_{H/D}$ is computed are the sites that give the largest perturbation upon CO chemisorption.

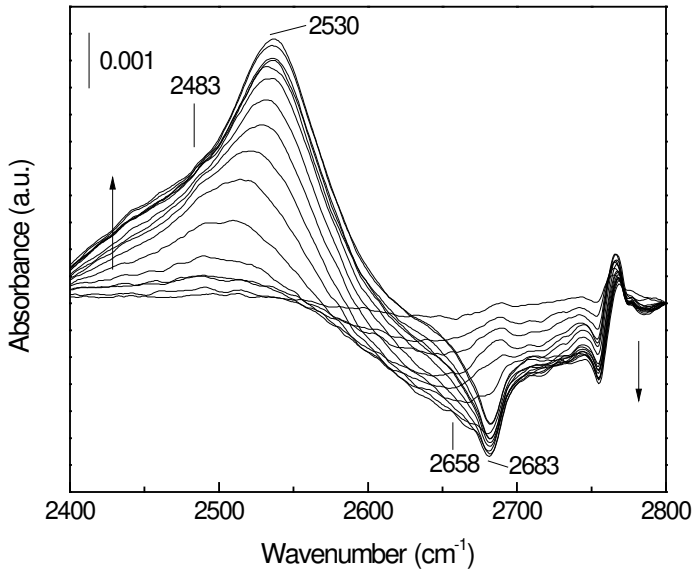

Figure 3.17: Infrared spectra at 80 K of the deuteroxyl region of H/D exchanged ASA(5/95, 1073) upon increasing CO chemisorption (doses of 0.05 μmol CO). The arrow indicates increasing CO coverage.

3.3.6 Strong Brønsted acidity in amorphous silica-aluminas

FTIR spectroscopy of H/D exchange aluminosilicates provides direct spectroscopic evidence for the presence of strong Brønsted acid sites in amorphous silica-aluminas. The intrinsic acidity is similar to the bridging hydroxyl groups in crystalline zeolites. Thus, the much lower Brønsted acidity of ASAs compared to zeolites originates from the very low concentration of acidic sites in ASAs. It can be reasonably concluded that the Brønsted acid sites are protons that compensate the negative charge of Al^{3+} substitution for Si^{4+} in the silica network [41,45]. Thus, structural models for strong BAS that invoke non-bridging paired (SiOH, Al) sites or the interface region between alumina patches and the mixed silica-alumina phase can be discarded. The presence of bridging hydroxyl groups in amorphous aluminosilicates has been reported before by Datka and co-workers [21,22]. In their case, structure-directing agents conducive to the formation of ZSM-5 were used in the synthesis of the aluminosilicates. This provides an explanation for the observation of the acidic hydroxyl band around 3610 cm^{-1} which is close to the frequency for ZSM-5. The spectra of the ASAs prepared in this work do not contain such a band, even not after prolonged evacuaton at high temperature.

A kinetic analysis of H/D exchange of the protons in the various aluminosilicates indicates that the intrinsic acidity of these sites in ASAs is between that of protons in steam stabilized faujasite and non-dealuminated faujasite zeolites. CO IR spectroscopy suggests that the intrinsic acidity of the sites in ASAs is much less uniform than in zeolites, which is undoubtedly related to the amorphous nature of the mixed oxide material. Yet, very similar to zeolites, the composition of the ASA influences the intrinsic acidity of the bridging hydroxyl groups: diluting aluminium in ASAs makes the bridging hydroxyl groups more acidic. The acidity may also depend on the presence of aluminium atoms at next-nearest neighbour tetrahedral sites. These small differences in acidity provide a tentative explanation for the deviations observed in the correlation between acid catalytic activity and the acid site density. Thus, a crystalline framework of AlO_4 and SiO_4 tetrahedra such as in zeolites and clays is not a prerequisite for the development of strong Brønsted acidity.

3.4 Conclusions

By following the selective H/D exchange of acidic hydroxyl groups in aluminosilicates by IR spectroscopy clear evidence is provided for the existence in amorphous silica-aluminas (ASAs) of Brønsted acid sites comparable in strength to the bridging hydroxyl groups in zeolites. The method distinguishes various types and strengths of strong Brønsted acid sites in aluminosilicates (zeolites, clays, ASAs) such as enhanced sites in steam calcined faujasite zeolites and can be used to quantify them. Following H/D exchange under conditions under which zeolites selectively exchange their bridging hydroxyl groups, weak bands are observed at 2630 and 2683 cm^{-1} in the deuteroxyl region of ASAs. Evidence for the strong acid strength of these groups is fortified by the similar large frequency shift upon CO chemisorption of the dominant IR band at 2683 cm^{-1} as observed for zeolites. The

concentration of strong Brønsted acid sites in ASAs is 2-3 orders of magnitude lower than in zeolites. The acid catalytic activity in *n*-alkane hydroconversion correlates well with the number of strong Brønsted acid sites for steam stabilized zeolites, clays and amorphous silica-aluminas. The strong Brønsted acid sites in these aluminosilicates consist of hydroxyl groups located between aluminium and silicon occupied oxygen tetrahedra. Differences in the Brønsted acidity of aluminosilicates are dominated by differences in the concentrations of strong Brønsted acid sites.

Acknowledgements

Mrs. Patricia Giltay is acknowledged for the catalytic activity measurements and dr. Pieter Magusin and Brahim Mezari for NMR measurements.

References

1. A. Corma, Chem. Rev. 95 (1995) 559.
2. G. Busca, Chem. Rev. 107 (2007) 5366.
3. M.S. Rigutto, J.A.R. van Veen, R. Huve Stud. Surf. Sci. Catal. 168 (2007) 85.
4. J.A. Rabo, G.J. Gajda Catal. Rev.-Sci. Eng. 31 (1990) 385.
5. R.A. van Santen, G.J. Kramer Chem. Rev. 95 (1995) 637.
6. A. Corma Curr. Opin. Solid State Mater. Sci. 2 (1997) 63.
7. A. Corma, M.S. Grande, A. Gonzalez-Alfaro, A.V. Orchillés J. Catal. 159 (1996) 375.
8. B. Xu, C. Sievers, J.A. Lercher, J.A.R. van Veen, P.Giltay, R.Prins, J.A. van Bokhoven J. Phys. Chem. C 111 (2007) 12075.
9. W.E. Farneth, R.J. Gorte Chem. Rev. 95 (1995) 615.
10. L.A. Pine, P.J. Maher, W.K. Wachter J. Catal. 85 (1984) 466.
11. J.R. Sohn, S.J. Decanio, P.O. Fritz, J.H. Lunsford J. Phys. Chem. 90 (1986) 4847.
12. P.O. Fritz, J.H. Lunsford, J. Catal. 118 (1989) 85.
13. M.A. Makarova, J.J. Dwyer, J. Phys. Chem. 97 (1993) 6337.
14. R.M. Lago, W.O. Haag, R.J. Mikovsky, D.H. Olson, S.D. Hellring, K.D. Schmitt, G. T. Kerr, Stud. Surf. Sci. Catal. 28 (1986) 677.
15. M.A. Makarova, S.P. Bates, J.J. Dwyer, J. Am. Chem. Soc. 117 (1995) 11309.
16. J.J. Fripiat, A. Léonard, J.B. Uytterhoeven, J. Phys. Chem. 69 (1965) 3274.
17. W.O. Haag, R.M. Lago, P.B. Weisz, Nature 309 (1984) 589.
18. G. Crépeau, V. Montouillout, A. Vimont, L. Mariey, T. Cseri, F. Maugé, J. Phys. Chem. B 110 (2006) 15172.
19. C.L. Thomas, Ind. Eng. Chem. 41 (1949) 2564.
20. M.W. Tamele, Disc. Faraday Soc. 8 (1950) 270.
21. K. Góra-Marek, M. Derewinski, P. Sarv, J. Datka, Catal. Today 101 (2005) 131.
22. K. Góra-Marek, J. Datka, Appl. Catal. A 302 (2006) 104.
23. J.D. Danforth, J. Phys. Chem. 59 (1955) 564.
24. J.H. De Boer, Disc. Faraday Soc. 52 (1971) 109.
25. G.B. McVicker, G.M. Kramer, J.J. Ziemiak, J. Catal. 83 (1983) 286.
26. L.L Murell, C. Dispenziere Jr., Catal. Lett. 2 (1989) 329.
27. B.Umansky, J. Engelhardt, W.K. Hall, J. Catal.127 (1991)128.
28. S. Blonski, S.H. Garolfini, J. Phys. Chem. 100 (1996) 2201.
29. M. Trombetta, G. Busca, S. Rossini, V. Piccoli, U. Cornaro, A. Guercio, R. Catani, R.J. Willey, J. Catal. 179 (1998) 581.
30. C. P-Hwang, C. T- Yeh, J. Catal. 182 (1999) 48.
31. W. Daniell, U. Schubert, R. Glockler, A. Meyer, K. Noweck, H. Knözinger, Appl. Catal. A 196 (2000) 247.

32. A. Zecchina, G. Spoto, S. Bordiga,. Handbook of Vibrational Spectroscopy 2002, Wiley, Vol. 4, p. 3042.
33. E.Payen, J. Grimblot, J.C- Lavalley, M.Daturi, F.Maugé, Handbook of Vibrational Spectroscopy 2002, Wiley, Vol. 4, p. 3005.
34. C. Chizallet, P. Raybaud, Angew. Chem. Int. Ed. 48 (2009) 2891.
35. L. W. Beck, T. Xu, J.B. Nicholas, J.F.Haw, J. Am. Chem. Soc. 117 (1995)11594.
36. V.L.C. Gonçalves, R.C. Rodrigues, R. Lorençato, C.J.A. Mota, J. Catal. 248 (2007)158.
37. O. Cairon, T. Chevreau, J.C-Lavalley, J. Chem. Soc., Faraday Trans. 94 (1998) 3039.
38. W. Daniell, N.Y-Topsøe, H. Knözinger, Langmuir 17 (2001) 6233.
39. US Patent 4503023, 1985.
40. R.J.M.J.Vogels, J.T. Kloprogge , J.W. Geus, Am. Mineral. 90 (2005) 931.
41. E.J.M. Hensen, D.G. Poduval, P.C.M.M. Magusin, A.E. Coumans, J.A.R. Van Veen, J. Catal. 269 (2010) 201.
42. US Patent 3536605, 1968.
43. G.E. Gianetto, G.R.Perot, M.R. Guisnet, Ind. Eng. Chem. Prod. Res. Dev. 25 (1986) 481.
44. J.W. Thybaut, C.S. Laxmi Narasimhan, J.F. Denayer, G.V. Baron, P.A. Jacobs, J.A. Martens, G.B. Marin, Ind. Eng. Chem. Res. 44 (2005) 5159.
45. M.F. Williams, B. Fonfé, C. Sievers, A. Abraham, J.A. van Bokhoven, J.A. Jentys, J.A.R. van Veen, J.A. Lercher, J. Catal. 251 (2007) 485.
46. M.A. Makarova, A.F. Ojo, K. Karim, M. Hunger, J.Dwyer, J. Phys. Chem. 98 (1994) 3620.
47. C.A. Emeis, J. Catal. 147 (1993) 347.
48. A. Omegna, J.A. van Bokhoven, R.J. Prins, J. Phys. Chem. B 107 (2003) 8854.
49. G.W. Wheland, J. Am. Chem. Soc. 64 (1942) 900.
50. A.M. Rigby, G.J. Kramer, R.A.Van Santen, J. Catal. 170 (1997) 1.
51. Handbook of Clay Science (F. Bergaya, B.K. Theng, G. Lagaly, Eds.), Elsevier, Oxford, 2006.
52. J.T. Kloprogge, R.L. Frost, Vib. Spectrosc. 23 (2000)119.
53. A. Zecchina, S. Bordiga, G. Spoto, L. Marchese, G. Petrini, G. Leonfanti, M.J. Padovan, J. Phys. Chem. 96 (1992) 4991.
54. A. Janin, M. Maache, J.C- Lavalley, J.F. Joly, F. Raatz, N. Szydlowski, Zeolites 11(1991)391.
55. J. Weitkamp, Solid State Ionics 131 (2000) 175.
56. J. Datka, B. Gil, P.J. Baran, J. Mol. Structure 645 (2003) 45.
57. C. Bisio, G. Gatti, E. Boccaleri, L. Marchese, G.B. Superti, H.O. Pastore, M.Thommes, Microporous Mesoporous Mat. 107 (2008) 90.
58. D.P. Zarubin, Phys. Chem. Minerals 27 (2000) 590.
59. A. Burneau, C. Carteret, Phys. Chem. Chem. Phys. 2 (2000) 3217.
60. J.A. van Bokhoven, B.A.Williams, W. Ji, D.C. Koningsberger, H.H. Kung, J.T. Miller, J. Catal. 224 (2004)50.
61. L. Kubelkova, S. Beran, J.A. Lercher, Zeolites 9 (1989) 539.
62. M. Maache, A. Janin, J.C- Lavalley, J.F. Joly, E. Benazzi, Zeolites 13 (1993) 419.
63. M.A.Makarova, K.M. Al-Ghefaili, J.Dwyer, J. Chem. Soc., Faraday Trans. 90 (1994) 383.

Chapter 4

Probing the nature of acidity in amorphous silica-aluminas

Summary

A number of techniques (CO IR, pyridine IR, alkylamine TPD, Cs^+ and $Cu(EDA)_2^{2+}$ exchange, ^1H NMR and *m*-xylene isomerization) stresses the heterogeneous composition of the surface of amorphous silica-alumina (ASA). The surface contains Brønsted and Lewis acid sites of varying acidity. The number of strong Brønsted acid sites of zeolitic strength is very low (< 10 μmol/g) as earlier determined by H/D exchange FTIR. Careful interpretation of IR spectra of adsorbed CO and pyridine confirms that the surface of ASA contains only very few of such sites. Other methods suitable to estimate strong Brønsted acid sites involve an adaptation of the well-known decomposition of alkylamines and their titration by a base during *m*-xylene isomerization. These sites originate from Al substitutions in the silica network. Besides, the surface contains between 50-150 μmol/g of a weaker form of Brønsted acid sites, which can be easily quantified by CO IR. $Cu(EDA)_2^{2+}$ exchange also appears to probe these sites. The structure of these sites remains unresolved, but there are indications that these sites involve the interaction of silanol groups with strong Lewis acid Al^{3+} sites. The surface is further made up of non-acidic aluminol and silanol sites (200-400 μmol/g). Finally, the surface of ASA contains two forms of Lewis acid sites: (i) a weaker form associated with segregated alumina domains and containing five-coordinated Al that make up the interface between such domains and the ASA phase and (ii) a stronger form which are undercoordinated Al sites grafted to the silica surface.

The acid catalytic activity in bifunctional *n*-heptane hydroconversion correlates with the density of strong Brønsted acid sites rather than to that of the weak Brønsted acid sites. The influence of the support electronegativity on the neopentane hydrogenolysis activity of supported Pt catalysts is considerably larger than that of the support Brønsted acidity. It is argued that five-coordinated sites of ASA and alumina provide anchoring points for the Pt; their density is much higher in ASA than in γ-alumina.

4.1 Introduction

Amorphous silica-alumina (ASA) is of considerable practical importance in industrial catalysis. They are used as solid acids or serve as supports for finely dispersed metal sulfides or metals [1-3]. ASAs are often present in modern composite hydrocracking catalysts to produce middle distillates from heavy oil fractions [2]. ASAs are much weaker acid catalysts than zeolites. Zeolites consist of crystalline frameworks made up of SiO_4 tetrahedra. The negative charge due to replacement of Si^{4+} by Al^{3+}, when compensated by a proton, gives rise to a Brønsted acid site (BAS). In contrast, ASAs lack an atomically ordered network and are X-ray amorphous. It is usually assumed that ASAs contain sites that are similar to the Brønsted acid sites in zeolites but, somehow, of lower strength. Hydrocarbon cracking experiments of Haag et al. [4] suggested that the low acidity of ASAs might be the consequence of a very low concentration of sites of similar acidity as the bridging hydroxyl groups in zeolites. Thus far, this issue has not been settled yet despite relevant contributions in literature [5-9].

Part of the complexity in studying acidity in ASAs relates to the strong surface heterogeneity. A reasonable surface model of ASAs [10] contains at least four different types of aluminium: Al substitutions in the silica network and, at the surface, isolated tetrahedral and octahedral Al as well as more aggregated forms of Al. The aggregation of aluminium may be that extensive that the presence of a separate alumina phase should be considered. Five-coordinated Al has been suggested to make up the interface between these domains and the mixed silica-alumina phase [10-12]. However, the main problem is that the acid sites in ASAs have eluded direct spectroscopic observation. Recently, IR spectroscopy after selective H/D exchange of the most acidic protons has provided quite strong evidence that ASAs contain BAS very comparable in acidity to the bridging hydroxyl groups in zeolites [13]. The concentration of BAS of zeolites, clays and ASAs of varying composition determined by this method correlates well with the acid catalytic activity of these aluminosilicates. As characterization of the surface acidity of ASAs has already been extensively addressed before, it is useful to compare this new method to some of the more established methods.

The standard method to probe acidity in aluminosilicates has been IR spectroscopy of adsorbed pyridine. Pioneering works [14, 15] have shown the versatility of this method to simultaneously probe Lewis and Brønsted acid sites. The use of CO as a weak base to probe strong acidity in zeolites by IR spectroscopy is well established [16]. Recently, this method has been employed to study the Brønsted acidity in ASAs [7, 17]. The presence of BAS of modest acidity is apparent from the work of Cairon et al. [17]. Comparison of the red shift of the OH stretch upon complexation with CO in ASAs to the shift observed in zeolites has been used as a criterion to judge the acid strength. Thus, Crépeau et al. [7] have found indications that ASAs contain sites similar in acidity to zeolites, yet quantification has proven to be difficult.

Other techniques involve temperature desorption of bases [18] such as ammonia. In the version of decomposition of alkylamines, this technique has been developed with success to

zeolites by Gorte and co-workers [19-21] to obtain accurate quantitative data about the BAS density. Decomposition of adsorbed alkylamines only occurs at Brønsted sites, not at Lewis sites [18]. Other methods to be investigated here are the exchange of the strong BAS in ASAs with Cs^+ [22] and the $Cu(EDA)_2^{2+}$ (EDA = ethylenediamine) complex [23] and ^1H MAS NMR [24]. The present set of ASAs was already characterized in an acid catalytic test, *viz.*, the hydroisomerization of *n*-heptane [10]. The catalytic characterization of acidity is extended here by measuring the inhibition by lutidine of the activity of some ASAs in the liquid phase isomerization of *m*-xylene.

By investigating how results for various methods compare with respect to the acid strength and their quantification, two questions are addressed, that is (i) is there a well-defined set of strong acid sites in ASAs and (ii) can we learn anything specific about the surface heterogeneity of ASAs. The results of various characterization methods will be compared to the results of FTIR spectroscopy of H/D exchanged ASAs of which the surface composition is known in detail [10] as well as, where necessary, to zeolites and clays. An attempt will be made to formulate a model for the surface acidity of ASAs. Finally, we will present results of neopentane hydrogenolysis that show that the rate of C-C bond hydrogenolysis of Pt nanoparticles strongly depends on the acidic nature of the support.

4.2 Experimental section

4.2.1 Infrared spectroscopy of adsorbed CO

Infrared spectra (1200-4000 cm^{-1}) were recorded in transmission mode in a Bruker IFS-113v FTIR spectrometer equipped with a DTGS detector. Typically, an amount of catalyst was pressed into a self-supporting wafer (wafer thickness about 9 mg/cm^2). The catalyst wafer was placed in a controlled atmosphere transmission cell equipped with CaF_2 windows. Prior to CO adsorption, the sample was heated to 823 K at a rate of 5 K/min in flowing oxygen. The sample was then kept at this temperature for 2 h and evacuated before cooling to room temperature. At room temperature, the pressure in the cell was below 2×10^{-6} mbar. Special measures were taken to remove residual water from the cell by heating its stainless steel body during calcination of the sample. The sample was then cooled by flowing liquid nitrogen through a capillary spiralled around the catalyst wafer. The final temperature was around 80 K. At this stage, an initial spectrum was recorded. Carbon monoxide (Praxair, 99.999 %) was dosed via a sample loop connected to a six-way valve. In this manner, accurate doses of 0.04 μmol CO were administered to the cell. Dosing was carried out by a computer-controlled sequence in which a spectrum was recorded 30 s after each dose. Each spectrum was recorded by accumulating 20 scans at a resolution of 4 cm^{-1}. Difference spectra were obtained by subtracting the initial spectrum of the dehydrated catalyst from the spectra obtained at increasing CO coverage.

4.2.2 Infrared spectroscopy of adsorbed pyridine

A Perkin Elmer 2000 spectrometer operating at a 4 cm^{-1} resolution was used to obtain infrared spectra of adsorbed pyridine. Prior to recording spectra, the sample was evacuated in vacuum (pressure lower than 10^{-6} mbar) at 673 K for 1 h. A background spectrum was recorded at 423 K. The sample was then exposed at 423 K to 10^{-2} mbar pyridine for 30 min. After removing the excess of adsorbate by outgassing at 423 K for 1 h, a first spectrum was recorded. Subsequently, the sample was heated to 673 K, kept at this temperature for 1 h and cooled to 423 K. Then, a second spectrum was recorded. A comparison of the spectra before and after thermal treatment gave the amount of strongly adsorbed pyridine.

4.2.3 Temperature-programmed decomposition of isopropylamine

Temperature-programmed decomposition of isopropylamine (IPAm) was carried out in a plug-flow quartz reactor. In a typical experiment, an amount (1 g for ASA or 100 mg for zeolite) of catalyst in a sieve fraction between 125 and 250 μm was loaded into a quartz reactor tube and kept between two layers of quartz wool. Prior to adsorption of IPAm, the sample was calcined in a mixture of 20 vol% O_2 in He at a total flow rate of 100 ml/min, whilst heating from room temperature to 823 K at a rate of 5 K/min (2 K/min for zeolites) followed by an isothermal period of 1 h. The temperature was then lowered to 373 K at a rate of 15 K/min. At 373 K the sample was exposed to IPAm by passing 100 ml/min He through a saturator containing isopropylamine (Merck, purity 99 %). The saturator was kept at 273 K by a thermostated bath. The vapour pressure of IPAm under these conditions is 26 kPa. The flow of IPAm in He was led over the catalyst for 10 min. Subsequently, physisorbed IPAm was removed by purging with He at 100 ml/min for 16 h. The removal of IPAm was monitored by online mass spectrometry (quadrupole mass spectrometer, Balzers TPG-300). Temperature programmed decomposition of IPAm was started by heating the sample at a rate of 5 K/min to 773 K. The number of acidic sites was calculated from the number of propene molecules from IPAm decomposition. The total amount of propene was corrected for the fragmentation of IPAm present due to molecular desorption during the mass spectrometry analysis. The weight-based acid site densities were calculated taking into account physisorbed water in the samples.

4.2.4 Ion exchange with Cs^+

The exchange of strong BAS with the soft Cs^+ cation was investigated. To this end, solutions of varying CsCl (Merck, purity 99.9 %) concentration were prepared from an original mother solution containing 1.6 mg Cs/g. After the initial pH of the solution was recorded, 1 g of ASA previously dried at 573 K was suspended in the solution. After 5 min, the pH was measured again. Subsequently, the flasks were gently shaken for 1 h. The pH was once again recorded at the end of the experiment. The solutions were then recovered by filtration using a filter (Millipore 0.75 μm) .The initial and final Cs^+ concentration were

determined by inductively coupled plasma measurements. Control experiments were also carried out on pure γ-alumina (Ketjen CK-300) and pure silica (Sipernat-50).

4.2.4 Ion exchange with Cs^+

The exchange of strong BAS with the soft Cs^+ cation was investigated. To this end, solutions of varying CsCl (Merck, purity 99.9 %) concentration were prepared from an original mother solution containing 1.6 mg Cs/g. After the initial pH of the solution was recorded, 1 g of ASA previously dried at 573 K was suspended in the solution. After 5 min, the pH was measured again. Subsequently, the flasks were gently shaken for 1 h. The pH was once again recorded at the end of the experiment. The solutions were then recovered by filtration using a filter (Millipore 0.75 μm) .The initial and final Cs^+ concentration were determined by inductively coupled plasma measurements. Control experiments were also carried out on pure γ-alumina (Ketjen CK-300) and pure silica (Sipernat-50).

4.2.5 Ion exchange with Cu-EDA

The exchange of hydroxyl groups of strong BAS was investigated by exchange with the $Cu(EDA)_2^{2+}$ complex. Initially, 1 M solutions of $CuCl_2.2H_20$ (Merck, purity 98 %) and ethylene diamine (EDA) (Merck) were prepared. The two solutions were then mixed in 1:2 ratio by volume ($CuCl_2$:EDA) and, from the resulting solution, a 0.03 M solution was prepared by dilution. 0.25 g of ASA previously dried at 573 K was then suspended in the solution. The flask was shaken for 30 min and the solution was recovered by centrifugation. The initial and final Cu^{2+} concentration were determined by inductively coupled plasma measurements.

4.2.6 ^1H MAS NMR

Prior to ^1H MAS NMR measurement, a known amount of ASA was introduced in a special glass tube (Wilmad Glass Company) suitable for NMR measurements and dehydrated according to a literature procedure [24]. After connecting the tube to a vacuum line, the sample was heated at a final pressure lower than 10^{-5} mbar from room temperature to 723 K at a rate of 10 K/min. The sample was kept at 723 K for 4 h. After cooling the sample to room temperature, the glass ampoule was sealed and placed in a 4 mm MAS rotor. ^1H MAS NMR measurements were performed at room temperature using a Bruker AVANCE 500 MHz spectrometer. The MAS rate was 7.5 kHz. The inversion recovery pulse sequence was applied with a recycle delay of 80 s. The spectra were carefully deconvoluted. The sample amount for NMR measurements was corrected for the initial water content of the ASA samples as determined by TGA analysis. Water was used as the reference for computing the absolute amount of protons.

4.2.7 Isomerization of *m*-xylene

Isomerization of *m*-xylene was carried out in the liquid phase in a plug-flow reactor. About 1 g of aluminosilicate catalyst with a sieve fraction between 125 and 250 μm was contained between two layers of SiC in a stainless steel reactor with an average grain size of 180 μm. The sample was first dehydrated in 100 ml/min He, while heating from room temperature to 823 K followed by an isothermal period of 2 h. Then, the reactor was cooled to the reaction temperature of 573 K. Liquid *m*-xylene was fed to the reactor by a HPLC pump at a flow rate of 50 μl/min. The reaction pressure was increased and kept at 80 bar by a back-pressure regulator. Prior to use, *m*-xylene (Merck, purity 99 %) was percolated through a batch of activated alumina (Merck) to remove possible contaminants. To facilitate accurate gas chromatographic analysis, the effluent stream was diluted with *n*-heptane delivered by a second pump at a flow rate of 0.8 ml/min. This mixture was analyzed by a HP-5890 gas chromatograph equipped with a Stabilwax column (30 m × 0.32 mm id, d_f = 0.5 μm) and a flame ionization detector. Poisoning experiments were carried out by introducing calibrated amounts of 2,6-dimethylpyridine (Alfa Aesar, 99 %) dissolved in *m*-xylene via a sample loop into the feed mixture. The change in conversion was then monitored online until a stable value was attained. In a typical experiment, the base was introduced three times in this manner.

4.2.8 Hydrogenolysis of neopentane

The hydrogenolysis of neopentane was carried out in a gas-phase parallel microflowreactor system. About 100 mg of Pt-loaded catalyst was held between two quartz wool plugs in a quartz tube with an internal diameter of 4 mm. Prior to reaction, the catalysts were reduced in a mixture of 20 vol% H_2 in He at a flow rate of 50 ml/min whilst ramping the temperature from ambient to 573 K at a rate of 10 K/min. The catalysts were then exposed to a mixture of 1 vol% neopentane in H_2 at a flow rate of 50 ml/min. The reactor effluent was analyzed by online gas chromatography (Interscience CompactGC, Plot KCl/Al_2O_3, 10 m × 0.32 mm, d_f = 1 μm, TCD). The main reaction products were iso-butane and methane with very small amounts of other products such as olefins. The selectivity to iso-butane and methane was over 95 %. Neo-pentane conversions below 8 % allowed to calculate the reaction rate for neopentane hydrogenolysis. In a control experiment, no neo-pentane conversion was found for ASA(5/95, 1073). Pt loading of the dried supports was done by pore volume impregnation with a solution of $Pt(NH_3)_4(NO_3)_2$ of such concentration that a final metal loading of 0.8 wt% was achieved. The supports form a subset of the ASAs described earlier [10,13], having equal Brønsted acidity. For comparison, SiO_2 (Degussa, 190 m^2/g, Al content below 0.01 wt%), SiO_2:Al (Shell, 196 m^2/g, Al content 0.5 wt%), γ-Al_2O_3 (Ketjen, 267 m^2/g) and an industrial ASA (Shell, 55 wt% Al_2O_3, 375 m^2/g) were included in these catalytic tests. The Pt metal particle size of the reduced catalysts was measured by H_2 chemisorption via the double isotherm method on a Micromeritics ASAP2020.

4.3 Results and discussion

4.3.1 Infrared spectroscopy of adsorbed CO

Fig. 4.1 shows the carbonyl and hydroxyl stretch regions of the IR spectra of USY(8.1,II). With increasing CO coverage a band at 2180 cm^{-1} becomes more intense and another band appears at 2170 cm^{-1}. These bands further grow into the spectra. At higher coverage, weak shoulders at 2158 cm^{-1} and 2190 cm^{-1} become apparent. The final spectrum after saturation of the band at 2180 cm^{-1} also shows bands around 2141 and 2130 cm^{-1}. The band at 2180 cm^{-1} is due to CO coordinating to the strong acidic hydroxyl groups of the zeolite [16, 17]. The band around 2170 cm^{-1} is due to CO coordinating to hydroxyl groups of weaker acidity such as those in extraframework silica-alumina debris. The band just below 2200 cm^{-1} is due to weak Lewis acid sites (LAS) [16, 17].

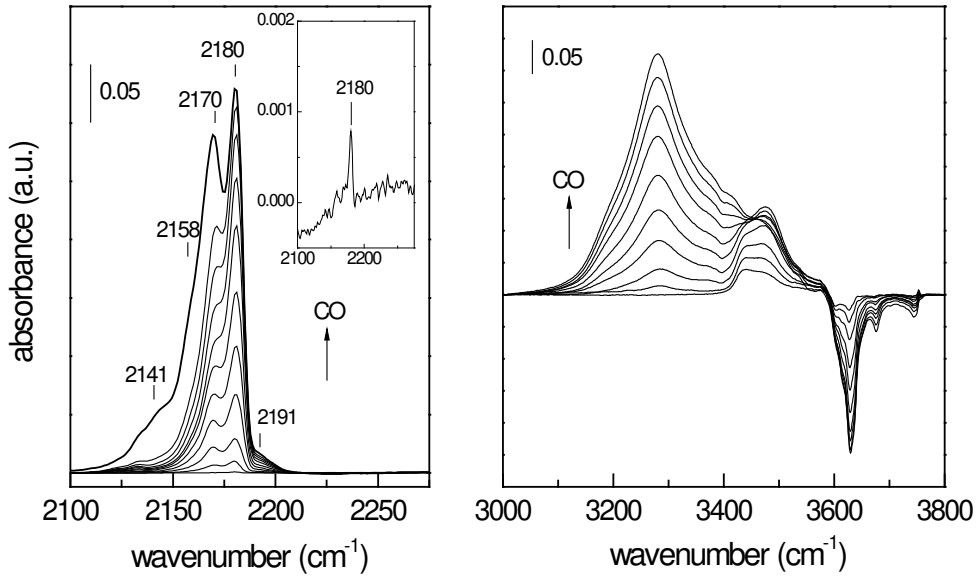

Figure 4.1: Carbonyl (left) and hydroxyl (right) stretch regions of the infrared spectra of well-dehydrated USY(8.1,II) at 80 K as a function of the CO coverage. The inset shows the spectrum after the first dose of CO.

Bands at 2158, 2141 and 2130 cm^{-1} relate, respectively, to CO coordinating to silanols, physisorbed CO and CO coordinating to the surface via its oxygen atom. The spectra in the hydroxyl region initially show a negative feature at relatively low CO coverage due to perturbation of sites of enhanced acidity in the supercages at 3604 cm^{-1}. With increasing CO coverage, this feature becomes a shoulder of the much more pronounced negative band at 3630 cm^{-1} due to perturbation of the high-frequency (HF) OH groups in the supercages. The calculated shifts of the OH stretch upon interaction with CO ($\Delta\nu_{OH}$) are 360 cm^{-1} and 416 cm^{-1} for the regular and enhanced sites, respectively. The higher shift of the enhanced OH groups agrees with their higher acidity due to the presence of extraframework Al [17, 25, 26]. The low-frequency (LF) OH groups at 3566 cm^{-1} are not perturbed by CO, because CO cannot access the smaller cages. Further OH groups at 3677 cm^{-1} and 3745 cm^{-1} interact with carbon monoxide at higher coverage. Cairon et al. [17] have related the occurrence of perturbed OH

bands in the region of 3440-3475 cm^{-1} to acidic sites of an extraframework silica-alumina phase. These bands are apparent in Fig. 4.1. The frequency shift of around 190 cm^{-1} is

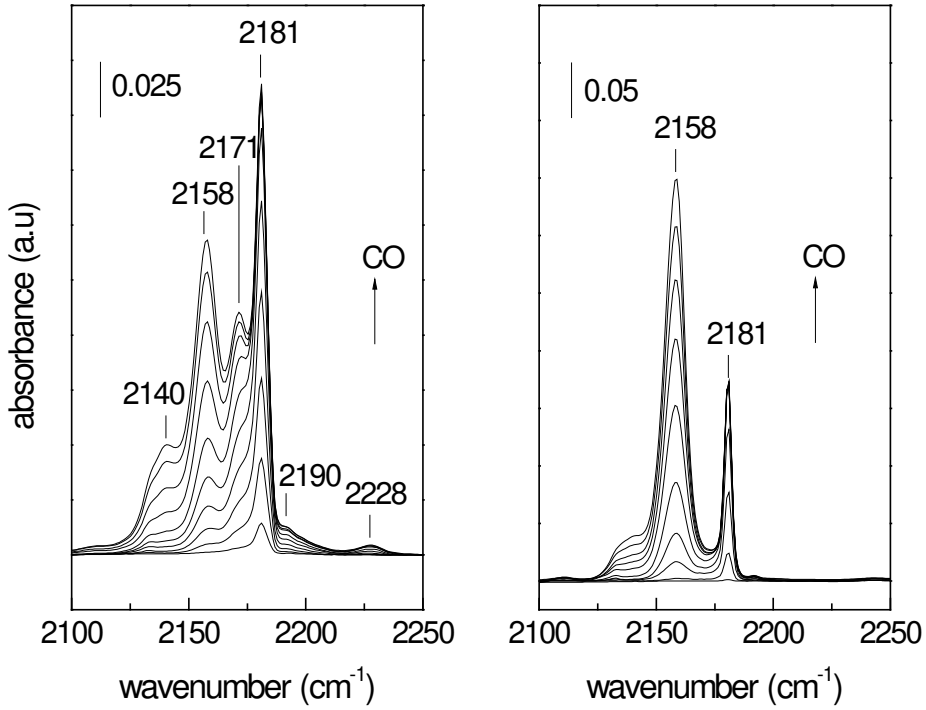

indicative of the intermediate acidity of these groups. Therefore, the band in the CO region at 2171 cm^{-1} should be linked to this weaker type of BAS. The perturbed silanol groups which should appear at 3660 cm^{-1} cannot be clearly discerned here because of their low concentration.

Figure 4.2: Carbonyl stretching region of the infrared spectra of well-dehydrated VUSY(33) (left) and XVUSY(85) (right) at 80 K as a function of the CO coverage.

Fig. 4.2 shows the IR spectra of the CO region of VUSY(33) and XVUSY(85). The evolution of these spectra is qualitatively similar to those of USY(8.1,II). The most striking differences are the presence of more silanol groups with increasing silica-to-alumina (SAR) ratio and the lower intensity of the band at 2171 cm^{-1}. The latter band is nearly absent in the spectra of XVUSY(85). Deeper ultra-stabilization has resulted in more defects and, hence, in more silanol groups. The siliceous zeolite contains only a very small amount of an extraframework silica-alumina phase as a result of acid leaching steps. This is evident from the absence of the band at 2171 cm^{-1}. The frequency shift $\Delta\nu_{OH}$ for (HF) OH of around 360 cm^{-1} for these two zeolites corresponds to the value for USY(8.1). A similar experiment for HY(5) gave a CO stretch at 2178 cm^{-1} and a value of 297 cm^{-1} for $\Delta\nu_{OH}$. The shift of the CO band and the significantly lower shift of the OH stretch upon complexation by CO signify the somewhat lower acidity of the bridging hydroxyl groups of non-dealuminated Y zeolite. Beside these bands, the interaction of CO with LAS is observed for VUSY(33) and XVUSY(85). For VUSY(33), bands around 2190 and 2228 cm^{-1} develop. The latter feature is absent in XVUSY(85).

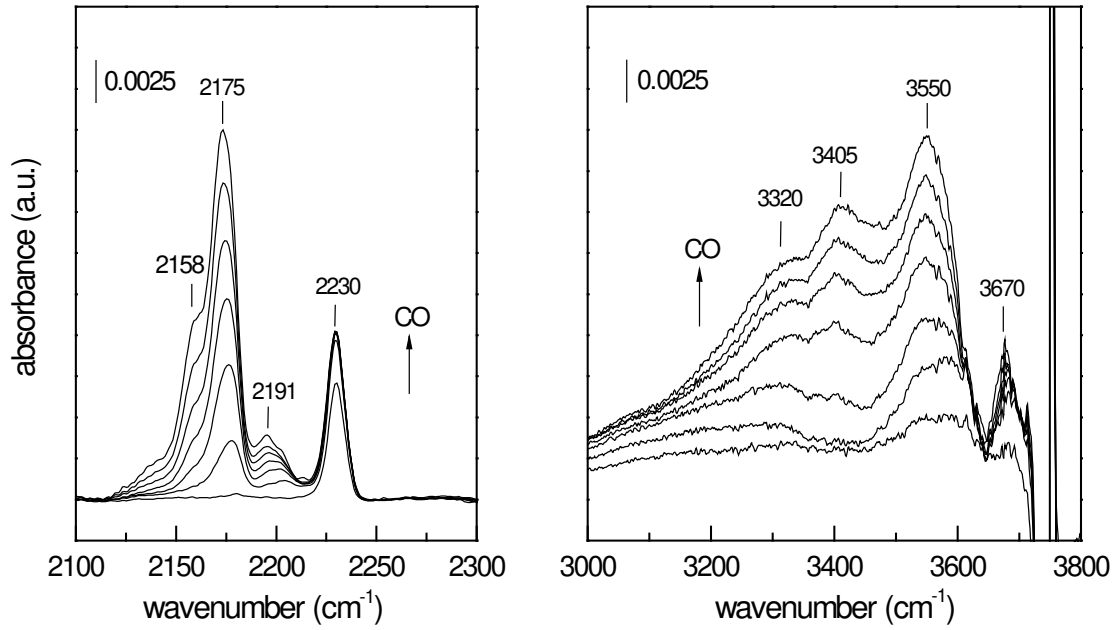

Figure 4.3: Carbonyl (left) and hydroxyl (right) stretch regions of the infrared spectra of well-dehydrated ASA(5/95, 1073) at 80 K as a function of the CO coverage.

Fig. 4.3 shows IR spectra of ASA(5/95, 1073). After the first CO dose, a band at 2230 cm^{-1} is visible which corresponds to CO coordinating to strong LAS and a very small feature around 2177 cm^{-1}. In the difference spectrum of the hydroxyl region a very weak broad feature around 3320 cm^{-1} becomes visible along with a significant negative-positive feature around 3750 cm^{-1}. With increasing CO coverage, the small feature at 2177 cm^{-1} becomes more notable and the band shifts to 2175 cm^{-1}. Additional bands at 2158 cm^{-1} and 2190 cm^{-1} become apparent. The bands around 2190 cm^{-1} and 2230 cm^{-1} are assigned to coordinatively unsaturated Al^{3+} sites, the former being of lower strength than the latter [25, 27, 28]. The bands at 2158 cm^{-1} and 2177 cm^{-1} are due to CO perturbation with silanol groups and more acidic hydroxyl groups, respectively. Examination of the perturbed hydroxyl region shows the development of broad bands at 3320, 3405, 3550 and 3670 cm^{-1}. The latter three bands were earlier noted by Cairon et al. [17] and Crépeau et al. [7]. The band at 3670 cm^{-1} is assigned to silanol groups perturbed by CO. The bands at 3405 and 3550 cm^{-1} are indicative of the presence of OH groups with a higher acidity than silanols. From the presence of a perturbed OH band around 3382 cm^{-1} linked to a CO stretch at 2178 cm^{-1}, Crépeau et al. [7] inferred that ASAs contain strong BAS. The perturbed OH band appears here around 3405 cm^{-1}. Strong BAS are described as paired (SiOH, Al) sites [7], based on earlier suggestions [6, 30, 31]. The strong negative band at 3750 cm^{-1} upon perturbation by CO is attributed to the closure of the paired site as shown in Scheme 4.1. Similar bands are observed in the present study. A problem with this interpretation is the magnitude of the negative-positive feature in relation to the very low concentration of BAS in ASAs. The relatively weak

perturbed OH band does not agree with the large negative band around 3750 cm^{-1}. Moreover, quantification of the negative-positive adsorbance shows that the total intensity in the region does not change in this region, suggesting that, instead, CO adsorption results in a small shift of the frequency of the silanol groups. An alternative explanation is as follows. Silanol groups interact with the coordinatively unsaturated Al^{3+} LAS on the surface. This interaction results in a weaker OH bond of the silanol groups. Such a weakening is evident from the gradual shift of the silanol stretch with increasing aluminium content of the ASA. The stretching frequency is at 3747 cm^{-1} for SiO_2, at 3745 cm^{-1} for ASA(5/95, 1073) and at 3737 cm^{-1} for ASA(20/80, 1073). CO interacts quite strongly with the LAS [30], resulting in the formation of a CO stretch at 2230 cm^{-1}. The interaction of CO with Lewis acid sites is stronger than with hydroxyl groups. This should result in a shift of perturbed silanol stretch to higher frequencies, because they do not interact with the LAS anymore. This line of reasoning explains the strong negative-positive feature in the difference spectra. In support of this interpretation is that the negative-positive feature appears concomitant with the band at 2230 cm^{-1}. A further suggestion is that, in certain geometries, the CO molecule which coordinates to the Lewis site can interact with the silanol group leading to a negative shift of the silanol frequency. This may explain the broad band just below 3600 cm^{-1}. This proposal suggests the reverse of closure of the bridge between silanol groups and LAS and is also illustrated in Scheme 4.1.

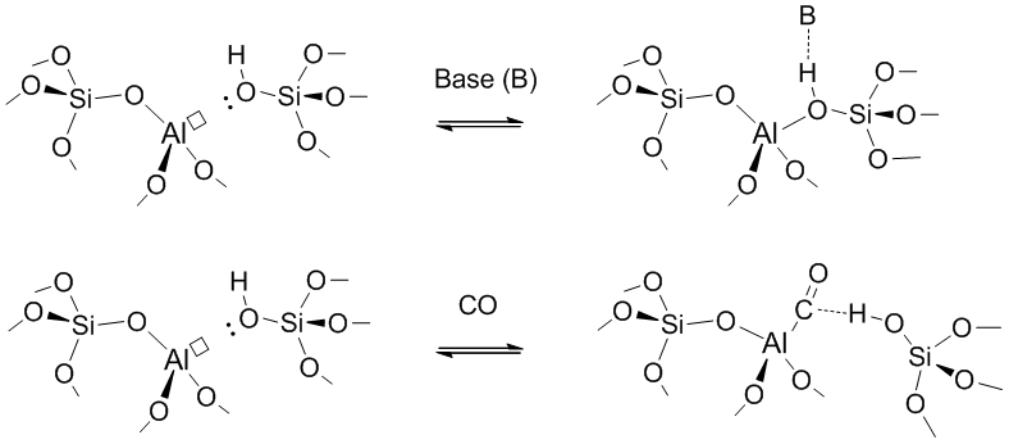

Scheme 4.1: (top) Formation of a bridging hydroxyl group in the presence of a base as originally proposed by Trombetta et al. [5] and (bottom) new proposed effect of CO on the weak interaction of silanol groups with Lewis acid Al^{3+} sites.

FTIR spectroscopy of partially H/D exchanged ASAs [13] has provided strong indications that ASAs should contain distinct OH groups around 3635 cm^{-1} and perhaps 3564 cm^{-1} in such low concentrations that they are not observed in the hydroxyl part of IR spectra of dehydrated ASAs. Only after their selective deuteration, they are visible as the corresponding OD bands. The IR spectra after CO adsorption contain a rather weak feature around 3320 cm^{-1}, which is perhaps already present in the spectra after the second and third dose at lower wavenumbers. We propose that this weak band is linked to the CO stretch at 2177 cm^{-1}. The negative feature arising from perturbation of the suspected band at 3635 cm^{-1} cannot be

discerned due to the presence of other perturbed bands in this region, although the spectra suggest that some sites become perturbed with increasing CO coverage in this part of the spectrum. The frequency shift of the OH band is 315 cm^{-1} under the assumption that the unperturbed bridging OH vibrates at 3635 cm^{-1}. The fact that the feature is quite broad suggests that a distribution of sites of varying strengths exists. The shift of 315 cm^{-1} places the acidity of the protons in ASA(5/95, 1073) between that of strongly acidic dealuminated Y zeolites (340-360 cm^{-1}) and its less acidic non-dealuminated form (297 cm^{-1}). This result is in good agreement with the zeolitic strength of the BAS in ASAs derived by FTIR spectroscopy of H/D exchanged ASAs [13]. With increasing CO coverage, the band at 2177 cm^{-1} shifts to 2175 cm^{-1} which is explained by the presence of sites of weaker acidity. With increasing aluminium content of the ASAs, the trends in the IR spectra are very similar, except that the feature around 3320 cm^{-1} cannot be discerned anymore. This seems to be due to the increasing contribution of the broad band around 3425 cm^{-1} with increasing Al content of the ASA.

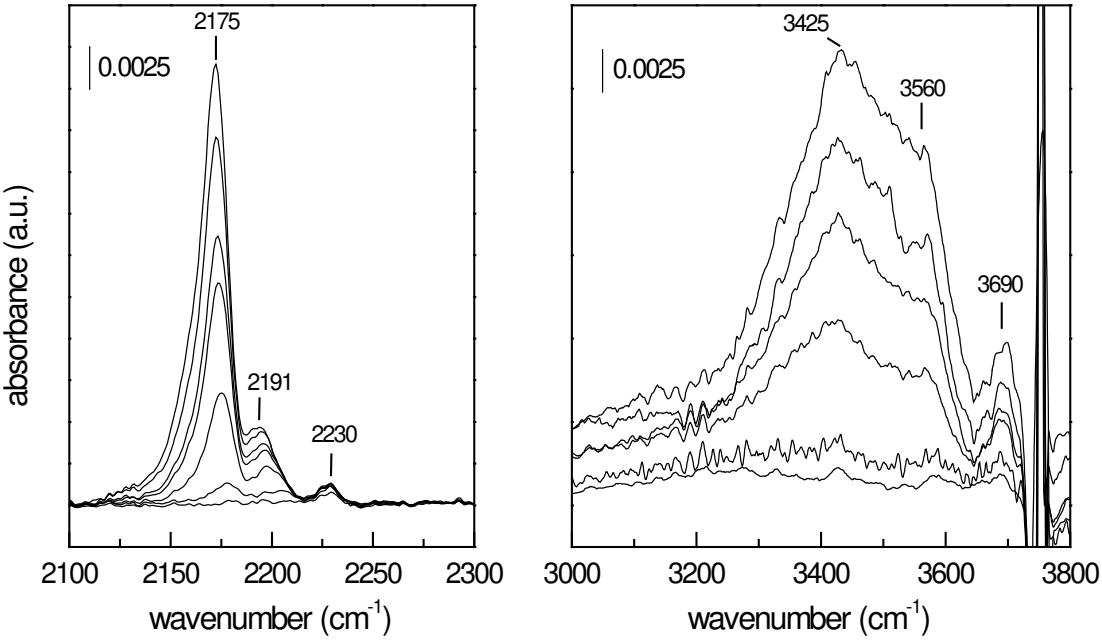

Figure 4.4: Carbonyl (left) and hydroxyl (right) stretch regions of the infrared spectra of well-dehydrated ASA(20/80, 1073) at 80 K as a function of the CO coverage.

The spectra for ASA(20/80, 1073) are given in Fig. 4.4. Similar to ASA(5/95, 1073), the first CO dose results in the appearance of a band around 2230 cm^{-1} and a negative-positive feature around 3750 cm^{-1}. Increasing CO coverage results in the development of a band at 2177 cm^{-1} and a shift of this band to lower wavenumbers occurs. Broad perturbed hydroxyl bands are observed at 3430 and 3560 cm^{-1}, respectively. The perturbed band at 3660 cm^{-1} is more difficult to discern in the spectra of the ASA(20/80,1073). This should be due to the further decrease of the silanol groups as a result of the much higher surface aluminium loading [10]. Table 4.1 summarizes the positions of the bands belonging to strong BAS in

aluminosilicates in the CO and perturbed OH region and the shift upon CO complexation for a large set of zeolites, clays and ASAs. The position of the CO band for the ASAs is quite similar to the position for Y zeolites and clays. The shift of 315 cm^{-1} is also quite close to values found for zeolites and the clays.

Table 4.1: Infrared band positions of OH...CO complex in the carbonyl and hydroxyl regions after adsorption of small doses of carbon monoxide at 90 K. The shifts in the hydroxyl region ($\Delta\nu_{OH}$) are relative to the positions of the (HF)OH and (HF')OH bands for the zeolites.

Sample	ν_{CO} (cm^{-1})	$\nu_{perturbed\ OH}$ (cm^{-1})	$\Delta\nu_{OH}$ (cm^{-1})
HY(5)	2178	3346	297
USY(9.6, F)	2181	3285	345
USY(8.1,II)	2182	3270 (3190[a])	360 (416[a])
VUSY(26.5)	2181	3276 (3190[a])	354 (416[a])
XVUSY(70)	2180	3278	356
MgSAP(13)	2180	3260	338
MgSAP(33)	2180	3268	337
ASA(5/95,1073)	2177	3320	315
ASA(10/90,1073)	2178	n.o.[c]	n.o.
ASA(15/85,1073)	2177	n.o.	n.o.
ASA(20/80,1073)	2177	n.o.	n.o.
ASA(5/95,773)	2175	n.o.	n.o.
ASA(5/95,3,1073)	2177	n.o.	n.o.
ASA(5/95,co-gel)	2177	n.o.	n.o.

[a] enhanced hydroxyl groups (HF')OH in supercages; [b] shift relative to ν_{OH} = 3634 cm^{-1} based on H/D exchange FTIR [13]; [c] not observed.

The CO stretch region of the various spectra was deconvoluted in order to determine strong BAS densities. The molar extinction coefficient of adsorbed CO was determined following the procedure of Cairon et al. [17]. The extinction coefficient is assumed to be constant over the narrow frequency range of 2158 to 2182 cm^{-1}. As the component at 2158 cm^{-1} stems from a complex between silanol groups and CO, its intensity is directly related to the decrease in intensity of the corresponding silanol band in the hydroxyl region via

$$\Delta I_{OH} = \Delta I_{CO} \times \varepsilon_{OH}/\varepsilon_{CO} \qquad (4.1),$$

in which ΔI_{OH} and ΔI_{CO} are the integrated intensities of the silanol and carbonyl bands, respectively, and ε_{OH} the molar extinction coefficient of the silanol band. The value of the molar extinction coefficient of silanol groups is 3 cm/μmol [17]. By plotting the change in the hydroxyl band intensity against the change in the carbonyl band intensity, ε_{CO} is determined. The extinction coefficient of 2.6 cm/μmol compares well to the value of 2.7 cm/μmol reported by Cairon et al. [17]. With this value, the concentrations of the various hydroxyl groups in the aluminosilicates were determined. Spectra were deconvoluted starting from low CO coverage so as to determine the coverage at which band that initially appears in

the region 2177-2182 cm^{-1} was saturated. This deconvolution procedure was straightforward for the faujasite zeolites and clays. From the intensity of the relevant band, the number of BAS was computed by employing Beer-Lambert's law

$$N = \frac{A}{\varepsilon.\rho} \qquad (4.2),$$

in which N is the density of the vibrating species (mmol/g), A the intensity of the band (cm^{-1}), ε the molar extinction coefficient of CO (cm/μmol) and ρ the wafer thickness (mg/cm^2)

.

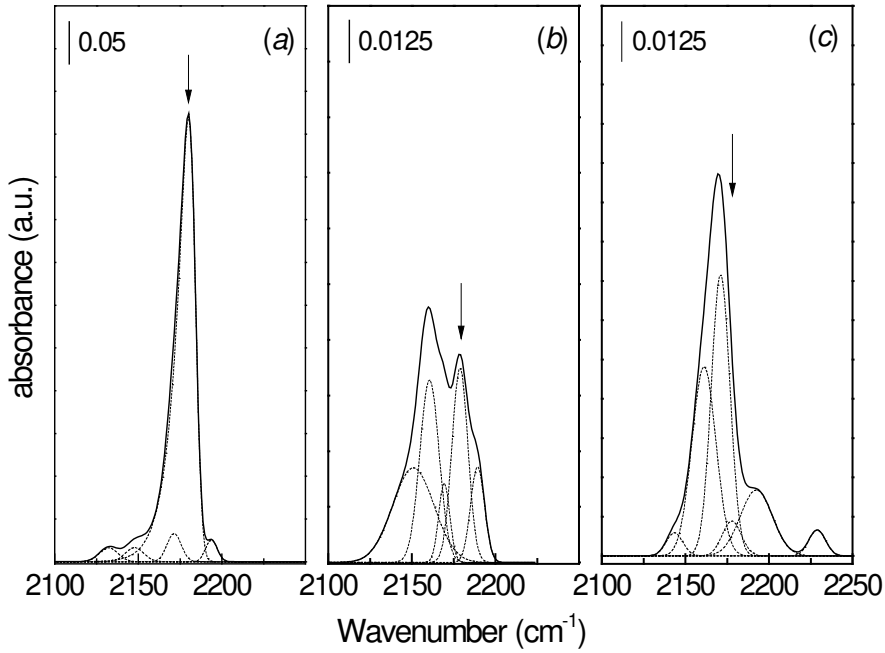

Figure 4.5: Deconvolution of the carbonyl stretch region of the IR spectra of CO adsorbed to USY(8.1,II) (a), MgSAP(33) (b) and ASA(15/85,1073) (c) after saturation of the band due to strong BAS (indicated by arrow).

Quantification of BAS in the ASAs was carried out in a similar manner. Deconvolution was not straightforward, because the band initially present at 2177 cm^{-1} cannot be distinguished as a separate band at higher CO coverage due to the much stronger band around 2175 cm^{-1}. This feature can be fitted by one contribution with a Gaussian shape taking into account a small shift in its frequency with increasing CO coverage. However, assuming that a few strong Brønsted acid sites represent the band at 2177 cm^{-1} next to a much larger number of sites of modest acidity (2175 cm^{-1}), an alternative approach consists of deconvoluting the spectra by two bands. The procedure was to first use a single band to describe the initial spectrum after the first CO dose, fix the fit parameters except the area and then deconvolute subsequent spectra by adding a band at lower wavenumbers and other necessary bands. Fig.

4.5 shows typical fits for a zeolite, a clay and an ASA. The other bands are due to Lewis acid sites (ν_{CO} > 2180 cm^{-1}) and hydroxyl groups of weaker acidity (ν_{CO} < 2170 cm^{-1}).

Table 4.2: Concentration of strong Brønsted acid sites ($N_{strong\ BAS,\ CO\ IR}$) for aluminosilicates based on saturation of infrared carbonyl band around 2177-2182 cm^{-1}. Values from H/D exchange FTIR ($N_{strong\ BAS,\ H/D}$) have been included for comparison. For the zeolites, H/D exchange values correspond to number of sites located in supercages.

Sample	$N_{strong\ BAS,\ CO\ IR}$ (μmol/g)	$N_{strong\ BAS,\ H/D}$ (μmol/g)
USY(8.1,II)	424	434
VUSY(26.5)	305	338
XVUSY(70)	194	210
MgSAP(13)	12	16
MgSAP(33)	48	28
ASA(5/95,1073)	3.8	3.6
ASA(10/90,1073)	7.6	4.8
ASA(15/85,1073)	9.1	8.6
ASA(20/80,1073)	10.8	5.2
ASA(5/95,773)	2.8	2.3
ASA(5/95,3,1073)	7.6	5.7
ASA(5/95,co-gel)	8.0	7.5

Table 4.2 lists the concentrations of BAS for a number of aluminosilicates. For the steam calcined Y zeolites, the concentration of BAS probed by CO IR corresponds well to the concentrations of BAS located in the supercages found by H/D exchange FTIR. The values for the clays correspond less well and especially the number for MgSAP(33) is substantially higher than the value determined by H/D exchange FTIR.

The values for the ASAs fall in the same range as the values from H/D exchange FTIR measurements. The data correspond well for ASAs with relatively low aluminium content, but the deviations become larger for the more aluminium-rich compositions. Clearly, the concentration of strong BAS increases with the aluminium content and ASA(20/80,1073) is most acidic according to CO IR. However, ASA(15/85,1073) is the most acidic ASA according to the acid activity and H/D exchange FTIR measurements. The reason for this discrepancy seems to be the difficulty in separating the relative weak feature around 2177 cm^{-1} from the much stronger band at 2175 cm^{-1}. The stronger the band at 2175 cm^{-1}, the larger the fitted component at 2177 cm^{-1}. As the former band increases with the aluminium content, so does the band at 2175 cm^{-1}. Thus, the spectra in the CO stretch region cannot be fitted with such accuracy that the contribution of strongly acidic OH groups can be separated from the weaker ones.

The IR spectra of adsorbed CO give additional insight into the surface composition of the various ASAs. At complete saturation with CO, the intensity of the carbonyl band at 2158 cm^{-1} (not shown) is much higher than the one around 2175 cm^{-1} for ASA(5/95, 1073), while

the reverse is true for ASA(20/80, 1073). Similar trends are found in the hydroxyl region, where the intensity of the perturbed OH band of the less acidic groups around 3450 cm^{-1} increases with the aluminium content of the ASAs. The concentrations of weak BAS (band around 2175 cm^{-1}) and non-acidic silanols (band at 2158 cm^{-1}) were determined from the spectra after complete saturation by CO (Table 4.3). The total concentration of weak BAS increases with the aluminium content of the ASA and is one order of magnitude higher than the concentration of strong BAS. The higher the concentration of weak BAS, the lower the concentration of silanol groups. The concentration of silanol groups in the starting silica aerogel to prepare the HDP ASAs is around 2700 μmol/g. Thus, only a small number of silanol groups remain in the calcined materials. This strong decrease agrees well with the surface model for these ASAs, which involves the grafting of aluminium to the silanol groups [10].

Table 4.3: Concentration of weak Brønsted acid sites ($N_{\text{weak BAS}}$) and silanol groups (N_{silanol}) for various ASAs determined from infrared spectra of adsorbed CO at complete saturation.

Sample	ν_{CO} (cm^{-1})	$N_{\text{weak BAS}}$ (μmol/g)	N_{silanol} (μmol/g)
ASA(5/95,1073)	2175	75	387
ASA(10/90,1073)	2175	101	345
ASA(15/85,1073)	2175	152	292
ASA(20/80,1073)	2175	160	212
ASA(5/95,773)	2171	63	357
ASA(5/95,3,1073)	2172	64	423
ASA(5/95,co-gel)	2174	65	360

LAS of varying strength are also present in these ASAs. The band at 2191 cm^{-1} is attributed to a σ-bond of CO with tetrahedral Al^{3+} sites in patches of regular low index planes [25]. The band at higher wavelength is assigned to a stronger form of CO adsorption on coordinatively unsaturated Al^{3+} sites at defect sites. Based on the surface model for HDP ASAs [10], the bands at 2191 and 2230 cm^{-1} are tentitatively assigned to Al^{3+} of segregated alumina domains and isolated Al^{3+} grafted to the surface, respectively. Fig. 4.6 shows the intensities of the two bands as a function of the aluminium content. As the extinction coefficient will likely differ because of the substantially different mode of bonding of CO in OH…CO and Al^{3+}…CO complexes, no estimate of the surface density was made. The surface of ASA(5/95,1073) contains mainly LAS of the stronger type. The surface consists mainly of a mixed silica-alumina phase with a high content of Al^{3+} atoms dispersed over the surface. The amount of agglomerated Al is very low. The band at 2230 cm^{-1} does not vary very much with the aluminium content. However, the band at 2191 cm^{-1} becomes much more intense and this is undoubtedly related to the increasing amount of segregated domains of aluminium oxides on the ASA surface.

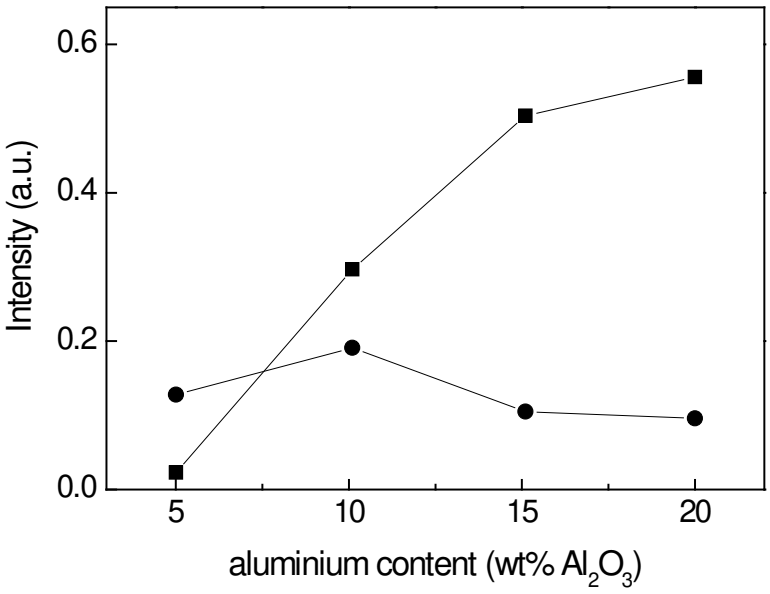

Figure 4.6: Concentrations of weak (■) and strong (●) Lewis acid Al^{3+} sites identified by respective carbonyl stretching bands around 2191 and 2230 cm^{-1} as a function of the aluminium content of ASAs calcined at 1073 K.

To summarize, infrared spectroscopy of adsorbed CO is useful to show the presence of Brønsted and LAS in ASAs. The band at 2177 cm^{-1} appears to be linked to BAS similar in strength to those in zeolites, but accurate quantification is hampered by a band at 2175 cm^{-1} due to sites of modest acidity. Likewise, strong and weaker LAS are present. The concentration of weak BAS and LAS increases with the aluminium content.

4.3.2 Infrared spectroscopy of adsorbed pyridine

Fig. 4.7 shows IR spectra after adsorption of pyridine on two representative ASAs. The bands at 1623, 1492 and 1456 cm^{-1} correspond to pyridine coordinating to LAS. The shoulder at 1638 cm^{-1} and the band at 1544 cm^{-1} are characteristic for pyridinium ions, indicating the chemisorption of pyridine on strong BAS. After evacuation at 673 K for 1 h, the intensity of these bands has decreased. Bands are still observed at 1623, 1492, 1456 cm^{-1} together with a weak band at 1544 cm^{-1}. The shoulder at 1638 cm^{-1} has disappeared. The observation that the band related to the pyridinium ion (PyH^+) remain chemisorbed after evacuation at high temperatures is indicative of the high acidity of the acid sites that can protonate pyridine. Similarly, the presence of strong LAS is evident in these spectra. The intensities of the relevant bands after outgassing at 673 K were used to determine the concentrations of strong BAS and LAS. The differences between these concentrations after outgassing at 423 and 673 K was taken as the concentrations of the weaker form of such sites. The concentrations were calculated by use of the molar extinction coefficients given by Emeis [32]. The results are given in Table 4.4.

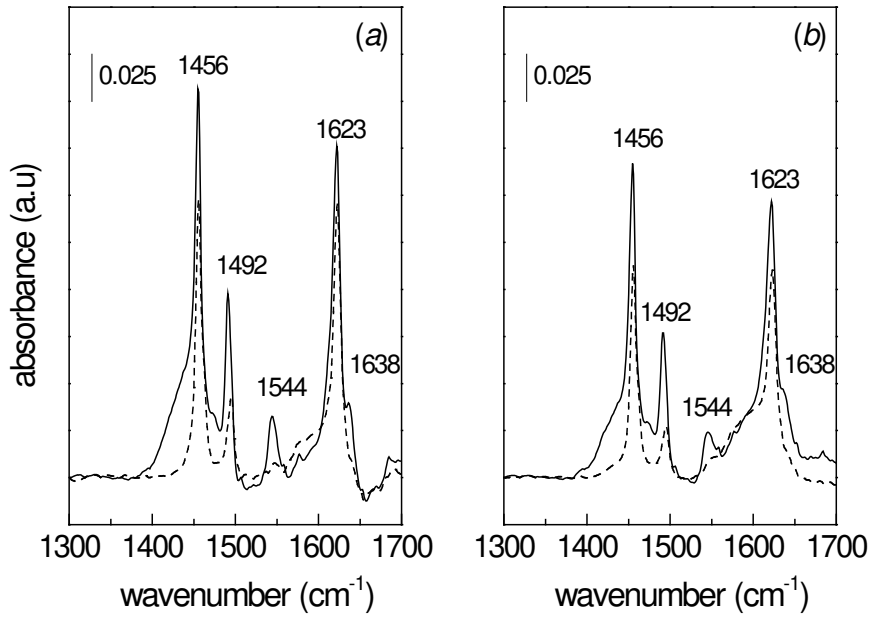

Figure 4.7: Infrared spectra of adsorbed pyridine recorded at 423 K after pyridine absorption at 423 K (0.01 mbar pyridine) followed by evacuation at 423 K for 1 h (full line) and subsequently at 673 K for 1 h (dashed line) for ASA(5/95, 1073) (a) and ASA(20/80, 1073) (b).

The ASAs contain weak BAS and LAS in concentrations of 15-20 μmol/g and 15 μmol/g, respectively. The concentration of strong BAS in the various ASAs is around 2-3 μmol/g. These values are of the same order of magnitude as those found by H/D exchange FTIR [13] and IR spectroscopy of adsorbed CO. However, the values by pyridine IR show little variation for this subset of ASAs compared to the differences probed by the other methods. Pyridine IR spectroscopy did not evidence strong BAS in ASA(5/95,1073) in contrast to results of acid activity, H/D exchange FTIR and CO IR measurements.

Table 4.4: Concentration of Brønsted and Lewis acid sites for various amorphous silica-aluminas and a clay from IR spectra of adsorbed pyridine. Concentration of total Brønsted and Lewis acid sites ($N_{total\ BAS}$ and $N_{total\ LAS}$) determined after evacuation at 423 K. Concentration of strong Brønsted and Lewis acid sites ($N_{strong\ BAS}$ and $N_{strong\ LAS}$) determined after evacuation at 673 K.

Sample	$N_{total\ BAS}$ (μmol/g)	$N_{total\ LAS}$ (μmol/g)	$N_{strong\ BAS}$ (μmol/g)	$N_{strong\ LAS}$ (μmol/g)
ASA(5/95,1073)	16	59	0	46
ASA(5/95,3,1073)	21	75	2.8	62
ASA(5/95,co-gel)	23	77	2.3	64
ASA(20/80,1073)	17	74	2.4	62
MgSAP(13)	57	182	17	101

The other ASAs have lower concentrations of BAS than suggested by H/D exchange FTIR. A too high desorption temperature may explain these lower than expected values. Another aspect worth noting is the quite large spread in reported molar extinction coefficients [27,28]. IR spectroscopy of adsorbed pyridine, however, evidences that these ASAs contain a relatively high concentration of strong LAS which are able to chemisorb pyridine quite strongly up to high temperature. The Lewis acidity is dominated by strong sites, whereas the Brønsted acidity is dominated by a relatively weak form. Infrared spectroscopy of adsorbed pyridine indicates the presence of strong BAS, yet the dataset leaves some doubt whether the values are accurate enough to compare the various ASAs in terms of strong Brønsted acidity.

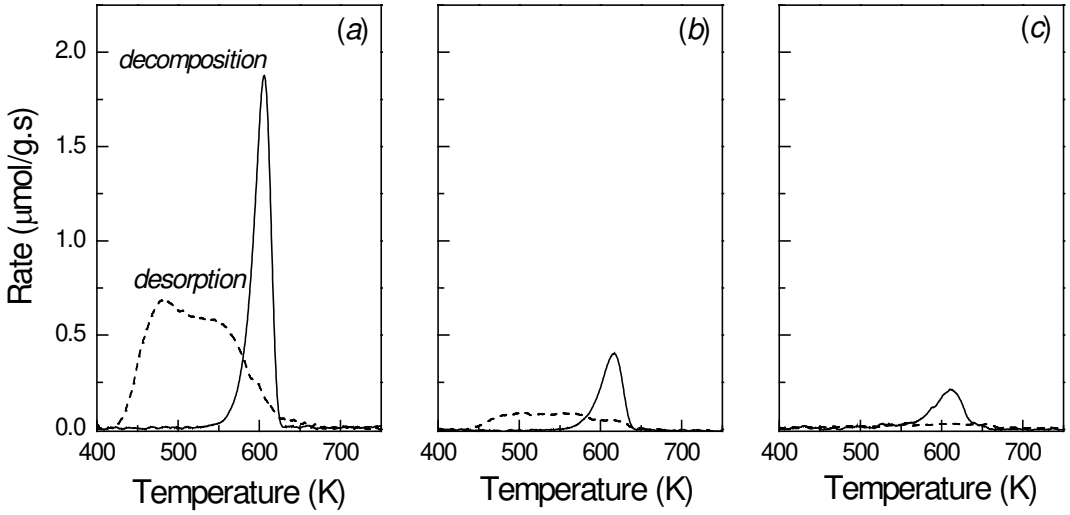

Figure 4.8: Rate of IPAm desorption (dashed line) and decomposition (full line) of USY(8.1, I) (a), VUSY(33) (b) and XVUSY(85) (c) as a function of temperature.

4.3.3 Temperature-programmed decomposition of isopropylamine

Figs. 4.8 and 4.9 shows the evolution of decomposed and desorbed IPAm for three representative Y zeolites, two ASAs and γ-alumina. Decomposition of adsorbed isopropylamine to propene and ammonia proceeds between 550 K and 640 K [19-21]. Quantification of BAS is based on the assumption that each Brønsted acid site forms a complex with one molecule IPAm [19]. This complex decomposes into propene and ammonia via the Hoffman elimination of alkylamines. Figs. 4.8 and 4.9 also show that a substantial amount of IPAm desorbs molecularly for most of the aluminosilicates except for USY(9.6, F). Similarly, no IPAm desorption was found for HZSM-5 (not shown). Longer evacuation at 373 K did not result in noticable changes, suggesting that part of the IPAm is strongly adsorbed on the catalyst. The desorption of IPAm occurs predominantly below the temperature at which decomposition starts. However, a small fraction of IPAm desorption takes place at temperature at which its decomposition can also take place.

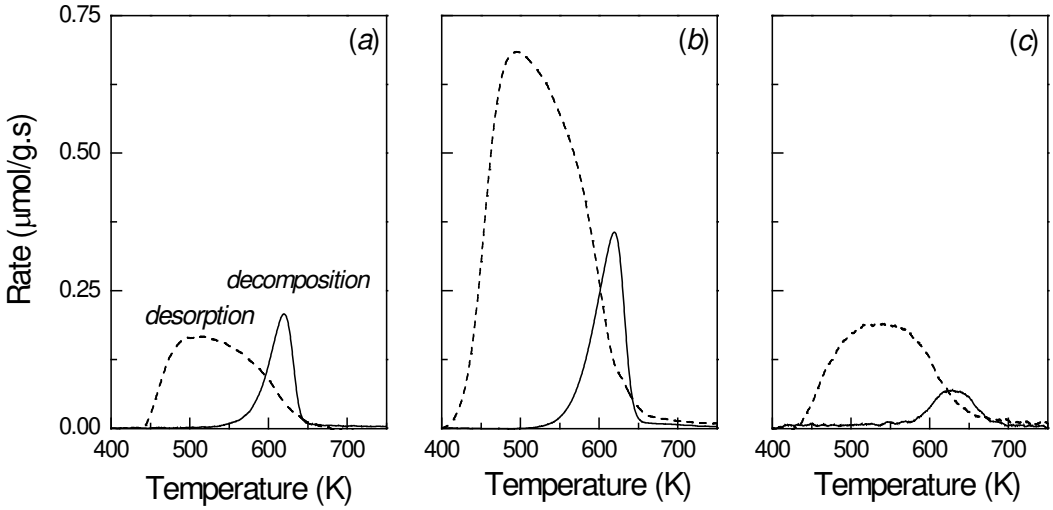

Figure 4.9: Rate of IPAm desorption (dashed line) and decomposition (full line) of ASA(5/95, 1073) (a), ASA(20/80, 1073) (b) and γ-Al_2O_3 (c) as a function of temperature.

Table 4.5 collects the amounts of IPAm decomposed ($N_{IPAm,decomposed}$) and desorbed ($N_{IPAm,desorbed}$) for a suite of zeolites, ASAs, γ-alumina and silica. For HZSM-5 in which all aluminium ions are tetrahedrally coordinated in the framework, $N_{IPAm,decomposed}$ equals the Al content. For reasons of comparison, the concentrations of BAS by H/D exchange FTIR are included. For the set of faujasite zeolites, values of the sites in the supercages are given, because complexation of IPAm occurs only with these sites [19]. The amount of decomposed IPAm agrees well with the expected concentration of strong BAS for the high-silica end members of the steam-calcined Y zeolites and for USY(9.6, F).

With increasing aluminium content, however, $N_{IPAm,decomposed}$ is considerably higher than the expected BAS concentration. What sets the high-silica zeolites apart from the rest is the presence of an extraframework silica-alumina phase in the aluminium-rich Y zeolites. The larger the difference in acid site density between IPAm TPD and H/D exchange FTIR, the larger the amount of IPAm desorption during the TPD experiment. Thus, a tentative explanation is the importance of a contribution of IPAm decomposition adsorbed to an extraframework phase containing aluminium. Similar observations were made for γ-alumina, but not for silica. For γ-alumina, $N_{IPAm,decomposed}$ is 39 μmol/g which compares well to the reported value of 29 μmol/g for another γ-alumina [21]. The presence of IPAm adsorbed at different sites than the BAS may contribute in two ways to the total conversion of IPAm to propene and ammonia. Firstly, decomposition of IPAm strongly bound to these sites. Secondly, desorption of IPAm from such sites, re-adsorption on Brønsted acid sites and decomposition should also be considered.

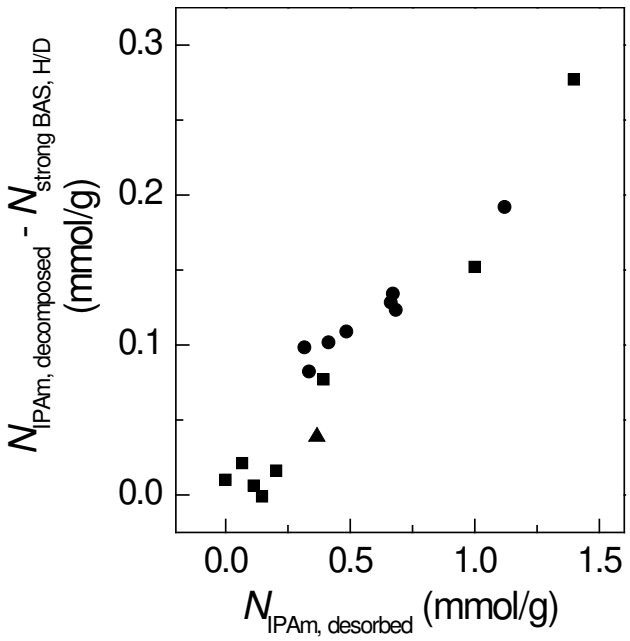

Figure 4.10: The amount of decomposed *i*-propylamine not related to strong Brønsted activity as a function of the the amount of desorbed *i*-propylamine for zeolites (■), ASAs (●) and γ-Al_2O_3 (▲).

For ASAs, $N_{IPAm,decomposed}$ varies between 80 and 200 μmol/g. These values are one to two orders of magnitude higher than the BAS concentrations suggested by other techniques. The difference is due to a substantial contribution of IPAm decomposing on sites different from strong BAS. The analogy with zeolites containing an extraframework silica-alumina phase is evident. Thus, the surface of ASAs contain a large number of acid sites other than the strongly Brønsted acid ones. Fig. 4.10 shows the difference between the total amount of IPAm decomposed and the BAS concentrations determined by H/D exchange FTIR as a function of $N_{IPAm,desorbed}$. The clear correlation strongly suggests that the higher than expected values of $N_{IPAm,decomposed}$ relate to the IPAm desorbing from the catalyst surface. The nature of these sites is not directly clear. Aluminol sites do not appear to be the cause, as such sites are much more abundant in γ-Al_2O_3, *i.e.* typically at a concentration of 1.2 mmol/g, than IPAm TPD shows for a typical γ-Al_2O_3. The role of silanols can also be ruled out as they are even less acidic and, in any case, silica did not show any decomposition of IPAm. BAS of modest acidity were observed in ASAs and zeolites by CO IR spectroscopy. The concentration of such sites ranges from 60-150 μmol/g for the set ASAs (Table 4.3) and is approximately 100 μmol/g for the aluminium-rich Y zeolites.

Table 4.5: Amount of IPAm decomposed ($N_{IPAm,\ decomposed}$) and desorbed ($N_{IPAm,\ desorbed}$) during IPAm TPD experiment for a set of aluminosilicates. Values from H/D exchange FTIR ($N_{strong\ BAS,\ H/D}$) have been included for comparison. For the zeolites the value of the $N_{strong\ BAS\ ,H/D}$ corresponding to concentrations in supercages is given.

Sample	$N_{strong\ BAS,\ H/D}$ (μmol/g)	$N_{IPAm,\ decomposed}$ (μmol/g)	$N_{IPAm,\ desorbed}$ (μmol/g)
HZSM-5(40)	n.d.[1]	830	0
USY(9.6, F)	1522	1700	0
USY(8.1, I)	435	712	1398
USY(8.1, II)	770	922	1000
USY(9.3)	167	244	394
VUSY(26)	340	356	203
VUSY(33)	168	167	147
XVUSY(70)	210	231	66
XVUSY (85)	106	112	114
ASA(5/95,773)	2.3	104	413
ASA(10/90,773)	3.2	112	485
ASA(15/85,773)	2.7	137	671
ASA(20/80,773)	4.7	128	683
ASA(5/95,1073)	3.6	102	316
ASA(10/90,1073)	4.8	87	335
ASA(15/85,1073)	8.6	137	667
ASA(20/80,1073)	5.2	197	1120
γ-Al_2O_3	0	39	366
SiO_2	0	0	0

[1] not determined.

The pyridine IR data show that only a small fraction of these Brønsted acid sites is strong enough to retain this base at 473 K. For example, ASA(5/95,1073) contains 75 μmol/g weak BAS from CO IR, but only 16 μmol/g of these sites are of sufficient strength to retain pyridine at 473 K. As pyridine is a stronger base than IPAm, it is expected that only a small fraction of these sites contribute to the excess decomposition. LAS are more reasonable candidate sites, as their interaction with bases is stronger. This is readily apparent from the finding that substantial amounts of pyridine remain adsorbed on ASAs up to a temperature of 673 K. For instance, ASA(5/95,1073) and ASA(20/80,1073) contain 46 and 62 μmol/g Lewis acid sites, respectively. As the strength of these sites is sufficiently high to adsorb pyridine at 673 K, it may be expected that IPAm also remains adsorbed up to temperatures high enough for its decomposition to occur. Typical values for the amount of LAS on γ-Al_2O_3 are around 0.1 Al^{3+}/nm^2 [25], which corresponds to a concentration of 44 μmol/g for the γ-Al_2O_3 employed here. In conclusion, IPAm decomposition is not able to probe selectively the strong BAS in ASAs. A problem is the relatively strong adsorption of the alkylamine base to Brønsted acid sites of varying acidity and to strong Lewis acid sites. This form of chemisorbed IPAm also gives rise to IPAm decomposition, either directly or via readsorption on acid sites.

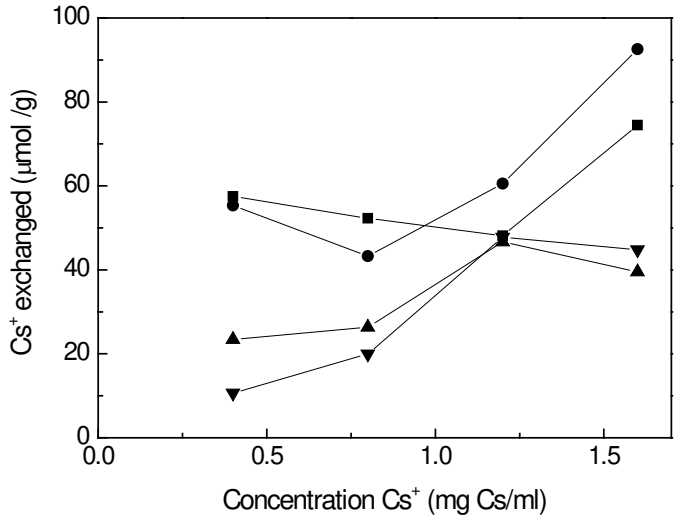

Figure 4.11: Adsorption isotherms of CsCl of ASA(5/95, 1073) (■), ASA(10/90, 1073) (●), ASA(15/85, 1073) (▲) and ASA(20/80, 1073) (▼).

4.3.4 Ion exchange with Cs^+

Fig. 4.11 shows the relation between the fraction of Cs^+ ions adsorbed by the support and the Cs^+ concentration in the solution. Clearly, these plots do not represent well-behaved adsorption isotherms nor does the amount of adsorbed ions remain constant as a function of the Cs^+ concentration. Similar experiments with zeolites gave well-behaved adsorption isotherms. Control experiments on pure γ-alumina and pure silica did not evidence exchange under the experimental conditions where the pH was kept below 6. At pH below 6 one expects that exchange is limited to relatively strong Brønsted acid hydroxyl groups. This was verified by monitoring the pH of the solutions at the beginning and end of each experiment (Table 4.6). A reason for the difficulty in determining the ion-exchange capacities in this way can be the considerable variation of the pH per sample and as a function of the Cs^+ concentration. Although no accurate concentrations of Brønsted acid sites can be determined from these experiments, it is clear that the surfaces are able to exchange Cs^+ in amounts in the range 10-100 µmol/g. This implies the presence of a large number of BAS. The end pH is higher for the high aluminium content ASAs than for other two ASAs. This effect can be explained by a buffering effect due to the presence of alumina in the former two ASAs.

Table 4.6: pH values observed during adsorption of Cs^+ for set of amorphous silica-aluminas. The subscript in the pH indication refers to the contact time of the support (min) with the CsCl solutions.

Cs content	ASA (5/95, 1073)			ASA (10/90, 1073)			ASA (15/85, 1073)			ASA (20/80, 1073)		
mg/ml	pH_0	pH_5	pH_{60}	pH_0	pH_5	pH_{60}	pH_0	pH_5	pH_{60}	pH_0	pH_5	pH_{60}
1.6	4.4	2.8	2.7	4.0	2.7	2.7	5.5	4.4	4.6	5.5	4.4	4.7
1.2	4.0	2.7	2.7	4.1	2.7	2.7	5.6	4.2	4.5	5.4	4.2	4.7
0.8	4.0	2.5	2.4	4.0	2.7	2.6	5.8	4.4	4.4	5.7	4.3	4.7
0.4	4.5	2.8	2.7	3.8	2.6	2.5	5.8	4.4	4.4	6.0	4.7	4.6

4.3.5 Ion exchange with Cu-EDA complex

For clays, the cation exchange capacity can be determined by exchange with a Cu^{2+}-EDA complex [23]. The Cu^{2+}-EDA complex does not undergo a compositional change in solutions with a pH between 6 and 8 [34] and is able to displace most exchangeable cations and even heavy metals [35]. The complex binds strongly to clay surfaces, possibly through covalent bond formation. Table 4.7 lists the cation exchange capacities for three ASAs. These values are two orders of magnitude higher than the expected ones. Clearly, this method probes a wide range of hydroxyl groups on the surface of varying acidic strength.

Table 4.7: Concentration of strong Brønsted acid sites ($N_{\text{Cu-EDA}}$) for aluminosilicates determined by exchange of hydroxyl groups with Cu-EDA complex. For comparison , the values from the H/D exchange FTIR is also included ($N_{\text{strong BAS, H/D}}$).

Sample	$N_{\text{Cu-EDA}}$ (μmol/g)	$N_{\textit{strong BAS, H/D}}$ (μmol/g)
ASA(5/95,1073)	140	3.6
ASA(10/90,1073)	120	4.8
ASA(15/85,1073)	120	8.6

4.3.6 ^{1}H MAS NMR

Fig. 4.12 compares the ^{1}H NMR spectra and their deconvolution into various peaks for ASA(5/95,1073) and ASA(20/80,1073). The spectra can be fitted with peaks around 1.8, 2.3 and 3.8 ppm relative to liquid tetramethylsilane. Very small resonances are noted at 0.9 and 1.2 ppm, the latter of which is due to isolated silanols in silicas [24]. The dominant signal in all spectra are non-hydrogen bonded single and/or geminal silanol groups, which are observed around 1.8 ppm in amorphous silica-aluminas [36]. The peak at 2.3 ppm is due to isolated non-acidic aluminol groups [37]. Signals in the range 3.6-7 ppm have been assigned to various forms of bridging hydroxyl groups in zeolites [24]. At the same time, hydroxyl groups in typical aluminum hydroxydes and oxides have been reported in the range 2.9-5.8 ppm [37]. The exact position depends amongst others on the Al coordination number of the hydroxyl group. The corresponding fit results for the most prominent signals are given in Table 4.8. The silanol density decreases somewhat with increasing aluminium content in line with the CO IR results. The trend is similar for the isolated aluminol groups, which agrees with the surface agglomeration of isolated aluminium species with increasing aluminium loading. The relatively broad feature around 3.8 ppm is due to a range of bridging hydroxyl groups attached to more than one aluminium ion and likely also to those between Si and Al atoms. The concentration of such sites is in the order of 0.2 mmol/g, which is higher than values for weak acidic sites predicted by CO IR and other techniques. Thus, ^{1}H NMR probes a wider range of bridging hydroxyl groups than do these other techniques.

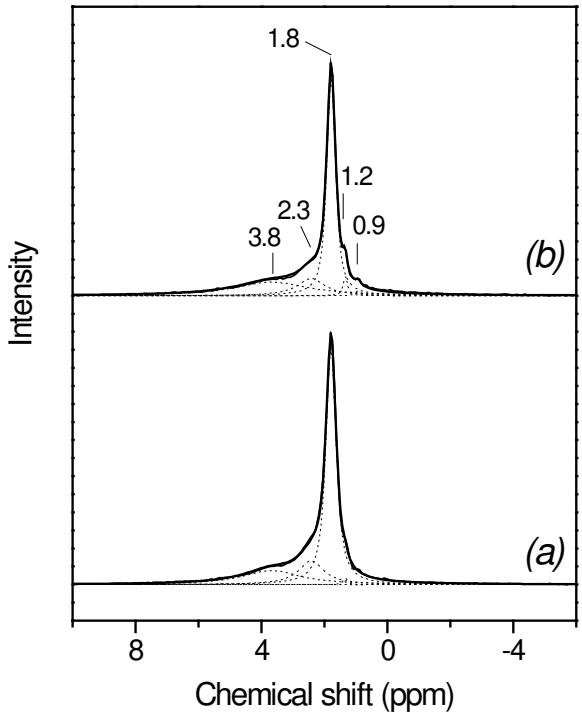

Figure 4.12: ^{1}H MAS NMR spectra of ASA(5/95,1073) (a) and ASA(20/80,1073) (b).

Table 4.8: Concentration of various protons as derived from deconvolution of ^{1}H MAS NMR measurements.

Sample	$N_{\delta=1.8\ ppm}$ (mmol/g)	$N_{\delta=2.3\ ppm}$ (mmol/g)	$N_{\delta=3.8\ ppm}$ (mmol/g)
ASA(5/95,1073)	0.57	0.22	0.21
ASA(10/90,1073)	0.55	0.17	0.21
ASA(15/85,1073)	0.40	0.11	0.20
ASA(20/80,1073)	0.41	0.12	0.20
ASA(5/95,co-gel)	0.57	0.19	0.20

4.3.7 Isomerization of *m*-xylene

As isomerization of xylenes is catalyzed by strong BAS [38], another potential method to probe their concentration is to determine the acid catalytic activity upon selective poisoning of such sites. Typically, *m*-xylene isomerization has been carried out in the gas phase with the disadvantage that coke formation leads to catalyst deactivation. Diphenylmethanes, which are intermediates in the disproportionation reaction, strongly inhibit the isomerization reaction. Further condensation of the heavy intermediates causes coke formation and irreversible deactivation. Takaya et al. [38] have shown that catalyst deactivation can be avoided by carrying out the reaction in the liquid phase.

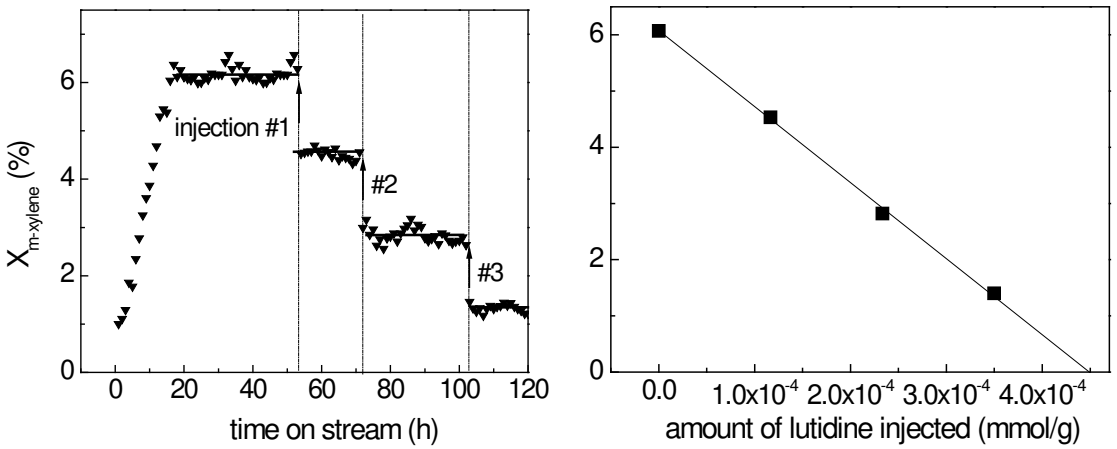

Figure 4.13: Liquid phase *m*-xylene isomerization of dehydrated ASA(5/95, 773) (liquid phase, p = 80 bar, WHSV = 0.85 h^{-1}): conversion of *m*-xylene as a function of time on stream and during three consecutive pulses of lutidine (left) and as a function of the amount of lutidine introduced during the isomerization reaction (right).

Thus, the activity of an amorphous silica-alumina catalyst was found to be stable for prolonged reaction time. The increased stability was explained by the solvation of diphenylmethanes by liquid *m*-xylene. Here, *m*-xylene isomerization was carried out in the liquid phase at 573 K. Lutidine (2,6-dimethylpyridine) was chosen to poison strong BAS following the findings in prior work of Benesi et al. [39] and Heylen et al. [40] that substituted pyridines react selectively with bridging hydroxyl groups in the presence of Lewis acid sites up to a temperature of 673 K. Initial experiments showed that strong catalyst deactivation occurred, even during liquid phase operation. The reason was found to be the presence of trace impurities of peroxide stabilizers in *m*-xylene. Their removal by percolating the *m*-xylene feedstock through a bed of activated alumina prior to use resulted in stable catalytic activity.

Fig. 4.13 shows the catalytic activity of ASA(5/95,1073) as a function of the time on stream. Introduction of well-calibrated amounts of lutidine result in a stepwise decrease of the *m*-xylene conversion. The conversion linearly decreases with the amount of introduced base. By extrapolation the concentration of strong BAS is estimated. Table 4.9 summarizes the results for three ASAs. Clearly, the concentrations of strong BAS are lower than the estimates from FTIR H/D exchange. A tentative explanation is that *m*-xylene isomerization probes a different fraction of strong acid sites and this may hint at a quite heterogeneous distribution of the acid sites in ASA. The slightly lower value of for instance ASA (5/95,co-gel) determined by pyridine IR compared to *m*-xylene isomerization may be due to the higher temperature of evacuation of the IR experiment (673 K) than the reaction temperature of the catalytic test (573 K). To summarize, selective poisoning of liquid phase *m*-xylene isomerisation by lutidine is a promising novel method to determine the concentration of strong BAS in ASAs. The number of strong Brønsted acid sites in ASAs fall in the same range as those determined by CO IR and H/D exchange FTIR.

Table 4.9: Concentration of strong Brønsted acid sites ($N_{\text{strong BAS, isom}}$) for aluminosilicates determined by poisoning of acid sites with 2,6 dimethyl pyridine during *m*-xylene isomerisation. Values from H/D exchange FTIR ($N_{\text{strong BAS, H/D}}$) have been included for comparison.

Sample	$N_{\text{strong BAS, isom}}$ (μmol/g)	$N_{\text{strong BAS, H/D}}$ (μmol/g)
ASA (5/95, 773)	0.4	2.0
ASA(10/90, 1073)	2.6	4.8
ASA(5/95, co-gel)	2.7	7.5

4.4. General discussion

4.4.1 Comparison of techniques of acidity characterization

Of the various techniques discussed in this contribution, infrared spectroscopy of adsorbed carbon monoxide provides quite strong indications of the presence of a very small number of BAS of zeolitic strength in ASAs. Firstly, a strongly shifted hydroxyl stretching frequency at 3320 cm^{-1} for ASA(5/95,1073) is observed in line with the findings of Crépeau et al. [7]. This band cannot be distinguished anymore for ASAs with a higher Al content. Secondly, at low CO coverage a carbonyl stretching band is observed with a frequency very close to that of a band observed upon interaction of CO with the bridging hydroxyl groups of zeolites. This band can only be distinguished as a separate band at very low CO coverages. Higher CO coverage results in the appearance of a much more intense IR band at slightly lower wavenumbers, which represents a weaker form of BAS. Only under stringent fitting conditions, the band can be deconvoluted into two separate contributions providing an estimate of the concentration of strong Brønsted acid sites. The resulting values are of the same order of magnitude as concentrations of BAS determined by H/D exchange FTIR. Yet, the method is not reliable, because the values are clearly correlated to the concentration of weak BAS, which depend strongly on the aluminium content of the ASA. CO IR spectroscopy also evidences the presence of weak and strong Lewis acid sites on the ASA surfaces. Analysis of the spectra as a function of CO coverage shows that the interaction of CO with strong Lewis acid sites results in a slight shift of the IR signal of a certain fraction of silanol groups. This is interpreted as coordination of CO to a SiOH…Al pair formed by a silanol group with strong isolated Lewis acid Al^{3+} surface sites. Here, it is proposed that these paired sites exhibit Brønsted acidity between that of silanols and the strong bridging hydroxyl groups. Several groups have pointed out the acidity of such paired sites before [7,9].

Infrared spectroscopy of adsorbed pyridine is a similar method. The adsorption strength of pyridine with hydroxyl groups is much higher than that of carbon monoxide. In this case, the infrared spectra after desorption at various temperatures is used to differentiate between weak and strong forms of acid sites. After desorption at 673 K, the amount of pyridine retained by hydroxyl groups is very similar to the acid site density determined by H/D exchange FTIR. Drawbacks of this method are the somewhat arbitrary choice of the desorption temperatures and the inconsistencies in reported extinction coefficients of the pyridinium ion.

Whereas Brønsted and Lewis acid sites can be distinguished in the pyridine method by their individual IR signatures of the acid site-pyridine complexes, this turns out not to be possible by following the formation of the propene and ammonia decomposition products from IPAm as the probe molecule. Although it has earlier been suggested that this method is useful for determining the concentration of strong BAS in ASAs [21], the present results show that most likely Lewis acid sites retain IPAm during a temperature-programmed experiment to such temperatures that it decomposes. The resulting overestimation of the concentration of BAS also occurs for steam-calcined Y zeolites with an extraframework silica-alumina phase. A modification of this method, which involves an isothermal period of 4 h at 573 K during the temperature-programmed decomposition, was evaluated. In a control experiment with XVUSY(85), the concentration of strong BAS was found to be 115 μmol/g. In this case, no desorption of IPAm at temperatures above 573 K was observed. The respective strong BAS concentrations for ASA(5/95,1073) and ASA(15/85,1073) were 4.7 and 5 μmol/g. Thus, the excess IPAm on less acidic sites can be removed by flushing at a temperature below the IPAm decomposition temperature.

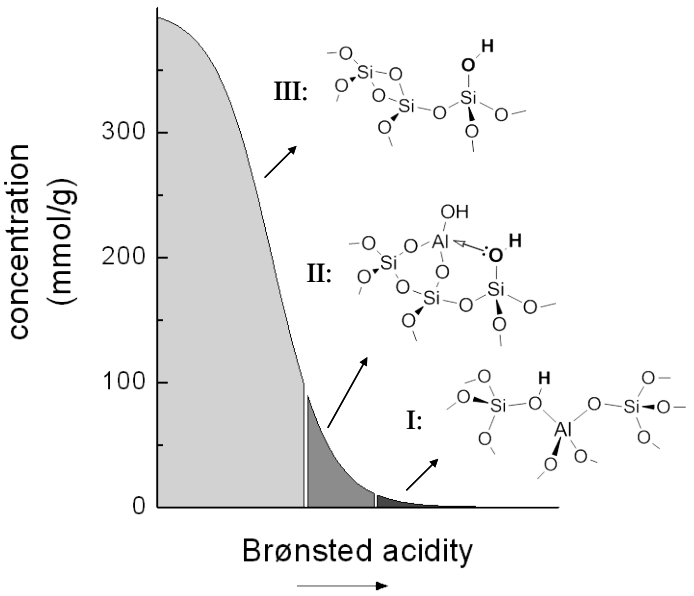

Figure 4.14: Schematic representation of the three types of Brønsted acid sites in a typical amorphous silica-alumina support. Due to the amorphous nature, these sites are much less defined than the acid sites in zeolites. Methods to probe the various types of sites are discussed in Table 4.10.

Ion-exchange methods titrate a much larger number of BAS of the order of the concentrations of weak and strong BAS determined by CO IR. $Cu(EDA)_2^{2+}$ probes a larger amount than does Cs^+. The Cs^+ adsorption isotherms are not well behaved.

^1H MAS NMR spectra show the presence of abundant silanol and aluminol groups. A signal at 3.8 ppm is related to a more acidic form, but cannot be exclusively assigned to a proton located on a bridging oxygen between silicon- and aluminium-occupied oxygen

tetrahedra. Bridging hydroxyl groups between aluminium centers as also present on the surface also contribute to this feature

Isomerization of *m*-xylene can be employed to determine Brønsted acidity by using a nitrogen base such as lutidine. Similar to the H/D exchange FTIR method, the isomerization of *m*-xylene appears to be the presence of strong Brønsted acid sites. The strong Brønsted acid site densities determined were of the same magnitude as those obtained the H/D exchange, CO IR and pyridine adsorption, but further validation for a larger set of catalysts is required. The variation in values of strong BAS between the various techniques may at least in part be explained by the inhomogeneity in the acid strengths of these sites. Indications that this is the case were already outlined before [13].

Table 4.10: Brief overview of various techniques employed to characterize the various types of hydroxyl groups in amorphous silica-aluminas.

Type	Technique	Remarks
I: Strong Brønsted acid bridging hydroxyl groups (1 - 10 μmol/g)	H/D exchange FTIR [13]	Quantitative
	CO FTIR [7]	Quantification difficult because of overlap with CO_{ads} bands due to type II (in some cases signature found by studying perturbed hydroxyl bands)
	Pyridine FTIR [this work]	Quantification difficult because of arbitrary choice of desorption temperature
	IPAm TPD [this work]	Quantitative after modification of method by Gorte et al. [19-21]
II: Weak Brønsted acid bridging hydroxyl groups (50 - 150 μmol/g)	CO FTIR [this work]	Quantitative
	Pyridine FTIR [this work]	Quantification difficult because of arbitrary choice of desorption temperature
	^{1}H NMR [this work]	Determines wide range of weak BAS groups, overlap with acidic aluminol groups
	$Cu(EDA)_2^{2+}$ and Cs^+ exchange [this work]	Cs^+ adsorption isotherms not well behaved
III: Non-acidic silanol & aluminol groups (250 - 400 μmol/g)	CO FTIR [this work]	Quantitative (silanol and aluminol not distinguished)
	^{1}H NMR [this work]	Quantitative, silanol and non-acidic aluminol groups

To summarize, a thorough comparison of various characterization techniques stresses the heterogeneous nature of the surface acidity in ASAs. Fig. 4.14 distinguishes three types of hydroxyl groups, i.e. (i) strong Bronsted acid bridging ones in the silica network, (ii) a weaker and more abundant form, likely due to silanol groups interacting with strong Lewis acid sites and (iii) non-acidic silanol and aluminol groups. Table 4.10 reviews the various techniques useful to probe these sites. Besides, the surface also contains Lewis acid sites. The stronger form identified by a CO IR band at 2230 cm^{-1}, the concentration of which depends on weakly on the aluminium content, is due to grafted isolated Al^{3+}. The weaker form gives rise to a band at 2190 cm^{-1}. Its abundance strongly increases with aluminium content, which suggests that it is due to Lewis acid sites constituent of the aluminium domains.

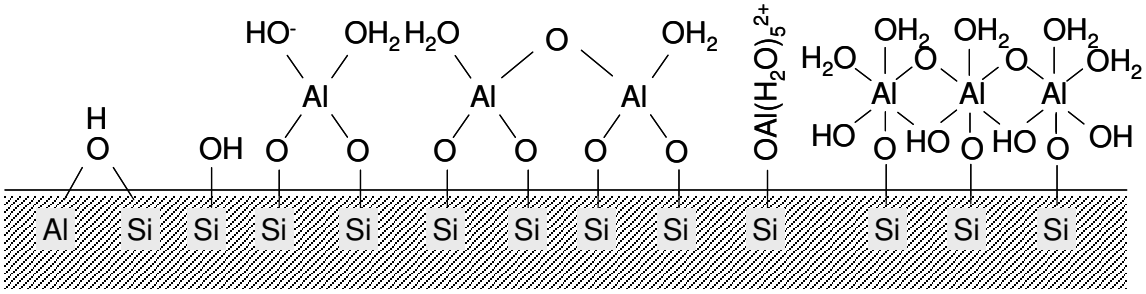

Figure 4.15: Schematic representation of the surface of ASA.

4.4.2 Surface composition ASA and active sites in acid catalysis

Fig. 4.15 gives a simplified representation of the surface of ASA. Next to the very small amount of Al substitutions in the silica network, which give rise to strong BAS, the surface contains abundent isolated and slightly agglomerated Al sites. Upon dehydration, the interaction of such Lewis acid sites with silanol groups results in weak BAS. The Al agglomeration can be such that small seggregated domains on the surface are formed that mainly consist of octahedral Al. In ASA formulations with high Al content also free γ-alumina occurs. Dehydration results in the presence of five-coordinated Al. This type of Al coordination seems to be primarily related to the interface between the seggregated aluminium oxide domains and the ASA phase. Finally, the surface contains non- or at least very weakly acidic aluminol and silanol groups

As the present set of data evidences the presence of two forms of Brønsted acid sites in ASA, it is useful to explore how the earlier correlation of the acid activity with the strong BAS concentration as probed by H/D exchanges compares to one with the weak BAS concentration. Fig. 4.16 shows the correlation between acid activity in *n*-heptane hydroconversion and the density of Brønsted acid sites of zeolites and ASAs. For the ASAs data of strong BAS and of weak BAS are included. This figure makes immediately clear that the catalytic performance does not correlate to the density of weak BAS. In essence, this result implies that this latter type of acid site is not strong enough for the protonation of the intermediate olefins formed during the hydroconversion reaction.

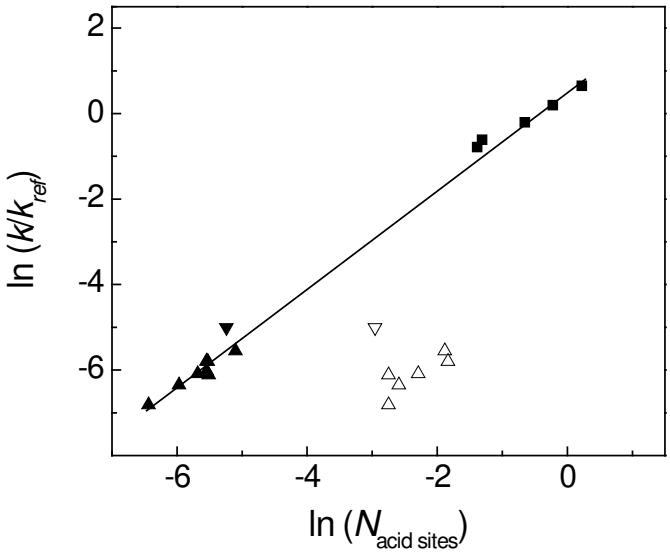

Figure 4.16: Relation between the catalytic activity in the hydroconversion of *n*-heptane and the concentration of acid sites (mmol.g^{-1}) determined by H/D exchange FTIR for (■) zeolites and (▲) ASAs prepared by homogeneous deposition-precipitation and (▼) the ASA prepared by co-gelation. The corresponding open symbols refer to the weak Brønsted acid sites as determined by CO IR. The line is a guide to the eye.

4.4.4 Catalytic activity in neopentane hydrogenolysis

A set of Pt-containing catalysts was tested in the hydrogenolysis of neopentane. The Pt particle size was about 2 nm for Pt/SiO_2:Al and Pt/Al_2O_3 and 8 nm for Pt/SiO_2. The reason for the larger particle size of the Pt/SiO_2 catalyst is tentatively attributed to the absence of Al in this support in contrast to Pt/SiO_2-Al. The latter support contains about 0.5 wt% Al. As the Al density is higher than the Pt density, it may be expected that interactions between the Pt precursor and Al leads to improved dispersion of the reduced catalyst. A very similar result has been obtained for gold nanoparticles supported on these two types of silica [41]. The ASA-supported Pt catalysts contain metal nanoparticles around 4-5 nm.

Analysis of the reaction products of neopentane hydrogenolysis between 0.2 and 6% indicated that the dominant reaction products were methane and isobutane. Very small amounts of isopentane (product of isomerization) and further cracking products were observed (selectivity to methane+isobutane > 96%). The turnover frequencies (TOF) in the hydrogenolysis of neopentane for these Pt catalysts are given in Table 4.11. The TOF of the ASA-supported catalysts is much higher than that of the alumina- and silica-supported ones. Within the ASA series, the activity decreases strongly with more aluminium-rich composition of the support. Pt/Al_2O_3 has a very low activity, similar to Pt/SiO_2. On the other hand, Pt/SiO_2-Al has a notably higher activity than Pt/SiO_2.

Table 4.11: Turnover frequencies (TOF) of neopentane hydrogenolysis for a set of supported Pt catalysts (T = 573 K, 1 vol% C_5H_{12} in H_2, reduction at 573 K, WHSV = 0.01 h^{-1}).

Catalyst	TOF (h^{-1})
Pt/SiO_2	0.4
Pt/SiO_2:Al	10
Pt/ASA(5/95,3,1073)	104
Pt/ASA(10/90,3,1073)	70
Pt/ASA(15/85,3,1073)	69
Pt/ASA(20/80,1073)	46
Pt/ASA(55/45)	43
Pt/Al_2O_3	0.8

Before, experimental indications have been found that the the acid/base properties of the support influence the reactivity of reduced Pt particles in aromatics hydrogenation [42]. Similar effects have been noted for the hydrogenolysis of neopentane [43-45] and also for the sulfur tolerance in this particular reaction of Pt catalysts [46]. It is usually assumed that the increased activity is due to a more electron deficient nature of the noble metal particles on acidic supports. Changes in the Pt electronic structure have been probed by X-ray absorption spectroscopy [47]. More recently, the effect of the Pt-H bond strength has been used to explain the catalytic activity differences [48]. Lercher and co-workers have found that Pt/ASA is much more active in neopentane hydrogenolysis than Pt/Al_2O_3 [12]. They explained this difference in terms of the support electronegativity rather than by stressing the difference in acid sites.

Within the present set of ASA catalysts the support Brønsted acidity as determined by *n*-heptane hydroconversion has been kept constant. It is then immediately clear that the Brønsted acidity is not the determining factor to explain the differences in activity in neopentane hydrogenolysis. An alternative explanation is that the electronic structure is influenced by the electronegativity of the support [12,49]. The more electronegative the support, the more electronegative the Pt particles and the higher the activity in C-H bond cleavage. The data for the silica-supported Pt catalysts show that a prerequisite is that the support interacts with the Pt particles. Without Al, such interactions are very weak and the intrinsic acitivity of the Pt metal phase is found. The somewhat higher activity of Pt/SiO_2:Al is probably due to a few more active Pt particles in interaction with the silica surface through surface Al species with a more dominant fraction of relatively inactive Pt particles that do not interact with the silica support. The coverage with Al species in ASA(5/95,3,1073) is close to the monolayer coverage and the electronegativity of this support is highest among the ASA supports. The support electronegativity decreases with Al content and so does the turnover frequency. Recent work [50] has produced rather convincing evidence that during the preparation of γ-alumina supported Pt catalysts the Pt precursor interacts with five-coordinated Al sites on the alumina surface. A tentative explanation for the relatively large

activity difference between the ASA- and the Al_2O_3-supported catalysts is the much lower density of such undercoordinated Al sites in γ-alumina. It may thus well be that the electronic effect depends on (i) the electronegativity of the support and (ii) interactions via undercoordinated Al sites that are much more abundant on the surface of amorphous silica-alumina surfaces than that of γ-Al_2O_3.

4.5 Conclusions

A number of techniques (CO IR, pyridine IR, alkylamine TPD, Cs^+ and $Cu(EDA)_2^{2+}$ exchange, ^1H NMR and *m*-xylene isomerization) give further insight into the heterogeneous surface composition of ASA. The surface contains Brønsted and Lewis acid sites of varying acidity. The number of strong Brønsted acid sites of zeolitic strength is very low (< 10 μmol/g). H/D exchange FTIR is a technique that can identify these sites semi-quantitatively [13]. Careful interpretation of IR spectra of adsorbed CO and pyridine confirms that the surface contains only very few of such sites. Other methods suitable to estimate strong Brønsted acid sites involve an adaptation of the well-known decomposition of alkylamines and titration of such sites by a base during *m*-xylene isomerization. These sites originate from Al substitutions in the silica network. Besides, the surface contains between 50-150 μmol/g of a weaker form of Brønsted acid sites, which can be easily quantified by CO IR. $Cu(EDA)_2^{2+}$ exchange also appears to probe these sites. Their structure remains unresolved, but some indications exist that these are related to paired sites, involving the interaction of strong Lewis acid sites with silanol groups. The surface is further made up of non-acidic aluminol and silanol sites (200-400 μmol/g). Finally, the surface of ASA contains two forms of Lewis acid sites: (i) a weaker form associated with segregated alumina domains and probably containing five-coordinated Al species that make up the interface between such domains and the ASA phase and (ii) a stronger form which are undercoordinated Al sites grafted to the silica surface.

The acid catalytic activity in bifunctional *n*-heptane hydroconversion correlates to the density of strong Brønsted acid sites rather than to that of the weak Brønsted acid sites. The influence of the support electronegativity on the neopentane hydrogenolysis activity of supported Pt catalysts is larger than that of the support Brønsted acidity. It is argued that five-coordinated sites of ASA and alumina provide anchoring points for the Pt; their density is much higher in ASA than in γ-alumina.

Acknowledgements

The authors thank prof. Johannes Lercher and dr. Benjamin Fonfé of TU Munich for their kind help with the pyridine IR measurements. Dr. Marcello Rigutto of Shell Global Solutions is acknowledged for useful discussions. Dr. Yejun Guan, dr. Volkan Degirmenci and dr. Pieter Magusin are acknowledged for neopentane hydrogenolysis and NMR measurements.

References

1. A. Corma, Chem. Rev. 95 (1995) 559.
2. J. Scherzer, A. J. Gruia, Hydrocracking Science and Technology, Dekker, New York, 1996, pp. 215.
3. G. Busca, Chem. Rev. 107 (2007) 5366.
4. W. O. Haag, R. M. Lago, P. B. Weisz, Nature 309 (1984) 589.
5. M. Trombetta, G. Busca, S. Rossini, V. Piccoli, U. Cornaro, R.J.J. Willey, Catal. Today 179 (1998) 581.
6. W. Daniell, U. Schubert, R. Glockler, A. Meyer, K. Noweck, H. Knözinger, Appl. Catal. A 196 (2000) 247.
7. G. Crépeau, V. Montouillout, A. Vimont, L. Mariey, T. Cseri, F.J. Maugé, J. Phys. Chem. B 110 (2006) 15172.
8. B. Xu, C. Sievers, J.A. Lercher, J.A.R Van Veen, P. Giltay, R. Prins, J.A. Van Bokhoven, J. Phys. Chem. C 111 (2007) 12075.
9. C. Chizallet, P. Raybaud, Angew. Chem. Int. Ed. 48 (2009) 2891.
10. E.J.M. Hensen, D.G. Poduval, P.C.M.M. Magusin, A.E. Coumans, J.A.R. Van Veen, J. Catal. 269 (2010) 201.
11. A.Omegna, J.A van Bokhoven, R.J. Prins, J. Phys. Chem. B 107 (2003) 8854.
12. M.F.Williams, B. Fonfé, C. Sievers, A. Abraham, J.A. van Bokhoven, A. Jentys, J.A.R. van Veen, J.A.Lercher, J. Catal. 251 (2007) 485.
13. Chapter 3 of this thesis; J. Phys. Chem. C (2010) & Chem. Commun. (2010)
14. M.R. Basila, T.R. Kantner, K.H. Rhee, J.Phys.Chem, 68 (1964) 3197.
15. T.R. Hughes, H.M. White, R.J. White, J.Catal, 13 (1969) 58.
16. W. Daniell, N-Y. Topsøe, H. Knozinger, Langmuir 17 (2001) 6233.
17. O.Cairon, T. Chevreau, J-C. Lavalley, J. Chem. Soc., Faraday Trans. 94 (1998) 3039.
18. W.E. Farneth, R.J. Gorte, Chem. Rev. 95 (1995) 615.
19. A.I. Biaglow, C. Gittleman, R.J. Gorte, R.J. Madon, J. Catal, 129 (1991) 88.
20. D.J. Parrillo, A.T. Adamo, G.T. Kokotailo, R.J. Gorte, Appl. Catal., 67 (1990) 107.
21. J.G. Tittensor, R.J. Gorte, D.M. Chapman, J. Catal, 138 (1992) 714.
22. J.A. Rabo, R.D. Bezman, M.L. Poutsma, Acta.Phys.Chem, 24 (1978) 39.
23. F. Bergaya, M. Vayer, Appl. Clay. Sci, 12 (1997) 275.
24. M. Hunger, Catal. Rev.-Sci. Eng. 39 (1997) 345.
25. A. Zecchina, E. E. Platero, C.O. Arean, J. Catal. 107 (1987) 24.
26. M.A. Makarova, J.J. Dwyer, Phys. Chem. 97 (1993) 6337.
27. E. Selli, L. Forni, Microporous Mater 1 (1999)129.
28. J. Datka, B. Gil, A. Kubacka, Zeolites 17 (1996) 428.
29. R.S. Hansford, Ind. Eng. Chem. 39 (1947) 849.
30. M. Trombetta, G. Busca, S. Rossini, V. Piccoli, U. Cornaro, A. Guercio, R. Catani, R.J. Willey, J. Catal. 179 (1998) 581.
31. S. Khabtou, T. Chevreau, J.C. Lavalley, Microporous Mater. 3 (1994) 243.
32. C.A. Emeis, J. Catal. 41 (1993) 347.
33. M. Stadler, P.W. Schindler, Clays Clay Miner 42 (1994)148.
34. M. Auboiroux, P. Baillif, J.C. Touray, F. Bergaya, Appl. Clay Sci.11 (1996) 117.
35. J.R. Hopper, D.S. Shigemura, J. AIChE. 19 (1973) 1025.
36. C.E. Bronnimann, I.-S. Chuang, B.L. Hawkins, J. Am. Chem. Soc. 109 (1987) 1562.
37. G. Piedra, J.J. Fitzgeral, N. Dando, S.F. Dec, G.E. Maciel, Inorg. Chem. 35 (1996) 3474.
38. H. Takaya, N. Todo, T. Hosoya, T. Minegishi, M. Yoneoka, H. Oshio, Bull.Chem.Soc.Jap. 44 (1971) 2296.
39. H.A. Benesi, J.Catal. 28 (1973)176.
40. P.A. Jacobs, C.F. Heylen, J. Catal. 34 (1974) 267.
41. Y. Guan and E.J.M. Hensen, Appl. Catal. A 361 (2009) 49.
42. S.D. Lin and M.A. Vanice, J. Catal. 143 (1993) 539.
43. S.T. Hoymeyer, Z. Karpinski and W.M.H. Sachtler, J. Catal. 123 (1990) 60.
44. Z. Karpinski, S.N. Gandhi and W.M.H. Sachtler, J. Catal. 141 (1993) 337.
45. G. Larsen and G.L. Haller, Catal. Today 15 (1992) 431.

46. J.T. Miller, D.C. Koningsberger, J. Catal. 162 (1996) 209.
47. B.L. Mojet, D.E. Ramaker, J.T. Miller and D.C. Koningsberger, Catal. Lett. 62 (1999) 15.
48. D.C. Koningsberger, M.K. Oudenhuijzen, J. de Graaf, J.A. van Bokhoven and D.E. Ramaker, J. Catal. 216 (2003) 178.
49. Chapter 6 of this thesis.
50. J.H. Kwak, J. Hu, D. Mei, C.-W. Yi, D.H. Kim, C.H.F. Peden, L.F. Allard, J.Szanyi, Science 325 (2009) 1670.

Chapter 5

Promotion of thiophene hydrodesulfurization by ammonia over amorphous-silica-alumina-supported CoMo and NiMo sulfides

Summary

Contrary to the commonly accepted notion that ammonia inhibits the hydrodesulfurization (HDS) of organosulfur compounds, an unexpected promotional effect of ammonia on the hydrodesulfurization of thiophene over amorphous-silica-alumina(ASA)-supported sulfides of CoMo (CoMo/ASA) and NiMo is reported. Addition of ammonia may increase the activity up to a factor of 1.5. The effect is specific to Co- and Ni-promoted MoS_2 supported on an acidic amorphous silica-alumina support. Over CoMo sulfides supported on γ-alumina and carbon the HDS of thiophene is inhibited by ammonia. The effect is related to the presence of Brønsted acid hydroxyl groups on the amorphous silica-alumina support, as it is found that after ion-exchange with Na^+, the HDS activity decreases with the NH_3 partial pressure. A comparison of infrared spectra of adsorbed CO over alumina- and ASA-supported CoMo following various pre-treatments (H_2S/H_2 *vs.* $H_2S/NH_3/H_2$) points to an electronic effect of the acidic ASA support on the active Co-Mo-S phase. It is speculated that the sulfur bond energy is increased due to this interaction. While the desulfurization of thiophene is sensitive to these changes, sulfur removal from (di)benzothiophene is not and ammonia only acts as an inhibitor, likely due to the stronger adsorption of these reactants.

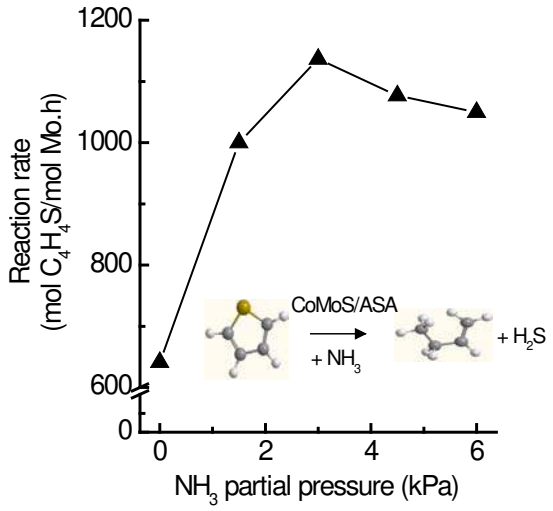

Published in *Industrial Engineering and Chemistry Research 46 (2007) 4202-4211.*

5.1 Introduction

Hydrodesulfurization (HDS) consisting of the removal of organic sulfur compounds from refinery streams is one of the most important catalytic processes in a modern refinery [1]. Environmental regulations are set to come in force by 2009 which require zero sulfur fuels [2] spurring research to further increase the performance of existing CoMo and NiMo sulfide catalysts and to develop alternative processes [3]. Industrial Co(Ni)Mo catalysts consist of MoS_2 slabs promoted by Co(Ni) dispersed on γ-alumina [1]. The active Co-Mo-S phase is made up of atomically dispersed Co atoms located on the edges of the MoS_2 particles. It is generally accepted that there are two types of Co-Mo-S structures [1, 4]. Type I Co-Mo-S is characterised by a lower HDS activity because of the presence of residual linkages with the subjacent alumina support. More active are fully sulfided type II Co-Mo-S structures. The strong interaction between γ-alumina and MoS_2 in principle leads to type I structures unless special precautions are taken [5]. Activated carbon supports have a lower tendency to interact with Mo, resulting in highly active type II structures [5]. In recent years, developments have therefore been aimed at obtaining a maximum amount of type II Co-Mo-S structures [6, 7] in view of the need of more active alumina-supported catalysts for the production of ultra low sulphur diesel (ULSD) fuels.

The sulfur tolerance of HDS catalysts is of paramount importance in industrial practice, because hydrogen sulfide decreases the rate of desulfurization of organosulfur compounds by competitive adsorption. Recently, it has been established that the choice of support has a strong influence on the extent of H_2S inhibition [8, 9]. For sulfided CoMo and NiMo catalysts supported by activated carbon (C), γ-alumina (Al_2O_3) and amorphous silica-alumina (ASA), the inhibiting effect of H_2S in thiophene HDS tended to increase in the order ASA < Al_2O_3 < C. In addition to an electronic effect of the support, a direct interaction between (acid) support hydroxyl groups and the active phase was suggested [8, 10]. As nitrogen bases interact with the acid support hydroxyl groups, we here investigate the effect of ammonia on the thiophene HDS activity for Mo-based hydrotreating catalysts. A second reason is to understand the influence of nitrogen bases on the HDS activity of organosulfur compounds, ammonia being the simplest representative of this class of inhibitors.

In the present study, it will be shown that NH_3 promotes the desulfurization of thiophene over sulfided Co(Ni)Mo/ASA. Besides kinetic experiments, the active metal sulfide phase will be studied as a function of the gas phase composition by infrared spectroscopy of adsorbed CO. As shown by others [11-16] the latter approach helps to understand the constitution of the active edge surface. The main finding will be that the Brønsted acidic hydroxyl groups change the quality of the active sites of the Co-Mo-S phase. This electronic effect negatively affects the catalytic performance and can be (partly) alleviated by adsorbing ammonia to these hydroxyl groups or replacing them by Na^+ ions. The relevance of this unusual effect for the industrially more important hydrodesulfurization of dibenzothiophene will also be discussed.

5.2 Experimental section

5.2.1 Catalyst preparation

A commercial $CoMo/Al_2O_3$ catalyst (Shell C444) was used as received. For the preparation of CoMo/ASA, NiMo/ASA, Mo/ASA and CoMo/C, amorphous silica-alumina (Shell, 455 m^2/g, 0.67 cm^3/g, 45 wt.% silica) and activated carbon (Norit RX-3 EXTRA, 1190 m^2/g, 1 cm^3/g) supports were used. The ASA support material was calcined at 573 K for 2 h. All catalysts were prepared by pore volume impregnation with solutions of ammonium heptamolybdate and cobalt nitrate. For the carbon support, the complexing agent nitrilotriacetic acid was used [5]. The catalysts were dried in air at 383 K for 16 h and, with the exception of CoMo/C, calcined in static air at 723 K for 2 h. Table 5.1 lists the loadings of the various catalysts.

Table 5.1: Metal loading of the catalysts as determined by ICP analysis.

Catalyst	Metal loadings (wt%)		
	Co	Ni	Mo
CoMo/C[a]	1.6	-	8
$CoMo/Al_2O_3$	3.4	-	9.8
CoMo/ASA	3.6	-	10.8
NiMo/ASA		1.2	8.1
Mo/ASA			8

[a] prepared with nitrilotriacetic acid (NTA).

5.2.2 Characterization

For infrared spectroscopic measurements, the catalysts were ground and pressed into self-supporting wafers (density 7.5 mg/cm^2) and placed into a transmission cell with CaF_2 windows. Prior to recording spectra, the catalyst was sulfided in a flow of 10 vol.% H_2S in H_2 at a total flow rate of 100 cm^3/min whilst heating from room temperature to 673 K at a rate of 6 K/min. After an isothermal period of 2 h, the temperature was lowered to 573 K. Typically, the catalyst was subjected to four consecutive treatments with intermittent acquisition of infrared spectra of adsorbed carbon monoxide: (i) sulfidation in a flowing mixture of H_2S:H_2 (volume ratio 10:90); (ii) exposure to a flowing mixture of H_2S:H_2 (volume ratio 1:99) for 1 h; (iii) exposure to a flowing mixture of NH_3:H_2S:H_2 (volume ratio 0.1:0.9:99) for 1 h and (iv) evacuation at 673 K for 15 min. Prior to recording IR spectra of adsorbed CO, the cell was evacuated for 15 min to a pressure better than 10^{-4} mbar. After admitting high-purity He (5 mbar) to the cell, the catalyst was cooled to 85 K. A background spectrum was recorded at this temperature. Subsequently, infrared spectra of adsorbed carbon monoxide were recorded at increasing CO partial pressures. Finally, the catalyst was evacuated and heated to room temperature followed by sulfidation in a mixture of 10 vol.% H_2S in H_2 at 673 K for 15 min before the next gas treatment.

For transmission electron microscopy measurements, $CoMo/Al_2O_3$ and CoMo/ASA were sulfided in a mixture of 10 vol.% H_2S in H_2 at a total flow rate of 60 cm^3/min. The

temperature was increased from room temperature to 673 K at a rate of 6 K/min. After an isothermal period of 2 h, the catalyst was cooled to room temperature to 473 K in the sulfiding mixture and further in flowing He. The catalyst was then transferred via a nitrogen-flushed glove-box into a glass ampoule and transported to the TEM facility. The ampoule was opened in a glove-box. A few drops of ground sample suspended in n-hexane was then mounted on a carbon polymer supported on a copper grid. The sample was transferred to the microscope in a special vacuum-transfer sample holder to exclude air to prevent reoxidation. The measurements were carried out using a Philips CM30T electron microscope with a field emission gun as the source of electrons at 300 kV.

5.2.3 Catalytic activity measurements

Atmospheric gas-phase thiophene HDS was carried out in a single-pass quartz reactor. Prior to reaction, the catalysts were sulfided in a mixture of 10 vol.% H_2S in H_2 at a total flow rate of 60 cm^3/min. After reaching steady-state activity after 13 h at 673 K in a mixture of 4 vol.% thiophene in H_2, the temperature was lowered to 623 K or 573 K. Kinetic measurements were carried out by varying the partial pressure of NH_3 and H_2S between 0 and 0.2 kPa and 0 and 1 kPa, respectively. A medium-pressure stainless-steel microflow reactor system was used to test catalysts for gas-phase HDS of thiophene, benzothiophene (BT) and dibenzothiophene (DBT) at 30 bar. The reactor bed consisted of an amount of 50 mg catalyst diluted with 5 g SiC. After sulfidation at atmospheric pressure in a similar fashion to the atmospheric thiophene HDS experiments, the temperature was lowered to the desired reaction temperature and the pressure was increased to 30 bar. The reactor feed consisted of hydrogen flow of 500 cm^3/min into which a flow of 0.1 cm^3/min liquid feed was evaporated which consisted of a mixture of DBT (1 wt.%) or BT (5 wt.%) in *n*-decane. This resulted in reactant concentrations of BT and DBT of 0.1 and 0.02 vol.%, respectively. In the case of thiophene HDS, the liquid flow consisted of pure thiophene and the rate was chosen such that the thiophene gas-phase concentration was 4 vol.%. The first order reaction rate constants for BT and DBT were determined as a function of the NH_3 partial pressures. The reaction experiments at elevated pressure were carried out in the absence of H_2S in the feed.

5.3 Results

Fig. 5.1 depicts the thiophene HDS activity of CoMo/ASA as a function of the NH_3 partial pressure. Clearly, the HDS activity increases strongly upon addition of ammonia to the feed at the various H_2S partial pressures. The effect is more pronounced when the H_2S partial pressure in the feed is increased. In the absence of ammonia, the HDS activity decreases with increasing H_2S partial pressure. On the contrary, at the highest NH_3 partial pressure employed here the HDS activity is highest for intermediate H_2S partial pressure. Moreover, when no H_2S is added to the feed there is a clear maximum in the HDS activity with increasing ammonia partial pressure.

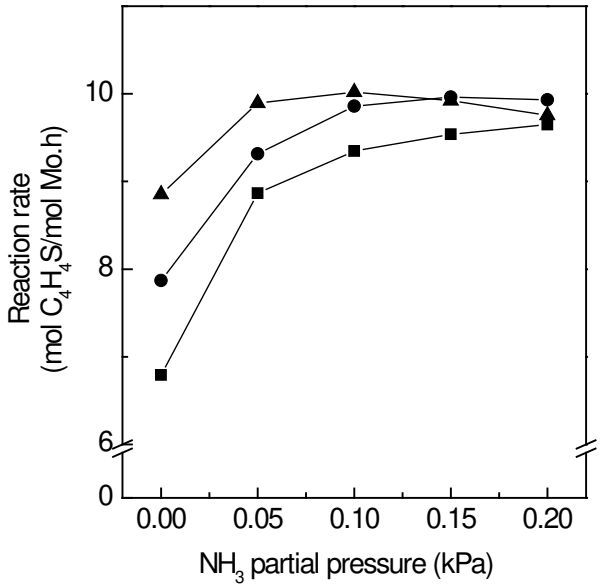

Figure 5.1: Thiophene HDS activity (p = 1 bar, $p_{thiophene}$ = 4 kPa, T = 623 K) as a function of the NH_3 partial pressure for CoMo/ASA at various H_2S partial pressures: 0 kPa (▲), 0.1 kPa (●) and 1 kPa (■).

For comparison, Fig. 5.2 shows the HDS activities of carbon- and alumina-supported CoMo sulfide catalysts. In the absence of NH_3, the activity of CoMo/C is considerably higher than that of CoMo/Al_2O_3. The much higher activity of CoMo/C derives from the presence of type II Co-Mo-S structures. Moreover, the use of an inert carbon support is known to result in higher HDS activities. In contrast, the strong interaction between Mo and Al_2O_3 leads to less active type I structures in CoMo/Al_2O_3. The HDS activity CoMo/Al_2O_3 is about two times higher than that of CoMo/ASA in the absence of ammonia. CoMo/Al_2O_3 and CoMo/C exhibit inhibition by ammonia in a manner which strongly points to competitive adsorption of ammonia for the active sites of thiophene HDS.

To establish whether the promoting effect of ammonia on thiophene HDS is specific to Co-promoted MoS_2 supported on amorphous silica-alumina, similar HDS experiments were performed for sulfided NiMo/ASA and Mo/ASA catalysts. Fig. 5.3 shows that the HDS activity of a sulfided NiMo/ASA catalyst also strongly increases with the NH_3 partial pressure. Different from the observations for CoMo/ASA is that the promoting effect of ammonia is almost similar for H_2S partial pressures of 0 and 0.1 kPa but is less pronounced at

the highest H_2S partial pressure for NiMo/ASA. For unpromoted Mo/ASA, ammonia acts as an inhibitor to thiophene HDS. Thus, it follows that the promotional effect is associated with the presence of Co or Ni promoter ions at the MoS_2 edges and not with MoS_2 itself.

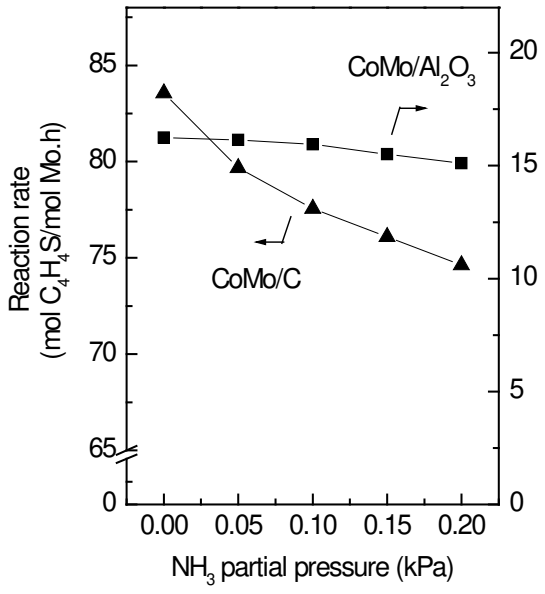

Figure 5.2: Thiophene HDS activity (p = 1 bar, $p_{thiophene}$ = 4 kPa, T = 623 K, no H_2S added) as a function of the NH_3 partial pressure for CoMo/ASA (▲) and CoMo/C (■) at various H_2S partial pressures.

The next step is to determine whether the NH_3 promotion effect is specific to the desulfurization of thiophene. Because of its importance in industrial hydrotreating, dibenzothiophene (DBT) was selected as reactant. Benzothiophene (BT) was included because it has an intermediate reactivity. Table 5.2 collects the first-order rate constants for the conversion of DBT over CoMo/ASA, CoMo/Al_2O_3 and CoMo/C and of BT over CoMo/ASA. As expected, the reactivity of BT is an order of magnitude higher than that of DBT. The activity differences for DBT HDS in the absence of NH_3 between CoMo/Al_2O_3 and CoMo/ASA are smaller than for thiophene HDS. Ammonia clearly inhibits the HDS activity in all cases. To ensure that the absence of promotion by ammonia is not due to the higher (H_2) reaction pressure, a thiophene HDS activity experiment was carried out for CoMo/ASA at 30 bar. Fig. 5.4 shows that the promotional effect is reproduced under these reaction conditions. Strikingly, the trend is very similar to that observed for thiophene HDS at atmospheric pressure under otherwise similar conditions.

Differences in the MoS_2 dispersion were evaluated from TEM micrographs for sulfided CoMo/Al_2O_3 and CoMo/ASA. Despite the higher surface area of the ASA support, the dispersion of the MoS_2 phase is somewhat lower for CoMo/ASA. The difference is mainly caused by the preference of Mo for absorption to the alumina part of the ASA support during preparation [17]. The amorphous silica-alumina support contains alumina patches in an amorphous aluminosilicate matrix. Additionally, this leads to a somewhat higher stacking degree on the ASA support in agreement with earlier differences between sulfided Mo/Al_2O_3

and Mo/ASA [18]. The dispersion of MoS_2 in sulfided CoMo/ASA is approximately 20 % lower than in sulfided $CoMo/Al_2O_3$.

Table 5.2: First-order Reaction Rate Constants for Benzothiophene (BT) and Dibenzothiophene (DBT) HDS as a Function of the Ammonia Partial Pressure.

Catalyst	CoMo/ASA		$CoMo/Al_2O_3$	CoMo/C
$p_{ammonia}$ (kPa)	k_{BT}[a]	k_{DBT}[b]	k_{DBT}[b]	k_{DBT}[b]
0.0	35	3.7	4.3	9.5
1.5	30	2.9	3.9	8.7
3.0	26	2.2	3.6	8.1
4.5	24	1.8	3.5	n.d.[c]

[a] first order rate constant (mol BT/$kg_{catalyst}$.h); [b] first order rate constant (mol DBT/$kg_{catalyst}$.h); [c] not determined.

To obtain more insight into the promotional effect of ammonia, the HDS activity was studied in detail following step changes in the NH_3 concentration for CoMo/ASA at a temperature of 573 K. Fig. 5.5 shows the intrinsic thiophene reaction rate and the ratio of 1-butene and 2-butenes (r_{C4}) in the reactor effluent during a prolonged experiment. After obtaining a steady-state conversion at 573 K in the absence of NH_3, a step change in the NH_3 partial pressure to 0.05 kPa was imposed. The HDS activity increases from 2.7 to 3.5 mol/mol.h. Upon removal of NH_3 from the feed, there was an instantaneous increase of the HDS activity to a value of 4.0 mol/mol.h after 5 min followed by a gradual decrease over a period of several hours to the steady-state value before NH_3 addition.

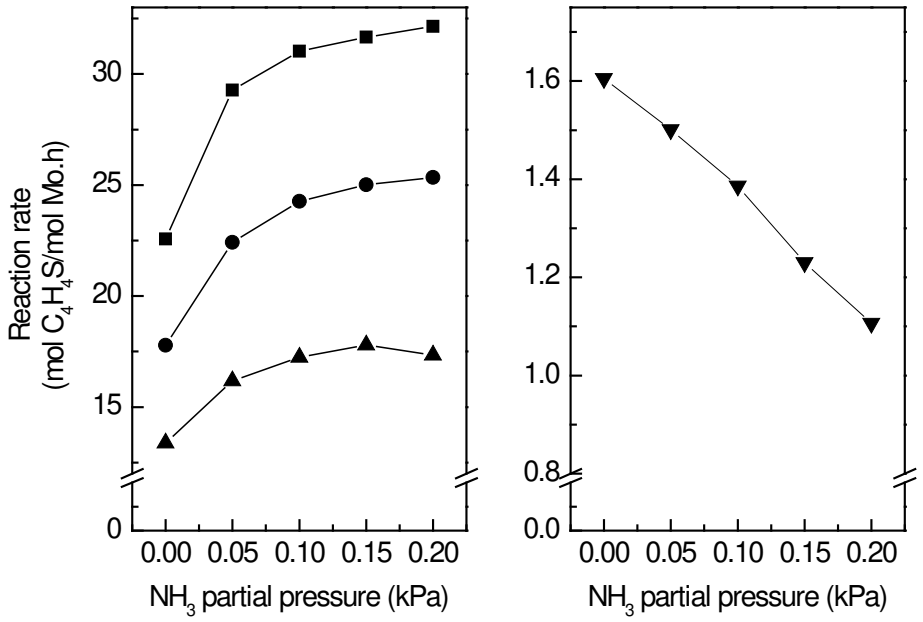

Figure 5.3: Thiophene HDS activity (p = 1 bar, $p_{thiophene}$ = 4 kPa, T = 623 K) as a function of the NH_3 partial pressure for (left) NiMo/ASA at various H_2S partial pressures: 0 kPa (▲), 0.1 kPa (●) and 1 kPa (■) and (right) Mo/ASA (▼) without addition of H_2S to the feed.

Similar behaviour was observed when the NH_3 partial pressure was raised to 0.20 kPa. The increase in HDS activity to a value of 3.1 mol/mol.h was less pronounced. Removal of NH_3 from the reactor feed led to an increase of the activity to 4.1 mol/mol.h and again was followed by a decrease to the steady-state value of 2.7 mol/mol.h. The ratio of 1-butene over 2-butenes displays interesting behaviour as a function of the NH_3 partial pressure. A ratio well above the thermodynamic equilibrium is generally observed in the HDS of thiophene [19]. This suggests that 1-butene is either the primary product of thiophene HDS via a butene-thiolate or of the hydrogenation of 1,3-butadiene. The subsequent isomerization to 2-butenes is catalyzed amongst others by the Brønsted acid sites of the support. Fig. 5.5 clearly shows that 1-butene isomerization is inhibited by the addition of NH_3. The ratio instantly increases from about 0.23 to 0.46. The thermodynamic equilibrium ratio of 1-butene over 2-butenes at this temperature is 0.18. When ammonia addition to the feed is stopped, the value slowly decreases to a final value of 0.26. Similarly, subsequent step changes to 0.20 kPa and 0 kPa NH_3 result in an instant increase of the ratio to 0.51 and a gradual decrease to a final value of 0.27, respectively.

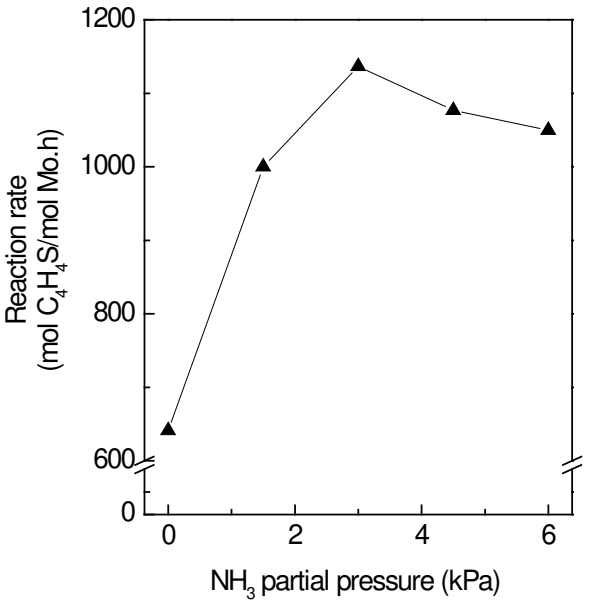

Figure 5.4: Thiophene HDS activity (p = 30 bar, $p_{thiophene}$ = 4 kPa, T = 623 K, no H_2S added) as a function of the NH_3 partial pressure for CoMo/ASA (▲).

To study the influence of the presence of Brønsted acidity of the ASA support, the Brønsted acid protons of sulfided CoMo/ASA were ion-exchanged with a 2 M $Na(CH_3COO)$ solution at room temperature for 1 h according to the procedure of Bezman [20]. A similar method employed to sulfided Mo/ASA led to a Na^+ content of 1.5×10^{-4} mol/g. After resulfidation, the HDS activity of Na^+-exchanged CoMo/ASA ([Na^+]-CoMo/ASA) catalyst was studied as a function of the NH_3 partial pressure in the absence of H_2S (Fig. 5.6). The HDS activity of [Na^+]-CoMo/ASA was somewhat higher than that of CoMo/ASA under comparable conditions. The ratio of 1-butenes to 2-butenes for [Na^+]-CoMo/ASA was higher

than that of CoMo/ASA in the absence of NH_3. For both catalysts, the ratio increased with ammonia partial pressure although the effect was smaller for [Na^+]-CoMo/ASA. The value of r_{C4} for $CoMo/Al_2O_3$ only shows small changes with increasing NH_3 partial pressure

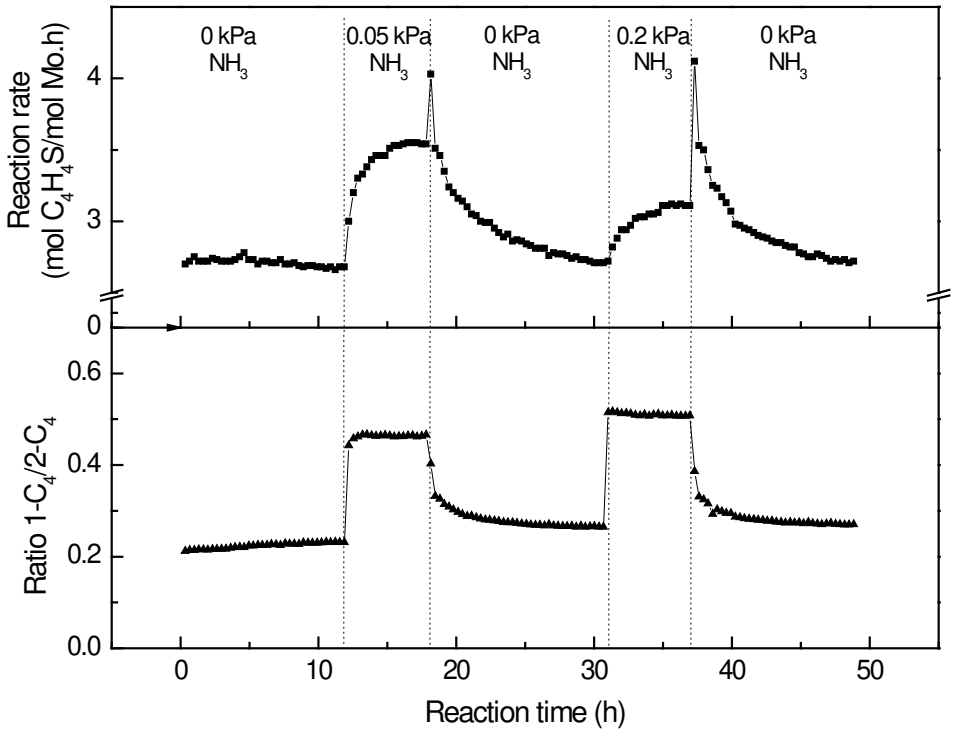

Figure 5.5: (Top) thiophene HDS activity (p = 1 bar, $p_{thiophene}$ = 4 kPa, T = 573 K, no H_2S added) and (bottom) corresponding ratio of 1-butene and 2-butenes in the product mixture as a function of the reaction time upon step changes in the NH_3 partial pressure

To understand in more detail the effect of NH_3 on the active phase, infrared spectra of adsorbed CO were recorded at 85 K. Fig. 5.7 shows the IR spectra of adsorbed CO on $CoMo/Al_2O_3$ and CoMo/ASA after the various gas treatments. After sulfidation, the IR spectrum of $CoMo/Al_2O_3$ shows four distinct bands around 2072, 2110, 2156 and 2189 cm^{-1}. The latter two bands can be readily assigned to CO interacting with hydroxyl groups and Lewis acidic Al^{3+} sites, respectively. The band at 2110 cm^{-1} is assigned to CO on the Mo edge as reported in detail by Travert et al [12] while the one around 2072 cm^{-1} appears to be related to the sites that are promoted by Co [16]. The band at lower wavenumbers is composite and contains contributions of CO adsorbed to Co atoms or possibly of a 5-fold coordinated Mo atom adjacent to a Co atom (~ 2070 cm^{-1}) and of 4-fold coordinated Mo atoms close to the Co atoms (below 2060 cm^{-1}). Travert et al [16] have argued that introduction of Co in the MoS_2 edge leads to decrease of the coordination of adjacent Mo atoms. With increasing Co/Mo ratio, the band at 2070 cm^{-1} has been found to increase at the expense of the intensity of the band at 2110 cm^{-1} [16]. Although the spectrum of sulfided CoMo/ASA is similar, there are some pronounced differences. First, the intensities of the infrared bands corresponding to CO adsorption to the support Lewis acid sites (2189 cm^{-1}) and hydroxyl groups (2156 cm^{-1}) are lower. This is obviously due to the lower aluminium

content of the ASA support and the weaker acidity of the predominant silanol groups in the ASA support. Second, the intensity of the bands related to CO adsorption on Mo and Co sites is considerably lower. Moreover, compared to $CoMo/Al_2O_3$ the bands show a small shift to higher wavenumbers. Such shifts of υ(CO) for sulfide phases supported on acidic supports have been reported before by Maugé and co-workers [13,15,21] and has been explained in terms of an electronic effect exerted by the support on the sulfide phase.

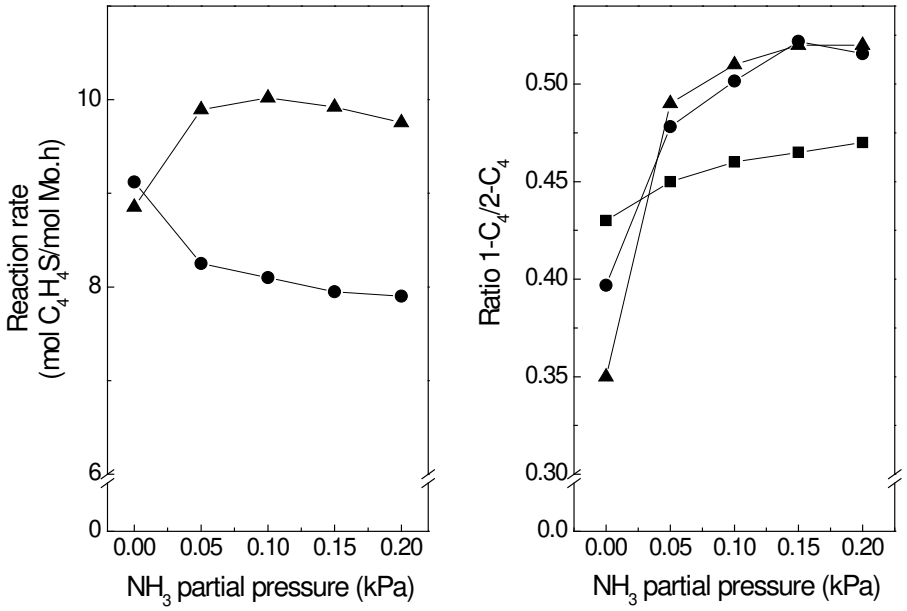

Figure 5.6: (Left) thiophene HDS activity (p = 1 bar, $p_{thiophene}$ = 4 kPa, T = 623 K, no H_2S added) and (right) corresponding ratio of 1-butene over 2-butenes in the product mixture as a function of the NH_3 partial pressure for CoMo/ASA (▲) and [Na^+]-CoMo/ASA (●) reaction time upon step changes in the NH_3 partial pressure. The ratio of 1-butene over 2- butenes for $CoMo/Al_2O_3$ (■) is also given.

Upon treatment in a mixture of 1 vol.% H_2S in H_2 for 1 h several changes are observed in the infrared spectra of both catalysts. There is a clear decrease in the intensity of the band at 2110 cm^{-1} for $CoMo/Al_2O_3$ concomitant with a shift of the band at lower wavenumbers from 2072 cm^{-1} to 2063 cm^{-1}. These changes are likely due to a decrease of the sulfur coordination around the Mo atoms resulting from the lower H_2S partial pressure. The number of 6-fold coordinated Mo atoms (2110 cm^{-1}) decreases while the resulting higher number of 4- and 5-fold Mo atoms lead to an increased intensity of the bands below 2060 cm^{-1}. A different behaviour is observed for CoMo/ASA where the intensities of the bands at 2110 and 2074 cm^{-1} slightly increase. There do not appear to be large changes in the sulfur coordination for CoMo/ASA upon exposure to a lower H_2S partial pressure. After exposure to a mixture of 1 vol.% H_2S, 0.1 vol.% NH_3 in H_2 for 1 h, the spectrum for $CoMo/Al_2O_3$ has totally changed. Most importantly, the bands related to exposed Mo sites have strongly decreased.

Not only can the band at 2110 cm^{-1} hardly be distinguished anymore, but also the intensity of CO absorption bands below 2060 cm^{-1} has strongly eroded. Additionally, the bands related with the Co-Mo-S phase at 2073 cm^{-1} have become less intense but to a lesser extent. Another difference is the complete disappearance of the band related to CO adsorption on Lewis acid sites. This is due to the strong adsorption of ammonia on such sites. Moreover, the band due to hydroxyl groups has increased.

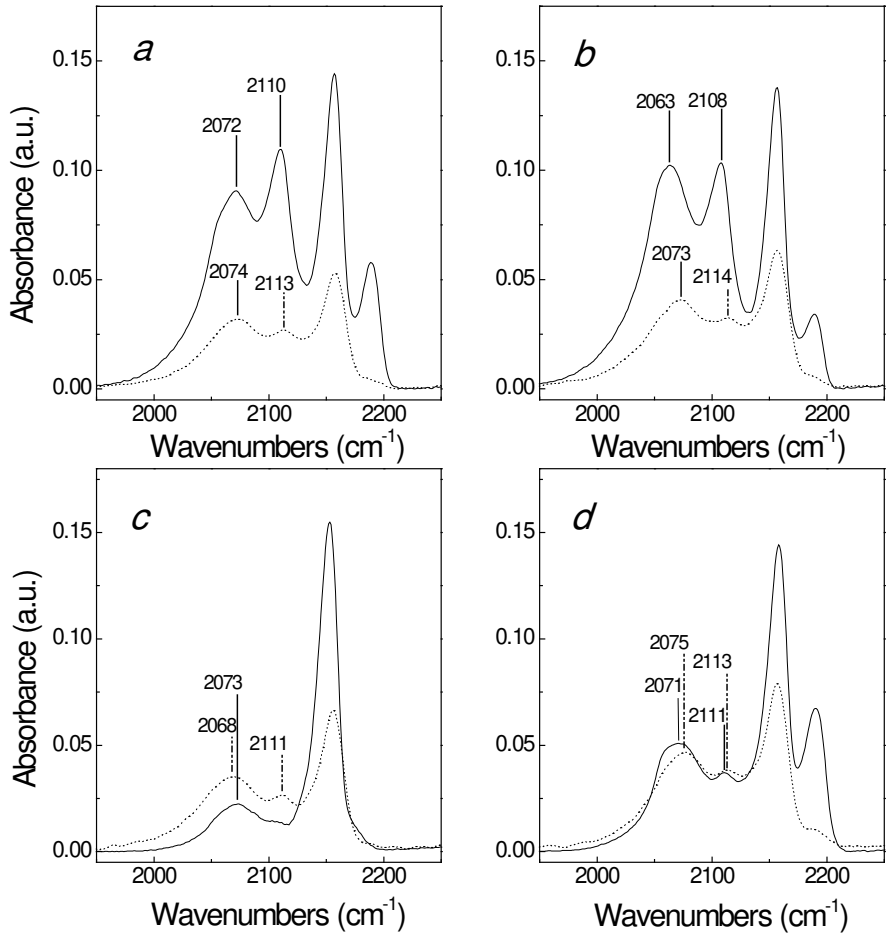

Figure 5.7: Infrared spectra of adsorbed CO at 85 K at a CO loading of 800 μmol/g for $CoMo/Al_2O_3$ (full line) and CoMo/ASA (dotted line) after consecutive treatments: (a) exposure to a mixture of 10 vol.% H_2S in H_2 for 1 h; (b) exposure to a mixture of 1 vol.% H_2S in H_2 for 1 h; (c) exposure to a mixture of 1 vol.% H_2S and 0.1 vol.% NH_3 in H_2 for 1 h and (d) evacuation at 673 K for 15 min.

After evacuation at 673 K for 15 min, the intensities of the bands at 2110, 2073 and below 2060 cm^{-1} have increased again due to ammonia desorption. The band at 2189 cm^{-1} has been restored. For CoMo/ASA, the effect of ammonia addition is very different. The band at 2114 cm^{-1} shifts to 2111 cm^{-1} together with a small decrease of its intensity. Also the band at 2073 cm^{-1} has shifted to 2068 cm^{-1}. Following the assignments of Travert et al., it seems that ammonia adsorbs to the Co-Mo-S-related sites (~ 2073 cm^{-1}), whereas the bands related to Mo sites remain largely unaffected. After evacuation at 673 K, the positions of the bands at

2111 and 2068 cm^{-1} shift back to 2113 and 2075 cm^{-1}, respectively. Moreover, the intensities of these bands have increased somewhat and are notably higher than after the treatment in 1 vol.% H_2S in H_2.

5.4 Discussion

It is well established that organic nitrogen compounds and ammonia inhibit the hydrodesulfurization of organosulfur compounds [1, 22, 23]. Specifically, they decrease the rate of aromatic saturation reactions which is problematic in the removal of the most refractory DBT-like sulfur compounds because pre-hydrogenation of the aromatic ring(s) of dibenzothiophenes greatly facilitates sulfur extrusion. These inhibiting effects are generally explained in terms of competition of the organosulfur and –nitrogen species for adsorption on the same active sites. In contrast, the present results show that thiophene HDS over Co- or Ni-promoted MoS_2 supported on amorphous silica-alumina is promoted by NH_3. Fig. 5.1 shows that the HDS activity may increase by a factor of 1.4 for CoMo/ASA when ammonia is added to the feed. Evidently, the changes in catalyst activity in the absence of H_2S in the feed derive from two competing effects, that is (i) a decrease related to competitive NH_3 adsorption for the active sites for HDS and (ii) an increase due to a yet unknown phenomenon. Accordingly, an optimum in HDS activity is observed under these conditions. In the presence of H_2S in the feed, only a promoting effect of NH_3 is found for the given range of ammonia partial pressures. It is likely that ammonia also inhibits the reaction rate here to some extent. The difference can be understood in terms of a higher sulfur coverage in the presence of added H_2S, resulting in less severe inhibiting effect of NH_3. The promoting effect is also clearly observed for NiMo/ASA, whereas the HDS activity of Mo/ASA strongly decreases with ammonia partial pressure. It follows that the promoting effect of ammonia is associated with the presence of Co and Ni promoter ions at the MoS_2 edge rather than with exposed Mo edge sites. Furthermore, ammonia has a clear inhibiting effect on the thiophene HDS activity when the Co-Mo-S phase is supported on γ-Al_2O_3 or activated carbon (Fig. 5.2). This result implies that the origin of the promoting effect should be found in differences in the nature of the support.

Earlier work has pointed out the increased sulfur tolerance of ASA-supported CoMo over alumina- and carbon-supported CoMo catalysts in the HDS of thiophene [8] and DBT [9] Hensen et al [8,10] speculated that a direct interaction between the acidic hydroxyl groups of the ASA support and the active phase plays a role. This may influence the concentration of vacancies but also electronic effects that change the quality of the active sites need to be considered. Indeed, work of the groups of Maugé and Breysse [13, 15] has identified small shifts in the stretching frequency of adsorbed CO when the sulfide phase is supported on an acidic support such as an amorphous silica-alumina rather than alumina and larger ones when the sulfide phase interacts with an acidic zeolite. Both ASA and Al_2O_3 support materials contain a substantial number of Lewis acidic Al^{3+} sites which suggests that such sites cannot explain the observed differences. Thus, a starting hypothesis would entail the interaction of

ammonia with Brønsted acidic hydroxyl group altering the way the support electronically influences the active Co-Mo-S phase or directly influences the active metal sulfide phase through bonding.

The results of the transient experiments carried out at 573 K in Fig. 5.5 further underpin that ammonia induces two competing effects on the thiophene HDS activity, *i.e.* a positive one by interacting with the acidic support and a negative one by competitive adsorption on the active sites. Upon addition of NH_3, the HDS activity increases while at the same time the isomerization rate of 1-butene (r_{C4}) decreases (increases). The almost instantaneous increase in r_{C4} may be understood in terms of the relatively strong interaction of NH_3 with Brønsted acid hydroxyl groups. This leads to a decrease of the number of Brønsted acid sites that are strong enough to isomerize 1-butene [24]. It is important to note that increases in the NH_3 partial pressure during thiophene HDS over $CoMo/Al_2O_3$ and CoMo/C (Fig. 5.2) led to an almost instantaneous decrease of the activity to lower steady-state values. The gradual increase for CoMo/ASA, on the other hand, suggests that there is an indirect effect which may relate to changes in the quality of the active sites. When the NH_3 partial pressure is stepped to 0 kPa, r_{C4} decreases gradually. Surprisingly, the HDS acitivity after removal of NH_3 from the feed substantially increases at first and then gradually decreases in a similar manner as r_{C4}. Under these specific conditions, the maximum HDS activity is about 1.5 times higher than under the steady-state conditions before ammonia addition and about 1.15 times higher than the steady-state activity in the presence of NH_3. This initial increase is explained by desorption of ammonia from the active sites for HDS. This process should be much faster than desorption of ammonia from the acidic hydroxyl groups because the latter interaction is much stronger. Accordingly, the surface coverage of the active metal sulfide phase with NH_3 will decrease resulting in a higher number of vacancies and a higher HDS activity. The subsequent decrease in activity correlates very well with the decrease in r_{C4}. Similar observations are made when the NH_3 partial pressure is stepped to 0.20 kPa. The lower steady-state activity compared to the 0.05 kPa NH_3 case should be due to a higher NH_3 surface coverage of the active sulfide phase. The difference between the activities at 0.05 and 0.20 kPa is higher at 573 K (Fig. 5.5) than at 673 K (Fig. 5.1). It is also noteworthy that the HDS activity after removal of NH_3 (0.20 kPa) from the feed is very similar to that after exposure to 0.05 kPa NH_3. This indicates that the promotional effect of NH_3 is already brought about almost completely by addition of 0.05 kPa NH_3. This further supports the supposition that the promotional effect is linked to the relatively strong ammonia adsorption to the acidic hydroxyl groups. A further increase of the NH_3 partial pressure mainly increases the NH_3 surface coverage of the active sites of the sulfide phase and decreases the catalytic activity.

More direct evidence for the involvement of Brønsted acid hydroxyl groups of the ASA support is derived from the results in Fig. 5.6. After exchange of the hydroxyl groups by Na^+ the dependence of the HDS activity on the ammonia partial pressure has totally changed. Instead of a strong promoting effect, ammonia now clearly inhibits the HDS activity of

[Na^+]-CoMo/ASA. The value of r_{C4} for [Na^+]-CoMo/ASA is also higher than for CoMo/ASA in the absence of NH_3, showing that at least some acidic protons have exchanged. As the acidity apparently lowers the activity of CoMo/ASA, one would expect higher HDS activities after their exchange by sodium. Indeed, the HDS activity in the absence of NH_3 is somewhat higher. In another experiment the HDS activity of [Na^+]-CoMo/ASA in the presence of 1 kPa H_2S was 8.9 mol/mol.h which is substantially higher than the corresponding activity of CoMo/ASA (6.7 mol/mol.h). On the other hand, there is still a considerable increase in r_{C4} with increasing NH_3 partial pressure for [Na^+]-CoMo/ASA, suggesting that the ion-exchange was not complete. Venezia et al [26] have studied the effect of Na^+ addition to amorphous silia-alumina prior to metal impregnation. These authors found a maximum in catalytic activity for thiophene HDS as a function of the sodium content which was explained by structural changes of the support and the base metal oxide precursor. In the present study, the sodium exchange was carried out over a sulfided CoMo/ASA catalyst, thus precluding changes in the metal oxide phase or the surface area of the support. Hence, an alternative to the explanation of Venezia et al. for the increase of the HDS activity at low sodium contents may thus be the here noted positive effect of replacement of acidic hydroxyl groups on the thiophene HDS. Finally, Fig. 5.6 also shows that the changes in the rate of isomerization with ammonia addition for $CoMo/Al_2O_3$ are relatively small. This observation is important because it implies that the changes in isomerization rates for CoMo/ASA and [Na^+]-CoMo/ASA stem from changes in the support acidity and not from inhibiting effects of the isomerization reaction catalyzed by the metal sulfide phase.

The infrared spectra of adsorbed CO in Fig. 5.7 give further insight into the changes taking place in the active Co-Mo-S phase upon ammonia addition. An important difference in the spectra between $CoMo/Al_2O_3$ and CoMo/ASA is the much larger change in the intensities of the bands related to the active sulfide phase as a function of the gas phase composition for the former catalyst. The total intensity of these bands for CoMo/ASA is substantially lower than for $CoMo/Al_2O_3$. There does not appear to be a correlation between the intensity of the bands and the catalytic performance. Moreover, addition of NH_3 strongly lowers the amount of CO adsorption sites in $CoMo/Al_2O_3$ but only to a relatively small extent in CoMo/ASA. Another salient finding is that there are small but pronounced shifts in the υ(CO) for CoMo/ASA. These are particularly evident for the band around 2110 cm^{-1}. In the absence of NH_3, the band is observed around 2114 cm^{-1} for CoMo/ASA. This value is somewhat higher than for $CoMo/Al_2O_3$. The positive shift is in line with the changes in the IR spectra noted by Maugé and co-workers [15, 21] for ASA-supported sulfide phases. Larger shifts that correlated with the Brønsted acidity were noted for Mo-sulfide particles supported on β-zeolite [13]. In the presence of NH_3 the CO band shifts downwards to 2111 cm^{-1} followed by a positive shift after evacuation at high temperature. Such shifts were not observed for $CoMo/Al_2O_3$. Similar to the work of Maugé and co-workers [13, 15, 21] these changes suggest that υ(CO) probes the electronic influence of the acidic support on the Co-Mo-S phase. The electronic effect appears to be diminished upon adsorption of ammonia on the Brønsted acid hydroxyl groups.

These shifts cannot be derived unequivocally for the promoted sites because the bands in this region consist of several overlapping bands. Although the band around 2073 cm^{-1} in CoMo/ASA clearly shifts to lower wavenumbers upon NH_3 exposure, close inspection of the spectra give good grounds to state that this change is rather due to stronger poisoning of the band at 2073 cm^{-1} compared to that of the bands at lower wavelengths. This implies that the sites related to the Co-Mo-S phase (Co sites or 5-fold coordinated Mo adjacent to Co) adsorb preferentially ammonia over the 4- and 6-fold coordinated sites or that the former sites are already occupied to a large extent. This contrasts the findings for $CoMo/Al_2O_3$ where NH_3 very strongly erodes particularly these bands.

This infrared study strongly suggests that acidity of the support strongly influences the electronic state of the Co-Mo-S phase and the unpromoted MoS_2 sites. Although the changes in band intensities for $CoMo/Al_2O_3$ correlate to some extent to the catalytic activity, this does not hold for CoMo/ASA. Therefore, it seems fair to conclude that the Brønsted acidity of the ASA support decreases the intrinsic activity of the active Co-Mo-S phase in sulfided CoMo/ASA. Elimination of the Brønsted acidity by adsorption of ammonia decreases the electronic effect and increases the intrinsic activity. Moreover, after ion-exchange of part of the Brønsted acidic hydroxyl groups by sodium, the activity decreases upon ammonia addition in a similar manner as found for $CoMo/Al_2O_3$ and CoMo/C. All this suggests strongly that the presence of Brønsted acidity is crucial in explaining the electronic effect. It is very difficult to conclude firmly on the nature of this interaction. The acidity of the support might influence the active phase indirectly although direct interactions between the protonic sites and the sulfide phase should not be excluded.

Table 5.2 shows that ammonia strongly inhibits the HDS of BT and DBT over CoMo/ASA. Similarly, the rate of DBT desulfurization is inhibited by ammonia for $CoMo/Al_2O_3$ and CoMo/C. The absence of a promoting effect of NH_3 for CoMo/ASA in these cases cannot be explained by the different reaction conditions, because it was found that ammonia improves the HDS of thiophene when the reaction was carried out at a total pressure of 30 bar under otherwise equivalent conditions (Fig. 5.4). The difference is thus more likely due to the higher adsorption strengths of (di)benzothiophenes compared to thiophene. Due to the weaker adsorption of thiophene on the active phase, its desulfurization may be more sensitive to the changes in the quality of the active sites arising from NH_3 adsorption on the acidic hydroxyl groups of the support. BT and DBT adsorb much more strongly on the active sites, possibly even in another configuration, so that the comparatively small electronic effect does not present itself in the catalytic performance. Further support for this is the finding that the difference in DBT HDS activity between $CoMo/Al_2O_3$ and CoMo/ASA corresponds very well with the difference in MoS_2 dispersion as derived from a TEM analysis (Table 5.3) in contrast to the difference in thiophene HDS activity. In other words, for strongly adsorbing molecules such as dibenzothiophene the rate of hydrodesulfurization is proportional to the number of active sites. Thiophene adsorbs less

strongly and probes the electronic effects on the Co-Mo-S phase more strongly. Accordingly, also the rather weakly adsorbing CO probe molecule probes these differences.

Table 5.3: Average Slab Length, Stacking Degree and MoS_2 Dispersion.

Catalyst	$d_{average}$ (nm)	$S_{average}$	f_{Mo} [a]
$CoMo/Al_2O_3$	2.7	1.2	0.42
CoMo/ASA	3.3	1.5	0.34

[a] dispersion of MoS_2 expressed as the fraction of Mo at the edges of the MoS_2 particles [18].

Speculating that the electronic effect of support acidity on the active phase changes the metal-sulfur bond energies, the infrared spectra suggest that sulfur binds more strongly on the active metal sulfide phase in CoMo/ASA. First of all, the intensity of the CO absorption bands related to the active sites is much lower for CoMo/ASA than expected on the basis of the difference with $CoMo/Al_2O_3$. Second, whereas NH_3 has a pronounced effect on these bands for $CoMo/Al_2O_3$, the decrease is almost negligible for CoMo/ASA. A higher sulfur coverage due to a higher sulfur bond energy for CoMo/ASA would be in line with such a difference, because ammonia has to compete with the more strongly interacting H_2S adsorbate. When, through adsorption to the Brønsted acid hydroxyl groups, ammonia diminishes the electronic effect and decreases the sulfur bond energy, the number of vacancies increases. It might be that the relatively small change in intensity of the relevant CO bands for CoMo/ASA upon ammonia adsorption is in fact a consequence of a decrease due to NH_3 adsorption and an increase due to H_2S desorption. Moreover, the desorption of H_2S might be a rather slow process corresponding to a gradual increase in HDS activity (Fig. 5.5). Hinnemann et al [27] have concluded from DFT studies that oxygen linkages with the support at the sulfur edge of MoS_2 increase the sulfur bond energy. Besides influencing the electronic states locally, these linkages also induce changes in the surroundings and specifically in the electronic states of neighbouring Co promoter atoms. The associated higher sulfur bond energy provides an explanation for the lower reactivity of type I Co-Mo-S structures when vacancy creation is assumed to be rate limiting. Although their model clearly differs from the one in this study as the strong influence of ammonia on the HDS activity points to the role of accessible hydroxyl groups rather than hydroxyl groups that have been consumed by interaction with the active phase, there is an analogy in the changes in the sulfur bond energy of the active phase. The active Co-Mo-S phase in sulfided CoMo/ASA should exhibit a type I character. Tentatively, the negative effect of the linkages might be enhanced by the presence of Brønsted acidic hydroxyl groups in close vicinity as such effects would be expected to be rather local. Indeed, compared to $CoMo/Al_2O_3$ the thiophene HDS activity of CoMo/ASA is much lower than expected on grounds of the MoS_2 dispersion. In the presence of ammonia, this difference becomes smaller.

This line of reasoning can also help to understand the strong increase in HDS activity during the transient experiments (Fig. 5.5). Upon removal of NH_3, the number of sulfur vacancies increases further due to removal of ammonia that competes with thiophene from

the metal sulfide active sites. Accordingly, the thiophene HDS activity increases further. Ammonia desorption from the Brønsted acid hydroxyl groups is much slower as corroborated by the gradual decrease in r_{C4}. In terms of this tentative model, this desorption leads to a increasing sulfur bond energy and accordingly a build-up of sulfur species on the surface. These sulfur species must derive from the desulfurization of thiophene for the experiment in Fig. 5.5 was carried out in the absence of H_2S in the feed. For NiMo/ASA, the promotional effect is similar to the one for CoMo/ASA at the highest H_2S partial pressure. Only, at the highest H_2S partial pressure for NiMo/ASA the effect is less pronounced. Although it is difficult to provide an explanation, the different behaviour might be related to the lower sulfur bond energy on Ni-Mo-S surfaces [27] or to the tendency of Ni promoter ions to adsorb to both molybdenum and sulfur edges [28]**.** The promotional effect is not observed for Mo/ASA, despite the finding that the acidic support also influences the position of the CO absorption band at 2110 cm^{-1} for CoMo/ASA. Likely, NH_3 adsorbs more strongly to coordinatively unsaturated Mo sites as is suggested by the relatively strong decrease in HDS activity (Fig. 5.3).

Finally, as mentioned above the reason that these electronic effects are not observed for BT and DBT HDS for CoMo/ASA may be due to the strong adsorption of these reactants compared to thiophene and H_2S. Hence, the much stronger adsorption on the active sulfide phase makes the desulfurization of these reactants less sensitive to subtle changes in the sulfur surface coverage. The difference in adsorption properties is also evident from recent quantum-chemical studies indicating that the sulfur vacancy requirement for the HDS of methylsulfide [29] and thiophene [30] is much less pressing than for DBT and 4,6-dimethyl-DBT [31]

5.5 Conclusions

The presence of ammonia increases the rate of thiophene HDS for sulfided CoMo and NiMo catalysts supported on acidic amorphous silica-alumina. For alumina- and carbon-supported CoMo sulfides ammonia inhibits the desulfurization of thiophene. The effect is also related to the presence of promoter ions because the activity of Mo/ASA is strongly inhibited by NH_3. The promotional effect for Co(Ni)Mo/ASA appears to be related to the presence of Brønsted acid hydroxyl groups that are eliminated through ammonia adsorption. Ion-exchange of those hydroxyl groups by sodium slightly increases the activity and, more importantly, leads to substantial decreases of the HDS activity in the presence of ammonia in a manner similar to $CoMo/Al_2O_3$ and CoMo/C. The promotion can be reversed upon desorption of ammonia from the support. Also transient thiophene HDS experiments show that the HDS activity correlates well with the number of free Brønsted acidic hydroxyl groups as probed by the rate of 1-butene isomerization. Infrared spectra of adsorbed CO point to an electronic effect of the acidic ASA support on the active metal sulfide phase. This effect becomes less pronounced upon ammonia adsorption to the support. These promotional effects are also not observed for the HDS of benzothiophene and dibenzothiophene, which is

explained by the stronger adsorption on the active sites of these reactants. It is speculated that the Brønsted acidity increases the sulfur bond energy which negatively affects the HDS performance. A tentative structural model is the one where Brønsted acidic hydroxyl groups influence the (vicinal) well-known linkages between the support and the active phase that are at the basis of the lower activity of type I Co-Mo-S structures.

Acknowledgment

The authors thank Dr. P.J. Kooyman of the National Centre for High-Resolution Microscopy at the Delft University of Technology for performing the TEM measurements.

References

1. H. Topsøe, B.S. Clausen, F.E. Masssoth., Hydrotreating Catalysis, Springer, Berlin, 1996.
2. J. Chen, Z. Ring, Fuel. 83 (2004) 305.
3. I.V. Babich, J.A. Moulijn, Fuel. 82 (2003) 607.
4. H. Topsoe, R. Candia, N.-Y. Topsoe, B.S. Clausen, Bull. Soc. Chim. Belg. 93 (1984) 783.
5. J.A.R. van Veen, E. Gerkema, A.M. van der Kraan, A. Knoester, J. Chem. Soc. Chem. Commun. 22 (1987) 1684.
6. E.J.M. Hensen, V.H.J de Beer, J.A.R. van Veen, R.A. van Santen, Catal. Lett. 84 (2002) 59.
7. B. Hinnemann, J.K. Nørskov, H. Topsøe, J. Phys. Chem. B. 109 (2005) 2245.
8. E.J.M. Hensen, V.H.J. de Beer, J.A.R. van Veen, R.A. van Santen, J. Catal. 215 (2003) 353.
9. W.R.A.M. Robinson, J.A.R. van Veen, V.H.J. de Beer, R.A. van Santen, Fuel Process. Technol. 61 (1999) 89.
10. E.J.M. Hensen, G.M.H.J. Lardinois, V.H.J. de Beer, J.A.R. van Veen, R.A. van Santen, J. Catal.187 (1999) 95.
11. F. Maugé, A. Vallet, J. Bachelier, J.-C. Duchet, J.-C. Lavalley, J. Catal. 162 (1996) 88.
12. A. Travert, C. Dujardin, F. Maugé, S. Cristol, J.-F. Paul, E. Payen, D. Bougeard, Catal. Today 70 (2001) 255.
13. C.E. Hedoire, C. Louis, A. Davidson, M. Breysse, F. Maugé, M. Vrinat, J. Catal. 220 (2003) 433.
14. B.M. Vogelaar, P. Steiner, A.D. van Langeveld, S. Eijsbouts, J.A. Moulijn, Stud. Surf. Sci. Catal. 145 (2003) 319.
15. F. Maugé, G. Crepeau, A. Travert, T. Cseri, Abstr. Pap. Am. Chem. Soc. 225 (2003) U853.
16. A. Travert, C. Dujardin, F. Maugé, E. Veilly, S. Cristol, J.-F. Paul, E. Payen, J. Phys. Chem. B 110 (2006) 1261.
17. M.J. Vissenberg, L.J.M. Joosten, M.M.E.H. Heffels, A.J. van Welsenes, V.H.J. de Beer, R.A. van Santen, J.A.R. van Veen, J. Phys. Chem. B. 104 (2000) 8456.
18. E.J.M. Hensen, P.J. Kooyman, Y. van der Meer, A.M. van der Kraan, V.H.J. de Beer, J.A.R. van Veen, R.A. van Santen, J. Catal. 199 (2001) 224.
19. E.J.M. Hensen, M.J. Vissenberg, V.H.J. de Beer, J.A.R. van Veen, R.A. van Santen, J. Catal. 163 (1996) 429.
20. R. Bezman, Catal. Today. 13 (1992) 143.
21. G. Crepau, PhD thesis, Caen, 2002.
22. V. LaVopa, C.N. Satterfield, J. Catal. 110 (1988) 375.
23. S. Blanchin, P. Galtier, S. Kasztelan, S. Kressmann, H. Penet, G. Pérot, J. Phys. Chem. A. 105 (2001) 10860.
24. A. Clark, The Theory of Adsorption and Catalysis; Academic Press: New York, 1970, pp.376-379.
25. A.M. Venezia, F. Raimondi, V. La Parola, G. Deganello, J. Catal.194 (2000) 393.
26. B. Hinnemann, J.K. Nørskov, H. Topsøe, J. Phys. Chem. B. 109 (2005) 2245.
27. A. Travert, H. Nakamura, R.A. van Santen, S. Cristol, J.-F. Paul, E. Payen, J. Am. Chem. Soc. 124 (2002) 7084.
28. H. Schwieger, P. Raybaud, H. Toulhoat, J. Catal. 212 (2002) 33.

29. T. Todorova, R. Prins, T.A. Weber, J. Catal.236 (2005) 190.
30. S. Cristol, J.-F. Paul, C. Schovsbo, E. Veilly, E. Payen, J. Catal.239 (2006) 145.
31. S. Cristol, J.-F. Paul, E. Payen, D. Bougeard, F. Hutschka, S. Clemendot, J. Catal. 224 (2004) 138.

Chapter 6

On the nature of the sulfur tolerance of ASA-supported NiMo(W) sulfide and Pt hydrogenation catalysts

Summary

Amorphous silica-alumina (ASA) based NiMo and NiW sulfide and Pt hydrogenation catalysts were prepared and compared in toluene hydrogenation to alumina- and silica-supported catalysts with the aim to elucidate the influence of (strong) Brønsted acidity of the support on the sulfur tolerance. To this end, ASAs were used with equal strong Brønsted acidity and varying composition as well as a more acidic ASA. Despite precautions to prepare NiMo sulfide catalysts with equal morphology, it was found that the stacking degree of the MoS_2 phase decreased with the Al_2O_3 content of the ASA. Similar but more pronounced differences of the stacking degree were observed for NiW sulfide catalysts. The variation in stacking degree had a substantial effect on the dibenzothiophene hydrodesulfurization activity.

A general conclusion is that ASA based catalysts have a higher aromatics hydrogenation activity than the silica- and alumina-supported ones. The sulfur tolerance of NiMo(W) sulfide and Pt metal active phases is also substantially improved by the use of ASA. The resistance against sulfur poisoning does not correlate with the number of strong Brønsted acid sites nor with the total Brønsted acidity. Instead, the sulfur tolerance decreases with increasing Al content of the ASA and can be understood in terms of the intermediate electronegativity of the support. Higher electronegativity leads to higher sulfur tolerance. Silica-supported catalysts do not follow this trend, which is understood in terms of Lewis acid sites inducing the electronic metal-support effect. Optimum sulfur tolerance is found for ASA supports with surfaces containing close to a monolayer of isolated Al^{3+} species. The work predicts that a further increase of the sulfur tolerance is possible by optimizing catalyst preparation towards increasing the interaction between the active phase and the Lewis acid sites.

6.1 Introduction

Amorphous silica-aluminas (ASAs) are technologically important acid catalysts, which are extensively used in the oil refining and petrochemical industry [1-3]. Although ASAs are less acidic than zeolites, present-day composite hydrocracking catalysts often contain ASA next to steam stabilized Y zeolite. ASAs are the main acid component in Diesel-selective hydrocracking catalysts [3]. In hydrocracking catalysts, an additional purpose of ASA is to disperse the hydrogenation function, which nearly always consists of the mixed metal sulfides of Ni and Mo or Ni and W. The use of noble metals such as Pt and PtPd has also been explored [4], specifically for two-stage hydrocracking processes [2] and for deep hydrogenation of aromatics [5]. Mixed sulfide combinations of NiMo, CoMo and NiW are also the essential ingredients of hydrotreating catalysts extensively used to remove hetero-atoms from organosulfur and organonitrogen compounds in distillate streams in oil refineries [6-8].

The resistance of hydrogenation catalysts against sulfur poisons is a critical issue in refinery practice because of the high sulfur content in crude oil feedstocks. Noble metals such as Pt exhibit a lower sulfur tolerance than mixed metal sulfides [4]. The acidity of the support has long been known to enhance the tolerance of noble metal catalysts towards poisons. This beneficial effect is more substantial for zeolites than for less acidic amorphous silica-aluminas [9,10]. A similar influence of the support acidity on the sulfur tolerance has been reported for CoMo and NiMo sulfide catalysts [11-14].

Despite considerable efforts the mechanism of sulfur poisoning of hydrogenation catalysts has not been unequivocally determined. An explanation that is well accepted for the combination of acidic zeolite-noble metal is a change in the metal-sulfur bond strength due to enhanced electron deficiency of the metal particles [15-17]. It has been argued that very small noble metal particles interact with strong Brønsted acid sites. An alternative is the direct involvement in hydrogenation of the acidic sites at the perimeter of the metal nanoparticles [18-21].

The role of acidity on amorphous silica-alumina based hydrogenation catalysts is less well-developed. Lercher and co-workers have shown that the aromatics hydrogenation activity of Pt/ASA varies with the intermediate electronegativity of the support containing Lewis acid sites [22]. The role of Lewis acid sites interacting with the metal particles was stressed. More recently, the same group attributed the higher sulfur tolerance of Pt/ASA compared to Pt/Al_2O_3 to reactant adsorption at Brønsted acid sites close to the metal particles, in case the metal surface is covered by sulfur-containinig compounds [21]. Hensen et al. have discussed the increased sulfur tolerance of sulfided Co(Ni)Mo/ASA in terms of a direct interaction between the support Brønsted acid sites and the mixed metal sulfides [23].

The purpose of this work is to establish whether the sulfur tolerance of ASA-based catalysts is indeed due to the Brønsted acidity of the support and, if so, whether this

relates to the very few Brønsted acid sites of zeolitic strength. An alternative to consider is the role of the composition of the mixed oxide support. To this end, the tolerance towards poisoning by hydrogen sulfide in toluene hydrogenation of a set of ASA catalysts with equal acidity but different composition (5-55 wt% Al_2O_3) and a more acidic ASA prepared by cogelation with a nominal Al_2O_3 content of 5 wt% was measured. Alumina and silica supported catalysts were included for comparison. As hydrogenation function Pt and the sulfides of NiMo and NiW were employed. With the aim to verify that only support acidity and composition were varied the thiophene and dibenzothiophene hydrodesulfurization activities of the NiMo and NiW sulfide catalysts were measured. The dispersion and the morphology of these active phases were investigated by transmission electron microscopy.

6.2 Experimental section

6.2.1 Catalyst preparation

A set of supported NiMo-NTA and NiW catalysts was prepared by pore volume impregnation. The preparation of the ASA supports has been described elsewhere [24] and their acidic properties were extensively characterized [25-27]. γ-alumina and silica were included for reasons of comparison. The textural and acidic properties of these support materials are collected in Table 6.1. Prior to impregnation, the supports were calcined at 573 K for 2 h. For NiMo-NTA catalysts, the impregnation solution contained the complexing agent nitrilotriacetic acid (VWR, 99% purity), ammonium heptamolybdate (Merck, 99% purity) and nickel nitrate (VWR, 99% purity) in such concentrations that a final Mo loading of 8 wt% and an atomic Co/Mo ratio of 0.3 was obtained. The molar NTA to Mo ratio was 1.2. The catalysts were dried at room temperature for 1 h and then at 383 K for 16 h in air. NiW catalysts were prepared by pore volume impregnation of the support with an appropriate solution of ammonium metatungstate (VWR, 99 % purity) and nickel nitrate (VWR, 99 % purity). A nominal W loading of 15 wt% and atomic Ni/W ratio of 0.3 was targetted. The catalysts were dried at room temperature for 1 h, dried overnight at 393 K and calcined at 723 K for 2 h in static air.

Pt catalysts were prepared by pore volume impregnation of the support with appropriate concentration of the platinum tetramine nitrate solution (Alfa Aesar) to give a final loading of 0.8 wt % Pt. After impregnation the catalysts were dried at room temperature of 1 h, dried overnight at 393 K and calcined at 723 K for 2 h in static air. Besides a set of ASA supports, two silica supports were employed with residual Al_2O_3 contents of 0.5 wt% (SiO_2) and <0.01 wt% (SiO_2-D). The metal content of the catalysts was determined by elemental analysis (ICP). Hydrogen chemisorption was employed to measure the Pt dispersion.

6.2.2 High resolution Transmission Electron Microscopy

The morphology of the active phase was analyzed by transmission electron microscopy of sulfided samples. Catalysts were sulfided in a mixture of 10 vol% H_2S in H_2 at a total flow rate of 60 ml/min. The temperature was increased from room temperature to 673 K at a rate of 6 K/min (2 K/min for NiMo-NTA catalysts). After an isothermal period of 2 h, the catalyst sample was cooled to 473 K in the sulfiding mixture and then in He to room temperature. The sample was then transferred via a nitrogen-flushed glove-box into a glass ampoule and transported to the TEM facility at the Delft University of Technology. The ampoule was opened in a glove-box. A few drops of ground sample suspended in n-hexane were then mounted on a carbon polymer supported on a copper grid. The sample was transferred to the microscope in a special vacuum-transfer sample holder to exclude air to prevent re-oxidation. The measurements were carried out using a Philips CM30T electron microscope with a field emission gun as the source of electrons at 300 kV. For each sample, 15 micrographs were recorded. Detailed analysis of the micrographs was carried out by measuring the length and stacking degree of at least 450 MoS_2 (WS_2) slabs for each catalyst.

Table 6.1: Textural properties and Brønsted acidity of the support materials.

Support	Al_2O_3 (wt%)	Surface area[1] (m^2/g)	Pore Volume[2] (ml/g)	T_{40} (K)[3]
ASA(5/95, 3)	4.3	419	2.0	612
ASA(5/95, cogel)	5.1	463	1.6	599
ASA(10/90, 3)	9	397	1.8	612
ASA(15/85, 3)	12.1	373	1.6	612
ASA(20/80)	10	364	1.4	611
ASA(55/45)	55	350	0.67	613
Al_2O_3	100	250	0.6	n.d.
SiO_2[4]	-	260	1.25	n.d.

[1]low temperature N_2 sorption; [2]water pore volume; [3]temperature required for 40% conversion during *n*-heptane hydroconversion [24]; [4] contains 0.5 wt% Al_2O_3.

The MoS_2 (WS_2) dispersion, which is defined as the average fraction of Mo(W) atoms at the MoS_2 (WS_2) edge surface and denoted by f_{Mo} (f_W), was calculated assuming that these MoS_2 slabs are present as perfect hexagons [28]. The MoS_2 (WS_2) dispersion is evaluated by dividing the total number of Mo atoms at the edge surface by the total number of Mo atoms using the slab sizes. The former number is determined from the slab size (L in Å) via

$$L = 3.2(2n_i\text{-}1) \qquad (6.1)$$

with n_i is the number of Mo (W) atoms along one side of a MoS_2 (WS_2) slab. Next to WS_2 slabs, nanometer sized round particles were observed in the micrographs of sulphided NiW catalysts.

6.2.3 Thiophene hydrodesulfurzation

Atmospheric pressure gas-phase thiophene hydrodesulfurization was carried out in a single-pass quartz microflow reactor with an internal diameter of 4 mm. Gaseous thiophene was obtained by passing hydrogen (99.95%, Hoekloos) through thiophene liquid (Merck, ≥ 99% purity) maintained in a saturator at a constant temperature of 293 K. The required thiophene concentration was obtained by diluting this flow with pure hydrogen. Thermal mass flow controllers (Brooks Instruments), driven by a computer system using D/A converters were used to feed the gaseous flows. The experiments were carried out under differential conditions by diluting an amount of catalyst (sieve fraction 125-250 μm) with silicon carbide of the same sieve fraction. Prior to reaction, the catalysts were sulfided in a mixture of H_2S/H_2 gas (Scott, 10 vol% H_2S in H_2) at a total flow rate of 60 ml/min. The samples were heated to 673 K at a ramp rate of 6 K/min (2 K/min for the NTA-containing catalysts). The temperature was kept at 673 K for 2h. After sulfidation, the catalyst was exposed to a mixture of 4 vol% thiophene and 1 vol% H_2S at this temperature. The total flow rate was maintained at 100 ml/min (STP). After the thiophene conversion was stabilized after 13 h, the temperature was lowered to 623 K and kinetic measurements were started. Intrinsic reaction rate constants were calculated from the thiophene HDS conversion. Hydrocarbon reactants and products were analyzed by an online gas chromatograph (ATI Unicam 610 series) equipped with a Chrompack CP-SIL 5 CB column (L = 50 m, d_i = 0.25 mm, d_f = 4 μm, FID).

6.2.4 Dibenzothiophene hydrodesulphurization

The dibenzothiophene (DBT) hydrodesulfurization activity was determined in a stainless-steel microflow reactor system. The reactor has an inner diameter of 18 mm and is heated in a three–zone oven. The reactor was loaded with an appropriate amount of catalyst diluted with 5 g SiC. H_2 (Linde, purity 99.95%) and H_2S/H_2 (Scott, 10 vol% H_2S) flows were controlled by Brooks Instruments mass flow controllers. Prior to reaction, the catalysts were sulfided in situ in a flow of 60 ml/min of 10 vol% H_2S/H_2 at atmospheric pressure. The samples were heated to 673 K at a rate of 6 K/min (2 K/min for the NiMo-NTA catalysts). The temperature was maintained at 673 K for 2h. Subsequently, the temperature was lowered to 533 K and the pressure raised to 30 bar. A mixture of DBT, *n*-decane and *n*-heptane (internal standard) was introduced via a Beckman 114M Solvent delivery pump. The final gas phase concentration of DBT was 200 ppm. The total H_2 gas flow was 500 ml/min (STP). Conversion and selectivity were

determined at three temperatures (533 K, 553 K and 573 K). At least 6 samples (approximately 6 h) were taken at each temperature. Online gas chromatographic analysis was performed by a Shimadzu GC-17A GC equipped a CPSIL- 5CB capillary column (L = 50 m, d_i = 0.25 mm, d_f = 4 μm) and a flame ionization detector. The pseudo first-order DBT reaction rate constant (k_{HDS}) was calculated from

$$k_{HDS} = -(F/W) \times \ln (1-X), \quad (6.2)$$

with F being the feed gas flow, W the molar amount of Mo (or W) in the catalyst and X the conversion of DBT. The apparent activation energies (E_{act}) and the pre-exponential factors (ν_{pre}) were evaluated from a plot of the first-order rate constant as a function of reaction temperature (533-573K).

6.2.5 Toluene hydrogenation

The same microflow system as employed for DBT HDS measurements was used to determine the catalytic performance in toluene hydrogenation. Sulfidation was carried out in the same manner as for DBT HDS. The Pt catalysts were reduced in H_2 at a flow rate of 60 ml/min at 573 K for 2 h after heating to this temperature at a rate of 10 K/min. The reaction feed consisted of a hydrogen flow of 500 ml/min (STP) with 1000 ppm toluene and varying concentrations (500-2000 ppm) of H_2S at a total pressure of 30 bar. The reaction temperature was 573 K. The liquid flow was controlled by a Beckman 114M Solvent delivery pump. Toluene (VWR, > 99%) was dissolved in *n*-decane to obtain a final gas-phase concentration of 1000 ppm toluene. Online GC analysis was similar to the DBT HDS experiments. Kinetic measurements were started after a stabilization period of 6 h at standard reaction conditions (1000 ppm toluene, 500 ppm H_2S). Reaction orders of the different components were determined by reaction rate measurements as a function of the component partial pressure (toluene: 500–2000 ppm, H_2S: 500–4000 ppm) under differential conditions.

6.3 Results

Table 6.2 summarizes the metal loadings of the various NiMo and NiW catalysts as determined by ICP analysis. The values for the Mo loadings include the presence of NTA. The W loadings are slightly lower than the targetted loading of 15 wt %. The Ni/Mo ratios are around their optimum of 0.3, except for the NiMo-NTA/ASA(5/95, cogel) and the non-NTA catalysts, which contain a slightly higher amount of promoter ions. The Ni/W ratios were kept at 0.3, which is somewhat lower than optimum values reported in literature [29].

Table 6.2: Metal loadings of NiMo and NiW catalysts.

Catalyst	Mo (wt%)	W (wt%)	Ni (wt%)	Ni/Mo(W) molar ratio
NiMo-NTA/SiO_2	6.2	-	2.7	0.4
NiMo-NTA/ASA(5/95, 3)	5.9	-	1.7	0.3
NiMo-NTA/ASA(5/95, cogel)	6.2	-	2.7	0.4
NiMo-NTA/ASA(10/95, 3)	6.0	-	1.8	0.3
NiMo-NTA/ASA(15/85, 3)	6.3	-	1.8	0.3
NiMo-NTA/ASA(20/80)	5.9	-	2.3	0.4
NiMo-NTA/ASA(55/45)	7.0	-	2.0	0.3
NiMo-NTA/Al_2O_3	6.4	-	1.9	0.3
NiW/SiO_2	-	13.5	3.9	0.3
NiW/ASA(5/95, 3)	-	13.5	4.1	0.3
NiW/ASA(5/95, cogel)	-	13.2	4.0	0.3
NiW/ASA(10/90,3)	-	13.7	4.0	0.3
NiW/ASA(15/85, 3)	-	13.7	4.0	0.3
NiW/ASA(20/80)	-	13.7	4.0	0.3
NiW/ASA(55/45)	-	14.2	4.1	0.3
NiW/Al_2O_3	-	13.8	4.0	0.3

Fig. 6.1 shows representative electron micrographs of sulfided NiMo-NTA/SiO_2, NiMo-NTA/ASA(5/95, 3), NiMo-NTA/ASA(20/80) and NiMo-NTA/Al_2O_3. All catalysts contain monolayer and stacked MoS_2 slabs. Fig. 6.2 gives the corresponding MoS_2 slab size distribution. Average slab size and stacking degree are collected in Table 6.3. The MoS_2 dispersion is reasonably constant for this set of materials, which is due to the use of NTA [30]. The distribution of the active phase over the silica support in NiMo-NTA/SiO_2 is rather inhomogeneous. The catalyst contains areas with multilayered and relatively large slabs and areas with a very low slab density. NiMo-NTA/ASA(5/95, 3) shows a similar distribution with areas containing monolayer MoS_2 slabs and areas containing particles consisting of multiple stacked slabs. With increasing aluminium concentration of the ASA support, the contribution of areas with monolayer slabs increases as reflected by the decrease in the average stacking degree. NiMo-NTA/Al contains a homogeneous distribution of MoS_2 particles consisting of one or two slabs in line with earlier reports [31]. The morphology of sulfided NiMo-NTA/ASA(55/45) is comparable with that of sulfided NiMo-NTA/Al. However, in some micrographs areas of multilayered slabs up to three layers are observed, whereas in other parts single layer MoS_2 slabs dominate. The ASA(55/45) support is manufactured through a process that shows similarity with deposition precipitation route. Due to the high Al content aluminium hydroxides precipitate, which leads to the formation of γ-Al_2O_3 domains next to an amorphous silica-alumina part [24]. The heterogeneous composition of the support explains the slab size distribution with single slabs on the γ-Al_2O_3 alumina part and multilayered slabs on the ASA part. The

morphology of the sulfided NiMo-NTA/ASA(5/95, cogel) catalyst is very similar to that of sulfided NiMo-NTA/ASA(5/95, 3). The use of NTA served the goal to exclude metal-support interactions and end up with very similar NiMo sulfide phases after sulfidation. Clearly, this was not completely successful and the active phase is not a pure type II phase as suggested before [30]. Dugulan has recently discussed the more complex type I/II phase behaviour of $CoMo/Al_2O_3$ catalysts than assumed hitherto [32].

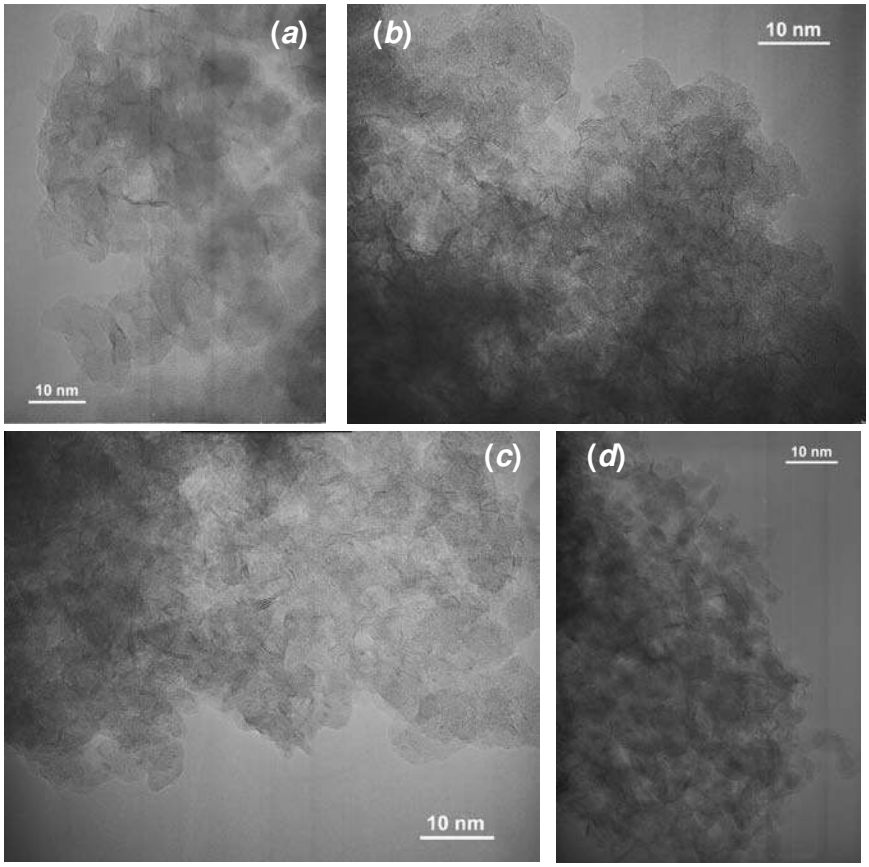

Figure 6.1: High resolution transmission electron micrographs of sulfided (a) NiMo-NTA/SiO_2, (b) NiMo-NTA/ASA(5/95, 3), (c) NiMo-NTA/ASA(20/80) and (d) NiMo-NTA/Al_2O_3.

Fig. 6.3 shows representative transmission electron micrographs of NiW/SiO_2 (a), NiW/ASA(5/95, 3) (b), NiW/ASA(20/80) (c) and NiW/Al_2O_3 (d). The slab size distributions of the WS_2 slabs for NiW/ASA(5/95, 3), NiW/Al_2O_3 and NiW/SiO_2 are given in Figure 6.4 and Table 6.3 contains the most important morphological parameters of the sulfided NiW catalysts. The active phase of NiW/SiO_2 contains multilayered slabs. Similar to NiMo-NTA/SiO_2, the slabs are not distributed homogeneously over the support surface. Besides the WS_2 slabs, a relatively high density of nanometer-sized round particles were observed. These particles have been observed before for sulfided W-containing catalysts [31,33] and are thought to result from incomplete sulfidation of tungsten oxides. Similar to its NiMo-NTA counterpart,

the slabs are inhomogeneously distributed over the surface in NiW/ASA(5/95, 3). With increasing aluminium concentration of the ASA support, the amount of monolayer slabs increases. The active phase of NiW/Al_2O_3 mainly contains particles consisting of one or two slabs. The fraction of the round particles decreases with increasing concentration of aluminium of the support. While for NiW/SiO_2 many nanometer-sized particles were observed in all the micrographs, their density decreases strongly with increasing Al content of the ASA support. In NiW/ASA(20/80) only a very few of such particles were observed and these were absent in the micrographs of NiW/Al_2O_3. The active phases in sulfided NiW/ASA(5/95, 3) and NiW/ASA(5/95, cogel) are very similar.

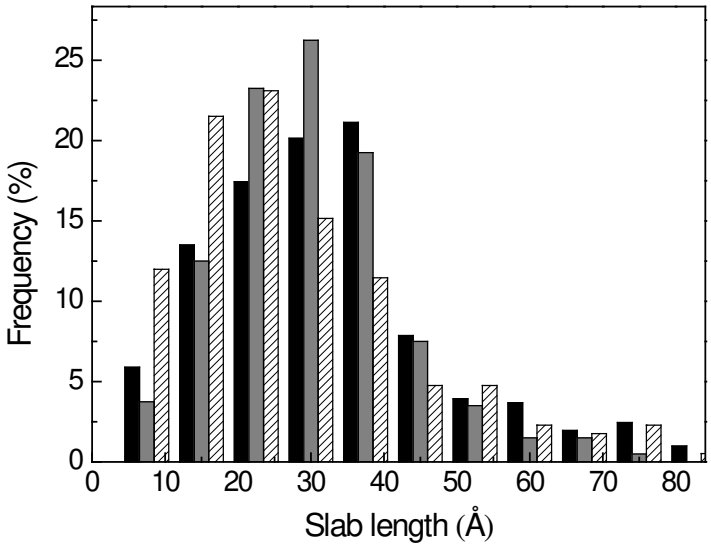

Figure 6.2: Slab size distribution of sulfided (black) NiMo-NTA/SiO_2, (grey) NiMo-NTA/ASA (5/95, 3) and (patterned) NiMo-NTA/Al_2O_3.

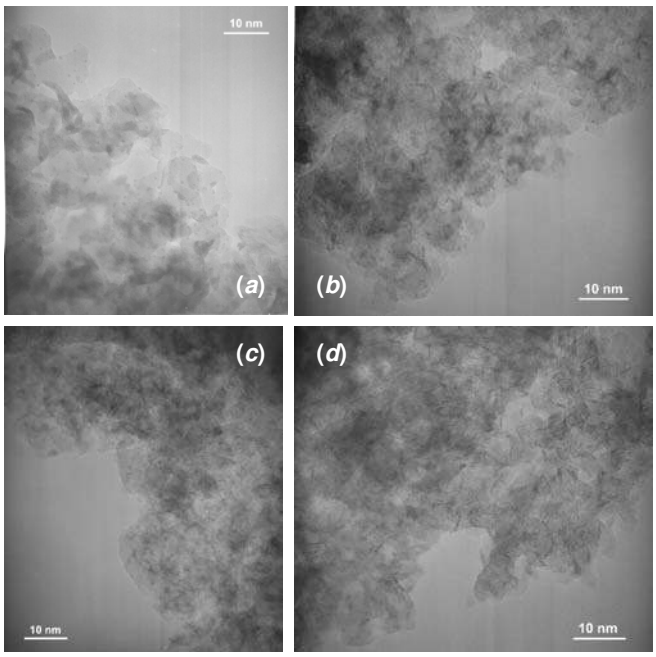

Figure 6.3: High resolution transmission electron micrographs of sulfided (a) NiW/SiO_2, (b) NiW/ASA(5/95, 3), (c) NiW/ASA(20/80) and (d) NiW/Al_2O_3.

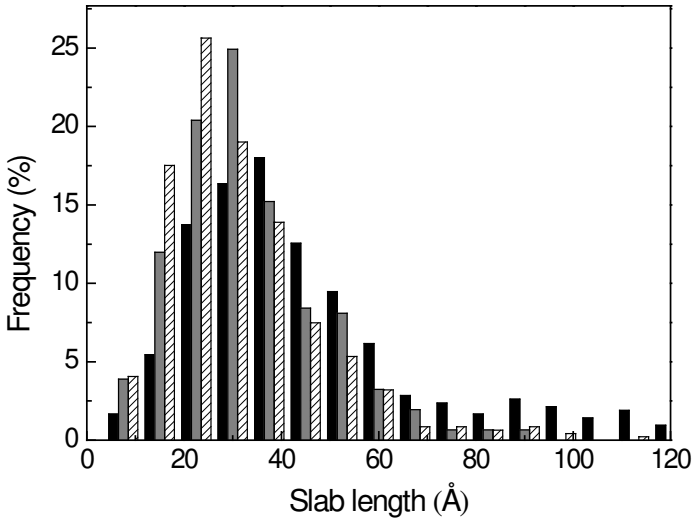

Figure 6.4: Slab size distribution of sulfided (black) NiW/SiO_2, (grey) NiW/ASA (5/95, 3) and (patterned) NiW/Al_2O_3.

6.3.2 Thiophene and dibenzothiophene HDS

The thiophene HDS reaction rates of the sulfided NiMo-NTA and NiW catalysts are listed in Table 6.4. The reaction rate is expressed on a per mol total Mo(W) basis. For the NiMo-NTA catalysts, the overall reaction rate is nearly constant as a function of the support material. This finding is in line with results reported by Van Veen et al. [30] that the use of the complexing agent NTA results in equal thiophene HDS activities independent of the type of support. Their idea was that the use of complexing agents minimizes the metal-support interaction during catalyst preparation and sulfidation. It has also been shown that their use retards the sulfidation of promoter ions such as Co and Ni up to the point where the molybdenum component is completely sulfided [34]. This has been interpreted in the formation of the fully sulfided and more active Type II Co-Mo-S phase. Recent infrared studies on CO adsorption on sulfided CoMo catalysts with varying NTA amounts showed that the presence of NTA results in a more optimal edge dispersion of the Co promoter phase [35, 36]. Nevertheless, as outlined above, the differences in stacking degree indicate that there may be some differences between the catalysts in terms of phase I/II behaviour.

Table 6.3: Morphological parameters of the sulfided catalysts.

Catalyst	Average slab length (nm)	Average stacking degree	$f_{Mo(W)}$
NiMo-NTA/SiO_2	3.3	2	0.35
NiMo-NTA/ASA(5/95, cogel)	2.9	1.7	0.39
NiMo-NTA/ASA(5/95, 3)	3.2	1.6	0.36
NiMo-NTA/ASA(10/95, 3)	2.8	1.5	0.40
NiMo-NTA/ASA(15/85, 3)	3.0	1.4	0.38
NiMo-NTA/ASA(20/80)	3.2	1.5	0.36
NiMo-NTA/ASA(55/45)	2.9	1.4	0.4
NiMo-NTA/Al_2O_3	2.8	1.4	0.4
NiW/SiO_2	4.5	2.9	0.26
NiW/ASA(5/95,cogel)	3.3	2.1	0.33
NiW/ASA(5/95, 3)	3.3	2.3	0.33
NiW/ASA(10/90, 3)	3.3	2.2	0.35
NiW/ASA(15/85, 3)	3.2	2.2	0.36
NiW/ASA(20/80)	2.8	2	0.40
NiW/ASA(55/45)	2.8	1.5	0.40
NiW/Al_2O_3	3.1	1.4	0.37

The thiophene HDS activities of the sulfided NiW catalysts depend more strongly on the exact nature of the support which partly could be explained by the absence of NTA or similar complexing agents during the catalyst preparation. The sulfidation degree of NiW catalysts is lower than of NiMo ones [29]. The ASA- and alumina-supported NiW catalysts display slightly higher activity than the silica-supported ones. This difference is at least partly due to the relatively large amount of incompletely sulfided particles in the latter catalyst. Among the set of ASA supports prepared by deposition-precipitation, the thiophene HDS activity decreases with increasing aluminium content of the support. The reason for this trend is not clear. The electron micrographs shows a decreasing contribution of oxysulfidic particles with increasing Al content, which suggests that the sulfidation degree is not the explanation for the lower activity of NiW/ASA(15/85, 3) and NiW/ASA(20/80). The activity of NiW/ASA(55/45) and NiW/Al_2O_3 is nearly equal in line with earlier work [29], which is explained by the preference of the metatungstate precursor for the γ-alumina part of the support [38].

The pseudo first-order rate constants (k_{DBT}) and the selectivities to biphenyl (BP) and cyclohexylbenzene (CHB) for DBT HDS are reported in Table 6.5. The rate constants have been corrected for the dispersion of MoS_2 and WS_2. A clear support influence is observed. In agreement with the trends in thiophene HDS, the activity differences are more substantial for the NiW than for the NiMo-NTA catalysts. For the latter set, the DBT HDS activity does not strongly depend on the composition of the ASA with relatively low alumina content. However, NiMo-NTA/ASA(55/45) and NiMo-

NTA/Al_2O_3 are substantially more active than the SiO_2- and other ASA-supported catalysts.

Table 6.4: Thiophene HDS activities for sulfided NiMo-NTA and NiW catalysts (623 K, 1 bar, 4 vol% thiophene and 1 vol% H_2S in H_2).

Support	Reaction rate (mol thiophene/mol Mo(W).h)	
	NiMo-NTA	NiW
SiO_2	40	7
ASA(5/95,cogel)	42	12
ASA(5/95, 3)	41	12
ASA(10/95,3)	42	12
ASA(15/85, 3)	39	9
ASA(20/80)	41	8
ASA(55/45)	41	15
Al_2O_3	41	14

Another substantial difference is the higher CHB selectivity for the ASA catalysts than for the sulfided NiMo catalysts supported on the ASA(5/95, cogel), SiO_2 and Al_2O_3. The higher CHB selectivity is due to a higher contribution of the hydrogenative route of DBT desulfurization. DBT HDS primarily occurs via direct desulfurization with biphenyl (BP) as the main product and via hydrogenation of one of the phenyl rings with cyclohexylbenzene as the product (CHB) [6-8]. Although it has been claimed that under typical conditions the hydrogenation of BP to CHB is negligible [12], others have shown that this interconversion can make a conclusive interpretation of the reaction pathways difficult [39-41]. The apparent activation energies for the catalysts (Table 6.6) are also substantially different. A notable result is also that the CHB selectivity and the apparent activation energy of NiMo-NTA/ASA(55/45) is in the same range of values of other ASA samples, whereas the activity is much more similar to that of NiMo-NTA/Al_2O_3.

The activity differences are more pronounced for the NiW series. Similar to thiophene HDS, the DBT HDS activity decreases with Al content of the ASA support up to ASA(20/80). The activity of NiW/SiO_2 is only slightly higher than that of NiW/ASA(5/95, 3) and NiW/ASA(5/95, cogel). Peculiarly, the activity of NiW/ASA(55/45) and NiW/Al_2O_3 is substantially higher than of the other catalysts. Very similar to NiMo-NTA, NiW/ASA(55/45) exhibits a high CHB selectivity, yet its activity is much closer to that of the alumina-supported NiW catalyst. The much higher activity of the catalysts prepared with ASA(55/45) and Al_2O_3 supports requires further discussion. The only substantial difference with the other catalysts is the stacking degree of the metal sulfide phase. The data suggest that the stacking degree has a more pronounced effect on the DBT HDS activity than on the thiophene HDS activity. Earlier

studies have attempted to correlate the DBT HDS activities to the MoS_2 morphology. Daage and Chianelli have found that the top and bottom MoS_2 layers of bulk MoS_2 (rim sites) are active in hydrogenation and hydrodesulfurization of DBT whereas the layers in between (edge sites) catalyze preferentially hydrodesulfurization [42]. Hensen et al. have found that the DBT HDS reaction rate of supported MoS_2 catalysts increases with the stacking degree [31].

Table 6.5: DBT HDS reaction rates and selectivities for sulfided NiMo-NTA and NiW catalysts.

Catalyst	k_{DBT} (h^{-1})			S_{CHB} (%)[1]	S_{BP} (%)[1]
	523 K	553 K	573 K		
NiMo-NTA/SiO_2	8.9	15.3	25.8	15	85
NiMo-NTA/ASA(5/95, cogel)	10.3	19.2	29.2	12	88
NiMo-NTA/ASA(5/95, 3)	8.6	18.9	35.8	27	73
NiMo-NTA/ASA(10/90,3)	8.2	19.2	37.8	30	70
NiMo-NTA/ASA(15/85, 3)	8.0	17.8	35.4	29	71
NiMo-NTA/ASA(20/80)	9.8	21.9	45.4	28	72
NiMo-NTA/ASA(55/45)	10.7	25.8	52.6	30	70
NiMo-NTA/Al_2O_3	14.6	26.0	43.2	11	89
NiW/SiO_2	3.1	5.0	8.0	15	85
NiW/ASA(5/95, cogel)	2.7	4.6	8.0	18	82
NiW/ASA(5/95, 3)	2.7	5.5	11.4	17	83
NiW/ASA(10/90, 3)	2.5	5.8	12.0	22	78
NiW/ASA(15/85, 3)	1.8	3.8	7.6	12	88
NiW/ASA(20/80)	1.8	3.8	7.6	19	81
NiW/ASA(55/45)	8.1	17.5	34.6	27	73
NiW/Al_2O_3	11.9	19.0	27.4	9	92

[1] selectivities to cyclohexylbenzene (CHB) and biphenyl (BP) at 553 K.

Clearly, these model studies do not provide an adequate explanation for the trends observed for the present Ni-promoted MoS_2 and WS_2. This is not surprising because the active phase is promoted by Ni in the present study. The data show that stacking of the Ni-promoted slabs has a negative effect on their DBT HDS activity, whereas it does not affect the thiophene HDS activity. To exemplify this trend, Fig. 6.5 shows the intrinsic rates of DBT and thiophene HDS as a function of the MoS_2 stacking degree for NiMo-NTA catalysts. The strong decrease of the DBT HDS activity with stacking degree suggests that the intrinsic activity of the first layer in direct contact with the support is considerably higher than that of subsequent layers on top of the first one. An alternative explanation involves a higher number of special hydrogenation (brim) sites [43] in catalysts with a lower stacking degree. However, this does not tally with the observation that direct desulfurization pathway remains dominant for all catalysts. Moreover, the ASA(55/45)- and Al_2O_3-supported catalysts have the same stacking degree, but exhibit

substantially different toluene hydrogenation activities and CHB selectivities (*vide infra*).

6.3.3 Toluene hydrogenation

Hydrogenation of toluene to methylcyclohexane was the dominant reaction over the sulfides with small amounts of ethylcyclopentane, 1,1-dimethylcyclopentane, 1,2-dimethylcyclopentane and 1,3-dimethylcyclopentane. The selectivity to these isomerized products was found to increase with the hydrogen sulfide partial pressure, indicating that perhaps sulfhydryl species play a role in the isomerization of an intermediate product. Very minor amounts of lighter alkanes were observed. A separate experiment under similar conditions with a feed only containing *n*-decane showed that these lighter alkanes are due to hydrocracking of the solvent. Solvent hydrocracking was absent for the alumina- and silica-supported catalysts.

Table 6.6: Kinetic parameters for the HDS of DBT in the temperature range 523-573 K (3 bar, 200 ppm DBT in H_2).

Support	NiMo-NTA		NiW	
	E_{act} (kJ/mol)	A (s)	E_{act} (kJ/mol)	A (s)
SiO_2	67	8.2	59	4.9
ASA(5/95, cogel)	66	8.3	68	7.1
ASA(5/95, 3)	91	13.5	92	12.5
ASA(10/95, 3)	97	14.9	98	14.0
ASA(15/85, 3)	94	14.2	101	12.0
ASA(20/80)	98	15.1	90	12.0
ASA(55/45)	101	16.1	92	13.8
Al_2O_3	69	9.1	53	5.3

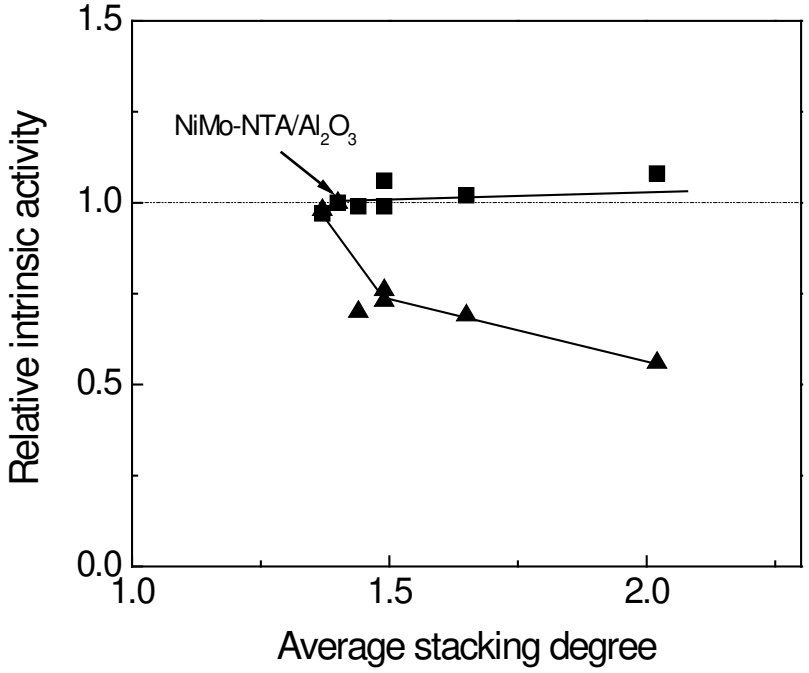

Figure 6.5: Relative intrinsic DBT HDS (▲) and thiophene HDS (■) activities of sulfided NiMo-NTA catalysts as a function of the average stacking degree. The reference catalyst is NiMo-NTA/Al_2O_3.

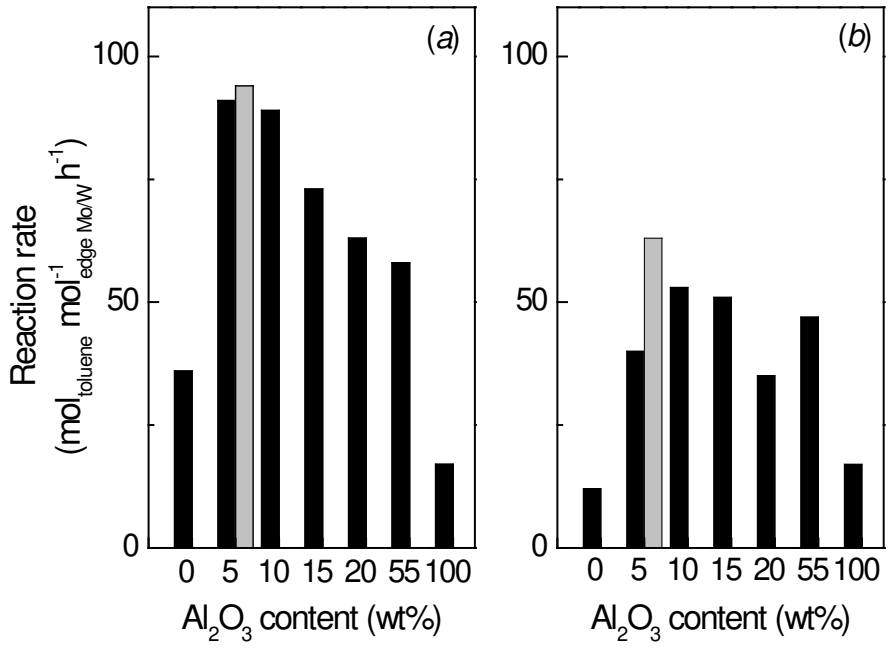

Figure 6.6: Hydrogenation of toluene over NiMo-NTA (a) and NiW (b) catalysts as a function of the Al_2O_3 content of the supports (573 K; 30 bar H_2; 1000 ppm toluene; 500 ppm H_2S). The grey bar refers to the cogel ASA samples.

Fig. 6.6 shows the intrinsic reaction rates in toluene hydrogenation for the sulfided NiMo-NTA and NiW catalysts at a total pressure of 30 bar and a temperature of 573 K. The activity of the ASA-supported catalysts is substantially higher than the silica- and alumina-supported ones. For the NiMo-NTA series, the reaction rate is highest for NiMo-NTA/ASA(5/95) and decreases with increasing Al content of the support. The rate of NiMo-NTA/ASA(5/95, cogel) is nearly equal to that of NiMo-NTA/ASA(5/95, 3). The trend is similar for the NiW/ASA catalysts. For these catalysts, the NiW/ASA(5/95,3) is less active than NiW/ASA(5/95, cogel). The activity of NiW/ASA(20/80) seems to be an outlier in this set of catalysts. The NiMo-NTA catalysts exhibit a higher hydrogenation activity than the NiW ones. This difference is due to the lower sulfur tolerance of the latter type of catalysts, but the lower W sulfidation degree may also play a role [29]. The higher hydrogenation activities of the ASA-supported catalysts are in line with the higher contribution of the hydrogenative desulfurization route in the DBT HDS measurements. However, as direct desulfurization in DBT HDS dominates over the hydrogenative route, the activity trends in toluene hydrogenation and DBT HDS are different.

Fig. 6.7 shows the reaction orders in H_2S for the two sets of sulfided catalysts. The closer the reaction order to zero, the higher the sulfur tolerance. The sulfur tolerance of the NiMo-NTA catalysts is higher than that of the NiW catalysts. The sulfur tolerance is highest for the metal sulfide phases supported on ASA(5/95, 3) and ASA(10/90, 3). With increasing Al content, the sulfur tolerance decreases and is lowest for the alumina-supported end member. The sulfur tolerance of the silica-supported catalysts is also lower than that of the ASA-supported ones. While NiMo-NTA/ASA(5/95, cogel) is less sulfur tolerant in hydrogenation than its less acidic counterpart with the same support composition, the corresponding two NiW samples have the same sulfur tolerance.

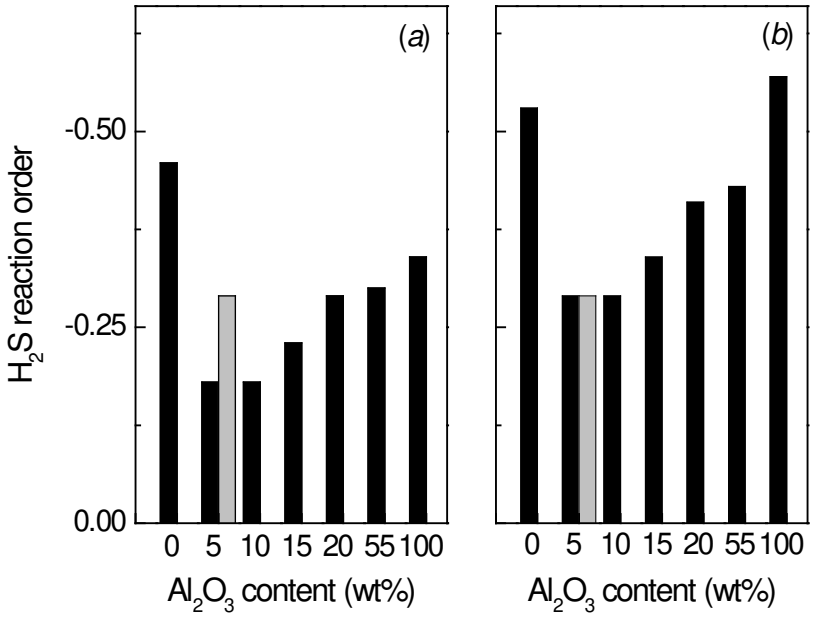

Figure 6.7: H_2S reaction orders in the hydrogenation of toluene over NiMo-NTA (a) and NiW (b) catalysts as a function of the Al_2O_3 content of the supports (573 K; 30 bar H_2; 1000 ppm toluene; 500-2000 ppm H_2S).

Next to the set of sulfided catalysts, the sulfur tolerance of Pt loaded samples was also determined. Because the sulfur resistance of Pt is much lower than that of the metal sulfides [13], it was not possible to perform these measurements under differential conditions. To evaluate the reaction order in hydrogen sulfide, an integral model was employed assuming a reaction order in toluene of 0.6, which followed from kinetic measurements of a number of Pt catalysts. The results are given in Table 6.7. The Pt particle size of the catalysts varied much more as a function of the support than reported earlier [44]. The metal particles were very small on Pt/SiO_2 and Pt/Al_2O_3 and somewhat larger for Pt/ASA. When a Al-free silica was employed the particles were much larger in correspondence to findings for Au/SiO_2 [45]. Despite the differences in Pt particle size, the effect of the acidic support on the hydrogenation activity of Pt is evident. The activities of the ASA-supported catalysts are quite similar and much higher than the activities of the silica- and alumina-supported catalysts. The activity of Pt/ASA(55/45) is somewhat lower than that of Pt/ASA(20/80). The sulfur tolerance of the ASA-supported catalysts decreases with increasing Al content of the support. The sulfur tolerance of Pt/ASA(5/95, 3) is very similar to that of Pt/ASA(5/95, cogel). These results clearly show that the sulfur tolerance strongly depends on the composition and not on the Brønsted acidity of the support. Pt/SiO_2(D) has a much lower activity, which is due to the lower dispersion and likely also to a support effect.

Table 6.7. Pt particle size, toluene hydrogenation activity and sulfur tolerance for supported Pt catalysts.[1]

Catalyst	Pt size (nm)	Rate constant $((mol/m^3)^{0.4})/s)$	order in H_2S (-)
$Pt/SiO_2(D)$	8.0	2.5×10^{-3}	-1.39
Pt/SiO_2	1.8	5.4×10^{-2}	-1.08
Pt/ASA(5/95, 3)	5.6	6.9×10^{-1}	-0.85
Pt/ASA(10/90, 3)	4.0	7.4×10^{-1}	-0.88
Pt/ASA(15/85, 3)	4.1	6.6×10^{-1}	-0.95
Pt/ASA(20/80)	3.4	7.6×10^{-1}	-0.93
Pt/ASA(55/45)	3.0	8.3×10^{-2}	-1.01
Pt/ASA(5/95, cogel)	4.8	5.8×10^{-1}	-0.83
Pt/Al_2O_3	1.5	1.0×10^{-3}	-1.36

[1] 573 K, 30 bar, 1000 ppm H_2S.

6.4 Discussion

The present work addresses the question whether the very few strong Brønsted acid sites in ASA bring about the improved sulfur tolerance in ASA-based hydrogenation catalysts. Variations in the composition of ASA usually lead to variations in the Brønsted acidity. However, by using controlled synthesis by deposition of Al^{3+} on a reactive silica-gel a set of ASA supports with constant Brønsted acidity at varying composition was obtained [24-26]. Another sol-gel preparation route provided an ASA of similar composition but with higher acidity. The dispersion of the active phase of NiMo and NiW sulfide catalysts is reasonably constant. Despite efforts to minimize metal-support effects by using NTA for NiMo catalysts, the stacking degree varies between the various supports and the active phase is probably not the targetted pure type II phase. The difference in stacking degree has a more pronounced influence on the DBT HDS than on thiophene HDS. Notwithstanding these morphological differences, the set of ASA-supported NiMo and NiW sulfide catalysts was evaluated for differences in sulfur tolerance in toluene hydrogenation. Additionally, a set of supported Pt catalysts has been prepared with the same supports.

The tolerance towards hydrogen sulfide in the hydrogenation of toluene was determined for NiMo and NiW sulfide and Pt metal catalysts. From the finding that the sulfur tolerance varies considerably for the ASA-based catalysts with similar Brønsted acidity, it is inferred that strong Brønsted acidity is not the cause of increased resistance against sulfur poisoning. The ASA supports contain a weaker form of Brønsted acidity next to the acid sites of zeolitic strength [27]. As the number of weak Brønsted acid sites increases with increasing Al content, it becomes clear that sulfur tolerance is also not induced by these Brønsted acid sites. Instead, the sulfur tolerance appears to be mainly determined by the composition of the support. The higher the aluminium

content, the lower the sulfur tolerance. An exception to this trend form the silica-supported catalysts that have a low sulfur tolerance, very similar to the alumina-supported catalysts. Optimal sulfur tolerance is found for catalysts based on the ASA containing 5 wt% Al_2O_3. The trends in the toluene hydrogenation activity also correlate to the composition. The ASA-based catalysts are much more active than their silica- and alumina-based counterparts.

Lercher and co-workers have also concluded that the substantial activity differences in aromatics hydrogenation for supported Pt particles are due to a compositional effect of the support [22]. They argued that the intermediate electronegativity of the support induces an electronic metal-support effect. From the finding that Pt/SiO_2 does not follow the trends, it is argued that Lewis acid sites of the support bring about the metal-support effect. The electronegativity (χ) of an atom refers to its ability to draw electrons to itself. The concept presents a way to differentiate between ionic ($\Delta\chi > 2$) and covalent bonding ($\Delta\chi < 0.5$).A scale for electronegativity of the atoms was first proposed by Pauling [46]. Others such as Mulliken [47] and Sanderson [48] have derived different scales for electronegativity. Of these, the Sanderson scale is particularly useful as he proposed the principle of electronegativity equalization, which allows the calculation of the electronegativity of mixed compounds. The Sanderson electronegativity scale is based on the realization that electronegativity depends on the effective nuclear charge felt by the outermost valence electrons. The Sanderson electronegativity relates to the compactness of an atom by using the ratio of the electron density of the atom, being the atomic number divided by the atomic volume based on the covalent radius, and the expected electron density, computed from extrapolation between the noble gas elements between which the atom is located in the periodic table. The principle of electronegativity equalization refers to the distribution of electrons in a compound such that the energy is minimized. This results in an intermediate electronegativity of the compound and provides a useful concept to compute effective charges rather than formal charges on the constituent atoms. Here, the intermediate electronegativity of (mixed) oxides is relevant. The intermediate electronegativity (χ_{int}) is the geometric mean of the individual electronegativities of the constituent atoms

$$\chi_{\text{int}} = \left(\prod \chi_i^{x_i}\right)^{\left(\sum x_i\right)^{-1}} \tag{6.3}$$

with χ_i is the electronegativity of atom i and x_i the atomic fraction in the solid. Note that it is required to use the Sanderson electronegativity scale for applying the equalization principle. Table 6.8 lists the intermediate Sanderson electronegativities of the support materials employed in this study. Owing to the larger electronegativity of Si (χ = 2.14)

than Al (χ = 1.71), the intermediate electronegativity of SiO_2 is larger than that of Al_2O_3. With increasing Al content of ASA, χ_{int} decreases.

Table 6.8: Intermediate electron negativity (χ_{int})of the supports materials calculation on the basis of the principle of electronegativity equalization. The values have been determined on the basis of the nominal composition.

Catalyst	χ_{int}
SiO_2	3.055
ASA(1/99)	3.051
ASA(5/95,cogel)	3.036
ASA(5/95, 3)	3.036
ASA(10/90, 3)	3.018
ASA(15/85, 3)	2.999
ASA(20/80)	2.980
ASA(55/45)	2.853
Al_2O_3	2.700

Fig. 6.8 shows the relation between the sulfur tolerance of NiMo and NiW sulfide catalysts and the intermediate electronegativity of the support. Clearly, the sulfur tolerance increases with increasing silica content. In general, the differences between the sulfur tolerances of Al_2O_3-, ASA(55/45)- and ASA(20/80)-supported catalysts are smaller than those within the range of the more silica-rich ASA compositions. The sulfur tolerance shows a maximum for the catalysts with a nominal Al_2O_3 content of 5 wt%. In line with Lercher's findings [22], the electronic metal-support effect is not present in silica-supported catalysts.

The results for the supported Pt catalysts (Fig. 6.9) are in very good agreement with those for the metal sulfide ones. The sulfur tolerance of the ASA-supported Pt catalysts is much higher than that of Pt/Al_2O_3 and Pt/SiO_2. Moreover, the sulfur tolerance decreases with increasing aluminium content of the ASA. Even a small amount of Al in the silica will result in an improved sulfur tolerance. The use of a very pure silica (SiO_2(D) in Fig. 6.9) results in a much lower sulfur tolerance. Similar to the NiMo and NiW case, the hydrogenation activity of Pt/ASA is higher than that of Pt/Al_2O_3, although the decrease of the activity with increasing Al content is less pronounced.

To interpret these trends in terms of Lewis acid sites the surface composition of the ASA will be briefly reiterated. ASA(5/95, 3) is a relatively pure ASA with only a very small fraction of segregated domains of alumina. The Al species are present in highly dispersed form. The number of isolated Al species decreases wth increasing Al content due to the formation of more agglomerated forms of Al. In ASA(20/80) about half of the Al atoms are part of a segregated alumina phase, the other half remaining in dispersed form on the silica surface. The surface contains two forms of Lewis acid sites [27]. Strong Lewis acid sites are associated with isolated or highly dispersed Al^{3+} on the

silica surface. The weaker form is related to more agglomerated forms of Al. The number of strong Lewis acid sites decreases with Al content of the ASA, whereas the number of weak Lewis acid sites associated with the segregated alumina domains strongly increases.

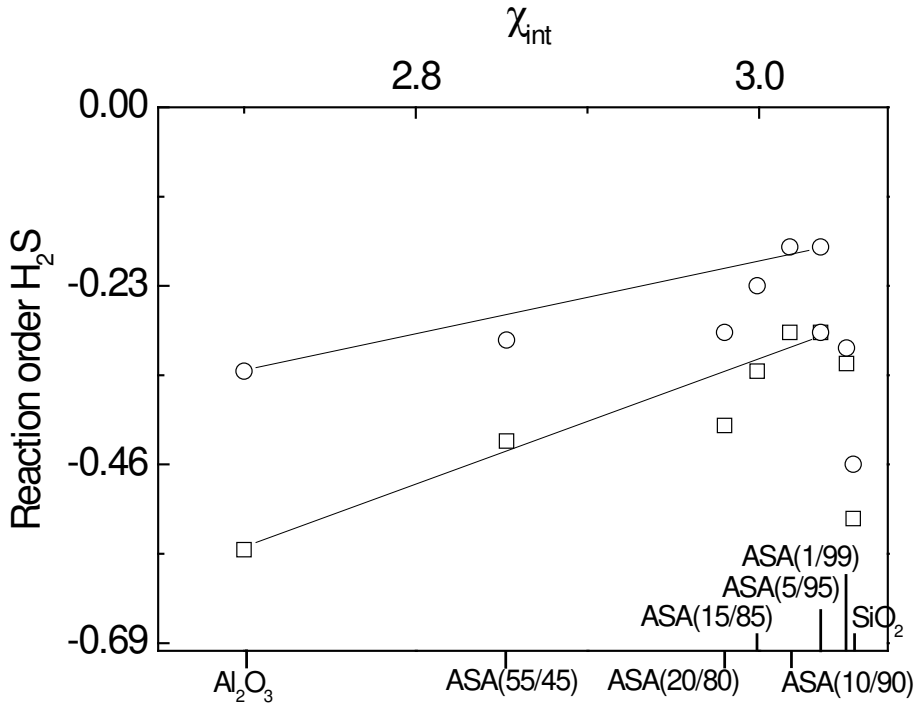

Figure 6.8: The reaction order in H_2S in toluene hydrogenation for a set of supported NiMo-NTA (○) and NiW (□) catalysts as a function of the intermediate electronegativity of the support. The lines are meant to guide the eye.

Based on the trends in Fig. 6.8 it is clear that both forms of Lewis acid sites are responsible for inducing the electronic metal-support effect. The monolayer coverage of (bipodal) Al^{3+} on the silica support corresponds to a nominal content of 6.5 wt% [24]. Therefore, one expects a maximum in the sulfur tolerance at this loading and this provides a satisfactory explanation for the nearly equal sulfur tolerance of ASA(5/95) and ASA(10/90). With increasing Al content the sulfur tolerance decreases stronger than expected on the basis of the linear relations (between ASA(5/95, 3) and Al_2O_3) given in Fig. 6.8. This deviation is most likely due to the assumption of a homogeneous mixed oxide for the calculation of the intermediate electronegativities in Table 6.8. Amorphous silica-aluminas contain most of the Al on their surface and this means that the active metal (sulfide) phase interacts on average with a surface containing locally a higher Al content than the nominal composition. The trend between sulfur tolerance and intermediate electronegativity is more linear for the Pt catalysts with an Al_2O_3 content higher than 5 wt%. This may be interpreted in terms of a stronger interaction of the Pt

precursor and the Lewis acid sites than between the Mo precursor and those sites during preparation.

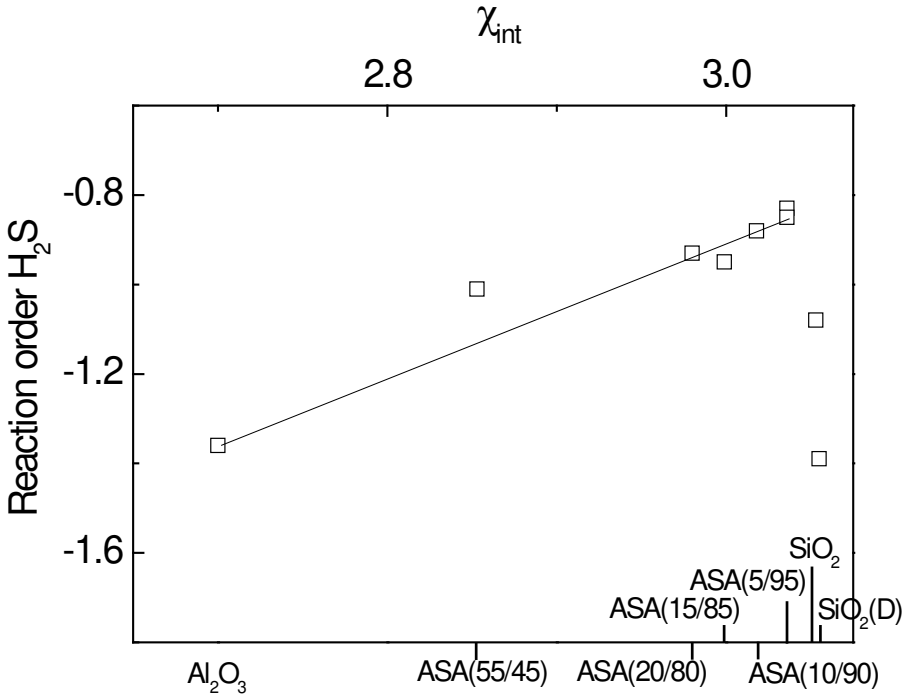

Figure 6.9: The reaction order in H_2S in toluene hydrogenation for a set of supported Pt catalysts as a function of the intermediate electronegativity of the support. The lines are meant to be a guide to the eye.

To verify further that ASA(5/95, 3) is the optimum composition for the metal sulfide catalysts, additional NiMo-NTA and NiW catalysts were prepared with an ASA with a nominal Al_2O_3 content of 1 wt%. This should be a pure ASA phase containing isolated Al species at a much lower density than in ASA(5/95). Fig. 6.8 shows that the sulfur tolerances of NiMo-NTA/ASA(1/99) and NiW/ASA(1/99) lie between those of their respective ASA(5/95, 3)- and SiO_2-supported counterparts. If one assumes an average $Mo(W)S_2$ particle size of 3 nm, each slab will contain about 66 Mo(W) atoms. The corresponding slab density is 7.6×10^{18} g^{-1}. At an Al_2O_3 content of 1 wt%, the Al density is 1.2×10^{20} g^{-1}. Thus, in theory there are enough Al centers to coordinate all the $Mo(W)S_2$ slabs in these catalysts. However, at 1 wt% Al_2O_3 content, not all of the Al sites appear to form Lewis acid sites. This would then explain why the sulfur tolerance of the catalysts on ASA (1/99) lies between those of pure silica and ASA(5/95). These results suggest that catalyst preparation needs to be further optimized when the goal is to optimize the sulfur tolerance of supported metal sulfide hydrogenation catalysts.

6.5 Conclusions

Amorphous silica-alumina based NiMo and NiW sulfide and Pt hydrogenation catalysts were prepared and compared in toluene hydrogenation to alumina- and silica-supported catalysts with the aim to elucidate the influence of (strong) Brønsted acidity of the support on the sulfur tolerance. NTA was employed in the preparation of NiMo sulfide phases with constant morphology. Although the dispersion was constant, the stacking degree of the MoS_2 phase decreased with the Al_2O_3 content of the ASA. Similar but more pronounced differences were found for NiW sulfide catalysts. The variation in stacking degree had a substantial effect on the dibenzothiophene hydrodesulfurization activity. Considerable variations in the Pt particle size were also noted.

A general conclusion is that ASA based catalysts have a higher aromatics hydrogenation activity than their silica- and alumina-supported counterparts. The sulfur tolerance of NiMo(W) sulfide and Pt metal active phases is substantially improved by the use of ASA as the support. The resistance against sulfur poisoning does not correlate with the number of strong Brønsted acid sites nor with the total Brønsted acidity. Instead, the sulfur tolerance decreases with increasing Al content of the ASA and can be understood in terms of the intermediate electronegativity of the support. Higher electronegativity leads to higher sulfur tolerance. Silica-supported catalysts do not follow this trend, which is understood in terms of Lewis acid sites inducing the electronic metal-support effect. Optimum sulfur tolerance is found for ASA with close to a monolayer of isolated Al^{3+} species on its surface. The data indicate that a further increase of the sulfur tolerance is possible by optimizing catalyst preparation towards increasing the interaction between the active phase and the Lewis acid sites.

References

1. A. Corma, Chem. Rev. 95 (1995) 559.
2. J. Scherzer, A.J. Gruia, Hydrocracking Science and Technology, Dekker, New York, 1996, pp. 215.
3. G. Busca, Chem. Rev. 107 (2007) 5366.
4. H.R. Reinhoudt, R. Troost, A.D. van Langeveld, J.A.R. van Veen, S.T. Sie, J.A. Moulijn, Stud. Surf. Sci. Catal. 127 (1999) 251.
5. B.H. Cooper, B.B.L. Donnis, Appl. Catal. A: Gen 137 (1996) 203.
6. H. Topsoe, B.S Clausen, F.E. Massoth, Hydrotreating Catalysis Science and Technology, Springer-Verlag New York, 1996.
7. C. Song, Cat. Today. 86 (2003) 211.
8. S. Eijsbouts, Appl. Catal. A: Gen. 158 (1997) 53.
9. P. Gallezot, Catal. Rev.-Sci. Eng. 20 (1979) 121.
10. M.V. Rahaman, M.A.J. Vannice, J. Catal. 127 (1991) 251.
11. H.R. Reinhoudt, M.van Gorsel, A.D. van Langeveld, J.A.R. van Veen, S.T. Sie, J.A. Moulijn, Stud. Surf. Sci. Catal. 127 (1999) 211.
12. W.R.A.M. Robinson, J.A.R. van Veen, V.H.J. de Beer, R.A. van Santen, Fuel. Proc. Tech. 61 (1999) 89.
13. W.R.A.M. Robinson, J.A.R. van Veen, V.H.J. de Beer, R.A. van Santen, Fuel. Proc. Tech. 61 (1999) 103.

14. E.J.M. Hensen, V.H.J. de Beer, J.A.R. van Veen, R.A. van Santen, J. Catal. 215 (2003) 353.
15. T.T. Phuong, J. Massardier, P. Gallezot, J. Catal. 102 (1986) 456.
16. R. Szymanski, H. Charcosset, P. Gallezot, J. Massardier, J.L. Tournayan, J. Catal. 97 (1986) 366.
17. P. Gazellot, G. Bergeret, Catalyst Deactivation, Marcel Dekker, New York, 1987, p. 263.
18. P. Chou, M.A.. J. Catal. 107 (1987) 129.
19. S.D. Lin, M.A. Vannice, J. Catal. 143 (1993) 563.
20. M.V. Rahaman, M.A. Vannice, J. Catal. 127 (1991) 251.
21. M.F. Williams, B. Fonfé, A. Jentys, C. Breitkopf, J.A.R. van Veen, J.A. Lercher, J. Phys. Chem. C. 114 (2010) 14352.
22. M.F. Williams, B. Fonfé, C. Woltz, A. Jentys, J.A.R. van Veen , J.A. Lercher, J. Catal. 251 (2007) 497.
23. E.J.M. Hensen, D.G. Poduval, J.A.R. van Veen, Ind. Eng. Chem. Res. 46 (2007) 4202.
24. E.J.M. Hensen, D.G. Poduval, P.C.M.M. Magusin, A.E. Coumans, J.A.R. van Veen, J. Catal. 269 (2010) 201.
25. E.J.M. Hensen, D.G. Poduval, J.A.R. van Veen, M.S. Rigutto, Chem. Commun. 46 (2010) 3466.
26. E.J.M. Hensen, D.G. Poduval, D.A.J.M. Ligthart, J.A.R. van Veen and M.S. Rigutto, J. Phys. Chem C. 114 (2010) 8363.
27. Chapter 4 of this thesis.
28. S. Kasztelan, H. Toulhoat, J. Grimblot, J.P. Bonnelle, Appl. Catal. 13 (1984) 127.
29. E.J.M. Hensen, Y. van der Meer, J.A.R. van Veen, J.W. Niemantsverdriet, Appl. Catal. A. 322 (2007) 16.
30. J.A.R. van Veen, E.R. Gerkema, A.M. van der Kraan, E. Knoester, J. Chem. Soc., Chem. Commun. 1987 1684.
31. E.J.M. Hensen, P.J. Kooyman, Y. van der Meer, A.M. van der Kraan, V.H.J. de Beer, J.A.R. van Veen, R.A. van Santen, J. Catal. 199 (2001) 224.
32. A.I. Dugulan, Ph.D. Thesis, Delft University of Technology, Delft, 2008.
33. H.R. Reinhoudt, A.D. van Langeveld, P.J. Kooyman, R.M. Stockmann, R. Prins, H. W. Zandbergen, J. A. Moulijn, J. Catal. 179 (1998) 443.
34. L. Coulier, V.H.J. de Beer, J.A.R. van Veen, J.W. Niemantsverdriet, J.Catal. 197 (2001) 26
35. M.A. Lélias, E. Le Guludec, L. Mariey, J. van Gestel, A. Travert, L. Oliviero, F. Maugé, Catal.Today. 150 (2010) 179.
36. M.A. Lélias, P.J. Kooyman, L. Mariey, L. Oliviero, A. Travert, J. van Gestel, J.A.R. van Veen, F. Maugé , J. Catal. 267 (2009) 14.
37. H.R. Reinhoudt, R. Troost, A.D. van Langeveld, J.A.R. van Veen, S.T. Sie, J. Moulijn, J. Catal. 203 (2001) 509.
38. M.J. Vissenberg, L.J.M. Joosten, M.E.H. Heffels, A.J. van Welsenes, V.H.J. de Beer, R.A. van Santen, J.A.R. van Veen, J. Phys. Chem. B. 104 (2000) 8456.
39. T.C. Ho, J.E. Sobel, J.Catal. 128 (1991) 581.
40. V.Meille, E. Schulz, M. Lemaire, M. Vrinat, J.Catal. 170 (1997) 29.
41. M. Egorova, R. Prins, J.Catal. 221 (2004) 11.
42. M. Daage, R.R. Chianelli, J. Catal. 149 (1994) 414.
43. H. Topsøe, Appl. Catal. A. 322 (2007) 3.
44. M.F. Williams, B. Fonfé, C. Sievers, A. Abraham, J.A. van Bokhoven, A. Jentys, J.A.R. van Veen, J.A. Lercher, J. Catal. 251 (2007) 485.
45. Y.J. Guan, E.J.M. Hensen, Appl. Catal. A. 361 (2009) 49.
46. L. Pauling, J. Am. Chem. Soc. 54 (1932) 3570.
47. R.S. Mulliken, J. Chem. Phys. 2 (1934) 782.
48. R.T. Sanderson, J. Am. Chem. Soc. 105 (1983) 2259.

Chapter 7

Summary

Amorphous silica-alumina (ASA) is widely used as a solid acid catalyst or as a carrier for well-dispersed metal sulfide or metal catalysts. They are often involved in hydrocracking catalyst formulations, especially so when the aim is to produce middle distillates from heavy oil fractions. With increasing demand for diesel and kerosene balanced acidity in these catalysts to combine high conversion with high middle distillates selectivity is crucial. An important advantage of amorphous silica-alumina as an acidic catalyst is its open texture with substantial mesoporosity as compared to zeolites that typically suffer from diffusion limitations when bulky hydrocarbons need to be converted. Strongly acidic supports also cause excessive coke formation and overcracking of the feedstock resulting in lower middle distillate yields. Therefore, the use of ASA as the acidic component in bifunctional hydrocracking has become important. Although moderate acidity is important for ASA supports, accurate control of the acidity is hampered by a lack of understanding about the origin of acid sites in these materials and how they are formed. Regarding the former, the nature of the Brønsted acid sites (BAS) has not been unequivocally established. The more widely shared opinion is that the Brønsted acidity derives from tetrahedral Al^{3+} in the silica network, as initially proposed by Thomas and Tamele in the late 1940s. This proposal however has remained inconclusive. Alternative explanations for the acidity have been also been proposed. These include Lewis acidic Al ions substituting for protons of surface silanol groups and the higher acidity of silanol groups in the presence of neighbouring aluminium surface atoms The other reason that surface acidity of ASAs is understood to a much lesser extent than that of zeolites relates to the complex surface composition of these mixed oxides. ASAs are made by co-precipitation, co-gelation or grafting processes and in nearly all cases, the resulting materials contain a non-random distribution of aluminium in silica

The present project was thus undertaken with the aim of (i) synthesizing a set of ASA materials by as controlled a method as possible for use in catalytic activity studies and (ii) to learn about the genesis of Brønsted acid sites in ASAs and their strength. The synthesis method chosen was a well-defined variant of grafting, *viz.*, homogeneous deposition-precipitation. The entire process of the deposition of aluminium on silica and subsequent calcination was followed by ^{27}Al NMR spectroscopy . The study showed that the aluminium species in the dried precursors is a function of pH and starting aluminium concentration. At pH of 3 and at low aluminium concentration, the surface mainly consists of tetrahedral and octahedral aluminium species. Under these conditions an increase in pH gives mainly rise to

tetrahedral aluminium species on the surface. This is attributed to the further condensation reaction occurring with the surface silanol groups. However, with increasing aluminium concentration, the deposition mechanism involves reaction of aluminium species in solution with species already grafted on the surface. This results in the formation of polymeric aluminium species. In addition, at higher aluminium concentrations some precipitation of aluminium hydroxide also occurs. When the dried precursors are then calcined, redistribution of the grafted aluminium species occurs, mainly with a small fraction of aluminium diffusing into the silica matrix thereby resulting in Brønsted acid sites. The formation of Brønsted acid sites upon calcination was also evidenced by n-alkane hydroconversion activity tests, which requires the presence of strong acid sites. From this systematic study the surface of amorphous silica- alumina could be described as consisting of three different species, namely a pure silica-alumina phase that originates from isolated aluminium grafted onto the silica surface, domains of aluminium oxide and a small fraction of aluminium in the silica network responsible for the strong Brønsted acidity.

By following the selective H/D exchange of acidic hydroxyl groups in aluminosilicates by IR spectroscopy clear evidence was provided for the existence in ASAs of BAS comparable in strength to the bridging hydroxyl groups in zeolites. The method is able to distinguish various types and strengths of strong BAS in aluminosilicates (zeolites, clays, ASAs) such as enhanced acidic sites in steam calcined faujasite zeolites. By carrying out the H/D exchange under conditions under which zeolites selectively exchange their bridging hydroxyl groups, weak bands were observed at 2630 and 2683 cm^{-1} in the deuteroxyl region of ASAs. By quantification it follows that the concentration of strong BAS in ASAs is 2-3 orders of magnitude lower than in zeolites. A number of techniques (CO IR, pyridine IR, alkylamine TPD, Cs^+ and $Cu(EDA)_2^{2+}$ exchange, ^1H NMR and *m*-xylene isomerization) was used to validate the H/D exchange FTIR results and provide further insight into the heterogeneous surface composition of ASA. The results show that the surface contains both Brønsted and Lewis acid sites of varying acidity. The number of strong Brønsted acid sites of zeolitic strength is very low (< 10 μmol/g). Careful interpretation of IR spectra of adsorbed CO and pyridine confirmed that the surface contains only very few of such sites. Other methods suitable to estimate strong BAS involve an adaptation of the well-known decomposition of alkylamines and titration of such sites by a base during *m*-xylene isomerization. These sites originate from Al substitutions in the silica network. Besides, the surface contains between 50-150 μmol/g of a weaker form of BAS, which can be easily quantified by CO IR. $Cu(EDA)_2^{2+}$ exchange also appears to probe weak BAS. The structure of these sites remains unresolved, but some of the results suggest that these are related to paired sites, involving the interaction of strong Lewis acid sites with silanol groups. In addition, the surface of ASA contains two forms of Lewis acid sites: (i) a weaker form associated with segregated alumina domains and probably containing five-coordinated Al species that make up the interface between such domains and the ASA phase and (ii) a stronger form which are lower coordinated Al sites grafted to the silica surface.

The second part of the thesis dealt with the role of the surface acidity and composition of ASAs in the catalytic activity of supported transition metal sulfides and noble metal phases. A critical issue in industrial practice is the sulfur and nitrogen tolerance, because hydrogen sulfide and ammonia, which are the products of hydrodesulfurization and hydrodenitrogenation reactions in hydrotreating and hydrocracking units, inhibit catalytic activity. Earlier work indicated that the acidic hydroxyl groups of ASAs influence the sulfur tolerance of CoMo and NiMo sulfides. It was observed the rate of thiophene HDS of ASA supported Co(Ni)Mo sulfides increases in the presence of ammonia, while a negative rate was observed for alumina and carbon supported Co(Ni)Mo sulfides. An explanation for the observed effects was the influence of the Brønsted acidic hydroxyl groups on the nature of active Co(Ni)MoS phase. Infrared studies using CO as probe molecule indicated that the support induces an electronic effect on the active metal sulfide phase.

In order to clarify the possible role of strong Brønsted acidity of the support on the sulfur tolerance in hydrogenation reactions, a set of NiMo-NTA and NiW sulfide and Pt metal catalysts were prepared on (i) ASAs varying composition but with equal Brønsted acidity and (ii) an ASA prepared at a similar composition but with a higher Brønsted acidity. Alumina- and silica-supported catalysts were included in these studies. Despite precautions to prepare NiMo sulfide catalysts with equal morphology, it was found that the stacking degree of the MoS_2 phase decreased with the Al_2O_3 content of the ASA. Similar but more pronounced differences of the stacking degree were observed for NiW sulfide catalysts. The variation in stacking degree had a substantial effect on the dibenzothiophene hydrodesulfurization activity, but not on the thiophene hydrodesulfurization activity. Similarly, the Pt dispersion was found not to be constant, with the ASA-supported catalysts having larger Pt particles than the alumina- and silica-supported ones.

A general conclusion is that ASA based catalysts have a higher aromatics hydrogenation activity than the silica- and alumina-supported ones. The sulfur tolerance of NiMo(W) sulfide and Pt metal active phases is also substantially improved by the use of ASA. The resistance against sulfur poisoning does not correlate with the number of strong Brønsted acid sites nor with the total Brønsted acidity. Instead, the sulfur tolerance decreases with increasing Al content of the ASA and can be understood in terms of the intermediate electronegativity of the support. Higher electronegativity leads to higher sulfur tolerance. Silica-supported catalysts do not follow this trend, which is understood in terms of Lewis acid sites inducing the electronic metal-support effect. Optimum sulfur tolerance is found for ASA supports with surface containing close to a monolayer of isolated Al^{3+} species. These results predict that a further increase of the sulfur tolerance is possible by optimizing catalyst preparation towards increasing the interaction between the active phase and the Lewis acid sites.

Samenvatting

Amorf silica-alumina (ASA) wordt op grote schaal gebruikt als vaste zure katalysator en als dragermateriaal voor goed gedispergeerde metaalsulfide- of metaalkatalysatoren. Deze materialen maken vaak onderdeel uit van *hydrocracking*-katalysatoren, met name wanneer het doel is middendestillaten te produceren uit zware oliefracties. Met de toenemende vraag naar diesel en kerosine is een evenwichtige zuurgraad in deze katalysatoren van belang, zodat hoge conversie gecombineerd kan worden met een hoge middendestillaten selectiviteit. Een belangrijk voordeel van ASA als zure katalysator is de open poriestructuur ten opzichte van zeolieten die typisch last van diffusiebeperkingen hebben bij de omzetting van volumineuze koolwaterstoffen. Sterke zuurheid resulteert in overmatige vorming van koolafzetting en het overkraken van de grondstof. Daarom is de toepassing van ASA als zure component in bifunctionele *hydrocracking*-katalysatoren belangrijk geworden. Nauwkeurige controle over de zuurgraad van ASA's wordt belemmerd door een gebrek aan begrip over de herkomst van de zure plaatsen in deze materialen en hoe ze gevormd worden. De aard van de Brønsted zure plaatsen is niet eenduidig bepaald. Algemeen geaccepteerd is een model waarin Brønsted zuurheid van aluminosilicaten voortvloeit uit de tetraëdrische omringing van Al^{3+} in het silicanetwerk, zoals aanvankelijk voorgesteld door Thomas en Tamele in de late jaren '40 van de vorige eeuw. Dit initiële voorstel is nog steeds niet onomstotelijk bewezen. Alternatieve verklaringen voor de zuurgraad omvatten Lewis zure aluminium ionen, die de de protonen van silanolgroepen aan het oppervlak vervangen en de hogere zuurgraad van silanolgroepen in de nabijheid van aluminium atomen aan het oppervlak. De andere reden dat de oppervlaktezuurheid van ASA in veel mindere mate begrepen wordt dan die van zeolieten heeft betrekking op de complexe oppervlaktesamenstelling van deze mengoxides. ASA's worden gemaakt door co-precipitatie, co-gelering of *grafting* processen. In bijna alle gevallen bevat het resulterende materiaal een niet-willekeurige distributie van aluminium in silica.

Het huidige project werd uitgevoerd met het doel om (i) een set van ASA's te synthetiseren op een gecontroleerde manier voor gebruik in katalytische activiteitsstudies en (ii) om de vorming en sterkte van Brønsted zure sites in ASA te begrijpen. De gekozen synthesemethode is een goedgedefinieerde variant van *grafting*, namelijk homogene-depositieprecipitatie. Het hele proces van de depositie van aluminium op silica en de daaropvolgende stappen werd onderzicht door middel van ^{27}Al NMR spectroscopie. Deze studie toonde aan dat de aard van het aluminium aluminium in de gedroogde materialen een functie is van de pH en de initiële aluminiumconcentratie. Bij een pH van 3 en bij een lage aluminiumconcentratie bevat het oppervlak voornamelijk tetraëdrisch en octaëdrisch aluminium. Onder deze omstandigheden leidt een verhoging van de pH vooral tot tetraëdrisch aluminium op het oppervlak. Dit wordt toegeschreven aan de verdere condensatiereactie die optreedt met de silanolgroepen aan het oppervlak. Echter, met toenemende aluminiumconcentratie verloopt het *grafting*-proces via de reactie van aluminium in de oplossing met aluminium die reeds gedeponeerd is op het oppervlak. Dit resulteert in de

vorming van polymere vormen van aluminium. Bovendien, bij hogere concentraties zal ook aluminiumhydroxide neerslaan. Wanneer de gedroogde materialen vervolgens gecalcineerd worden treedt een herverdeling van het aluminium op. Een kleine fractie van het aluminium diffundeert in de silicamatrix hetgeen resulteert in Brønsted zure plaatsen. De vorming van Brønsted zure plaatsen gedurende het calcineren werd ook aangetoond door n-alkaan hydroisomerisatie-experimenten. Uit deze systematische studie volgt dat het oppervlak van amorf silica-alumina bestaat uit drie verschillende vormen van aluminium, namelijk een zuivere silica-alumina fase die bestaat uit geïsoleerde aluminium aanwezig op het silicaoppervlak, domeinen van alumina en een kleine fractie van aluminium in het silicanetwerk dat verantwoordelijk is voor de sterke Brønsted zuurheid.

Door het volgen van de selectieve waterstofdeuteriumuitwisseling van zure hydroxylgroepen in aluminosilicaten met infraroodspectroscopie is duidelijk bewijs verkregen voor het bestaan van Brønsted zure plaatsen in ASA's vergelijkbaar in sterkte aan de bruggende hydroxylgroepen in zeolieten. De methode is in staat verschillende soorten en sterktes van sterke Brønsted zure plaatsen in aluminosilicaten onderscheiden (zeolieten, kleien, ASA's). Door het uitvoeren van de isotoopuitwisselingsexperimenten onder condities waaronder zeolieten selectief hun bruggende hydroxylgroepen uitwisselen zijn zwakke infraroodbanden waargenomen bij 2630 en 2683 cm^{-1} in het deuteroxylgebied voor ASA. Uit kwantificering volgt dat de concentratie van sterke Brønsted zure plaatsen in ASA 2-3 ordegroottes lager ligt dan in zeolieten. Een aantal technieken (CO IR, pyridine IR, alkylamine TPD, Cs^+- en $Cu(EDA)_2^{2+}$-uitwisseling, ^1H NMR en isomerisatie van *m*-xyleen) werd gebruikt om de isotoopuitwisselingsexperimenten te valideren en verder inzicht te krijgen in de heterogene samenstelling van het ASA oppervlak. De resultaten laten zien dat het oppervlak zowel Brønsted en Lewis zure plaatsen bevat van verschillende zuurgraad. Het aantal sterke Brønsted zure plaatsen van zeolitische sterkte is zeer laag (<10 μmol/g). Zorgvuldige interpretatie van de infraroodspectra van geadsorbeerd CO en pyridine bevestigt dat het oppervlak slechts zeer weinig van dergelijke sites bevat. Andere methodes geschikt om de hoeveelheid sterke Brønsted zure plaatsen omvatten een aangepast versie van de bekende ontleding van alkylamines en titratie van dergelijke sites middels isomerisatie van *m*-xyleen gevolgd door vergiftiging met een base. Deze sites zijn afkomstig van aluminium substituties in het silicanetwerk. Het oppervlak bevat tussen 50-150 μmol/g van een zwakkere vorm van Brønsted zure plaatsen, die gemakkelijk kunnen worden gekwantificeerd door CO IR. $Cu(EDA)_2^{2+}$-uitwisseling is ook een methode om deze zwak Brønsted zure plaatsen te kwantificeren. De structuur van deze plaatsen is nog niet helder, maar sommige van de resultaten suggereren dat deze voortkomen uit de interactie van sterke Lewis-zure plaatsen met silanolgroepen. Bovendien bevat het oppervlak van ASA twee vormen van Lewis-zure plaatsen: (i) een zwakkere vorm gerelateerd aan de gesegregeerde aluminadomeinen en waarschijnlijk bestaande uit vijfgecoördineerd aluminium die deel uitmaken van het grensvlak tussen deze domeinen en de ASA fase en (ii) een sterkere vorm, die besaat uit coördinatief meer onverzadigde aluminium atomen op het silica oppervlak.

Het tweede deel van dit proefschrift behandelt de invloed van de zuurgraad en de samenstelling van ASA op de katalytische activiteit van gedragen overgangsmetaalsulfiden en edelmetalen. Een kritiek punt in de industriële praktijk is de zwavel- en stikstoftolerantie, omdat waterstofsulfide en ammoniak - dat zijn de producten van ontzwavelings- en ontstikstoffingsreacties in *hydrotreating* en *hydrocracking* procesoperaties - de katalytische activiteit remmen. Uit eerder werk bleek dat de zure hydroxylgroepen van ASA de zwaveltolerantie van CoMo en NiMo sulfiden beïnvloedt. De reactiesnelheid van thiofeenontzwaveling van ASA gedragen Co(Ni)Mo sulfiden neemt toe in de aanwezigheid van ammoniak, terwijl een omgekeerd effect werd waargenomen voor alumina- en koolstofgedragen Co(Ni)Mo sulfides. Een verklaring voor de waargenomen effecten was de invloed van de Brønsted zure hydroxylgroepen op de aard van de actieve Co(Ni)MoS fase. Infraroodspectroscopische studies met behulp van CO tonen aan dat de drager een elektronisch effect heeft op de actieve metaalsulfidefase.

Met het doel oom de mogelijke rol van sterke Brønsted zure plaatsen van de drager op de zwaveltolerantie in hydrogeneringsreacties te bepalen werd een reeks NiMo-NTA en NiW katalysatoren bereid op (i) ASA dragers met wisselende samenstelling, maar met gelijke Brønsted zuurheid en (ii) een ASA bereid met een vergelijkbare samenstelling maar met een hogere Brønsted zuurheid. Ook alumina- en silica-gedragen katalysatoren werden bereid. Ondanks voorzorgsmaategelen om NiMo sulfide katalysatoren te maken met een gelijke morfologie van de actieve fase bleek de stapelingsgraad van de MoS_2 fase af te nemen met toenemende Al hoeveelheid van de ASA. Dergelijke verschillen werden ook waargenomen voor de NiW sulfide katalysatoren. Deze verschillen in stapelingsgraad leiden tot verschillende katalytische activiteiten in de ontzwaveling van dibenzothiofeen, maar niet in die van thiofeen. Ook de Pt dispersie bleek niet constant te zijn; de deeltjes op Pt/ASA waren typisch groter dan die op Pt/Al_2O_3 en Pt/SiO_2.

Een algemene conclusie is dat ASA-gebaseerde katalysatoren een hogere hydrogeneringsactiviteit van aromaten hebben dan silica- en alumina-gedragen katalysatoren. De zwaveltolerantie van NiMo(W) sulfide en Pt metaal actieve fases neemt toe door het gebruik van ASA als drager. Deze tolerantie correleert niet met het aantal sterk Brønsted zure plaatsen en ook niet met de totale Brønsted zuurheid. In plaats daarvan neemt de zwaveltolerantie af met toenemende Al hoeveelheid van de ASA. De verschillen worden veroorzaakt door verschillen in electronegativiteit van de drager. Een hogere electronegativiteit leidt tot een hogere zwaveltolerantie. silica-gedragen katalysatoren volgens deze trend niet. De reden hiervoor is dat silica geen Lewis zure oppervlakteplaatsen heeft die nodig zijnom het electronische metaal-drager effect te induceren. Een maximale zwaveltolerantie wordt verkregen voor een ASA drager met een oppervlakte dat bestaat uit een monolaag van geïsoleerd Al^{3+}. Uit deze resultaten volgt dat een verdere verhoging van de zwaveltolerantie mogelijk zou moeten zijn door de katalysatorsynthese te optimaliseren met het doel om de interactie tussen de actieve metaal (sulfide) fase en de Lewis zure plaatsen te verbeteren.

Acknowledgements

It has been a journey that started with a simple email inviting me over for an interview as a possible PhD candidate and has ended finally. The journey has not been without its fair share of ups and downs and in the end has been a rewarding experience. I would like to take these final words to acknowledge the people that have contributed to this thesis in some way.

First and foremost, I'm deeply indebted to Prof. Dr. Ir. Emiel Hensen, who has stood with me through thick and thin, guided and encouraged me through the four years I spent in the lab. I will not forget the trains trips back from our meetings in Amsterdam, where we've had exchanges that went beyond the project itself. Gave me an insight into what Emiel is and hopefully it's a feeling that is reciprocated.

Prof. Dr. Rob van Veen is gratefully acknowledged for his guidance throughout the project. I will never forget having our meetings in his Amsterdam office amongst what seemed hundreds of books and files. The subtle hints given by you, while not quite giving everything away, was something that I took time to get used to, but I can see the bigger picture now. Thank you for allowing me to work on this interesting project.

I also acknowledge the financial support provided by Shell Global Solutions for carrying out this research work and the input of dr. Hans Gosselink. The help and work of Arend-Jan van Welsenes and Patricia Giltay at Shell Global Solutions are appreciated.

I would also like to thank the reading committee – Dr. Marcello Rigutto, Prof. Dr. R.A.van Santen and Prof. Dr. Hans Geerlings for taking the time to evaluate my thesis.

Here I would also like to take the opportunity to highlight the role of Dr. Marcello Rigutto of Shell Global Solutions during my thesis research – obviously, his insightful comments on the further development of the spectroscopic technique for acidity determination were crucial. I would also like to thank Dr. Patricia Kooyman of Delft University of Technology for the TEM measurements and taking the time to discuss and improve the particle size analysis. In the end quite a number of samples ended up in the microscope and the time and effort put in for the measurements is appreciated.

The help provided by Dr. Pieter Magusin and Brahim Mezari during the innumerable NMR measurements is gratefully acknowledged. It is quite obvious that without NMR I would not have been able to discuss the synthesis of amorphous silica-alumina in such detail. Mrs. Adelheid Elemans-Mehring is acknowledged for her help with elemental analysis. These experiments were not my strongest point – your patience is appreciated.

The help provided by Wout van Herpen, Tiny Verhoeven, Robert van Teeffelen and the late Joop van Grondelle is appreciated. Of course, my nickname 'sloper' coined by Robert during

my initial months was well deserved and, although I tried hard to shed it, my colleagues would not allow! Looking back I can safely say I was not the worst going around.

To my officemate for the best part of four years - Neelesh (or Nelly) thanks for all the help in the initial weeks, the good atmosphere in the office, in the labs when at times it was just you and me. The company during the various social events is much appreciated. Good luck with your endeavours.

Subbu, your help with NMR measurements and also outside of the labs is deeply appreciated. Good luck with your future plans and was nice to have a friend like you around.

To Michel and Alessandro – not sure if I was the best guide for you both but the great work you carried out within various aspects of the project is deeply appreciated. Some of the results in this work would not have been possible without the input from you both. Thanks and good luck with whatever the future holds for you.

To my SASOL mates – Prabashini, Denzil and Abdool , it was great having you all around. Abdool – the very first game at PSV stadium I saw was with you and Han Wei, the U2 concert a few years back (and the effort it took to get those tickets) are good memories. Prabashini and Denzil , thanks a lot for the great company and the many dinners we've had together. Denzil – Champions League '08 final memories will stay with me forever. Hopefully I'll see you guys sometime in South Africa.

To my group of Spanish and Italian friends – Blanca, Chiara, David, Luigi, Jose and Dani, thanks for all the company at the FORT and beyond. The trip with a few of you guys to Barcelona and Madrid are good memories.

The administrative help provided at various times by the secretaries of the group – Elize Russell, Therese Anne Botman and Emma Eltink is gratefully acknowledged.

I would also like to thank my other colleagues of SKA for the nice time spent: Han Wei, Adelaida, Davy Neeskens, Emiel van Kimmenade, Evgeny Pidko, Yejun Guan, Volkan Degirmenci, Pieter van Grootel – thanks for everything.

Last but not the least, I'm deeply indebted to my parents and my sister who have provided me with all the encouragement I needed at various times away from home. This work would not have been possible without your help, prayers and good wishes.